FATIGUE AND FRACTURE MECHANICS ANALYSIS

OF THREADED CONNECTIONS

Feargal Peter Brennan

Submitted for the Degree of

Doctor of Philosophy

Department of Mechanical Engineering

University College London

September 1992

Abstract

This thesis aims to develop a comprehensive usable engineering design approach to the fatigue analysis of threaded connections. Although primarily concerned with the fatigue - fracture mechanics behaviour of screw threads, a broad review of stress analysis investigations in such connections is reported. Connection types, their functions and standardisation authorities are presented with the purpose of familiarising the reader with the subject and the options available to the design of threaded fasteners.

Fatigue crack initiation is discussed with reference to the specific setting of a critical thread root. A crack initiation model is adapted for employment in thread root design.

A novel weight function approach is developed for use in the determination of stress intensity factors for threaded connections. A generic solution is proposed valid for the fatigue crack growth from any thread root under any symmetrical stress system. Its development and discussion is examined in detail, remaining close to its proposed application.

Two engineering situations where the chief structural components are comprised of threaded members are taken as case studies. The background to each situation is elaborated in detail and full-scale fatigue tests were conducted on the critical components. In all, fourteen full-scale tests under constant and variable amplitude loading are reported.

The results of these are analysed and used to validate the fatigue crack initiation and propagation models. Useful observations which are helpful to understanding the fracture mechanisms operating during the fatigue of threaded connections are reported.

Material and environmental considerations are examined and a survey of relevant materials and their behaviour in environments associated with threaded fasteners is presented. The merits or otherwise of some common engineering practices are discussed with regard to fatigue.

A method has been developed for predicting fatigue life in large threaded connections under random loading. Experimental results have been gathered on two types of components used on certain oil rigs, tether joints and drill strings. The agreement found between prediction and experiment is appreciably better than by previous methods of analysis and also points to aspects open to further improvement.

Acknowledgments

The rotating bend drill collar tests reported in this thesis were undertaken by Dr R. F. Karé (TSC). I am grateful to Professor W. D. Dover for tactful and comprehensive supervision. I would like to thank the SERC for funding the most part of this work, and to Agip, BP and Norsk Hydro who permitted the use of their Drill String fatigue data in this thesis. I am also grateful to Dr J. H. Ong (Nanyang Technological University, Singapore) for access to his work prior to publication and to Dr L. P. Pook (UCL), Dr J. A. Witz (UCL) and Dr E. R. Jefferys (Conoco) for their suggestions and advice.

Table of Contents

Chapter Two - Fatigue Crack Initiation in Threaded Connections

Chapter Three - Fatigue Crack Propagation in Threaded Connections

Chapter Four - Experimental Work

Chapter Five - Failure Appraisal of Threaded Connections

List of Tables

List of Figures

Nomenclature

a	Crack depth
ACPD	Alternating current potential difference
ACFM	Alternating current field measurement
b	Fatigue strength exponet
B	Thickness of Compact Tension (CT) specimen / Relaxation exponent / Basquin exponent
BB	Bore back
BHN	Brinell hardness number
c	Crack half length / Fatigue ductility exponent
C	Paris coefficient / Compliance
C_B	Bending correction factor
C_p	Plastic flow stress distribution factor
CCT	Centre crack tension
CP	Cathodic protection
CT	Compact tension
d	Minor Diameter of Thread
da/dn	Crack growth rate
D	Major Diameter of Thread / Total damage / Ductility
DAC	Digital to analogue converter
DCPD	Direct current potential difference
D_i	Outer diameter of the pin
D_o	Inner diameter of the pin
e	Nominal strain
E	Modulus of elasticity

f	Function
$f_L(x)$	Probability distribution of applied load
$f_m(s,a)$	Weight function over a loading system 'm'
$f_S(x)$	Probability distribution of material strength
f_z	Mean zero crossing frequency
F	Westergaard stress function
$F(t)$	Wave excitation vector
g	Acceleration due to gravity
G	Strain energy release rate
$G_{yy}(\omega)$	Structure response spectrum
h	Step or Tooth height / Thread deflection factor
H	E for plane stress: $E/(1-\nu^2)$ for plane strain
H_s	Significant wave height
$HSLA$	High strength low alloy
$H(\omega)$	Structural Response transfer function
i	Tooth number / Particular stress range / Sea state
I	Irregularity Factor
Im	Imaginary part of complex function
K	Stress intensity factor (SIF)
K'	Cyclic strength or strain hardening coefficient
K_f	Fatigue concentration factor
K_{FS}^{θ}	SIF for a crack emanating from an angular corner 'θ' in a finite thickness strip
K_h	Hydrostatic stiffness matrix
K_{SF}^{θ}	SIF for a crack emanating from an angular corner 'θ' in a semifinite strip

K_t	Tether stiffness matrix
K_T	Theoretical stress concentration factor
K_ε	Actual strain concentration factor
K_σ	Actual stress concentration factor
l	Thread pitch
LEFM	Linear elastic fracture mechanics
LSF	Load stress factor
m	Crack growth exponent
M	Total mass matrix
M_0	Zeroth moment
M_2	Second moment
MPI	Magnetic particle inspection
M_t	Make-up torque
n	Number of applied cycles
n'	Strain hardening exponent
N *or* N_f	Number of cycles to failure
NA	Neutral axis
P	Applied load / Thread pitch / Potential energy
P_f	Probability of failure
P_h	Horizontal force
P_i	Probability of sea state 'i' occurring / Load on thread 'i'
P_t	Induced preload
q	Notch sensitivity
r	Notch root radius / Polar coordinate
r_i	Internal tube radius
r_y	Plastic zone size

R	P_{min}/P_{max}
R_c	Rockwell hardness number
Re	Real part of complex function
RA	Percentage reduction in area
RAO	Response amplitude operator
RPM	Revolutions per minute
R_{max}	Maximum tube radius
s	Crack surface area
S	Nominal stress
S_c	Section concentration factor
SCC	Stress corrosion cracking
SCF	Stress concentration factor
SIF	Stress intensity factor
SR	Stress relief
$S_{yy}(\omega)$	Wave elevation spectrum
t	Pin wall thickness / Time
TAC	Total alloy content
TBP	Tension buoyant platform
TLP	Tension leg platform
TPF	Taper per foot on the diameter
TPI	Threads per inch
$T(s)$	Arbitrary distributed tractions over the crack surface
T_z	Mean zero crossing period
u	Crack face displacement
U	Internal strain energy / Wind speed
W	External work done on a body / Width of CT specimen
$WASH$	Wave action standard history

WOB	Weight on bit
x	Displacement vector / Distance from notch root or crack origin in 'x' direction
$\dot{x}$	Velocity vector
$\ddot{x}$	Acceleration vector
Y	Stress intensity calibration factor
α	Slope of thread (pitch angle)
Γ	Gamma function
δ	Axial deflection of thread / Crack opening displacement
Δ	Range
ε	Strain
ε_f	True fracture strain
ε'_f	Fatigue ductility coefficient
ε_p	Plastic strain
ε_x	Longitudinal strain
ε_y	Circumferential strain / Yield strain
θ	Thread flank angle / Polar coordinate
μ	Coefficient of friction between threads
μ_c	Coefficient of friction at the pin and box shoulder
ν	Poisson's ratio
ρ	Notch / Thread root radius
σ	Stress
σ_f	True fracture strength
σ'_f	Fatigue strength coefficient
σ_{UTS}	Ultimate tensile strength
σ_y	Yield strength

$\Sigma P_i/P_i$	Ratio of axial stress to tooth bending stress
τ	Shear stress
ϕ	Complete elliptic integral of the second kind / Angle of friction / Airy stress function
ϕ'	Virtual angle of friction
ω	Frequency / Load per unit length of thread
ω_m	Mean value of load per unit length of thread
ω_o	Maximum value of load per unit length of thread
∞	Infinity

CHAPTER ONE - Introduction

1.1 Types of Threaded Connections

> *"Threaded Fasteners are considered to be any threaded part that, after assembly of the joint, may be removed without damage to the fastener or to the members being joined." [1.1]*

The screw form is a highly significant mechanical principle in that it is a basic relation between rotational and translational motion. Its applications are numerous, ranging from gears to conveyors. With the development of modern manufacturing techniques, the screw form could be utilised as an efficient reversible fastener. These fasteners or threaded connections are available in many different forms and types to suit their designed operation. Because the number of applications for these is vast, categorisation of the different connection types is difficult. However, connections are usually required to satisfy one or both of the following functions:

(a) To make a strong structural joint.

(b) To make a pressure sealed joint.

The most common geometrical characteristics used to fulfil each of these two functions are set out in the following two subsections respectively.

1.1.1 Structural Nuts and Bolts

Traditionally there have been quite a number of screw thread systems e.g. Whitworth, B.A., B.S.F., American National (Sellers) and System International. These were all basically symmetrical triangular thread forms having modifications such as rounded or flat crests and roots, and fine or coarse pitches. However, in 1965 the British Standards Institution (BSI) regarded these forms as obsolescent and made the internationally agreed International Organisation for Standardisation (ISO) metric thread its standard for structural friction grip

bolts. The basic form of this is shown in Fig 1.1 [1.2]. This thread form is recommended in three grades, general, higher - parallel shank and higher - waisted shank. The general grade is the basic thread form. The high grade parallel shank is geometrically similar but fabricated from high strength steel, despite this it is recommended that these only be used in joints subject to shear loading. The higher grade waisted shank form is shown in Fig 1.2, with this formation the limitations imposed on the parallel shank bolts due to their low shank ductility are overcome so that these can be used successfully for applications that require tensile as well as shear strength. The lower ductility of the parallel shank arrangement increases the risk of damage if the combined stresses from torque and tension approach the ultimate. The axial ductility of a connection will always be an important factor especially when designing against fatigue failure.

Within these grades other varying characteristics are bolt diameter, length, pitch and material. Obviously by increasing the bolt diameter the effective thread area is increased, reducing stress, however, this is usually only practical within certain limits. As will be seen later, the length (or number) of engaged thread(s) will not be advantageous over a critical value as the load is not evenly distributed along its length. Studies carried out on the influence of thread pitch (e.g. [1.3]) on critical tooth stress show advantageous stress reduction with increased pitch, however, threaded connections rely on frictional forces (analogous to sliding on an inclined plane - Appendix II) to hold the male and female sections firmly together. By increasing the pitch without the diameter the helix angle is increased thus introducing the possibility of untorquing the connection under axial loading.

Apart from the normal geometrical forms discussed above many other modifications to thread forms have been used. Differential pitches have successfully reduced the critical tooth stress, but the tolerances required in production make it an impractical option for general use. Also with ageing, strains within the connection may render the stress lowering modification ineffective.

Taper angles are quite common on pipe threads where the cross sectional area is limited, but the stress lowering effect is negligible when dealing with structural bolts having relatively large core cross-sectional areas.

Conical grinding of a frustum on the first threads of the nut improves fatigue life but detrimentally affects static capacity increasing the possibility of "jump out", similar effects are seen with truncated and rounded crests and roots [1.4].

Novel designs for strengthening screw fasteners are not uncommon, many producing encouraging results e.g. [1.5], however, manufacture of some of these on a large scale for general use is often unrealistic, as the effects can be so critical that relaxation due to aging strains and thread damage during service can offset their advantages with adverse effects.

1.1.2 Pressure Threaded Joints

British Standard (BS) 21 assimilates pipe threads for tubes and fittings where pressure-tight joints are made on the threads. These are tapered threads (internal or external) having the basic Whitworth form. This is shown in Fig 1.3, and is identical to the ISO standard for pressure-tight thread joints. However, because of the many diverse uses for pipe connections many modifications to the basic form exist. API's round thread coupling is quite similar and is used extensively in casings of drilled oil wells. There will always be, however, with this type of joint, a clearance between mated threads which provides a leak path. For this reason a special thread compound is required to maintain internal pressure.

The most common type of pressure sealed threaded connection is the long screw thread or modifications to this. These can be V-form or Buttress threads. Pressure-tight seals can be made directly between machined faces, with O-rings or by compressing a soft material on to the surface of the external thread by tightening a backnut against a socket. Depending upon the viscosity and pressure of the conveyed fluid, the most applicable thread form is used. For many fluids it is important that an internal rotary shoulder is present so that non turbulent

flow is encouraged by the smooth transition between pin and box. This is especially significant for multiphase flows, i.e. when conveying mixtures of fluids together (e.g. oil and gas). Gas "slugs" can under turbulent conditions create considerable dynamic bending loads contributing to fatigue damage.

Buttress threads are often used in pipe screw threads as the possibility of static failure by "jump out" is greatly reduced by the low flank angle. They also have a higher axial stiffness than V-form threads per unit thread height.

1.2 Stress Analysis of Threaded Connections

As an integral part of the fatigue analysis of any structural component, the stress analysis of the member is a critical step in the design process. Normally when assessing the structural integrity of a mechanical system, a global stress analysis is carried out on the system as a whole, determining the nominal static and dynamic stresses on individual members. This type of analysis can often be carried out using simple beam theory. However, as fatigue failure is a local phenomenon, detailed stress information is required at critical regions of the structure. These critical areas can usually be identified relatively easily using simple framework models. But quantifying the effects of local stress raising geometrical features is a far more complex process. Local stresses are important for crack initiation but are less influential on the crack growth rates and general characteristics of crack propagation.

Crack initiation may account for up to seventy percent of the total fatigue life for smoothly finished bodies, on the other hand, initiation effects may be negligible for fatigue in welded joints.

Threaded connections have complex geometrical features, suggesting them to be critical structural sections with regard to fatigue failure. It is accepted that a threaded connection does not bear its load evenly. As pointed out by Goodier [1.6], a screw and nut that fit before loading could not be in complete contact on loading due to the stretching of the screw and contracting of the nut (or vice versa). For convenience the stress analysis of such connections can be split up into two phases: (i) evaluation

of the load distribution within the entire connection, and (ii) evaluation of the stress state in the region of a loaded projection (i.e. critically loaded tooth). The former of these has received much attention, with Sopwith's theoretical solution [1.7] being probably the most rigorous. Heywood's photoelastic study of fillet stresses in loaded projections [1.8] showed that the stress concentration factor at the thread root was not solely due to the bending of the tooth but also on the proximity of the load to the fillet (i.e. notch effect). The following subsections summarise techniques used by investigators to solve the complex local stress distributions within threaded connections.

1.2.1 Theoretical Models

Classical engineering stress models are common where dealing with simple geometrical bodies, however, these theoretical solutions become quite involved, where dealing with complex geometrical facets. The first real effort at solving the load distribution within threaded fasteners was by Stromeyer in 1918 [1.9]. Here the three-dimensional loading of screw teeth is related to the planar problem of rivetted joints. Considerations were based purely upon elastic extensions. The resulting mathematical solution gives an exponential curve of load distribution, the highest load being taken by the thread or rivet furthest from the free end of a plate in shear. Acknowledging that this exponential distribution would only exist if the successive rivets were infinitely close together, led him to address the situation of a differential pitch. He thus suggested that the load distribution within a threaded connection could be optimised by varying the relative pitches. He also noted that the bending of threads affected the overall load distribution.

Den Hartog [1.10] in 1929 appreciated that an equally pitched nut and bolt when loaded will not bear its load evenly along the thread helix due to the variation of mating pitches caused by the elongation of the bolt and contraction of the nut. He also developed a parabolic solution of load distribution, considering the overall axial deformation of the nut and bolt, and equating this to the deformation of the thread. This he found by making the thread length along its helix analogous to a cantilever under shear and bending loads.

In 1948 Sopwith [1.7] developed Den Hartog's idea of equating strains within the connection. It involved computation of the relative axial displacement (or recession) between the roots of the nut and bolt threads due to:

(i) Bending deflection in nut and bolt threads (including axial recession).

(ii) Axial recession due to radial compression in the bolt and nut.

(iii) Axial recession due to the radial contraction of the bolt, and expansion of the nut caused by radial pressure between the bolt and nut.

(iv) Axial expansions of the bolt thread and of the nut thread in the same length.

This lead to a differential equation for the axial load per unit length of thread helix, which could be solved using the boundary conditions:

(i) At the free end of the bolt, the load intensity per unit distance along thread helix is zero.

(ii) The total distance along the thread helix from the bearing face of the nut is,

$$(Mean\ Thread\ Diameter) \times \pi \times (Number\ of\ Engaged\ Teeth) \qquad (1.1)$$

Sopwith's analysis assumed: (a) pitches were equal before loading, (b) there was no taper along the thread, (c) limiting friction only, (d) high stress concentrations at thread roots do not effect the overall load distribution, (e) load was concentrated at a mid-point on the thread face, and (f) no stiffening effect occurred due to rounding of thread roots. Despite these assumptions, this analysis is probably the most useful basic theoretical solution to load distribution within threaded connections to date. Sopwith used his formula to look at methods of improving the load distribution along the threads by varying pitch, length and material. He noted that a smaller pitch in the bolt than in the nut would improve distribution, similarly would a differential pitch. He observed that when the bolt was in

compression and nut in tension (turnbuckle case) the load distribution was more uniform. He also observed that a critical length of engaged thread exists, where beyond this length no advantage is reaped in overall load distribution. His final observation was that by using a nut with a lower modulus of elasticity, axial recessions in the bolt are reduced, allowing for a more uniform load distribution.

Stoeckly and Macke in 1952 [1.11] extended Sopwith's theory to incorporate a tapered thread on either nut or bolt. The effect of this taper introduces an initial axial recession at the thread roots which must be incorporated into the equation. However, the solution is not applicable to partly tapered threads, or changes in taper. The reason one element of the connection was tapered the other being parallel, was to redistribute the load within the connection, by essentially creating a variable pitch along the taper.

Yazawa and Hongo (1988) [1.12] had the fresh approach of defining a polynomial expression for load in a screw thread as a function of turning angle (angle of rotation of a point moving along the helix of a screw). This expression contained terms with undetermined coefficients and is continuous along the length of thread. To determine the coefficients, ten different constraints are formulated, by linear substitution the unknown values can be evaluated. The numerical values that result emanate from experimental results input into the constitutive expressions for five of the constraint conditions. The final equation for the axial load distribution in the screw thread of a bolt-nut connection is dependant on axial and tangential forces within the connection, also on the bending moment at the bearing surface of the bolt head. Unfortunately they did not compare their findings with other published results.

Returning to the earlier analyses of Sopwith and Stoeckly and Macke, Dragoni (1990) [1.13] modified further the old expressions to take account of the effect of nut material on the load distribution in screw threads. The three relative axial recessions described earlier (i, ii, iii) as components of Sopwith's deflection factor were redefined separating the material constants of the nut and bolt. These three terms determine to what extent the pitch can change if the screw was free

to stretch and the nut free to shorten. The predicted benefit in choosing a softer nut material was confirmed as a pronounced reduction in thread load concentration factor. A practical example was cited of a steel bolt engaging with an aluminium nut (ratio of elastic moduli respectively is 3) showing a 15 percent reduction in maximum thread load when compared to the equivalent steel bolt - steel nut connection. An interesting observation however, is that by no means can a uniform thread load distribution be reached by simply changing either screw or nut material behaviour, as an optimum relative nut compliance exists.

1.2.2 Photoelastic Models

Because a threaded fastener is a closed section, it is difficult to experimentally measure strains through sections of the joint. Photoelasticity was the first method used to experimentally measure the stress distribution within threaded connections. This method allows quantitative estimates of stresses in three dimensions of even the most complex geometries to be obtained. The most common photoelastic technique is the static stress freezing method. Specimens can be cast or machined out of photoelastic Bakelite or similar material. The specimens are loaded statically, heated in a controlled manner, followed by cooling, effectively freezing the stresses which can be sectioned and viewed with a fringe multiplying polariscope. One advantage of the photoelastic method is that it allows study of the overall stress field and in particular the stress distribution through the tube wall thickness. It is this distribution that determines the crack propagation behaviour.

Hetényi in 1943 [1.14] used a three dimensional stress freezing method to study six different nut designs. He criticised previous investigator's two-dimensional models stating that the exclusion of the three-dimensional deformations would lead to erroneous conclusions.

He studied nuts having a Whitworth thread form, however, besides the conventional control models, the following situations were investigated:

(i) Nut with an outer axial support

(ii) Nut with spherical washer

(iii) Tapered thread nut

(iv) Tapered lip nut

(v) Double start threaded nut

He found the only real advantages in load distribution occurred with tapered threads and with tapered lip nuts. For these he calculated that the maximum fillet stress value occurring in a conventional nut and bolt fastening can be reduced by about thirty percent. However, he noted that because this method of analysis assumed purely elastic conditions, application of his results should only be considered where similar conditions prevail. This would mean that these would not apply to static failure in normal temperatures, but may be applicable at elevated temperatures or under dynamic loading/fatigue conditions where the failure mechanism does not alter the overall load distribution within the connection significantly.

The majority of stress analyses on threaded fasteners were concerned with the global distribution of load through the teeth. In 1948, Heywood [1.8] used photoelasticity to study tensile fillet stresses in loaded projections. He loaded two dimensional photoelastic projections of different configurations on a strip. The models were arranged with several projections in series in order to ensure that the model behaviour was analogous to that of thread fillets. Heywood compared his results with the traditional Lewis (1893) formula for gear teeth which calculates the fillet stress from a consideration of the bending moment applied to the tooth. His results suggested that the proximity of the applied load to the fillet and not only applied bending moment greatly affected the tensile stresses. He therefore derived an empirical formula to take the load proximity into account. The effect of the first load was evaluated using a modified form of Neuber's stress concentration factors for axially loaded notches which were corrected to allow for the effect of a series of notches. As the stress concentration

due to the thread load is not on the same part of the root as that due to the axial load, a simple addition of terms would yield too great a stress. His empirical formula has the form:

$$SCF_{Total} = SCF_{Bending} + \frac{SCF_{Axial}}{1 + Constant\left(\frac{SCF_{Bending}}{SCF_{Axial}}\right)} \qquad (1.2)$$

The value of the constant differs for various thread forms. It was taken to be 1.9 for the Whitworth thread.

Heywood studied a variety of flank angles and shaped projections. Although this work did not derive any stress concentration factors for thread teeth as a function of overall applied load, the notch effect on the local tooth fillet stress was acknowledged.

Brown and Hickson [1.15], in 1952 also used a three dimensional photoelastic technique to study ordinary nuts and bolts as well as a turnbuckle (tension nut) connection. This study will be discussed later.

Gascoigne [1.16] (1987) presented photoelastic results for surface axial stress distributions for the wall surfaces opposite the threaded profiles on tubular connections. He concluded that the variations in the fillet and groove bottom stresses measured from the abrupt start of the first engaged thread were insignificant.

In 1987 Broadbent and Fessler [1.17] tested Araldite screwed tubular scale models under axial loading and preload, analysing them photoelastically. The load distribution in four models was determined from measurement of the shear stress distribution across the roots of the buttress form threads at various positions. These shear stresses were integrated between adjacent fillets to obtain the load carried by the thread. Empirical equations were derived to predict the distribution of shear forces acting on the threads and tension in the tube.

Dragoni (1992) [1.18] used a photoelastic stress freezing technique to examine the structural merits of lip nuts first reported by Hetényi [1.14]. Six araldite specimens were tested having varying thread pitches and nut lip dimensions whilst maintaining nut length and outside diameter. The only variable found to have any significant effect upon the maximum thread stress was the axial lip length. It was reported that a maximum stress reduction of forty percent was achieved with a nut lip extending for sixty percent of its height.

1.2.3 Strain Gauged Models

A useful method of finding surface stress in a member is to measure the local strain or deformation. There are various methods whereby these can be found. Often acrylic models are made of a scaled down member so that deformations can be measured in a laboratory. The most common type of strain gauge used is based on electrical resistance. These work on the principle that the change in electrical resistance of a conducting wire is directly proportional to its extension. Strains in different planes can be measured and analysed using Mohr's strain circle to yield principal strains, hence principal stresses. However, it is often impossible to put such gauges and their connecting wires on the surface of critical thread roots. Goodier (1940) [1.6] studied the distribution of load on the threads of screws and the types of deformation effecting it using extensometer measurements made on the outside of the nut. He measured radial extension with a lateral roller extensometer. This is an optical instrument from which the separation of two blocks (one on bearings) can be measured. The axial displacements were measured using a Martens extensometer, which is also an optical-mechanical device. The deformation characteristics of load concentrations on different parts of the thread were found using a bolt with all its threads removed except for one. This caused an artificial concentration of load at the nut thread. The bolt was set successively at the free end, middle and base of the nut. Only the resulting deformations for the base position resembled actual nut deformations for fully threaded nuts and bolts. He concluded that in actual nuts and bolts there is little load carried at the free end or middle, but a concentration at the base, the concentration being less marked at the higher loads.

To complement their theoretical solution for the effect of taper on screw-thread distribution [1.11], Stoeckly and Macke carried out experimental tests measuring displacements under loading. Axial displacements of the threads were determined by drilling small exploratory holes to the desired depth close to the base of the threads in both the bolt and nut. These displacements were measured using a dial indicator. Trials indicated that the repeatable accuracy of readings was in the order of 0.0003in. These axial displacements of the base of the bolt thread, relative to the base of the nut thread were determined for various axial positions along the nut. The axial thread displacements were converted to thread loads by coefficients determined from single and triple-threaded tests i.e. similar to those done by Goodier. Some important observations made from their studies are as follows:

(i) Within the elastic limit, the proportion of total load carried by each thread varies very little with applied load.

(ii) As the outside diameter of the nut is increased, the critical load concentration decreases only slightly.

(iii) The coefficient of friction between the bolt and nut as affected by lubrication has little effect on the thread load distribution.

(iv) For tapered threads, the total load carried by the bottom threads is decreased, and by the top threads (towards free end) increased, the amount depending upon the taper and total load imposed upon the bolt.

Seika, Sasaki, and Hosono (1974) [1.19], investigated stress concentrations in nut and bolt thread roots using the copper electroplating method of strain analysis. This is based on the principle that when a copper-plated specimen is subjected to cyclic strain, micrograins in the copper gradually grow provided that both the amplitude of cyclic shearing strain and the number of cycles are above certain threshold values. A value called the "proper strain" is the lowest value of shearing strain of the copper-plating for an assigned number of cycles. Seika *et al.* used plated round bar specimens for calibration by measuring the etched grains and relating these to the number of cycles at particular stress levels. From this the

stresses at each thread root could be obtained. Using this method they studied nuts with tapered lips and reported that increasing the depth of the taper reduced the maximum stress at the bolt-thread roots, but reduced the strength of the nut, leading to an optimum taper for overall strength of the connection. Also it was reported that using a nut with a lower modulus of elasticity reduced the stresses at the bolt thread roots.

The study revealed that when the distance between the nut face and the threaded end of the bolt was less than four pitches, the maximum stress at the root of the first engaged thread of the nut was raised remarkably due to the mutual interference of stress concentrations.

1.2.4 Finite Element Models

The introduction of modern computers made it feasible to use numerical techniques to solve differential equations which govern continuous systems. These continuums can be divided into substructures called finite elements, which are inter-connected at points called nodes. For stress analysis, the governing equations for each finite element are based on the principle of virtual work, in which all the integrals are carried out over the reference volume and surface of the element. Each element will have a governing stiffness matrix which can be nonlinear. This is the basic relationship between nodal loads and displacements. The nodal displacements and loads are transferred into a global coordinate system which maintains the continuity of the entire arrangement.

Depending upon the application and nature of the stress analysis, different element types can be used e.g. thin shell or three dimensional brick (isoparametric) elements. Naturally the more complex the elements and finer the mesh, the more computational effort is required. These must be optimised in terms of the requirements of the study.

In 1971 the first notable finite element analysis of threaded connections was reported by Pick and Burns [1.20]. They analysed the stress distribution of thick

walled pressure threaded connections. However, the analysis was two dimensional and the helix angle of the pitch was ignored i.e. the mesh was axi-symmetric about the longitudinal axis of the pipe. Their results compared well with those of previous studies, indicating the potential of future finite element stress analyses. In 1979 Bretl and Cook [1.21] used finite elements to model a threaded connection without geometrically defining the threads. Instead the zone which the threads normally occupy was replaced by a zone of orthotropic elements, which allowed for circumferential and radial displacement. The acquisition of the numerical properties associated with this orthotropic zone was made by a trial and error method, comparing results with Hetényi's [1.14] photoelastic results. Unfortunately the model was not verified with results from other studies, and hence it is impossible to estimate its value accurately.

Tanaka *et al.* [1.22], [1.23] developed a substructure approach to the finite element analysis of contact problems such as in threaded connections. Continuous elastic bodies can be modelled well with finite elements, however in threaded connections continuity is broken at contact surfaces such as those between thread flanks, bearing surface of the nut or under-head of the bolt. These analyses were some of the first closed loop finite element techniques to model elastic discontinuous structures with many contact surfaces and multiple connected elastic structures.

Patterson and Kenny (1986) [1.24], noted that a discrepancy existed between experimentally obtained photoelastic results and Sopwith's theoretical solution for the load distribution in threaded connections. This occurs at the loaded end of the bolt, and is due to the thread runout on the nut. This runout causes the incomplete thread to become progressively more flexible as the nut face is approached. It should be highlighted that this is only one form of runout peculiar to parallel threads, tapered threads normally runout in a manner that the thread becomes progressively less flexible. The result is a reduction of the load carried by these threads. Patterson and Kenny modified Sopwith's theory so that the deformation of the threads could be modelled using finite elements. They modelled three teeth in series using two dimensional elements. The core wall

was restrained along the axial direction and the load on each tooth face was uniformly distributed. The incomplete threads were modelled separately. The deflection factors for each tooth were calculated using the finite element analysis technique where,

$$h = \frac{\delta E}{\omega} \tag{1.3}$$

h is the thread deflection factor
δ is axial deflection of thread
ω is the load per unit length of thread
E is the modulus of elasticity

These were then substituted into Sopwith's modified solution.

This shows where finite element analysis may have its most effective role. The disadvantages of the method are, that it is time consuming and requires a lot of computational effort. However, if certain aspects of a complicated geometry are removed, analysing only extreme complex forms and resubstituting the results of these back into an analytical or theoretical solution, the efficiency of the analysis may be greatly increased. Newport [1.3] used a stress analysis technique proposed by Glinka, Dover and Topp [1.25] which incorporated a finite element technique to model the stress concentration due to the notch effect of the teeth. Three axi-symmetric thread teeth in series were analysed. Three teeth were chosen to ensure that the loading points and restraints applied to the ends of the model did not effect the stress distribution around the centre tooth, where the stress concentration factors were derived. Such analyses were carried out on a variety of differing aspects of the thread geometry i.e. varying pitch, tooth height, wall thickness and fraction of load taken by the tooth to the overall applied load. A parametric equation was derived from the results for the stress concentration factor in terms of the above variables.

In 1989 Rhee [1.26] presented a full three dimensional finite element analysis on a threaded joint. This was analysed and compared with a traditional two dimensional axi-symmetric model. The study concluded that the two dimensional finite element analysis underpredicts the critical stress by twenty percent, and that the pitch has a significant effect on the stress distribution. However, an extremely large pitch was used in the analysis relative to the diameter of the thread. This most certainly would have contributed to an amplification of the stress variation about the helix. Also thread run-out was neglected.

1.2.5 Electrical Analogue Model

Bluhm and Flanagan in 1957 [1.27] proposed the stress analysis of threaded connections could be considered as consisting of two phases: (a) Evaluation of the load distribution from thread to thread. (b) Evaluation of the tensile fillet stresses in the most severely loaded thread. For the latter case they recommended a photoelastic study of projections, or the use of Heywood's empirical equation [1.8] based on photoelastic experiments. They suggested an analytical solution to evaluate the load distribution within the connection. This was based on the following assumptions:

(i) Material behaves elastically.

(ii) Primary deflections are due to bending of the thread and axial movement of the nut or bolt body.

(iii) Forces exchanged between threads are transferred as point loads.

(iv) Helix angle of the thread is neglected.

An idealised mechanical system of cantilevers was developed where the bending deflections of the threads were transformed into axial deflections along with those of the nut and bolt body. From this an electrical analogy was made, where the current passing through the system is analogous to the applied load. Resistances in series were analogous to the deflections in the nut and bolt bodies,

those in parallel analogous to the teeth bending deflections. An electrical analogue was built with variable resistors, potentiometers and input current. Their results were not compared with experimental results, however, their resulting load distribution had all the features of previous respected studies.

Dover and Topp [1.28] in 1984, modelled the load distribution using a similar electrical analogy technique. However, this was produced in the form of a Fortran program making it much more flexible and usable. The model was developed to take account of tapered threads and preload. It was found that by using a simple finite element analysis to calculate the stiffness of the teeth, initial assumptions such as point loading and no consideration of thread runout could be forgotten. This method used with a parametric study (such as that discussed in Section 1.2.4) to evaluate the stress concentration at the critical tooth can yield a quick accurate design solution for the maximum stress in a threaded connection.

1.2.6 Review

The previous subsections described the main advancements in studying the stresses within threaded connections. However, it is necessary to compare the results of these in order to evaluate the validity of these approaches. The early investigations by Stromeyer [1.9] and Den Hartog [1.10] were proved to be valid by Goodier's [1.6] experimental extensometer results. All three agreed that a load concentration occurred on the first engaged thread of the bolt. Sopwith [1.7], who expanded Den Hartog's equal strain theory, also compared his theoretical results with Goodier's and Hetényi's [1.14] three dimensional photoelastic results. Agreement with Goodier's results was excellent, however, Hetényi's load diminished quickly after a peak at a point of the first fully engaged bolt thread. Sopwith explained this discrepancy by assuming that it was due to the proximity of the much more lightly stressed full section of the shank (Fig 1.4).

However, Patterson and Kenny [1.24] modified Sopwith's theoretical solution, measuring tooth deflection using finite element analysis. They were able to show

that Hetényi's results were correct and due to the thread runout on the nut. They compared their hybrid solution with two photoelastic experimental results as shown in Fig 1.5. Their deflection factors were over three hundred percent greater than those obtained by Sopwith, this they attributed to Sopwith's fixed cantilever assumption and his application of point loads, where photoelastic models suggested a distributed loading on the teeth. D'Eramo and Cappa [1.29] similarly modelled the individual teeth using finite elements evenly distributing the load along the flank. The deflection factors were then resubstituted into a Sopwith / Maduschka type formulation. These compared well with experimental strain gauge results made on the outside of the nut and interpolated to the thread root stresses.

Brown and Hickson's [1.15] three dimensional photoelastic study was carried out to try to verify Sopwith's formula. Their results for the tapered nut lip and standard bolt agreed very well with Hetényi's results (and of [1.18]) and also identified the discrepancy in load taken at the first engaged bolt thread where Sopwith's formula breaks down.

Maruyama's (1974) copper electroplating and finite element analyses [1.30] found that the use of a softer nut material reduces the stress in the critical bolt thread roots as suggested by Sopwith and confirmed by Dragoni [1.13], also that increasing the nut length reduced the maximum fillet stress, but with diminishing effect up to a critical length as predicted again by Sopwith.

Stoeckly and Macke's [1.11] theoretical and experimental analysis of tapered threads was once more in agreement with Den Hartog's and Sopwith's suggestions that the taper would essentially provide a differential pitch yielding a more uniform load distribution. Newport, [1.3] whilst developing parametric equations from finite element analyses, showed agreement with Maruyama's copper electroplating method demonstrating that increasing the fillet radius had little effect on load distribution but decreased the maximum root stress. Topp

[1.31] compared his electrical analogy method with photoelastic tests carried out Fessler [1.17], these showed a good likeness, but when using a hybrid finite element-electrical analogue method the results were even closer.

1.3 Fatigue Analysis

> *Fatigue: "Failure of a metal under a repeated or otherwise varying load which never reaches a level sufficient to cause failure in a single application.", [1.32]*

Structure or component failure can occur through many different modes. These failure modes can be expressed as static, e.g. yielding and buckling or dynamic e.g. impact and fatigue. Because of different areas of uncertainty associated with materials and loading on a structural component, the philosophical approach to strength assessment demands the need for a probabilistic or reliability analysis [1.33]. Such a study attempts to compute the probability of structural failure. This approach can be applied in two ways:

(i) Directly to the overall component by defining a probability density function in terms of static applied load or fatigue life for the overall structure.

(ii) As an aid to determining partial safety factors for each area of uncertainty within the design.

The evaluation of probability density functions or spectra generally relies on physical measurements to which mathematical distributions are applied. A simple example of the reliability approach is as follows:

The probability of applied load occurring is expressed by the function '$f_L(x)$' whereas the strength of material can be represented by '$f_S(x)$'.

The probability of failure, 'P_f' is given by the product of probabilities of events, summed over all possible outcomes.

i.e.

$$P_f = \int_{-\infty}^{\infty} f_L(x) f_S(x) dx \tag{1.4}$$

The reliability of the component is:

$$1 - P_f \tag{1.5}$$

As can be appreciated, under static failure modes where the loading and material characteristics can be relatively easily determined, safety factors can be applied to allow for any deviations from the designed system characteristics that may occur. However, with dynamic failure modes, the equation gets more difficult as global along with local structural and material attributes can progressively alter. The following subsections will deal with some of the more common techniques used to assess the reliability of components against fatigue failure.

1.3.1 S-N Approach

When dealing with fatigue failure of a structure, it is necessary to define foremost what constitutes failure. For example, with offshore steel platforms, sections of the structure may fracture. However, because of the high degree of redundancy in the structure, the overall platform is rarely in a situation where overall failure might occur. Also with threaded connections, the most highly stressed tooth may fracture, redistributing the overall load among its successive teeth, but does not necessarily mean overall failure of the connection. For this reason the constant amplitude cyclic stress range '*S*' to the number of cycles to failure '*N*' relationship has to be specific for a structure/component as well as for the material from which it is fabricated. For ferrous alloys and metals, their strength under cyclic stressing is usually given by the endurance or fatigue limit, i.e. the maximum stress range that can be repeatedly applied an infinite number of times without causing fracture. Most nonferrous metals do not exhibit an endurance limit, but in these cases the fatigue strength is defined as the maximum cyclic stress range that can be applied without causing fracture for a specified number of cycles (normally 1.0×10^7 cycles).

An S-N curve is obtained by fatigue testing a batch of specimens of equal geometry, and material in a controlled environment. Each specimen is tested at a different cyclic stress range and the resulting empirical curve is obtained by plotting results usually on logarithmic axes. These normally give straight line fits i.e. power law dependence.

e.g. $$N = C(\Delta S)^B \tag{1.6}$$

where 'C' and 'B' are constants specific to that specimen and test environment. This is normally known as Basquin relationship [1.34]. Coffin and Manson [1.35] suggested that it is better to use plastic strain range rather than stress range especially for low cycle fatigue. However, it is normally more difficult to measure the actual local plastic deformation than a nominal stress range remote from the failure site.

In practice most fatigue loading is not constant amplitude, both the frequency and amplitude being variable. Where no environmental corrosive effects are present, the frequency of stressing is not damaging. Miner [1.36] proposed a linear summation hypothesis whereby damage fractions caused by differing cyclic stress ranges could be summed to give the overall damage, e.g.

$$D = \Sigma_{i=1}^{n}\left(\frac{n_i}{N_i}\right) \tag{1.7}$$

Where,

D is the total damage to the structure

n is the number of stress ranges

n_i is the number of cycles at stress range 'i'

N_i is the number of cycles to failure at stress range 'i'

if $D = 1$, then failure would occur

However, work carried out by Suresh [1.37] and Druce, Beevers and Walker [1.38] has suggested that high-low block loading sequences result in crack retardation or arrest.

S-N curves are also specific to R loading ratios (P_{min}/P_{max}). Mean stress is usually accounted for by use of Goodman [1.39] diagrams. These are empirical relationships which equate non zero mean stress ranges to equivalent fully reversed cyclic stress ranges.

1.3.2 Deterministic Approach

This design method identifies average nominal load ranges. The most damaging of these are chosen and used to determine the nominal stress ranges they induce on a component. Using S-N curves or otherwise the damage fraction for each average stress range is calculated using their associated number of cycles. Using Miner's rule the total damage can be calculated, hence predicting fatigue life. This approach is useful only where blocks of similar amplitude loading can be identified and where these blocks are not very numerous. Depending upon which method is employed to calculate the fatigue damage overloading effects may or may not be taken into account.

1.3.3 Probabilistic Approach

Fatigue analysis may involve modelling of uncertain parameters e.g. environment, loading, structural response and fatigue strength. As fatigue strength is generally formulated for constant amplitude stressing, a probabilistic approach is required to define a damage accumulation law for random loading encountered in practice. An example of such an approach to determine the fatigue damage of an offshore structure using an S-N relationship is highlighted below [1.40].

(i) Obtain the one sided wave elevation spectrum, '$S_{yyi}(\omega)$' for a particular sea state 'i'

(ii) Evaluate the hot spot stress amplitude transfer function '$H(\omega)$' for each critical part of the structure from a global structural dynamic analysis.

(iii) The hot spot stress spectrum for each critical section in sea state 'i' is found:

$$G_{yyi}(\omega) = |H(\omega)|^2 S_{yyi}(\omega) \tag{1.8}$$

(iv) The zeroth and second moments of area, 'M_{0i}' and 'M_{2i}' of '$G_{yyi}(\omega)$', and hence the mean zero crossing period, 'T_{zi}' are evaluated,

$$M_{ni} = \int_0^{\infty} \omega^n G_{yyi}(\omega) d\omega \tag{1.9}$$

$$T_{zi} = 2\pi \sqrt{\frac{M_{0i}}{M_{2i}}} \tag{1.10}$$

(v) The probability of sea state 'i' occurring 'P_i', is obtained from the scatter diagram (or some other analysis of occurrence), and the number of cycles per annum 'n_i' is calculated,

$$n_i = \frac{P_i (31.5576 x\ 10^6)}{T_{zi}} \tag{1.11}$$

(vi) An appropriate S-N curve is chosen, of the form:

$$N_i = Const(\Delta\sigma_{Hotspot\,i})^B \tag{1.12}$$

where 'B' is a constant

(vii) Assuming a narrow band response, the stress range probability density function '$f(\Delta\sigma_{Hotspot\,i})$' will be in the form of a Rayleigh distribution, i.e.

$$f(\Delta\sigma_{Hotspot\,i}) = \frac{\Delta\sigma_{Hotspot\,i}}{4M_{0i}} \quad \exp\left(-\frac{\Delta\sigma_{Hotspot\,i}^{2}}{8M_{0i}}\right) \tag{1.13}$$

(viii) Damage for seastate 'i' is given by,

$$D_i = \int_0^{\infty} f(\Delta\sigma_{Hotspot\,i}) \quad \frac{n_i}{N_i} \quad d(\Delta\sigma_{Hotspot\,i}) \tag{1.14}$$

(ix) Integration can be performed as follows:

$$D_i = \int_0^{\infty} \frac{\Delta\sigma_{Hotspot\,i} \quad \exp\left(-\frac{\Delta\sigma_{Hotspot\,i}^{2}}{8M_{0i}}\right) n_i}{4M_{0i} \quad Const(\Delta\sigma_{Hotspot\,i})^{B}} d(\Delta\sigma_{Hotspot\,i})$$

let, $$t = \frac{(\Delta\sigma_{Hotspot\,i})^2}{8M_{0i}}$$

$\Rightarrow$ $$dt = \frac{\Delta\sigma_{Hotspot\,i}}{4M_{0i}} d(\Delta\sigma_{Hotspot\,i})$$

also $$(\Delta\sigma_{Hotspot\,i})^{B} = t^{\frac{B}{2}} \quad (8M_{0i})^{\frac{B}{2}}$$

$\Rightarrow$ $$D_i = \frac{(8M_{0i})^{\frac{B}{2}} n_i}{Const} \quad \int_0^{\infty} e^{-t} t^{\frac{B}{2}} dt$$

Using Gamma function,

$$D_i = \frac{(8M_{0i})^{\frac{B}{2}} n_i \Gamma\left(1+\frac{B}{2}\right)}{Const}$$

i.e.

$$D_i = \frac{(8M_{0i})^{\frac{B}{2}} n_i B \Gamma\left(\frac{B}{2}\right)}{2\,Const}$$

But

$$n_i = \frac{P_i\, 31.5576 x\, 10^6 M_{2i}^{\frac{1}{2}}}{2\pi M_{0i}^{\frac{1}{2}}}$$

$$\Rightarrow \quad D_i = \frac{(8M_{0i})^{\frac{B}{2}} B \Gamma\left(\frac{B}{2}\right) 2.5113 x\, 10^6 P_i M_{2i}^{\frac{1}{2}}}{Const \quad M_{0i}^{\frac{1}{2}}} \qquad (1.15)$$

(x) The above equation can be used to calculate the fatigue damage per annum for any number of seastates using a Miner's summation.

1.3.4 Cycle Counting Variable Amplitude Time Histories

Because each structural component or mechanical process undergos its own specific loading sequence, it would be impossible to provide material or component fatigue behavioural information for every different permutation and combination of load sequence. For this reason most material and structure fatigue properties are expressed in terms of a constant amplitude stress range. This gives rise for the need to break down broad band irregular loading sequences into individual cycles. The most common methods for doing this are:

Range Pair Cycle Counting Method.
Rainflow Cycle Counting Method.

Under narrow band variable amplitude loading, interaction effects between successive cycles are not as pronounced as in the case of broad band loading. Often in these situations it is convenient to calculate the root mean square (RMS) and mean stress amplitudes of the time history and treat the loading as its equivalent constant amplitude stress range [1.41].

(i) Range Pair Cycle Counting

With this method, small cycles are counted first in terms of mean stress and stress range. Their reversal points (peaks and valleys) are then eliminated from further consideration. This procedure may continue a number of times depending on the diversity of the stress ranges. Ultimately the results of the count can be expressed in a table of the occurrence of ranges with their corresponding mean values. Depending on the accuracy required, the range and mean increments can be scaled, however, there will usually be a compromise between actual accuracy obtainable and computational effort required.

(ii) Rainflow Cycle Counting

Fig 1.6 shows a section of a broad band time series. Considering the series to be plotted vertically downwards, a water flow is imagined to flow down the record. Flow starts at the beginning of the record, then at the inside of each peak in the order in which peaks are applied. It only stops when it encounters a flow from a higher peak, a flow from a higher level, or when it reaches the end of the series. Each separate flow is counted as a half cycle, in this case (Fig 1.6) there are five and a half cycles. Each cycle will have associated with it a pair of ranges and mean as before, and can be tabulated similarly. The advantages of rainflow cycle counting is that cycles can be identified as closed stress-strain hysteresis loops [1.42].

1.4 Fracture Mechanics Evaluation of Crack Growth

g stress intensity factor to the fatigue crack growth rate

As mentioned in Appendix I, a Linear Elastic Fracture Mechanics (LEFM) analysis is the most accepted approach to modelling the fatigue crack growth within a structural component. This approach seeks to define local stress and strain conditions in terms of global parameters, load and geometry. When dealing with complex loading and geometrical systems, it becomes difficult to relate the conditions at the crack tip to those remote from this critical area of interest. However, it is possible to combine experimental observations with simplified physical models (often incorporating numerical analyses) to condense a difficult theoretical three dimensional problem into a simpler workable form.

The idea of stress concentration factors has been around for quite some time. Inglis' well known relationship between the local stress and applied nominal stress in a plate with a notch:

$$\sigma_{max} = \sigma_{applied}\left(1 + 2\sqrt{\frac{a}{\rho}}\right) \tag{1.16}$$

where,

a = Crack or Notch Length
ρ = Crack or Notch Radius

works well for simple geometries. However, problems arise when applying this to sharp cracks, as ρ approaches zero, σ_{max} approaches infinity.

This paradox was resolved by Griffith who considered the energy required to separate atoms within the crystalline lattice of a solid. This theory was later extended to subcritical crack growth in metals by Irwin and Orowan to give,

$$G = \frac{dW}{ds} - \frac{dU}{ds} = \frac{1}{2} P^2 \frac{dC}{ds} \tag{1.17}$$

where,

G is the strain energy release rate
s is the crack surface area
W and U are the external work done on the body and its internal strain energy respectively
P is the applied load
C is the compliance of the body

Using expressions (based on stress functions) for the stress normal to the crack line, it was possible to relate the local stress at the crack tip to the nominal stress applied to the body. This made use of the relations,

$$(for\ plane\ stress) \qquad G = \frac{(\sigma\sqrt{\pi a})^2}{E} \tag{1.18}$$

$$(for\ plane\ strain) \qquad G = \frac{(\sigma\sqrt{\pi a})^2}{E}(1-\nu^2) \tag{1.19}$$

These relations justify the calculation of the strain energy release rate from a purely elastic local stress distribution. For convenience the stresses in the vicinity of a crack tip can be expressed in the form:

$$\sigma(r,\theta)_{ij} = \frac{K}{\sqrt{2\pi r}} f_{ij}(\theta) \tag{1.20}$$

where r and θ are the polar coordinates taken in the crack plane and from its leading edge.

'K', the stress intensity factor combines the nominal stress, crack and overall geometry so that the local stress field can be described by this single parameter. Stress intensity factors can be expressed in the general form,

$$K = Y\sigma_{nom}\sqrt{\pi a} \tag{1.21}$$

Y is a geometry correction factor
a is the crack depth

From this it can be appreciated that 'K' is the key parameter in fracture mechanics and much of the analysis is concerned with attaining suitable solutions for the geometry correction factor 'Y'.

1.4.1 Analytical SIF Solutions

The usefulness of stress intensity factors in the solution of fatigue crack growth problems is now well established. The advantage of this method is the assumption that the behaviour of a sharp crack is determined by the stress field at the tip, making it necessary to determine the stress intensity factory only. All theoretical approaches to solving the near crack tip stress state revert to the basic elasticity expressions of equilibrium (1.22) and compatibility (1.23).

$$\frac{\partial\sigma_{xx}}{\partial x}+\frac{\partial\sigma_{xy}}{\partial y}=0 \tag{1.22}$$

$$\frac{\partial\sigma_{yy}}{\partial y}+\frac{\partial\sigma_{xy}}{\partial x}=0$$

$$\frac{\partial^2\sigma_{xx}}{\partial x^2}+\frac{\partial^2\sigma_{xx}}{\partial y^2}+\frac{\partial^2\sigma_{yy}}{\partial x^2}+\frac{\partial^2\sigma_{xx}}{\partial y^2}=0 \qquad (1.23)$$

To simplify the model, the above equations are only a consideration of a plane stress condition.

Airy, first demonstrated that a function 'ϕ' in 'x' and 'y' could satisfy the elastic equilibrium and compatibility equations which would enable stresses to be related to the applied loads. These functions could be applied as follows:

$$\sigma_{xx}=\frac{\partial^2\phi}{\partial y^2}$$

$$\sigma_{yy}=\frac{\partial^2\phi}{\partial x^2} \qquad (1.24)$$

$$\sigma_{xy}=-\frac{\partial^2\phi}{\partial y\partial x}$$

for equilibrium and,

$$\frac{\partial^4\phi}{\partial x^4}+2\frac{\partial^4\phi}{\partial x^2\partial y^2}+\frac{\partial^4\phi}{\partial y^4}=\nabla^2(\nabla^2\phi)=0 \qquad (1.25)$$

where,

$$\nabla^2=\frac{\partial^2}{\partial x^2}+\frac{\partial^2}{\partial y^2}$$

for compatibility.

If the function satisfies the compatibility equation, the stresses are automatically determined by equations (1.24) above, provided the boundary conditions are also satisfied.

e.g. for a centre crack in an infinite plate,

$$\sigma_{xx} = 0$$

$$\sigma_{yy} = 0$$

$$\sigma_{xy} = 0$$

for $-a \leq x \leq a, \quad y = 0$

Westergaard [1.43] formulated an Airy stress function 'F', having the form:

$$F_I = Re(\bar{Z}_I) + y Im(\dot{Z}_I) \tag{1.26}$$

where,

$$\frac{d\bar{Z}_I}{dz} = \dot{Z}_I, \quad \frac{d\dot{Z}_I}{dz} = Z_I$$

$$z = x + i\,y$$

'I' refers to mode I

The simplest configuration of a centre crack in an infinite sheet subjected to tension at infinity is solved by,

$$Z_I = \frac{\sigma z}{\sqrt{z^2 - a^2}} \tag{1.27}$$

Using this approach the stress intensity factors are given [1.44] as,

$$K_N = \sqrt{2\pi}\lim_{z \to a} \quad (\sqrt{z-a}\, Z_N) \tag{1.28}$$

where,

$$N = modes\ I, II, III$$

By introducing a further complex variable 'ζ' of which 'z' is a function, a mapping technique can be set up, where 'ζ' corresponds to the geometry of a unit circle or a half-plane in an infinite body [1.45]. For computational ease, the function 'Z' can be expressed as a polynomial or expanded into a Fourier series.

Irwin [1.46] used Westergaard's approach and expressed the stresses in the vicinity of a crack tip in the form:

$$\begin{pmatrix} \sigma_{xx} \\ \sigma_{yy} \\ \sigma_{xy} \end{pmatrix} = \frac{K \cos\frac{\theta}{2}}{\sqrt{2\pi r}} \begin{pmatrix} 1 - \sin\frac{\theta}{2}\sin\frac{3\theta}{2} \\ 1 + \sin\frac{\theta}{2}\sin\frac{3\theta}{2} \\ \sin\frac{\theta}{2}\cos\frac{3\theta}{2} \end{pmatrix} + terms\ of\ order\ r^0 \tag{1.29}$$

see Fig 1.7 for polar notation.

1.4.2 SIF Solutions from Finite Element Analysis

Finite element analysis can be used in a number of ways to evaluate stress intensity factors. The stresses and displacements can be correlated at the nodal points of the finite element mesh with those at the crack tip using the expression,

$$K_I = \sigma_y(r,0)\sqrt{2\pi r} \tag{1.30}$$

'K_I' can be determined from '$\sigma_y(r,0)$' at small distances from the crack tip. However, it was noted by Cartwright and Rooke [1.44] that more accurate results are obtained by correlating the displacement of nodes 'u_y' at small distances 'r' from the crack tip i.e.:

$$K_I = \frac{E u_y}{4(1-\nu^2)}\sqrt{\frac{2\pi}{r}} \tag{1.31}$$

Another method used from a finite element analysis is termed an indirect method and is based on an energy integral over the entire crack surface area.

$$W = \frac{1}{2}\int_s \sigma_{ij} u_i \, ds \tag{1.32}$$

σ_{ij} is the stress distribution along the line on which the crack will grow

u_i is the displacement of the crack face due to σ_{ij}

The stress intensity factor can be determined by evaluation of 'W' numerically at a number of crack lengths. This can be differentiated with respect to crack area to give the strain energy release rate 'G' and hence 'K_I' using the expressions (1.18)(1.19).

The final finite element approach generally used is the employment of special elements. These elements require that the analytical form of the singularity be known, and would involve a specialist governing program.

Using the results of a three-dimensional finite element analysis employing special SIF elements, Newman and Raju [1.47] developed a stress intensity factor equation for semielliptical surface cracks. It is probably the most accurate generally applicable solution to date. It applies for cracks of arbitrary shape in finite plates for both tension and bending.

1.4.3 Experimental SIF Solutions

Any technique from which the local stress state within a body can be evaluated can potentially be used to evaluate stress intensity factors. A three dimensional frozen stress photoelastic analysis can be utilised in this way [1.48]. This can be accomplished by either measuring the maximum shear stress '$\sigma_{xy\,max}$' on lines perpendicular to and through the crack tip so that,

$$\sigma_{xy\,max} = \frac{(K_I^2 + K_{II}^2)^{\frac{1}{2}}}{2\sqrt{2\pi r}} \tag{1.33}$$

And also on a line outside and collinear with the crack given by

$$\sigma_{xy\,max} = \frac{K_{II}}{\sqrt{2\pi r}} \tag{1.34}$$

Or by directly using the approximate relationship,

$$K_I \sim \frac{\sqrt{\pi\rho}}{2}\sigma_{max} \tag{1.35}$$

Since the minimum principal stress at the crack tip is zero, 'σ_{max}' can be determined directly [1.49].

Another experimental technique is using the fatigue crack growth rate in a body, where the material constants have been found using a specimen for which the stress intensity factor is known as a function of stress and crack length e.g. Compact Tension (CT) specimen (Appendix I), rearranging the Paris law,

$$\Delta K = \left(\frac{1}{C} \frac{da}{dn} \right)^{\frac{1}{m}} \tag{1.36}$$

1.4.4 Weight Function SIF Solutions

Bueckner [1.50] (1970) proposed a novel principle for the computation of stress intensity factors for any symmetrical load system acting on a linear elastic body in plane strain. He suggested that if the displacement field and stress intensity factor are identified as functions of crack length, then the stress intensity factor for any other symmetrical load system on the same body can be determined directly. In effect the stress intensity factor can be represented in the form of a weighted average of the applied loading modes. These weight functions can be derived from the boundary displacements of the individual stress fields. The stress intensity factor can be expressed:

$$K = \int f_m(s,a) T(s) ds \tag{1.37}$$

where,

s is the crack surface area
a is the crack depth
$T(s)$ are arbitrary distributed tractions over the crack surface
$f_m(s,a)$ is a known weight function determined over a loading system 'm'

Rice [1.51] derived the weight function as follows:

From Griffith's equations (1.17),

$$G = \frac{1}{2} P_i P_j \frac{\partial C_{ij}(a)}{\partial a} = \frac{K_i(a) K_j(a)}{H} \tag{1.38}$$

$H = E$ for plane stress

$H = \frac{E}{(1-\nu^2)}$ for plane strain

where P_i and P_j are loads for two different loading patterns applied to the same configuration.

As K is a function of applied load, it can be written:

$$K = k(a)P \tag{1.39}$$

$$\Rightarrow \quad \frac{1}{2} \frac{\partial C_{ij}(a)}{\partial a} = \frac{k_i(a) k_j(a)}{H} \tag{1.40}$$

Letting a full solution be known for one of the loads 'm', then,

$$k_i(a) = \frac{H}{2} \frac{\partial C_{im}(a)}{\partial a} \frac{1}{k_m(a)} \tag{1.41}$$

$$\Rightarrow \quad K = \frac{H}{2} \frac{P_m}{K_m} \frac{\partial C_{im}(a)}{\partial a} P_i \tag{1.42}$$

So the weight function will be of the form,

$$f_m(s,a) = \frac{H}{2K_m}\frac{\partial C_{im}(a)}{\partial a}P_i \tag{1.43}$$

but,

$$\frac{1}{2}\frac{\partial C_{ij}(a)}{\partial a}P_iP_j = \frac{1}{2}P_i\frac{\partial u_i}{\partial a} \tag{1.44}$$

$$\Rightarrow \quad f_m(s,a) = \frac{H}{2K_m}\frac{\partial u_m(s,a)}{\partial a} \tag{1.45}$$

Niu and Glinka [1.52] developed a weight function for edge cracks emanating from the weld toe in T-butt joints of differing weld angles. Considering the analytical conformal mapping solution of Hasebe *et al.* [1.53], Niu and Glinka used the relationship,

$$\frac{K_{FS}^{\alpha}}{K_{FS}^{\beta}} = \frac{K_{SF}^{\alpha}}{K_{SF}^{\beta}} \tag{1.46}$$

where,

K_{FS}^{α} is the SIF for a crack emanating from an angular corner 'α' in a finite thickness strip with a step

K_{SF}^{α} is the SIF for a crack emanating from an angular corner 'α' in a semifinite strip

This enabled them to use the Hasebe *et al.* reference stress intensity factor '$K^{90^\circ}_{FS}$', and having obtained the reference stress distribution '$\sigma_r(x,90^\circ)$' from a finite element analysis the displacement field '$u_r(x,a,90^\circ)$' could be calculated using the Petroski and Achenbach [1.54] approximation. Hence a Bueckner type weight function could be derived. Niu and Glinka [1.55] subsequently provided a correction factor for surface cracks. To do this they used the precedent set by

Mattheck *et al.* [1.56] to extend the Petroski-Achenbach crack opening displacement field for elliptical surface cracks in flat plates. Here the reference stress intensity factor was the finite element solution of Newman-Raju [1.47].

Oore and Burns [1.57] developed a weight function solution for calculating the opening mode stress intensity factor at any point on the front of an irregular planar embedded crack in an infinite body. They suggested a correction factor be applied for application to a semi-elliptical surface crack. This correction factor is obtained assuming that the ratio of 'K' for a surface crack to its equivalent embedded crack is a constant for different stress states (i.e. uniform, linearly varying and parabolic). Hence, using the simplest case of an elliptical crack subjected to a uniform stress field, Irwin's solution was used for the embedded crack i.e.,

$$K = \frac{\sigma\sqrt{\pi a}}{\phi}\left(\sin^2\theta + \frac{a^2}{b^2}\cos^2\theta\right)^{\frac{1}{4}} \qquad (1.47)$$

where ϕ is the complete elliptic integral of the second kind.

Newman and Raju's empirical stress intensity factor equation for the equivalent surface crack [1.47] made it possible to calculate the correction factor for the weight function solution.

1.4.5 Crack Opening Displacement (COD)

The emergence of accurate quantitative crack inspection techniques (e.g. X-Ray, Ultra Sonic, ACPD and Eddy Current), has made it possible to tolerate cracked structural members in service. The assessment procedure requires the use of the fracture mechanics models discussed in the previous subsections to provide crack growth predictions. However, general yield fracture mechanics solutions are necessary to specify the tolerable flaw size before member failure for most structural steels.

Using a linear elastic approach to model extensive plasticity, Dugdale [1.58] and Barenblatt [1.59] proposed separately the COD concept. Fig 1.8 shows the Dugdale "Strip-Yield" model for crack tip plasticity. The model considered is an infinite plate with a central crack of length '$2a$' subjected to a uniform stress 'σ'. The crack length is assumed to incorporate the plastic zones ahead of growing cracks, making the total length '$2c$'. The restraining stress 't' acting on the crack faces resists crack growth. Wells [1.60] proposed that the crack opening displacement 'δ' is a measure of the crack tip deformation (which is virtually a square ended shape) and that fracture would occur when a critical value 'δ_{crit}' is reached.

Using Westergaard's stress solution for a centre crack in an infinite plate in tension (1.27), yields,

$$K = \frac{2\sigma_y}{\sqrt{\pi}}\sqrt{c}\,\frac{dx}{\sqrt{c^2 - x^2}} \tag{1.48}$$

Assuming t = yield strength 'σ_y'

Integrating between limits: $x = a$ and $x = c$, gives,

$$K = \frac{2\sigma_y}{\sqrt{\pi}}\sqrt{c}\cos^{-1}\left(\frac{a}{c}\right) \tag{1.49}$$

Equating the stress intensity factor for an elastic crack of length '$2c$',

$$\Rightarrow \qquad \sigma\sqrt{\pi c} = \frac{2\sigma_y}{\sqrt{\pi}}\sqrt{c}\cos^{-1}\left(\frac{a}{c}\right) \tag{1.50}$$

$$So, \qquad \left(\frac{a}{c}\right) = \cos\left(\frac{\pi\sigma}{2\sigma_y}\right) \tag{1.51}$$

From this it can be seen that,

as $\sigma \rightarrow \sigma_y$, $\frac{a}{c} \rightarrow 0$, i.e. $c \rightarrow \infty$
=> yielding spreads across the infinite plate

Using the cosine expansion, and as $\frac{\sigma}{\sigma_y} \rightarrow 0$,

$$dy = (c - a) = \frac{\pi^2 \sigma^2 a}{8 \sigma_y^2} = \frac{\pi K^2}{8 \sigma_y^2} \tag{1.53}$$

This value '*dy*' is twice the plastic zone size '*ry*'.

From a geometrical consideration of the crack , the COD is given by [1.61],

$$\delta = \frac{8}{\pi} \frac{\sigma_y}{E} a \ln \sec\left(\frac{\pi \sigma}{2 \sigma_y}\right) \tag{1.54}$$

If it is considered that fracture occurs at a critical COD, 'δ_{crit}', for quasi-elastic fracture where $\sigma >> \sigma_y$, only one term may be considered from an expanded form of (1.54) giving,

$$\delta_{crit} = \frac{K_{IC}^2}{\sigma_y E} \qquad (for\ plane\ stress)$$

(1.55)

$$\delta_{crit} = \frac{K_{IC}^2}{\sigma_y E}(1 - \nu^2) \qquad (for\ plane\ strain)$$

BS 5762 and BS 5447 give experimental methods and procedures for COD and Fracture Toughness evaluation respectively for metallic materials.

1.4.6 J-Integral

An alternative method for assessing the toughness of a cracked body is based on non-linear elasticity, giving a single analytical expression over the whole strain range of interest [1.62].

$$\frac{\varepsilon_p}{\varepsilon_y} = A\left(\frac{\sigma}{\sigma_y}\right)^N \tag{1.56}$$

where,

ε_p is the plastic strain
ε_y is the yield strain
A is a constant
N is the stress index for the plastic stress-strain relationship

It is possible to define a line integral 'J' on any curve 'Γ' surrounding the notch tip, starting on the lower surface, travelling anti-clockwise and ending on the crack's upper surface, where,

$$J = \int_{\Gamma}\left(W dy - T\frac{\partial u}{\partial x}\right)ds \tag{1.57}$$

where,

s is the arc length
T are the external forces
u are the corresponding displacements

$$W = \frac{strain\ energy}{unit\ volume} = \int_0^{\varepsilon} \sigma d\varepsilon$$

The integral is independent of crack path for a crack with stress free faces. Per unit thickness, the non-linear elastic term is equal to the potential energy release rate due to crack advancement.

$$i.e. \qquad J = -\frac{dP}{da} \qquad (J/m^2) \qquad (1.58)$$

This is similar to Griffith's strain energy release rate. The advantage of the J-Integral is that it can be determined directly from a load displacement diagram (which may display nonlinearities). Weaknesses in this approach are that it cannot take unloading or a remote elastic field into account.

1.5 Summary

The chapter introduced threaded connections in terms of function and appearance. The attributes and impediments of various features were discussed, and the standardisation authorities concerned with recommending safe designs of screw connections for specific applications were highlighted. Five general techniques used in stress analysis of threaded connections were discussed in detail. A historical review of the main investigations and their conclusions was reported for each analysis approach. The merits and short comings were compared and discussed.

An overview of fatigue analysis techniques was presented. This looked at random as well as constant amplitude cycling. Fracture mechanics and its relevance to fatigue evaluation was illustrated as were the approaches to stress intensity factor determination.

Finally brittle and unstable fatigue behaviour was approached with reference to tolerable flaw size and definition of fast fracture.

The following chapters in this thesis will build on the basic background of fatigue and fracture mechanics presented in this chapter, to provide a framework for the

fatigue analysis of threaded connections. This study hopes to establish a usable fatigue crack initiation and propagation procedure, that will enhance the engineering designer's understanding of the behaviour of threaded connections in service.

1.6 References

[1.1] Jensen, W. J., "Failures of Mechanical Fasteners", "Failure Analysis and Prevention", Metals Handbook, 9th Ed., vol 11, ASM, 1978.

[1.2] BS 3643 "ISO Metric Screw Threads", Part 1, "Principles and Basic Data", 1981.

[1.3] Newport, A., "Stress and Fatigue Analysis of Threaded Tether Connections", Ph. D. Thesis, University College London, 1989.

[1.4] Kawashima, H., "Effect of Incomplete Threads on the Jump-out Tensile Failure of Premium Connections for Oil or Gas Wells", JSME, Series I, vol 33, no 1, pp 107-112, 1990.

[1.5] Sparling, L. G. M., "Improving the Strength of Screw Fasteners", CME, pp 58-59, April 1982.

[1.6] Goodier, J. N., Ithaca, N. Y., "The Distribution of Load on the Threads of Screws", Journal of Applied Mechanics, Trans. of the ASME, vol 62, pp A10-A16, 1940.

[1.7] Sopwith, D. G., "The Distribution of Load in Screw Threads", Proceedings Institution of Mechanical Engineers, vol 159, pp 373-383, 1948.

[1.8] Heywood, R. B., "Tensile Fillet Stresses in Loaded Projections", Proceedings Institution of Mechanical Engineers, vol 159, pp 384-391, 1948.

[1.9] Stromeyer, C. E., "Stress Distribution in Bolts and Nuts", Trans. Inst. Naval Architects, vol 60, pp 112-121, 1918.

[1.10] Den Hartog, J. P., "The Mechanics of Plate Rotors for Turbo-Generators", Trans. ASME, J. App. Mech., vol 51, part 1, pp 1-10, 1929.

[1.11] Stoeckly, E. E. and Macke, H. J., "Effect of Taper on Screw-Thread Load Distribution", Trans. ASME, vol 74, pp 103-112, 1952.

[1.12] Yazawa, S. and Hongo, K., "Distribution of Load in the Screw Thread of a Bolt-Nut Connection Subjected to Tangential Forces and Bending Moments", JSME, Series I, vol 31, no 2, pp 174-180, 1988.

[1.13] Dragoni, E., "Effect of Nut Compliance on Screw Thread Load Distribution", Journal of Strain Analysis, vol 25, no 3, pp 147-150, 1990.

[1.14] Hetényi, M., "A Photoelastic Study of Bolt and Nut Fastenings", Journal of Applied Mechanics, vol 65, pp A93-A100, 1943.

[1.15] Brown, A. F. C. and Hickson, V. M., "A Photoelastic Study of Stresses in Screw Threads", Proc. I. Mech. E., 1B, pp 605-608, 1952.

[1.16] Gascoigne, H. E., "The Use of Precision Castings in the Three-Dimensional Photoelastic Analysis of Threaded Tubular Connections", Experimental Mechanics, pp 282-289, September 1987.

[1.17] Broadbent, T. P. and Fessler, H., "Distribution of Thread Load in Screwed Tubular Connections", "Cohesive Programme of Research and Development into the Fatigue Crack Growth of Offshore Structures, 1985-1987", Final Report, University College London, 1987.

[1.18] Dragoni, E., "Effect of Nut Geometries on Screw Thread Stress Distribution: Photoelastic Results", Journal of Strain Analysis, vol 27, no 1, pp 1-6, 1992.

[1.19] Seika, M., Sasaki, S. and Hosono, K., "Measurement of Stress Concentrations in Threaded Connections", Bull, JSME, vol 17, no 111, pp 1151-1156, 1974.

[1.20] Pick, R. J. and Burns, D. J., "Finite Element Analysis of Threaded End-Closures of Thick-Walled Vessels", Proc. 3rd Int. Conf. on High Pressure, "Engineering Solids Under Pressure", pp 15-25, 1971.

[1.21] Bretl, J. L. and Cook, R. D., "Modelling the Load Transfer in Threaded Connections by the Finite Element Method", Int. J. for Numerical Methods in Eng., vol 14, pp 1359-1377, 1979.

[1.22] Tanaka, M., Miyazawa, H., Asaba, E., Hongo, K., "Application of the Finite Element Method to Bolt - Nut Joints - Fundamental Studies on Analysis of Bolt - Nut Joints Using the Finite Element Method", Bull. JSME, vol 24, no 192, pp 1064-1071, 1981.

[1.23] Tanaka, M. and Hongo, K., "Stress Analysis of Threaded Connections by Finite Element Method", Bull. JSME, vol 24, no 194, pp 1454-1461, August 1981.

[1.24] Patterson, E. A. and Kenny, B., "A Modification to the Theory for the Load Distribution in Conventional Nuts and Bolts", J. of Strain Analysis, vol 21, no 1, pp 17-23, 1986.

[1.25] Glinka, G., Dover, W. D. and Topp, D. A., "Fatigue Assessment of Tethers", Proc. Int. Conf. on Fatigue and Crack Growth in Offshore Structures, I. Mech. E., pp 187-198, 1986.

[1.26] Rhee, H. C., "Three-Dimensional Finite Element Analysis of Threaded Joint", OMAE, pp 293-297, 1990.

[1.27] Bluhm, J. I. and Flanagan, J. H., "A Procedure for the Elastic Stress Analysis of Threaded Connections Including the use of an Electrical Analogue", Expl. Stress Analysis, vol XV, no 1, pp 85-100, 1957.

[1.28] Dover, W. D. and Topp, D. A., "Fatigue Crack Growth in Threaded Tether Connections", 6th Int. Conf. on Fracture, 1984.

[1.29] D'Eramo, M. and Cappa, P., "An Experimental Validation of Load Distribution in Screw Threads", Experimental Mechanics, pp 70-75, March 1991.

[1.30] Maruyama, K., "Stress Analysis of a Nut-Bolt Joint by the Finite Element Method and the Copper-Electroplating Method", Bull. JSME, 17, pp 442-450, 1974.

[1.31] Topp, D. A., "Fatigue / Fracture Mechanics Analysis of Threaded Tether Connections", Ph. D. Thesis, University College London, 1991.

[1.32] Pook, L. P., "The Role of Crack Growth in Metal Fatigue", The Metals Society, London, 1983.

[1.33] Roren, E. M. Q, Madsen, H. O. and Lereim, J., "Implementation of Reliability Concepts in Classification Rules", Det Norske Veritas.

[1.34] Morrow, JoDean, "Cyclic Plastic Strain Energy and Fatigue of Materials", ASTM STP 378, pp 45-87, 1965.

[1.35] Manson, S. S., "Fatigue: A Complex Subject - Some Simple Approximations", Experimental Mechanics, pp 193-226, July 1965.

[1.36] Miner, M. A., "Cumulative Damage in Fatigue", Journal of Applied Mechanics, pp A159-A164, September 1945.

[1.37] Suresh, S., "Micromechanisms of Fatigue Crack Growth Retardation Following Overloads", Engineering Fracture Mechanics, vol 18, no 3, pp 577-593, 1983.

[1.38] Druce, S. G., Beevers, C. J. and Walker, E. F., "Fatigue Crack Growth Retardation Following Load Reductions in a Plain C-Mn Steel", Engineering Fracture Mechanics, vol 11, pp 385-395, 1979.

[1.39] Sandor, B. I., "Fundamentals of Cyclic Stress and Strain", The University of Wisconsin Press, 1972.

[1.40] Madsen, H. O., Skjong, R. and Moghtaderi-Zadeh, M., "Experience on Probabilistic Fatigue Analysis of Offshore Structures", Proc. 5th Int. Symposium and Exhibit on Offshore Mechanics and Arctic Engineering (OMAE), Tokyo, Japan, pp 1-8, 1986.

[1.41] Pook, L. P., "Analysis and Application of Fatigue Crack Growth Data", "A General Introduction to Fracture Mechanics", I. Mech. Eng. Pub., pp 114-135, 1978.

[1.42] Watson, P., Dabell, B. J., "Cycle Counting and Fatigue Damage", Journal of the Society of Environmental Engineers, pp 3-8, September 1976.

[1.43] Westergaard, H. M., "Bearing Pressures and Cracks", Trans. ASME, Journal of Applied Mechanics, Serial A, vol 61, pp A49-A53, 1939.

[1.44] Cartwright, D. J. and Rooke, D. P., "Evaluation of Stress Intensity Factors", "A General Introduction to Fracture Mechanics", I. Mech. Eng. Pub., pp 54-73, 1978.

[1.45] Paris, P. C., Sih, G. C., "Stress Analysis of Cracks", ASTM, STP 381, pp 30-83, 1965.

[1.46] Irwin, G. R., "Analysis of Stresses and Strains near the end of a Crack Traversing a Plate", Trans. ASME, Journal of Applied Mechanics, vol 24, pp 361-364, 1957.

[1.47] Newman, J. C. and Raju, I. S., "An Empirical Stress-Intensity Factor Equation for the Surface Crack", Engineering Fracture Mechanics, vol 15, no 1-2, pp 185-192, 1981.

[1.48] Marloff, R. H., Leven, M. M., Ringler, T. N. and Johnson, R. L., "Photoelastic Determination of Stress Intensity Factors", Experimental Mechanics, pp 529-539, December 1971.

[1.49] Pook, L. P. and Dixon, J. R., "Fracture Toughness of High Strength Materials: Theory and Practice", ISI Pub., 120, pp 45-50, 1970.

[1.50] Bueckner, H. F., "A Novel Principle for the Computation of Stress Intensity Factors", Zeitschrift für Angewandte Mathematik und Mechanik, 50, pp 529-546, 1970.

[1.51] Rice, J. R., "Some Remarks on Elastic Crack-Tip Stress Fields", Int. J. Solids Structures, vol 8, pp 751-758, 1972.

[1.52] Niu, X., Glinka, G., "The Weld Profile Effect on Stress Intensity Factors in Weldments", Int. J. Fracture, no 35, pp 3-20, 1987.

[1.53] Hasebe, N., Matsuura, S. and Kondo, N., "Stress Analysis of a Strip with a Step and a Crack", Eng. Fracture Mech., vol 20, no 3, pp 447-462, 1984.

[1.54] Petroski, H. J. and Achenbach, J. D., "Computation of the Weight Function from a Stress Intensity Factor", Eng. Fracture Mech., vol 10, pp 257-266, 1978.

[1.55] Niu, X., Glinka, G., "Stress Intensity Factors for Semi-Elliptical Surface Cracks in Welded Joints", Int. J. Fracture, vol 40, pp 255-270, 1989.

[1.56] Mattheck, C., Munz, D. and Stamm, H., "Stress Intensity Factor for Semi-Elliptical Surface Cracks Loaded by Stress Gradients", Eng. Fracture Mech., vol 18, no 3, pp 633-641, 1983.

[1.57] Oore, M., Burns, D. J., "Estimation of Stress Intensity Factors for Embedded Irregular Cracks Subjected to Arbitrary Normal Stress Fields", Journal of Pressure Vessel Technology, Trans. ASME, vol 102, no 2, pp 202-211, May 1980.

[1.58] Dugdale, D. S., "Yielding of Steel Sheets Containing Slits", J. Mech. Phys. Solids, vol 8, pp 100-104, 1960.

[1.59] Barenblatt, G. I., "The Mathematical Theory of Equilibrium Cracks in Brittle Fracture", Advances in Applied Mechanics, vol 7, p 55, 1962.

[1.60] Wells, A. A., "Application of Fracture Mechanics at and Beyond General Yielding", British Welding Journal, 10, pp 563-570, 1963.

[1.61] Knott, J. F., "The Fracture Toughness of Metals", "A General Introduction to Fracture Mechanics", I. Mech. Eng. Pub., pp 17-31, 1978.

[1.62] Turner, C. E., "Yielding Fracture Mechanics", "A General Introduction to Fracture Mechanics", I. Mech. Eng. Pub., pp 32-53, 1978.

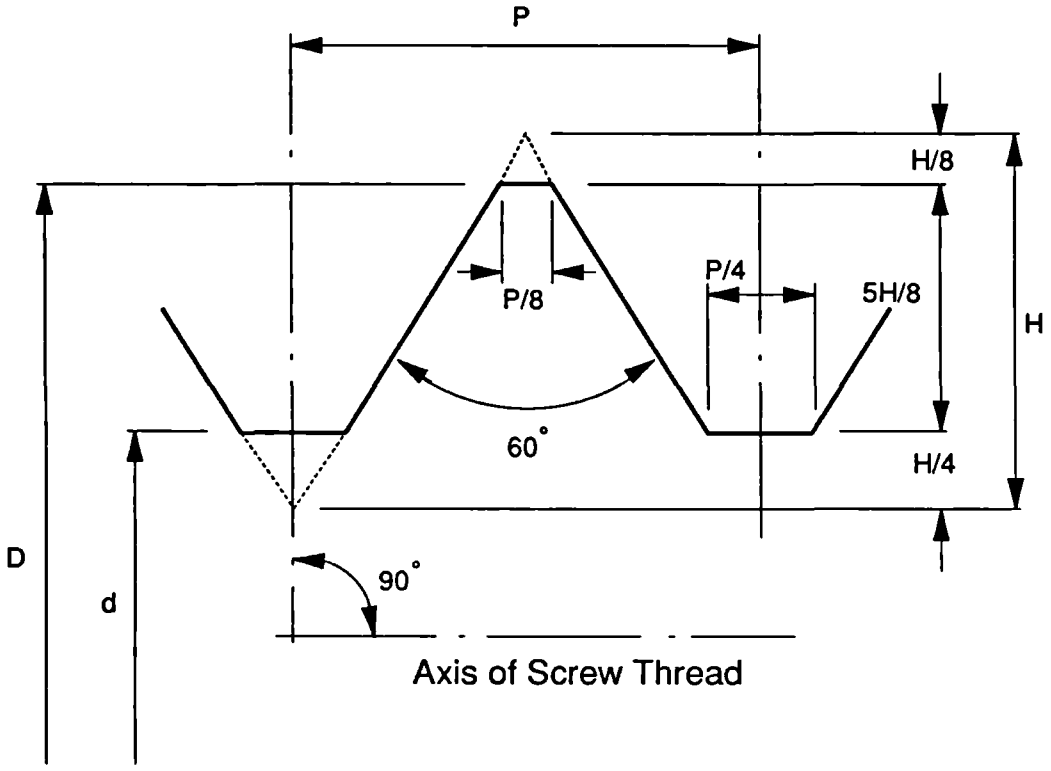

Fig 1.1

ISO Metric Thread Form

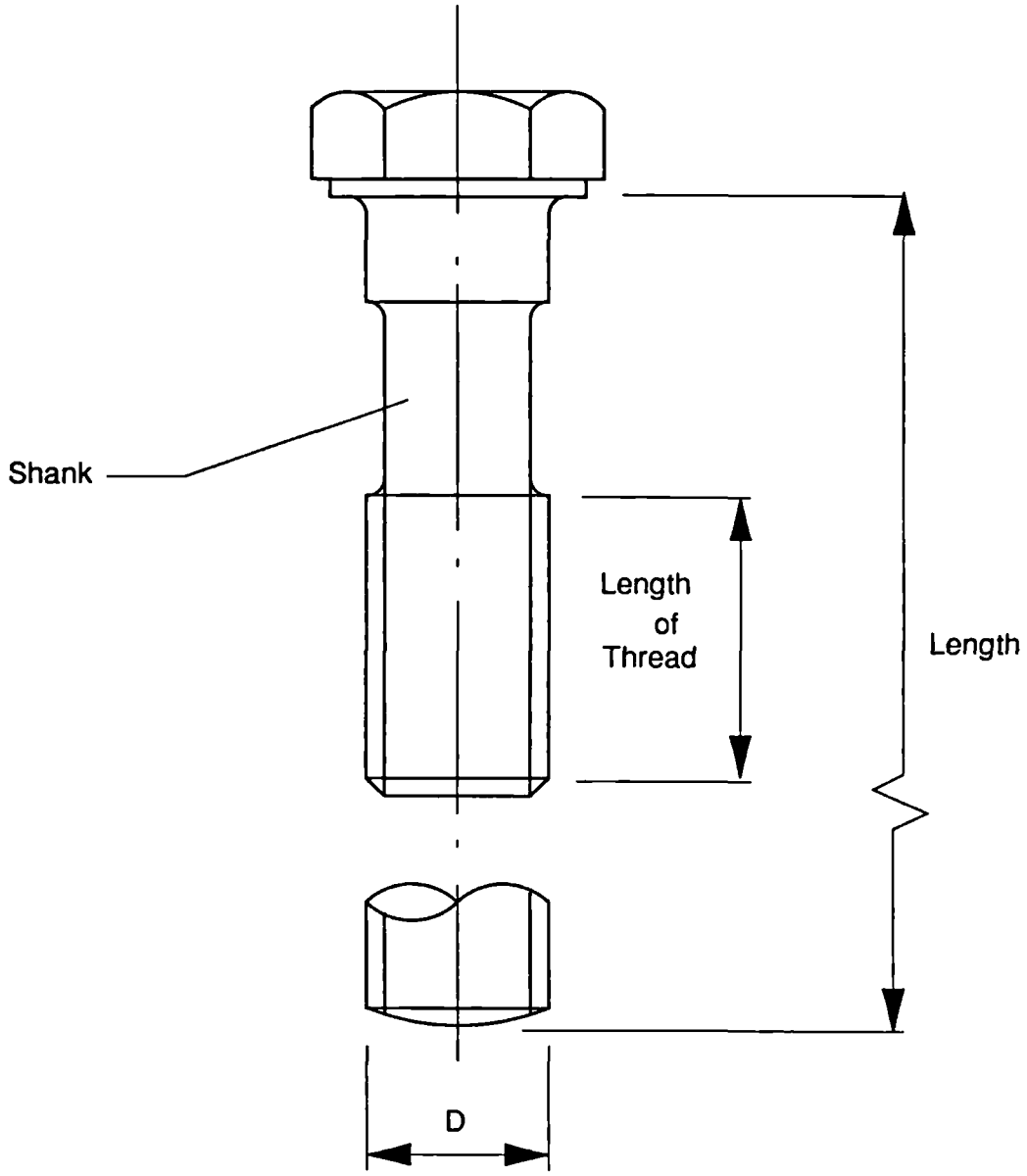

Fig 1.2

ISO Metric Waisted Shank

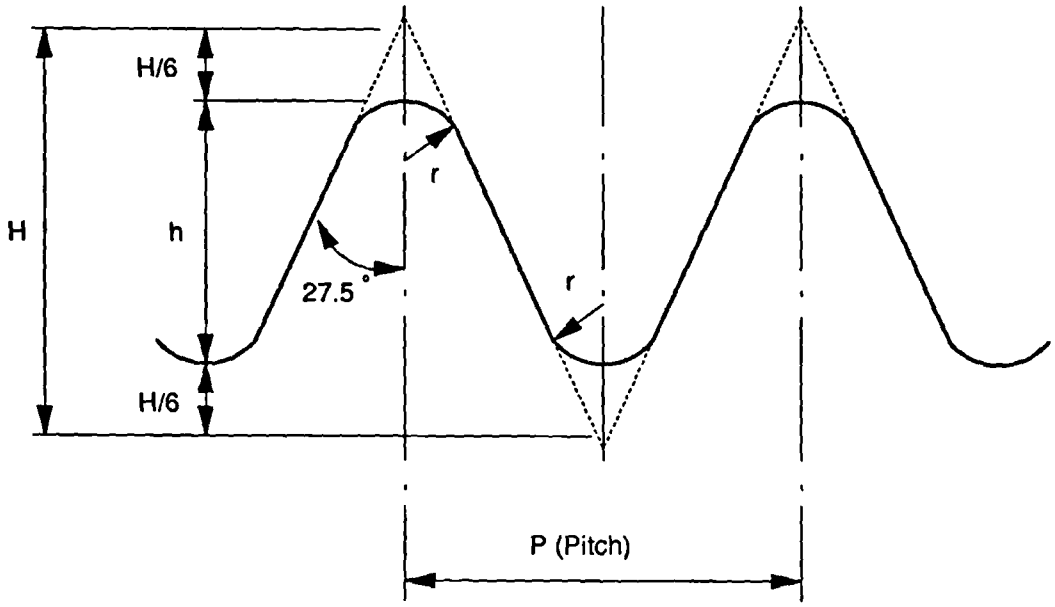

H = 0.960491 P

h = 0.640327 P

r = 0.137329 P

Fig 1.3

Whitworth Thread Form

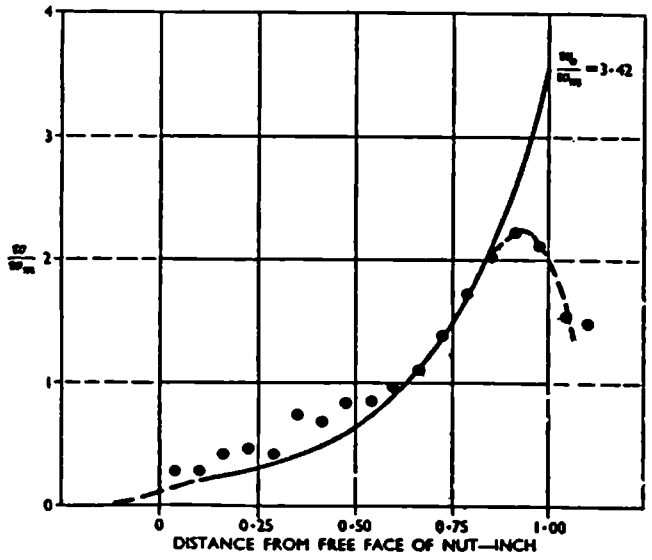

•	Hetényi's experimental results
———	Sopwith's calculated distribution ($\mu = 0.1$)
- - - - - - - - - - -	Effect of Change of loading at the ends

Fig 1.4

Distribution of Load Along Thread [1.7]

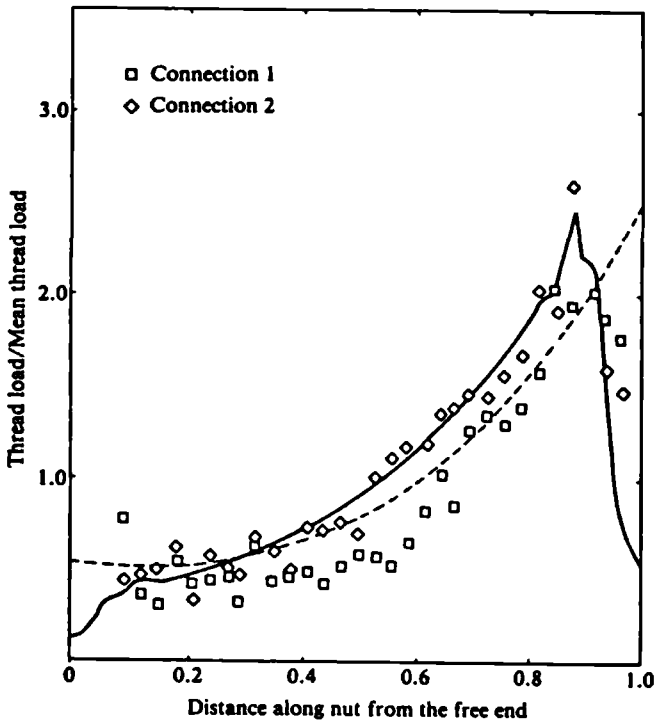

———————— Including the effect of Thread Runout

- - - - - - - - - - - - Neglecting the effect of Thread Runout

Fig 1.5

Patterson's Load Distribution [1.24]

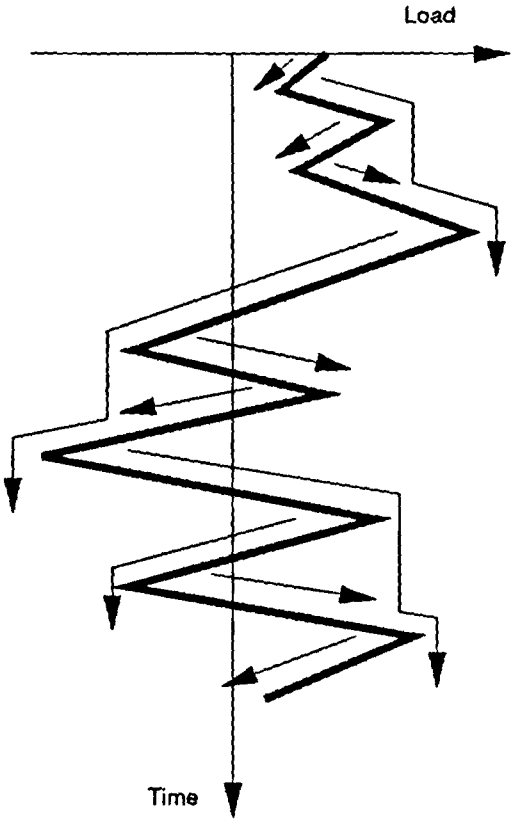

Fig 1.6

Rainflow Cycle Counting

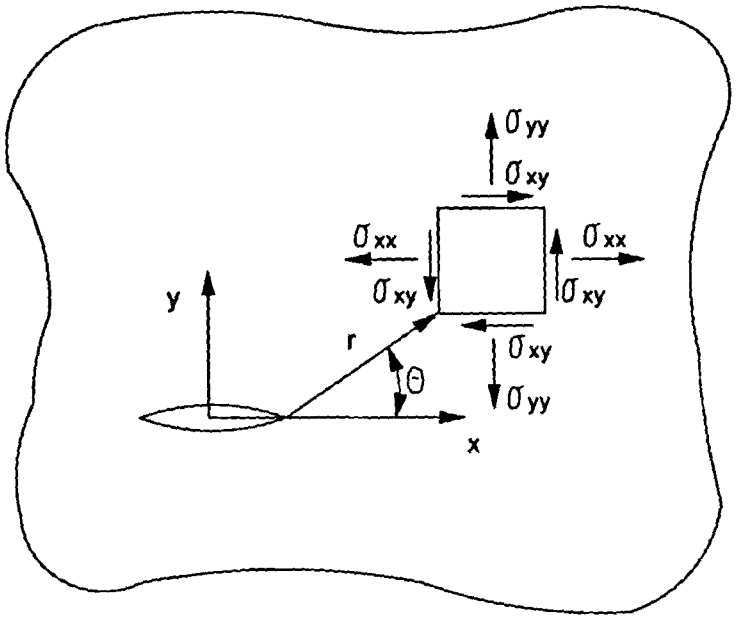

Fig 1.7

Polar Notation for an Embedded Crack

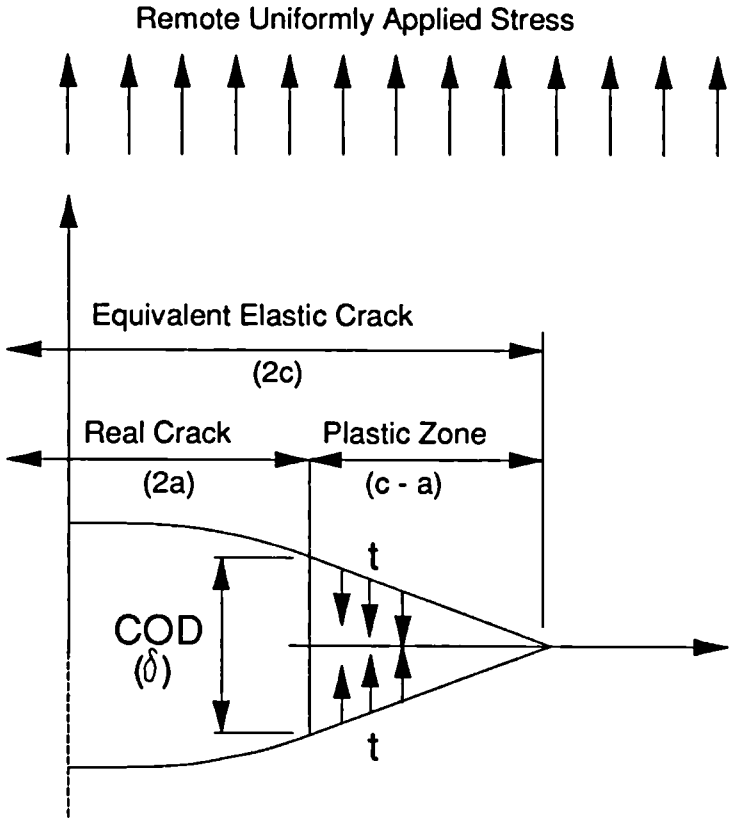

Fig 1.8

Dugdale "Strip Yield" Model for Crack Plasticity

CHAPTER TWO - Fatigue Crack Initiation in Threaded Connections

2.1 Introduction

The term "fatigue", in relation to the progressive structural deterioration of metal was first used in the title of a technical paper by Frederick Braithwaite in 1854 [2.1]. The concept was briefly introduced in chapter one, but more emphasis was brought on the philosophical *modus operandi* to the quantification of fatigue rather than a methodology of analysis. Crack growth in metals is relatively easy to define in terms of the bulk properties of the material it propagates through. This is a direct consequence of the relative momentum associated with stable crack growth, which is great enough to effectively ignore common material inconsistencies with the exception of those due to environmental and erratic loading conditions. The larger a crack gets, the less is the influence of the local geometrical and material conditions from where it has evolved. Geometrical design can rarely control the rate at which a crack grows once initiated, but it frequently can determine whether a crack is instituted or not. It is the crack generation that is discussed in this chapter. Defining crack initiation is not easy. Engineers will usually specify a detectable macrocrack length and depth (of the order 0.25mm), whereas the physicist may argue crack initiation from the time a crack depth is greater than the average grain size or even from the first evidence of cyclic slip.

Fatigue of structures in service is a truly multidisciplinary problem and study of crack initiation is generally outside the scope of the structural design engineer. However it is essential that aspects of metallurgical and material behaviour are understood so that the engineer can design to counteract mechanisms that contribute to crack generation. This chapter does not aim to develop a conclusive solution to quantify the fraction of component life implicated with fatigue crack initiation, but hopes to identify the instrumental elements associated with crack initiation specifically from thread roots. Identification of contributing factors means that empirical behavioural relations can be evaluated to describe their effects. These in turn can indicate the relative fatigue resistance of similar components with regard to certain aspects, assuming other quantities are unchanged. Knowing the effect of these aspects on the crack resistance of a thread root is of immense importance when

designing against fatigue failure. In order to appreciate the significance and interaction of these material and surface conditions on crack generation, some basic metallurgical and cyclic material properties must be understood.

In principle, two different fatigue design approaches can be adopted. The first is to design for an infinite life, the other to accommodate fatigue crack initiation and subsequent growth, i.e. a finite life. It is generally the case that avoidance of fatigue at any price can be highly uneconomical and unnecessarily overconservative. This certainly applies to aircraft [2.2], and is true for most other types of structures and components, especially where overall geometry and weight is restricted. This is very often the case with structural threaded fasteners. Crack generation can result from bad workmanship, accidental surface damage or environmental attack. These are not considered here . The first two can be controlled by quality assurance, the latter is considered in chapter six. This chapter assumes thread roots are machined to specification standard and do not contain macroscopic material defects. Crack generation is assumed to be due to impressed mean, residual and cyclic stress and is dependent upon material properties and notch sensitivity. The following section systematically sets out the present thinking on fatigue strain cycling crack initiation.

2.2 The Mechanics of Strain Cycling

When dealing with the micromechanics of materials it is more appropriate to consider local strain behaviour due to remotely applied stresses, as this can be directly related to dislocation movement and other crystalline mechanisms that determine physical material properties. Cyclic slip is essential for crack nucleation. The first microcrack may develop immediately due to local strain. Its initial growth is still dependent on surface condition and microstructural aspects of the surface material. As long as the crack size remains smaller than the average grain size, its growth can be a rather irregular and discontinuous process. The initial crack nucleation process is also complicated by the fact that microcracks frequently begin at material defects (inclusions, vacancies, intrusions, extrusions etc.), which can facilitate fast growth in the early stages. Also the free material surface provides a lower constraint on plastic deformation exhibiting a false perception of the material state. As a consequence it is possible that small cracks which are initiated will stop

growing afterwards [2.2]. Abundant literature is available of studies on such "short-crack" behaviour, addressing aspects such as branching, retardation, coalescence and closure. It has been suggested that the fatigue limit which was traditionally defined as the threshold stress amplitude, below which cracks are not initiated, be redefined as the stress amplitude, below which small microcracks will not propagate. However there is still a problem understanding the physical meaning of the threshold stress intensity factor range with regard to the contribution of low amplitude cycles in variable amplitude crack growth. This would require a material memory analysis for the past loading history which may constitute an unnecessary over complicated prediction model, yielding an inconclusive exponential number of possible growth scenarios.

Engineering experience has adopted a general empirical approach to crack generation that does not dwell upon the evolution of individual microcracks, but defines initiation in terms of bulk material properties and the local stress system. The cyclic nature of material can vary considerably from its static stress-strain behaviour. The reasons for the differing behaviour are similar to the change in material characteristics due to cold working. Materials can harden or soften in the same cyclic load sequence. To understand this a specimen can be considered to be subjected to axial reversed strain cycling i.e., it undergos a total strain range of '2ε' (Fig 2.1). In this cyclic situation different loads are required to accomplish a desired amount of strain depending on the number or prior applications of the strain. The example in Fig 2.1 shows the cyclic stress-strain curve above the monotonic stress-strain relationship, this indicating a strain hardening material. The cyclic behaviour stabilises after a number of cycles (usually quite quickly), this achievement of an asymptotic stress range is known as saturation hardening [2.3]. If the cyclic stress-strain behaviour of such a reversed load situation is plotted directly, the result is a hysteresis loop. This hysteresis loop stabilises after a number of cycles on realisation of saturation hardening for a given strain range. Definition of the cyclic stress-strain curve can be taken as the locus of tips of the stable hysteresis loops from several companion tests at different completely reversed constant strain

amplitudes [2.4]. The relationship between cyclic stress and plastic strain can be described mathematically by a power function similar to that used for the monotonic curve [2.5]:

$$\sigma_a = K' \left(\frac{\Delta \varepsilon_P}{2} \right)^{n'} \tag{2.1}$$

where:

σ_a is the stable local stress amplitude
$\frac{\Delta \varepsilon_P}{2}$ is the stable plastic strain amplitude
n' is the cyclic strain hardening exponent
K' is the cyclic strength/hardening coefficient

For the vast majority of metals, regardless of their initial state, the value of the cyclic strain hardening exponent falls between 0.1 and 0.2 and is surprisingly close to 0.15 in most cases. It can be generally asserted that metals with a high monotonic strain hardening exponent will cyclically harden, while those with a low initial value would cyclically soften to approach a cyclic strain hardening exponent of 0.15. There are several approaches used to determine the cyclic stress-strain curve of a material, all of these involve empirical local stress and strain measurements. Stress measurements can be calculated directly from servo-controlled test systems incorporating a load cell. Reference [2.6] measured strains by a clip gauge on uniform diameter specimens and by a diametral clip gauge on hourglass specimens (used for strain amplitudes higher than $\pm$ 0.01). The diametral or transverse strain measurements produce accurate values of true strain in the region where failure occurs.

The most straightforward approach to determine the cyclic stress-strain curve involves conducting each cyclic load test at a constant strain amplitude, considering the hysteresis loop at approximately half the specimen fatigue life. The method requires a specimen for each strain range which may prove costly and time consuming. Dugdale [2.7] showed that the hysteresis loop rapidly adjusts to a stable

steady state following sudden changes in cyclic strain amplitude. By cycling to about twenty percent of the fatigue life at a given strain amplitude, a reasonable amount of stability is achieved and a number of points on the cyclic stress-strain curve can be obtained from one specimen. A high to low strain sequence is preferable. Incrementally decreasing to zero strain and stress between blocks tends to reduce mean stress effects. Another method is to monotonically pull the specimen in tension to fracture after it has been cyclically stabilised by multiple or incremental cycle blocks. It is a feature that the monotonic tension curve is virtually coincident with the locus of hysteresis loop tips if the material has been cyclically stabilised. Finally, Morrow [2.5] suggested that the trace of a single stable hysteresis loop can be superimposed on the cyclic stress-strain curve if the stresses and strains from the loop tip are divided by two, i.e. the cyclic stress-strain curve can be approximated by one stable hysteresis loop.

Observation of material behaviour under high-low and low-high cyclic strain blocks shows that regardless of the strain level of the preceding block, the stress-strain behaviour tends towards the curve for the new strain level at the expended damage fraction. The material hardens or softens in order to approach the cyclic curve for the new strain range. This would support the practice of applying a linear damage rule to evaluation of crack initiation under variable amplitude fatigue loading [2.3].

The micromechanisms associated with cyclic hardening and softening are explained when considering the crystalline behaviour of metals. Grosskreutz [2.8] gives the explanation that the rapid hardening stage is accompanied by extensive dislocation multiplication. The more extensive their interaction with obstacles and other dislocations, the more rapid will be the hardening. Saturation hardening can be understood by any of the mechanisms associated with "dynamic recovery". These are: (a) obstacles to dislocation movement are removed as rapidly as they are generated; (b) no new obstacles are generated; (c) dislocation destruction equals dislocation generation; and (d) no new dislocations are created. These observations were concluded from extensive tests studied under transmission electron microscopy and X-ray diffraction patterns. Again favourable crystalline orientation is shown to be necessary for cyclic hardening. The effects of grain boundaries are not

considered important in the hardening mechanisms. However the degree of localised microplastic strains developed is sensitive to grain size [2.9] making microstructure a relevant factor. Cyclic hardening may at first appear beneficial, but the greater disorder within the grain boundaries may eventually serve as nuclei for fatigue cracking. Cyclic strain softening is somewhat harder to explain. One mechanism that is known to apply to dispersion strengthened materials (e.g. carbides in steels) is where the hard brittle particles are broken down by cyclic straining, wherever slip occurs along a plane intersecting them. Eventually they dissolve into the surrounding material matrix no longer presenting an obstacle to dislocation motion. Softening may also be a manifestation of the relief of residual stresses. Development of microcracks is understood when considering the irreversibility of slip along any one slip plane. Reversing the load that caused slip results in slip along a parallel plane never the original one, producing extrusions or intrusions.

Cyclic hardening and softening may appreciably alter the macroscopic stress distribution in an engineering component. The following sections elaborate on methods to predict these effects and thus indicate the resistance to fatigue crack initiation.

2.3 Fatigue Life from Materials Data

The concept that cyclic life was related to plastic strain was proposed by Coffin and Manson, however it is usually the total strain that is known rather than just the plastic component. The total strain range is a simple summation of elastic and plastic components but unlike its constitutive parts does not have a straight line on logarithmic axes relationship with the number of cycles to failure. The curve of total strain range against life is asymptotic to the plastic line in the lower cyclic-life range, and the elastic line in the higher cyclic-life range. Manson [2.3] detailed two methods whereby the total strain range to fatigue life relationship of a material can be evaluated from simple tension tests. The first of these is the four point correlation method. Knowing that the elastic and plastic strain components to life relationships are approximately straight lines, only two points are required to define each case. From observation of material behaviour the following points were suggested:

Elastic Line: (1) $N = {}^{1}/_{4}$, $\varepsilon_e = 2.5\,\sigma_f / E$

(2) $N = 10^5$ $\varepsilon_e = 0.9\,\sigma_{UTS} / E$

Plastic Line: (1) $N = 10$ $\varepsilon_p = 0.25\,D^{3/4}$

(2) $N = 10^4$ $\varepsilon_p = (0.0132 - \varepsilon_e) / 1.91$

where:

$D = \ln\left(\frac{1}{1-RA}\right)$, (ductility)

$\sigma_t \simeq \sigma_{UTS}(1+D)$, (true fracture stress)

RA is the percentage reduction in area due to waisting of the tensile specimens.

By using this approximation, only the elastic modulus and two tensile properties, the ultimate tensile strength and reduction in area, are needed to predict axial fatigue life for a specified local strain range (Fig 2.2).

The other approach is to assume that the slopes of the elastic and plastic lines are the same for all materials. Again Manson and Hirschberg studied the behaviour of twenty-nine materials varying from body centred cubic, face centred cubic, hexagonal close packed, precipitation hardened, hot and cold worked, notch ductile, notch sensitive, strain softening, strain hardening and a large variation in tensile strength, elastic modulus and ductility. They presented the following equation as a reasonable representation of the total strain range relationship with cycles to failure:

$$\Delta\varepsilon = \frac{3.5\sigma_{UTS}}{E} N_f^{-0.12} + D^{0.6} N_f^{-0.6} \qquad (2.2)$$

The accuracy of the above equation has proved quite remarkable, considering that only static properties are involved and that it has been applied to wide classes of materials. In a more recent study [2.10], Muralidharan and Manson, using extensive

data on forty-seven materials including steels, aluminium and titanium alloys, have derived a modified universal slopes equation for estimation of fatigue characteristics of metals. This is given as:

$$\Delta\varepsilon = 0.0266D^{0.155}\left(\frac{\sigma_{UTS}}{E}\right)^{-0.53} N_f^{-0.56} + 1.17\left(\frac{\sigma_{UTS}}{E}\right)^{0.832} N_f^{-0.09} \qquad (2.3)$$

The study proved that the influence of ductility on the elastic line is negligible. However, it is strongly influenced by the ratio of tensile strength to modulus of elasticity. Ductility is less important than indicated by the earlier universal slopes relation for plastic strain. The ductility exponent was 0.6 but is modified to 0.155. The exponent -0.12 has been revised to -0.09 for the elastic strain component implying a lesser drop in life as extrapolations are made to lives much greater than 10^6 cycles. However, before adoption of either (2.2) or (2.3) the particular material should be researched with regard to likely fatigue behaviour. For example, the modified universal slopes is less accurate for AISI 4130 - 4340 steels below 10^4 cycles but more accurate than the old equation in the high cycle regime. The major usefulness of these relations is to indicate the sensitivity of fatigue life on tensile strength and ductility.

Ideally relations should be obtained for particular materials. The most common form is given as [2.11]:

$$\frac{\Delta\varepsilon}{2} = \frac{\sigma'_f}{E}(2N_f)^b + \varepsilon'_f(2N_f)^c \qquad (2.4)$$

where:

σ'_f is the fatigue strength coefficient
b is the fatigue strength exponent
ε'_f is the fatigue ductility coefficient
c is the fatigue ductility exponent

The first term represents the elastic strain component, the second, the plastic strain component. Knowing these material constants, the strain-life relationship can be evaluated, then used to predict the onset of fatigue cracking. Unfortunately these material properties are often not readily available, the following subsections highlight the significance of these, their characteristics and methods for their determination.

2.3.1 Fatigue Ductility Properties

Morrow [2.12] proposed the form of the material properties and equation (2.4) which have since been adopted as standard. Unlike the previous approximate relations where Manson predicted the material cyclic behaviour from simple tensile test results, these empirical fatigue properties are established from a series of completely reversed axial fatigue tests carried to fracture on smooth specimens. From a series of tests at different strain ranges, a log-log plot of the stable plastic strain amplitude versus fatigue life produces a band of points which scatter slightly about a straight line. The slope of the line will vary depending on material, it will be displaced upwards for more ductile materials, and downwards the less ductile. The plastic strain intercept at one half cycle (one reversal) determines the level of fatigue ductility, i.e. the fatigue ductility coefficient 'ε'_f'. It can be approximated by [2.13]:

$$\varepsilon'_f = 0.002\left(\frac{\sigma'_f}{\sigma'_{YS}}\right)^{\frac{1}{n'}} \tag{2.5}$$

where:

σ'_{YS} is the cyclic 0.2% offset yield strength i.e., stress to cause 0.2% inelastic strain on the cyclic stress-strain curve.

The fatigue ductility coefficient is the true strain required to cause failure in one reversal i.e. the intercept of the plot:

$$\log\left(\frac{\Delta\varepsilon_p}{2}\right) - \log 2N_f \tag{2.6}$$

at $2N_f = 1$ ($2N_f$ is the number of reversals to failure)

It is related to the monotonic fracture ductility 'ε_f' which is defined as the "true" plastic strain required to cause fracture:

$$\varepsilon_f = \ln\left(\frac{100}{100 - \%RA}\right) \tag{2.7}$$

The true plastic fracture strain is the same value as Manson's Ductility '*D*'. ε'_f ranges between ε_f and $\varepsilon_f / 2$ and is between 0 and 1 in steels. The slope of the plastic strain-life line may also be considered a fatigue property and is called the fatigue ductility exponent '*c*'. It can be defined as the power to which the life (in reversals) must be raised to be proportional to the plastic strain amplitude and is taken as the slope of the plot

$$\log\left(\frac{\Delta\varepsilon_p}{2}\right) - \log(2N_f)$$

'*c*' is nearly a constant for metals and normally has a value between -0.5 and -0.7, with -0.6 as a representative value. It is reasonably independent of chemical composition, hardness and temperature. The plastic strain life relationship defined in terms of the ductility properties,

$$\frac{\Delta\varepsilon_p}{2} = \varepsilon'_f(2N_f)^c \tag{2.8}$$

is similar to the Manson-Coffin relation except that plastic strain amplitude is used and reversals instead of cycles.

2.3.2 Fatigue Strength Properties

The first term in equation (2.4) represents the elastic strain component. The fatigue strength coefficient can be related to the plastic strain component by:

$$\frac{\Delta\varepsilon_p}{2}=\left(\frac{\sigma_a}{K'}\right)^{\frac{1}{n'}}=\varepsilon'_f\left(\frac{\sigma_a}{\sigma'_f}\right)^{\frac{1}{n'}}=\varepsilon'_f(2N_f)^c \tag{2.9}$$

Letting $n'c = b$

$$\sigma_a=\sigma'_f(2N_f)^b \tag{2.10}$$

σ_a is the stable local stress amplitude

so,

$$2N_f=\left(\frac{\sigma_a}{\sigma'_f}\right)^{\frac{1}{b}} \tag{2.11}$$

The same expressions can be found by curve fitting using the stress amplitude and fatigue life on log-log coordinates. The fatigue strength coefficient 'σ'_f' becomes the "true" stress required to cause failure in one reversal, i.e. the intercept of the plot:

$$\log\left(\frac{\Delta\sigma}{2}\right)-\log 2N_f \tag{2.12}$$

at $2N_f = 1$

It is proportional to the true fracture strength ($\sigma'_f \simeq \sigma_f$) and ranges between about 690 MPa and 3400 MPa for heat treated metals [2.14]. The fatigue strength exponent can be defined as the power to which the life in reversals must be raised to be proportional to the stress amplitude, taken as the slope of the plot:

$$\log(\sigma_a) - \log 2N_f$$

It normally is a maximum of -0.12 for softened metals and decreases to a minimum value of about -0.05 with increasing hardness. The strength properties are also referred to as "Basquin" constants after his "exponential law" of fatigue (1910) which is similar to (2.10). It can be appreciated that only four of the six cyclic material constants discussed are unique, the other two can be derived from the four others.

2.3.3 Determination of the Local Strain

The theoretical stress concentration factor, 'K_T', applies only when the material at the notch remains elastic. The damage relations introduced in the preceding subsections all identified a plastic stress (strain) component of total applied stress. This component becomes increasingly less important for high cycle fatigue, but is all important in low to mid cycle fatigue crack initiation. Obviously the total strain range is not a simple multiplication of strain concentration factor with nominal strain as it would be within the linear elastic region. Neuber's rule [2.15] is the most often used when dealing with nonlinear material behaviour. Neuber stated that the theoretical stress concentration factor is equal to the geometric mean of the actual stress and strain concentration factors, i.e.,

$$K_T = (K_\sigma K_\varepsilon)^{\frac{1}{2}} \tag{2.13}$$

It would seem reasonable that the product of stress and strain concentration factors is a constant, because K_σ decreases and K_ε increases as yielding occurs. Small notches have less effect in fatigue than may be indicated by K_T [2.16]. This general phenomenon is denoted notch sensitivity. Notch sensitivity may be considered as a measure of the degree to which the theoretical stress concentration factor is true. Peterson [2.17] defined notch sensitivity 'q' as:

$$q = \frac{K_f - 1}{K_T - 1} \tag{2.14}$$

where K_f is the fatigue notch factor given as:

$$K_f = \frac{Fatigue\ \ Limit\ \ of\ \ unnotched\ \ specimen}{Fatigue\ \ Limit\ \ of\ \ notched\ \ specimen}$$

He suggested 'q' could be of the form:

$$q = \frac{1}{1 + \frac{Constant}{r}} \tag{2.15}$$

where 'r' is the notch root radius and the constant is specific to a material state.

The fatigue notch factor can then be expressed as:

$$K_f = 1 + \frac{K_T - 1}{1 + \frac{Constant}{r}} \tag{2.16}$$

'K_f' is defined as a constant which differs from 'K_T' only as a result of size effects and material. For notches having large radii, K_f approaches K_T, however for sharp notches the use of K_T is often unnecessarily conservative. 'K_f' can be expressed as:

$$K_f = \left(\frac{\Delta\sigma}{\Delta S} \frac{\Delta\varepsilon}{\Delta e} \right)^{\frac{1}{2}} \tag{2.17}$$

where ΔS and Δe are nominal stress and strain ranges.

$\Delta\sigma$ and $\Delta\varepsilon$ are local stress and strain ranges at the notch root.

It is more appropriate to equate K_f to the non linear function (2.17) rather than the commonly used value of K_T. This expression shows that a function of nominal stress and strain need only be multiplied by a constant concentration factor to obtain $(\Delta\sigma\Delta\varepsilon E)^{\frac{1}{2}}$ at the notch root. In most problems of engineering interest, the nominal stress and strain remain elastic, the expression (2.17) can then be written,

$$K_f \Delta S = (\Delta\sigma\Delta\varepsilon E)^{\frac{1}{2}} \tag{2.18}$$

The above expression indicates that the fatigue concentration factor K_f depends on the material behaviour, as a consequence will be not the same for low and high cycle fatigue. Cyclic hardening and softening cause cycle dependent changes in the fatigue concentration factor. Conle and Nowack [2.18] studied fatigue data from cyclically stabilised specimens and compared the actual fatigue concentration factors with long life K_f factors and a variable K_f determined from fatigue-life data. The variable K_f led to unconservative predictions whereas the long life K_f tended to overestimate the local stresses and strains. It would seem that long life fatigue concentration factors would be the most appropriate in design situations.

Fatigue concentration factors are specific to material behaviour and notch geometry, for this reason they generally cannot be found in handbooks nor are there any conclusive theoretical models for their determination.

Using the theoretical stress concentration factor however, will lead to conservative estimates of local stress. The Neuber relation is generally conceded to work well for plane stress loadings, but not as well when there are constraints causing plane strain loading as in the case of a thread root. A linear relation, $K_\varepsilon=K_T$ seems to work better in this case [2.19]. This means that employment of

the Neuber relation builds into the calculation yet a further conservative factor for mid to high cycle fatigue, but is not appropriate for very low cycle fatigue if K_ε is much greater than K_T. This implies that the local stress is assumed to be linearly dependant on the nominal stress and is a simple multiplication with the theoretical stress concentration factor. The strain amplitude is then given as [2.11]:

$$\frac{\Delta\varepsilon}{2}=\frac{\Delta\sigma(1-\nu^2)}{2E}+\left(\frac{\Delta\sigma}{2K'}\right)^{\frac{1}{n'}} \tag{2.19}$$

for the plane strain condition. If the fatigue concentration factor was known, it could be used directly instead of the stress concentration factor for a less conservative result. Equation (2.19) used with (2.4) gives a direct relationship for nominal stress to the number of cycles for crack initiation.

2.4 Mean and Residual Stresses

Up to this point fully reversed, zero mean cyclic stress in virgin material has only been considered. Unfortunately in practice this is rarely the case. From the very early stages of fatigue study, Wöhler (1870) observed that the number of cycles to failure depended on the stress range, the value of which to cause failure at any given number of cycles decreased as the mean stress increased. Thus the approach outlined in this chapter is inadequate without modification for predicting the effect of mean stress on the fatigue life of notched members. Even if the loading is completely reversed, local mean stresses may be created in changing from one amplitude of load to another. Large tensile loads tend to induce local compressive mean stresses for subsequent smaller cycles, whereas large compressive loads induce local tensile mean stresses. The ensuing fatigue life may be altered by more than two orders of magnitude. Another complication is that these mean stresses at the notch root tend to relax towards zero in the presence of sufficient cyclic plastic strain [2.16].

Mean stresses cause the most significant deviations in damage summations. Damage values are increased if the mean stress is tensile and generally reduced if the mean stress is compressive. Studying cyclic material behaviour, Topper *et al.* [2.6] observed that mean stresses rapidly stabilise following step changes in cyclic strain amplitude. It was also noted that a large cycle wipes out the effect of the previous history and that cycles with little inelastic action do not appreciably affect the relaxation of residual stress. The previous section introduced the fatigue concentration factor and identified it as a function of material and stress concentration factor. The strict definition of the fatigue concentration factor assumes symmetrical loading ($R = -1$) and room temperature. However if these are varied, they will also effect the fatigue concentration factor. Berkovits [2.20] studied these effects for a range of materials, including aluminium, steel, titanium and nickel alloys. He observed that with some exceptions the fatigue concentration factor in its classical form is independent of life, probably because plasticity effects during the tensile and compressive halves of the load cycle essentially cancel each other. When extended to apply to tension loading ($R \geq 0$), the fatigue concentration factor is generally an increasing function of life, and a decreasing dependence of stress ratio. In most cases 'K_f' is highest for fully reversed loading, and values of 'K_f' for positive stress ratios tend towards those for $R = 1.0$ with lower stresses and consequentially longer lifes.

The earliest representation of mean stress effects was by Gerber (1874), who proposed a parabolic relationship between the stress range and mean stress based on Wöhler's data, i.e.,

$$\frac{\Delta\sigma}{2} = \sigma_e \left(1 - \left(\frac{\sigma_{mean}}{\sigma_{UTS}} \right)^2 \right) \tag{2.20}$$

where

σ_e is the endurance limit
σ_{mean} is the mean stress, given as $\frac{\sigma_{max} + \sigma_{min}}{2}$

Fig 2.3 shows a schematic Gerber diagram with parabolic curves of constant fatigue endurance and superimposed constant R curves. In completely reversed bending, the mean stress is zero and $\Delta\sigma/2$ at 10^7 cycles is the endurance limit. If the mean stress is equal to the ultimate tensile strength, $\Delta\sigma/2$ is zero and the condition is that of static failure in one cycle. Goodman [2.21] noted that experimental data points fell within Gerber's parabola and proposed a straight line relation for conservative design purposes, i.e.,

$$\frac{\Delta\sigma}{2} = \sigma_e\left(1 - \left(\frac{\sigma_{mean}}{\sigma_{UTS}}\right)\right) \tag{2.21}$$

Goodman or constant life diagrams indicate the fatigue behaviour of materials in terms of constant life lines for all conditions of mean and alternating stress that are possible to apply. The diagrams may be regarded as a collection of sections made up of S-N curves, each at the appropriate mean stress. Fig 2.4 shows a conceptual fatigue square that represents all loading conditions and displays lines of constant R - ratio. A fuller version of the Goodman diagram is shown in Fig 2.5, showing lines of constant fatigue strength. The imaginary area in the fatigue square is neglected, also is the subtriangle on the compression side beyond $R = \infty$, as it represents no practical conditions. Sometimes the maximum and minimum stress axes are superimposed and it is often common practice to include both notched and unnotched life lines on the same diagrams. The stress amplitude is plotted against the mean cyclic stress on linear axes, using the same scale for both variables. A straight line called the Goodman line, drawn from the value of stress amplitude to a constant life line gives the allowable mean stress for that stress amplitude in terms of the chosen life line. Alternatively the diagrams can be used to determine an equivalent zero mean stress amplitude to a given non zero mean situation. Simple specimen S-N data can be generally considered stress-cycles to initiation as longer lives are primarily due to thicker sections associated with more complicated geometries.

Mean stress effects can be accounted for by using the equivalent zero mean stress amplitude into equation (2.19) instead of the actual stress amplitude. However if

S-N or Goodman data is available at all, it is likely that the given situation can be solved directly from these diagrams. A modification to equation (2.4) to account for mean stress was proposed by Morrow [2.22]. This is an empirical relationship and gives the equivalent zero mean stress amplitude as a linear relationship similar to that of Goodman (equation (2.21)) but as a function of the fatigue strength coefficient, i.e.,

$$\sigma_{cr} = \frac{\sigma}{1 - \frac{\sigma_{mean}}{\sigma'_f}} \tag{2.22}$$

where:

σ_{cr} is the completely reversed stress amplitude expected to cause failure in the same life as the actual combination of mean and amplitude, σ_{mean} and σ respectively.

A mean stress bias which causes plastic deformation in a notch region does not alter the notch stress state greatly unless a very high mean level is encountered. The material accommodates the mean stress by plastic deformation, transferring its share of the mean load to the surrounding elastic material developing a mean strain [2.23]. These low cycle mean effects need not be considered below plastic elastic transition life (the intersection point of the two straight lines in the strain-life plot). For predominantly elastic cycles where mean stress may be important, equation (2.22) can be used to correct equation (2.4) by the expression:

$$\frac{\Delta\varepsilon}{2} = \frac{(\sigma'_f - \sigma_{mean})}{E}(2N_f)^b + \varepsilon'_f(2N_f)^c \tag{2.23}$$

The above equation is useful for use with threaded connections, as it can account to some extent for the preload due to applied make-up torque.

Surface residual stress plays an important role in fatigue crack initiation from notches. In thread roots, residual stresses mainly occur due to forming, machining or surface processing treatments to improve mechanical durability. Cold rolling of threads is the most commonly used method of inducing residual compressive stresses in thread roots. The influence of inducing surface residual stresses on fatigue performance depends on local material properties, the service loading, and the magnitude and distribution of the residual stresses. The material behaviour will determine the depth of surface processing, in general this relates to the hardness of the material. The stability or resolution of the impressed residual stress will also be determined by the tendency of the material to cyclically soften or relax.

It is common to assess residual stress effects on fatigue by treating them as mean stresses. These would be expected to relax in the case of fully reversed elastic straining and may occur at lower than expected stress levels due to cyclic softening (particular to the type of steel). Jhansale and Topper [2.24] observed that while static creep or relaxation of mean stresses was a time dependent viscous phenomenon under a steady load at relatively high temperatures (greater than half melting temperature), cyclic mean stress relaxation is independent of time, but is a cyclic dependant decrease in the absolute value of mean stress under cyclic strain amplitude at much lower temperatures. Mean stresses relax at an exponential rate with cycles, the rate of relaxation becoming smaller with the increasing number of cycles. Higher reversed strain amplitudes correspond to faster rates of relaxation. Interestingly, they observed that the rate of relaxation does not appear to depend on the sign of the mean stress (tensile or compressive) and that a reversed loading is not necessary for residual or mean stress relaxation. This is important as a reversed loading situation is rarely encountered in a preloaded thread root. Experiment validated a model first proposed by Morrow, showing that the relation,

$$\sigma_{meanN} = \sigma_{mean} N^{B} \tag{2.24}$$

was valid for mild and 4340 steels. Where,

σ_{meanN} is the relaxed mean stress after 'N' cycles
(having the same sign as σ_{mean}).

B is the relaxation exponent, $B = f(\Delta\varepsilon)$

Landgraf and Chernekoff [2.25] identified a threshold strain amplitude below which relaxation would not be expected to occur. They also empirically expressed the relaxation exponent as a function of Brinell hardness for SAE 1045 steel as,

$$B = 8.5x10^{-2}(1 - \Delta\varepsilon/\Delta\varepsilon_{threshold}) \tag{2.25}$$

where

$$\frac{\Delta\varepsilon_{threshold}}{2} = \exp(-8.41 + 5.36x10^{-3}HB) \tag{2.26}$$

This type of expression can be evaluated for any material and is a useful way of predicting the transient nature of residual stresses.

Equation (2.23) for mid to high cycle fatigue can be expressed to take account of residual stress as,

$$\frac{\Delta\sigma}{2(\sigma'_f - \sigma_{mean} - \sigma_{residual})} = (2N_f)^b \tag{2.27}$$

The higher the magnitude the parameter on the left hand side of the above equation is, the shorter the fatigue life. If this parameter is a maximum at some depth through the component thickness other than at the free surface, then subsurface crack initiation is possible. This often occurs in surface processed members, where the

shallow case is not sufficient to transfer load to the bulk of the surrounding material in a continuous manner. This is again a useful approach in evaluating the necessary depth of a mechanically induced surface hardness.

Surface residual stresses can be predicted if the material properties and processing mechanics are known. Otherwise an experimental measurement of the residual stress may be required. One example of such a method is the hole drilling method [2.26]. This involves drilling a small shallow hole (depth $\simeq$ diameter) in the specimen. This removal of stressed material causes localised stress and strain relaxations around the hole location. The strain relaxations are conveniently measured using a purpose designed strain gauge rosette.

2.5 Variable Amplitude Cycling

In chapter one, cycle counting, deterministic and probabilistic methods to solve random cycle fatigue were generally discussed. The rainflow (or pagoda-roof) and range-pair methods of cycle counting identify occurrence of range amplitudes and associated mean values. Although it was noted that with the rainflow method, cycles can be identified as closed stress-strain hysteresis loops, a statistical representation of a time series is not enough to reproduce a load history exactly. This generally does not present a problem for fatigue crack growth prediction of stationary ergodic random processes where the statistical properties of the process remain constant over time, and that the statistics for one sample function over time equals those for all sample functions at a given point in time. The limitations of identification of discrete strain range intervals for fatigue applications lie with the feature that the reconstructed discrete history is not identical to the measured history [2.27]. This has been observed with the use of the Markov matrix technique for reproduction of the time histories. Problems are solely due to limitations in computational ability, which restricts the number (hence size) of strain range increments. This results in smaller cycles being omitted which may be considered non-damaging, however cyclic material behaviour is sensitive to the path taken to attain a particular event in time. The same could be said of overload effects in fatigue crack propagation, but these are generally ignored as they are extreme rather than normal behaviour.

The methods for prediction of fatigue crack initiation discussed in this chapter however, are not sufficient to merit a cycle-by-cycle damage analysis of the cyclic material state. Other methods such as in reference [2.28] demand a complete material memory. These in the future with more powerful computational ability may become practical, but unless an accurate picture of an initial material state is known, it seems that such models could not provide a conclusive prediction of crack initiation.

For stationary random processes such as a sea-state, the use of a weighted average stress range can be used to correlate data from variable amplitude cyclic load tests with data from constant amplitude tests. The concept states that, for an equal number of cycles, the equivalent (constant amplitude) stress range will cause the same fatigue damage as the sequence of variable amplitude stress ranges it replaces. To weight the individual stress ranges, a relationship between these and damage must be established. The simplest is the S-N relationship which when used gives the equivalent stress range as [2.29].

$$\Delta\sigma_e = [\sum \gamma_i (\Phi_i \alpha \Delta\sigma_D)^B]^{\frac{1}{B}} \qquad (2.28)$$

where

$\Delta\sigma_e$ is the equivalent weighted average stress range
γ_i is the frequency of occurrence of $\Delta\sigma_i$
Φ_i is the ratio of $\Delta\sigma_i$ to $\Delta\sigma_D$
α is the ratio of measured to computed stress range for the design stress range
$\Delta\sigma_D$ is the computed design stress range
B is the Basquin exponent

Similarly for crack growth, the Paris relationship* is used to weight an equivalent stress range, the expression for which is essentially the same as (2.28) but the Paris exponent is used rather than the slope of the S-N curve. A special case exists when

$$* \left(\frac{da}{dn} = C(\Delta K)^m \right)$$

both methods give identical life predictions i.e. when: (a) the crack initiation phase is negligible; (b) there are no interaction effects in high-low stress range sequences; (c) all stresses are above the constant amplitude fatigue limit; and (d) the inverse slope of the S-N curve and the slope of the crack growth rate curve are equal. A similar method of calculating damage from a narrow band variable amplitude spectrum using S-N behaviour was detailed in chapter one.

Unfortunately none of these methods take mean stress into account. The most realistic crack initiation prediction method is to calculate the damage fraction expended at each stress range (with corresponding mean value) and apply a linear damage accumulation relationship. Recently however, a two phase double linear model proposed by Miller and expanded in [2.30] and [2.31] is gaining acceptance. This differentiates between the process of forming small micro-cracks and the process of propagating those micro-cracks to form a dominant crack. However at this stage it is beyond the scope of practical engineering design.

2.6 Discussion

The previous sections examined the most established engineering fatigue crack initiation models and detailed various approximations and assumptions frequently employed. It is a useful exercise to study the implications of adopting approximations, especially where it is necessary to know if a fatigue life prediction is conservative, and the approximate degree of conservatism or otherwise. In order to do this, six steels whose cyclic material properties are documented were chosen. The mechanical properties of these are shown in Table 2.1. The values given are taken from reference [2.32] which includes many other steels, however the six chosen were judged to be representative of a broad range of steels and the cyclic material properties self-consistent. Many published material properties do not exhibit self-consistency and must therefore be regarded with scepticism. The consistency can be checked by the relations:

$$n' = bc \tag{2.29}$$

$$K' = \sigma'_f/(\varepsilon'_f)^n \tag{2.30}$$

A certain percentage error (up to 20%) is often tolerable depending on the number of decimal places each value is reported. For example in Table 2.1, n' is only given to two decimal places. Values of 0.104 and 0.095 would both be given as 0.01 but the lowest value is 8.7% less than the largest. However, in the literature it is quite common to find errors of fifty to one hundred percent when the above checks are applied. Most discrepancies in material values arise due to inaccurate regression or data analysis [2.33], or as previously discussed too many data points are frequently considered from one test specimen leading to adoption of data points before saturation hardening is achieved. Relations (2.29) and (2.30) are useful ways of assessing confidence in cyclic material data.

Fatigue life predictions using relation (2.4) were compared with the two universal slopes approximations (2.2) and (2.3), and with the four point correlation method for the six steels. The four point correlation method was used by employing a closed form solution devised by Ong [2.34]. Fig 2.6 shows the prediction as a line having a forty five degree slope. For each material the number of cycles required to give an equal total strain range given by relation (2.4) was calculated by the four point correlation method. These generally show an unconservative approximation at cycles to failure less than 10^5, and a conservative trend at higher values of fatigue life. The log-log scale can be misleading, the maximum error between the prediction and approximation at 10^7 cycles is an underestimation of 93.5%. Fig 2.7 is a similar comparison but with the Manson-Hirschberg universal slopes approximation (2.2). Again a very similar trend is apparent, the maximum underestimation at 10^7 cycles is 95.1%. However, remembering the simplicity of expression (2.2), it is a much more usable approach than the four point correlation method. The second updated universal slopes expression (Muralidharan-Mason, expression (2.3)) is shown compared to the prediction in Fig 2.8. This is a better approximation, as the maximum underestimation is 84.4% at 10^7 cycles. However, because of the better fit, the likelihood of an unsafe estimation is greater, despite the reduction in the overall percentage error. It must be borne in mind that comparison is made with a semi-empirical model which is itself open to variation or error. Only six materials

were used for comparative purposes, their material properties scrutinized before being accepted, undoubtedly much more scatter would be seen if similar comparisons were made with a casual sample of published cyclic material data. These should be regarded as the best approximation to the prediction obtainable, i.e. anything closer than a factor of two is good.

Having looked at estimations of the prediction, it is worth considering the sensitivity of the prediction to variation of the cyclic material properties. Fig 2.9 shows the resultant predicted fatigue lives of material '6' with a -10%, 0% and +10% error in σ'_f. Figs 2.10 - 2.12 similarly show the sensitivity of N_f to ε'_f, b and c respectively. Again because of the log-log scales, percent error in N_f is tabulated in Table 2.2. These are shown for typical low and high cycle situations. Overestimation of σ'_f and ε'_f and under estimations of b and c lead to unconservative predictions and vice versa. In the high cycle regime, errors in ε'_f and c give small changes to life predictions, but overestimation of σ'_f and b can lead to large underpredictions of fatigue life. This is worth keeping in mind as often an average value of a selection of material constants is chosen, whereas the lower end of σ'_f and the upper end of the b values may be more appropriate for design purposes. It is also worth noting that the error in N_f is not proportional to errors in the constitutive material constants of equation (2.4) as this expression is not linear. Finally two common approximations for the prediction of ultimate tensile strength and fatigue strength coefficient are examined for the six steels in Table 2.3. The empirical equations give reasonably good predictions of the material properties.

The metallurgical variables having the most pronounced effect on the fatigue behaviour of carbon and low-alloy steels are strength level, ductility, cleanliness of the steel (free from nonmetallic inclusions), residual stresses, surface conditions and aggressive environments. These factors have been considered in this chapter. There are other mechanisms associated with fatigue crack generation that generally cannot be modelled, but knowledge of their existence can be advantageous. Some of these are detailed in the following paragraphs.

A secondary fatigue crack initiation mechanism is one that is independent of the material but due to the deterioration of the material surface under cycling. Fretting is one such wear phenomenon that occurs between two mating surfaces. It is adhesive in nature, and vibration is its essential causative factor [2.32]. Usually, fretting is accompanied by oxidation, especially in the presence of the remnant lubricant that has for the most part been broken down chemically or mechanically worked out. Fretting usually occurs between two tight-fitting surfaces that are subjected to a cyclic, relative motion of small amplitude. This situation frequently occurs on loaded thread flanks and under bolt heads when insufficient make-up torque is applied to threaded connections subjected to cyclic loading. Fretted regions easily lead to fatigue cracking. Under fretting conditions, fatigue cracks are initiated at very low stresses, well below the fatigue limit of nonfretted specimens.

Miller and Hatter [2.35] identified a beneficial effect of introducing rest periods from cyclic loading on the fatigue resistance of alloy steels. They reported that the introduction of rest periods at zero load during fatigue tests increased the fatigue endurance of a hardened and tempered 2.5% Ni-Cr-Mo steel by almost a factor of two after a critical maximum gainful rest period of one hundred hours. Thereafter the improvement in endurance is approximately constant at thirty three percent. Explaining this effect it was suggested that during the rest periods the specimens are still subject to high residual stress which could assist the diffusion of carbon through the metastable tempered-martensite structure. This mobility, inducing dislocation freedom of movement can result in stress relaxation. The total duration of the rest period appears to be the most important parameter than the number of rest periods taken or the position of the rest within the lifetime. The same mechanisms may be responsible for the phenomenon known as coaxing. This circumstance arises as an improvement in fatigue resistance of a material after being subjected to a large number of cycles at stress amplitudes below fatigue endurance.

Resistance to fatigue crack initiation depends on impurities, grain size and generally material microstructure. These are related to the thermal or mechanical treatment of the material. Low carbon steels in a normalised condition with ferrite-pearlite structures have a high cracking resistance, the cyclic stress-strain response is

enhanced with increasing carbon content [2.36]. However, a recent study [2.37] has shown that for austempered ductile steels, under a large strain amplitude the best low cycle fatigue behaviour occurs from the material that has undergone austempering at 950°C, whereas under a smaller strain amplitude, the best low cycle fatigue behaviour is seen in similar materials austempered at 350°C. For a typical HSLA steel, AISI 4340, reference [2.38] suggests that fatigue strength under bending and torsion could be represented as a linear function of hardness using Brinell hardness numbers. Specimens given a super quench in liquid nitrogen showed higher hardness and fatigue strength than those subjected to the same heat treatment but with a straight oil quench. Grain size is also an important aspect when choosing fatigue resistant steels. Opposing microstructural requirements for good resistance to fatigue crack initiation (high fatigue limit) and good resistance to fatigue propagation are investigated in reference [2.39]. It is reported here, as elsewhere, that a fine grained material will give better resistance to fatigue crack initiation whereas materials of larger grain size will be better suited to resist crack nucleation and subsequent slow growth, if a pre-existing defect happens to be present in the structure.

An essential series of reference fatigue data for Unified, Whitworth and ISO metric threads is the ESDU [2.40] data series of fatigue data for screw threads. Relevant publications are item numbers 67020, 67034, 68045, 83012 and 84037. These report the findings of nearly two thousand fatigue tests on solid threaded bars varying a variety of factors. Item 67020, "Fatigue Strength of Steel Screw Threads with Large Root Radii Under Axial Loading", compares the improved fatigue resistance of threads with large root radii to those having smaller fillet radii. Scatter is shown in terms of two manufacturing techniques; (a) thread form-rolled and then heat treated, and (b) material fully heat treated, then surface ground before form-rolling of the thread. As anticipated threads having large fillet radii and manufactured by method (b) show the greatest resistance to fatigue crack initiation. Item 68045, "Fatigue Strength of Large Steel Screw Threads Under Axial Loading", again compares Unified and Whitworth thread fatigue performance with a variety of manufacturing and surface finishing techniques including cut, ground, form rolled and root rolled threads. The form and root rolled specimens were consistently stronger under

dynamic loading. Items 83012 and 84037 essentially consider similar comparisons but between titanium alloy screw threads and smaller diameter steel bolts respectively. Chapter six will consider some of the surface treatments mentioned with regard to fatigue crack initiation, however, for engineering fatigue crack initiation design data of standard structural threaded connections under axial loading, the ESDU data series contains a wealth of S-N information.

2.7 Summary and Conclusions

This chapter was concerned with the generation of fatigue cracks from thread roots, rather than their subsequent growth. The mechanisms of fatigue crack initiation were discussed with regard to metallurgical and mechanical aspects of material structure and behaviour. Mathematical representation of cyclic material performance was explored and constants specific to individual materials were defined. A concise history of the development of a strain-life approach to fatigue analysis was reported, giving reference to typical values of material constants and approximations to these.

Stress-strain relationships were investigated for inelastic behaviour. Notch sensitivity and fatigue concentration factors were identified as important aspects of fatigue crack initiation. Mean, residual and variable amplitude stresses were discussed in terms of their effect on fatigue crack generation. Methods of quantifying these effects were also considered.

Finally a discussion examined the consistency of published cyclic material properties and studied the sensitivity of predicted fatigue life on the accuracy of material data.

Determination of local strain in the thread root to cycles to fatigue crack initiation is the preferred method to calculate crack initiation life. Cyclic strength and ductility material properties are generally required for the strain-life relationship, however two universal slopes approximation methods estimate the strain-life behaviour without these quantities. In the plane strain loading at thread roots, a linear

relationship between the strain concentration factor and stress concentration factor (or fatigue concentration factor) is the most appropriate. Residual and mean stresses are significant at potential crack sites in thread roots. These can be calculated or measured and incorporated into the strain-life calculation.

2.8 References

[2.1] Braithwaite, F., "On the Fatigue and Consequent Fracture of Metals", M. Proc. I.C.E., pp 463-475, 1853-54.

[2.2] Schijve, J., "Predictions on Fatigue", JSME International Journal, Series I, vol 34, no 3, pp 269-280, 1991.

[2.3] Manson, S. S., "Fatigue: A Complex Subject - Some Simple Approximations", Experimental Mechanics, pp 193-226, July 1965.

[2.4] Landgraf, R. W., Morrow, JoDean and Endo, T., "Determination of the Cyclic Stress-Strain Curve", Journal of Materials, vol 4 no 1, pp 176-188, March 1969.

[2.5] Morrow, JoDean, "Cyclic Plastic Strain Energy and Fatigue of Metals", ASTM STP 378, pp 45-87, 1965.

[2.6] Topper, T. H., Sandor, B. I. and Morrow, JoDean, "Cumulative Damage Under Cyclic Strain Control", Journal of Materials, vol 4, no 1, pp 189-199, March 1969.

[2.7] Dugdale, D. S., "Stress-Strain Cycles of Large Amplitude", Journal of the Mechanics and Physics of Solids, vol 7, no 2, pp 135-142, 1959.

[2.8] Grosskreutz, J. C., "A Critical Review of Micromechanisms in Fatigue", Proceedings of the 10th Sagamore Army Materials Research Conference, pp 27-59, 1964.

[2.9] James, M. R. and Morris, W. L., "The Role of Microplastic Deformation in Fatigue Crack Initiation", ASTM STP 811, pp 46-70, 1983.

[2.10] Muralidharan, U., Manson, S. S., "A Modified Universal Slopes Equation for Estimation of Fatigue Characteristics of Metals", Journal of Engineering Materials and Technology, vol 110, pp 55-58, January 1988.

[2.11] Dowling, N. E., Brose, W. R. and Wilson, W. K., "Notched Member Fatigue Life Predictions by the Local Strain Approach", Fatigue Under Complex Loading, SAE, pp 55-84, 1977.

[2.12] Morrow, JoDean, "Cyclic Plastic Strain Energy and Fatigue of Metals", ASTM STP 378, pp 45-87, 1965.

[2.13] Raske, D. T. and Morrow, JoDean, "Mechanics of Materials in Low Cycle Fatigue Testing", ASTM STP, 465, pp 1-25, 1969.

[2.14] Osgood, C. C., "Fatigue Design", ISBN 0-08-026166-3, 1982.

[2.15] Neuber, H., "Theory of Stress Concentration for Shear Strained Prismatical Bodies with Arbitrary Non Linear Stress Strain Law", Journal of Applied Mechanics, pp 544-550, December 1961.

[2.16] Topper, T. H., Wetzel, R. M. and Morrow, JoDean, "Neuber's Rule Applied to Fatigue of Notched Specimens", Journal of Materials, vol 4, no 1, pp 200-209, March 1969.

[2.17] Peterson, R. E., "Stress Concentration Factors", John Wiley & Sons, 1973.

[2.18] Conle, A. and Nowack, H., "Verification of a Neuber-Based Notch Analysis by the Companion-Specimen Method", Experimental Mechanics, vol 17, no 2, pp 57-63, 1977.

[2.19] Sharpe, W. N., Wang, K. C., "Evaluation of a Modified Monotonic Neuber Relation", Journal of Engineering Materials and Technology, vol 113, pp 1-8, January 1991.

[2.20] Berkovits, A., "Variation of Fatigue Notch Factor with Lifetime, Stress Ratio and Temperature", Journal of Engineering Materials and Technology, vol 108, pp 179-185, April 1986.

[2.21] Goodman, J., "Mechanics Applied to Engineering", vol 1, Longmans Green, London, 1930.

[2.22] Morrow, JoDean, "Fatigue Properties of Metals", Section 3.2 of Fatigue Design Handbook, SAE, November 1964.

[2.23] Dubuc, J., "Effect of Mean Stress and of Mean Strain on Low Cycle Fatigue of A-517 and A-201 Steels", Journal of Engineering for Industry, ASME, pp 35-52, February 1970.

[2.24] Jhansale, H. R. and Topper, T. H., "Engineering Analysis of the Inelastic Stress Response of a Structural Metal Under Variable Cyclic Strains", Cyclic Stress-Strain Behaviour - Analysis, Experimentation, and Failure Prediction, ASTM, STP 519, pp 246-270, 1973.

[2.25] Landgraf, R. W. and Chernenkoff, R. A., "Residual Stress Effects on Fatigue of Surface Processed Steels", Analytical and Experimental Methods for Residual Stress Effects in Fatigue, ASTM STP 1004, R. L. Champoux, J. H. Underwood and J. A. Kapp, Eds., pp 1-12, 1988.

[2.26] Schajer, G. S., "Measurement of Non-Uniform Residual Stresses Using the Hole Drilling Method. Part 1 - Stress Calculation Procedures", Journal of Engineering Materials and Technology, vol 110, pp 339-343, October 1988.

[2.27] Pompetzki, M. A., Topper, T. H., and Dabell, B. J., "Determination of the Possible Error in Fatigue Damage for a Discrete Strain History", Fatigue Fract. Engng. Mater. Struct. vol 15, no 5, pp 491-505, 1992.

[2.28] Mróz, Z., "Hardening and Degradation Rules for Metals Under Monotonic and Cyclic Loading", Journal of Engineering Materials and Technology, vol 105, pp 113-118, April 1983.

[2.29] Albrecht, P., "S-N Fatigue Reliability of Highway Bridges", Probabilistic Fracture Mechanics and Fatigue Methods: Applications for Structural Design and Maintenance, ASTM STP 798, J. M. Bloom and J. C. Ekvail, Eds., American Society for Testing and Materials, pp 184-204, 1983.

[2.30] Karlson, A., "Crack Initiation at Notches", Proceedings 3rd Int. Conf. Numerical Methods in Fracture Mechanics, A. Luxmoore and R. Owen, Eds., Pineridge Press, Swansea, pp 619-630, 1984.

[2.31] Ben-Amoz, M., "Prediction of Fatigue Crack Initiation Life from Cumulative Damage Tests", Engineering Fracture Mechanics, vol 41, no 2, pp 247-249, 1992.

[2.32] "Fatigue Resistance of Steels", "Properties and Selection: Irons and Steels", ASM Handbook, 10th Ed, vol 1, 1990.

[2.33] Boardman, B. E., "Crack Initiation Fatigue - Data, Analysis, Trends and Estimation", Proceedings of the SAE Fatigue Conference, P-109, pp 59-73, April 1982.

[2.34] Ong, J. H., "An Evaluation of Existing Methods for the Prediction of Axial Fatigue Life from Tensile Data", Accepted for Publication in the International Journal of Fatigue, to appear in 1993.

[2.35] Miller, K. J. and Hatter, D. J., "Increases in Fatigue Life Caused by the Introduction of Rest Periods", Journal of Strain Analysis, vol 7, no 1, pp 69-73, 1972.

[2.36] Polák, J., "Cyclic Plasticity and Low Cycle Fatigue of Metals", ISBN O-444-98839-4, 1991.

[2.37] Hwang, Jiun-Ren, Perng, Chia-Chaw and Shan, Ying-Shyng, "Low-Cycle Fatigue of Austempered Ductile Irons", Int. J. Fatigue, 12, no 6, pp 481-488, 1990.

[2.38] Findley, W. N., "Effects of Extremes of Hardness and Mean Stress on Fatigue of AISI 4340 Steel in Bending and Torsion", Journal of Engineering Materials and Technology, vol 111, pp 119-122, April 1989.

[2.39] Mutoh, Y., Radhakishnan, V. M., "Effect of Yield Stress and Grain Size on Threshold and Fatigue Limit", Journal of Engineering Materials and Technology", vol 108, pp 174-178, April 1986.

[2.40] Engineering Sciences Data Unit, (ESDU), 4 Hamilton Place, London W1.

Mat[L]	Grade	Brinell Hardness (HB)	σ_{UTS} (MPa)	σ_y (MPa)	E (GPa)	RA %	K′ (MPa)	n′	σ'_f (MPa)	b	ε'_f	c
1	1020	108	392	233	186	64	1206	0.26	850	-0.12	0.44	-0.51
2	1030	128	454	248	206	59	1545	0.29	902	-0.12	0.17	-0.42
3	1045	500	1825	1259	206	51	2636	0.12	2165	-0.07	0.22	-0.66
4	4142	380	1412	966	206	48	2259	0.14	1820	-0.08	0.65	-0.76
5	4340	242	825	467	192	43	1384	0.17	1232	-0.08	0.53	-0.56
6	4340	409	1467	876	200	38	1950	0.13	1898	-0.08	0.67	-0.64

Table 2.1

Cyclic Material Properties of Selected Steels

	8.962 x 10^4 Cycles	**3.016 x 10^6 Cycles**
1.1 σ'_f **0.9 σ'_f**	+ 121.5% - 51.2%	+ 206.0% - 68.7%
1.1 ε'_f **0.9 ε'_f**	+ 6.14% - 6.14%	+ 1.3% - 1.3%
1.1 b **0.9 b**	- 46.9% + 140.0%	- 69.2% + 368.0 %
1.1 c **0.9 c**	- 32.3% + 77.8%	- 8.2% + 22.3%

\+ Overestimate

\- Underestimate

Table 2.2

Sensitivity of Fatigue Life Prediction
to Cyclic Material Properties

Mat[L]	$^{*}\sigma_{UTS}$ = 3.45 x BHN	% Error	$^{*}\sigma'_f = \sigma_{UTS} + 345$	% Error
1	373	-4.9	737	-13.3
2	442	-2.6	799	-11.4
3	1725	-5.5	2170	0.2
4	1311	-7.2	1757	-3.5
5	835	1.2	1170	-5.0
6	1411	3.8	1812	-4.5

\+ Overestimate

\- Underestimate

BHN Brinell Hardness Number

* Reference [2.33]

Table 2.3

Estimation of σ_{UTS} and σ'_f

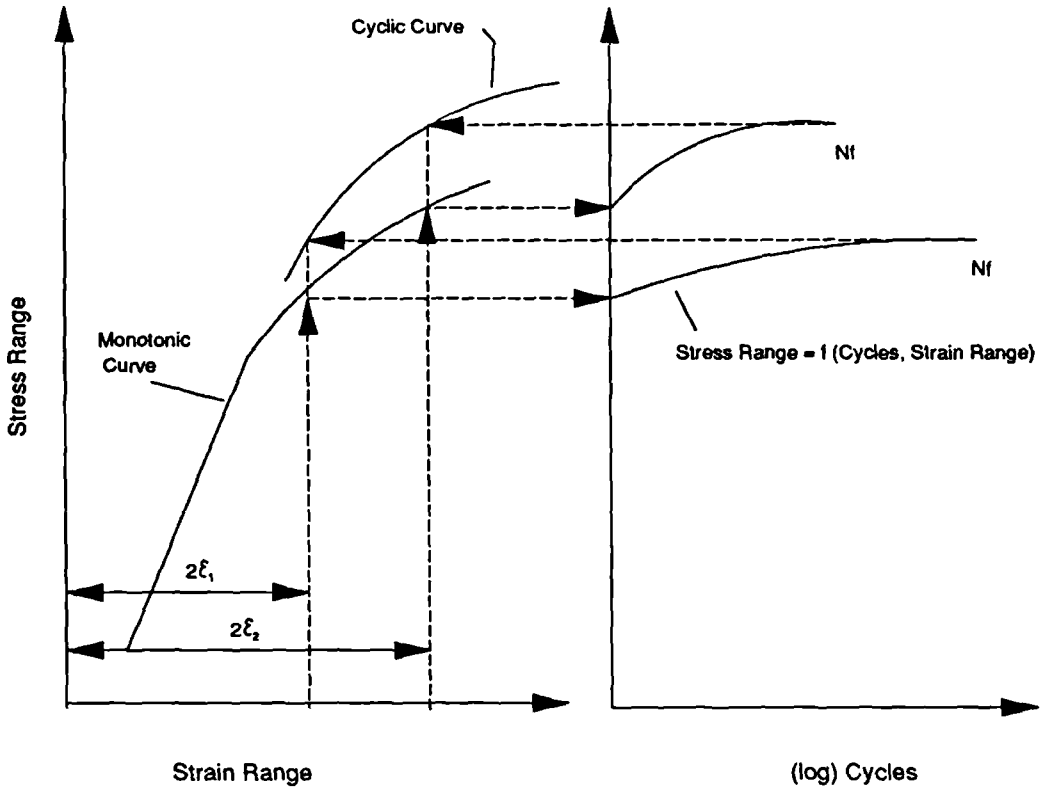

Fig 2.1

Cyclic Stress-Strain Behaviour

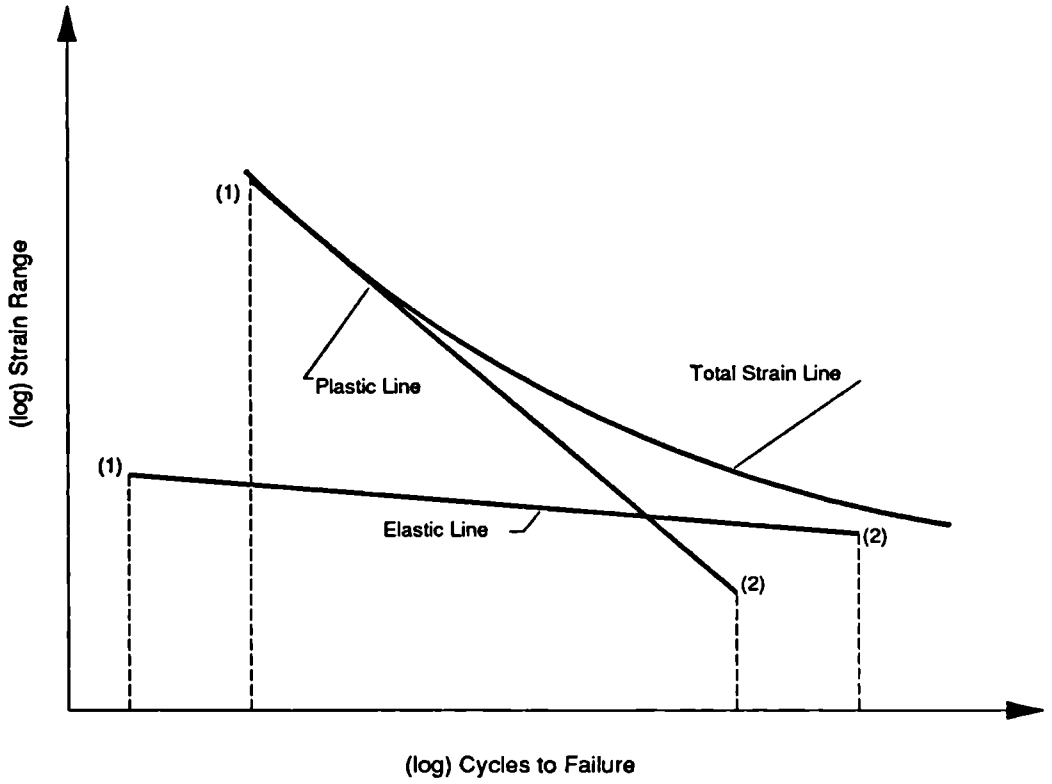

Fig 2.2

Strain-Life Diagram

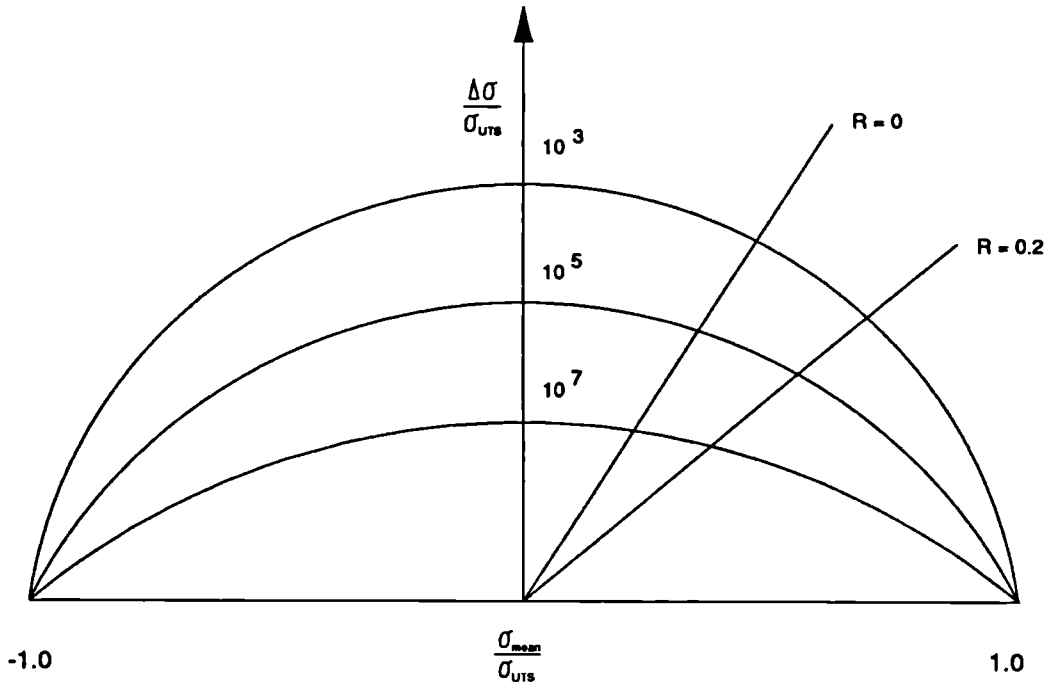

Fig 2.3

Gerber Diagram

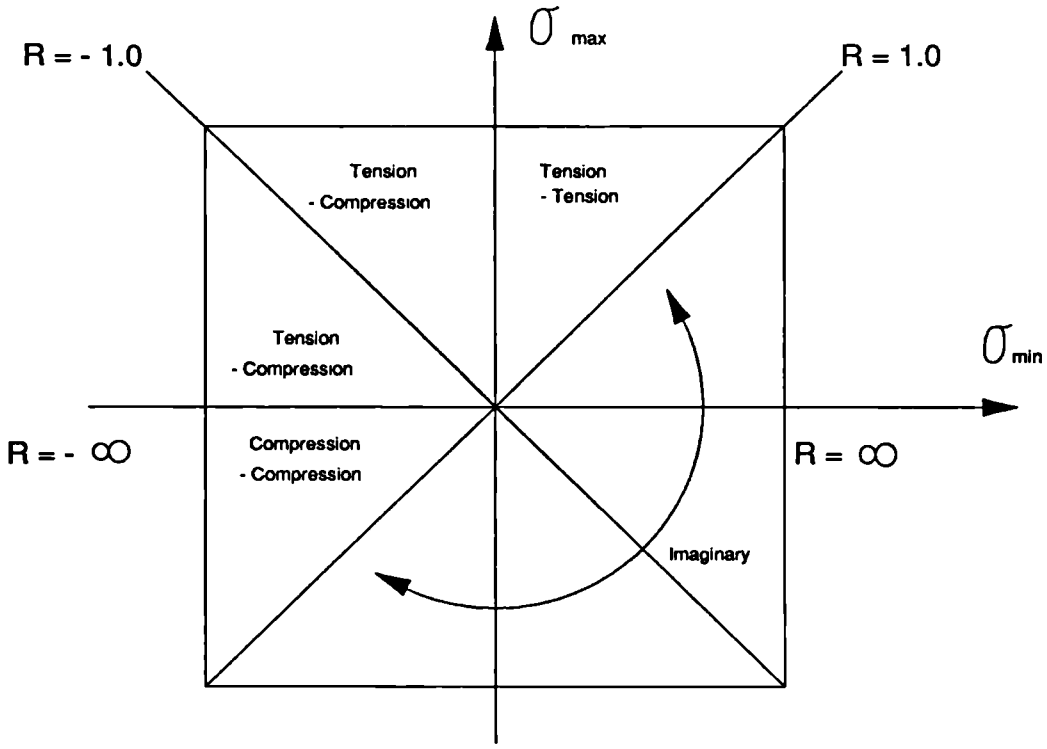

Fig 2.4

Fatigue Square

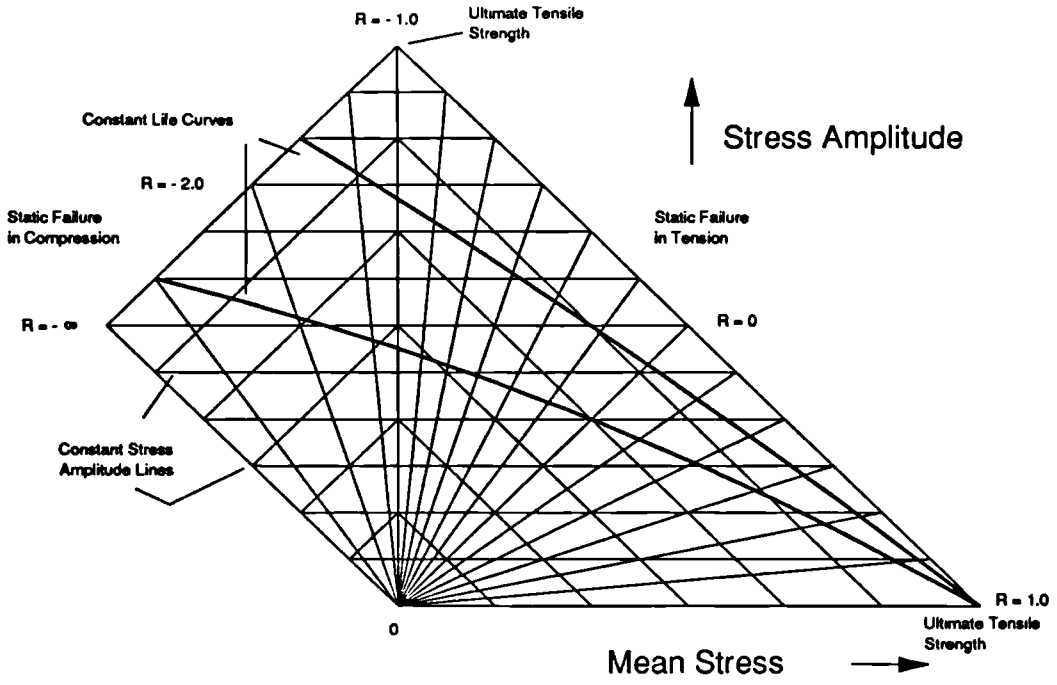

Fig 2.5

Goodman Diagram

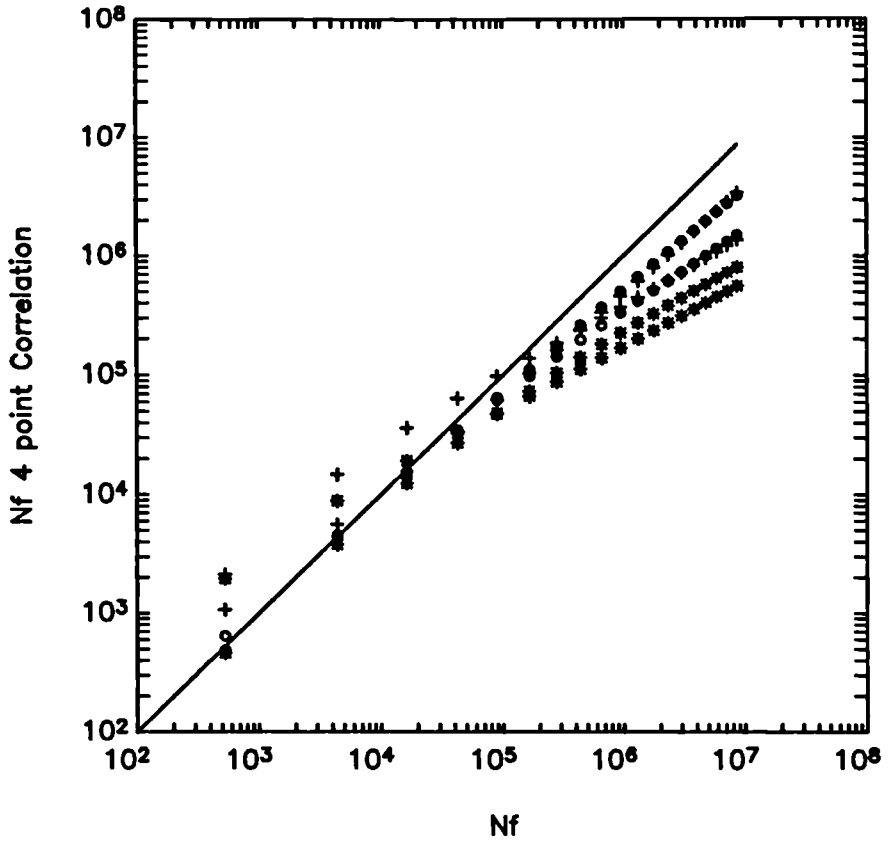

Fig 2.6

Fatigue Life Prediction and Four Point Correlation Approximation

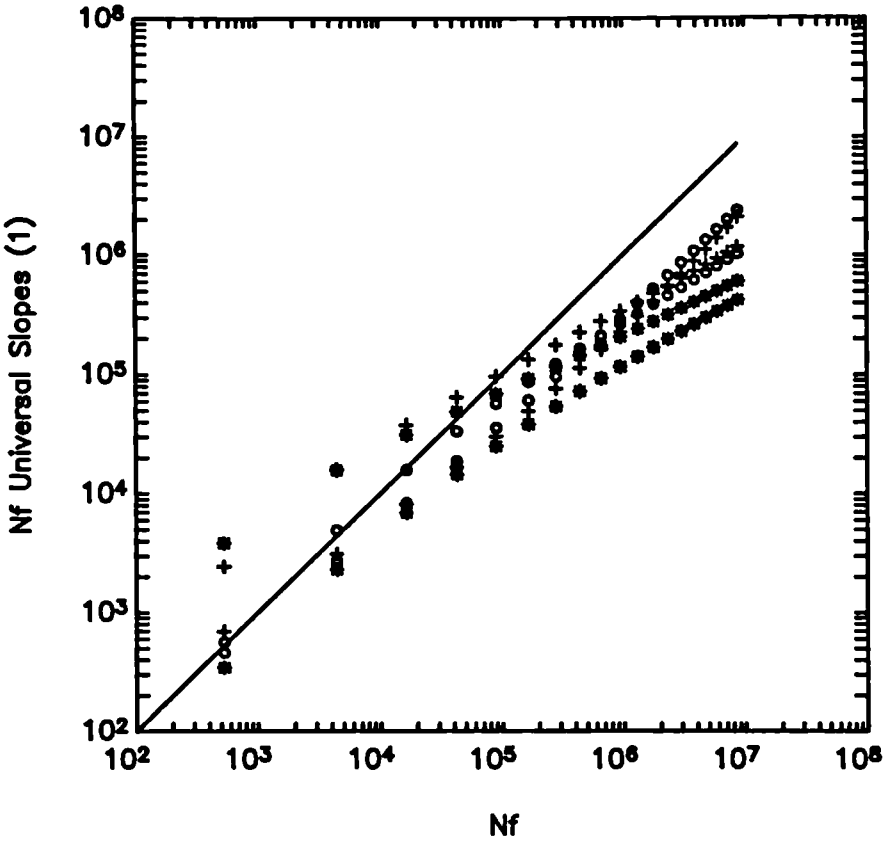

Fig 2.7

Fatigue Life Prediction and Manson-Hirschberg
Universal Slopes Approximation

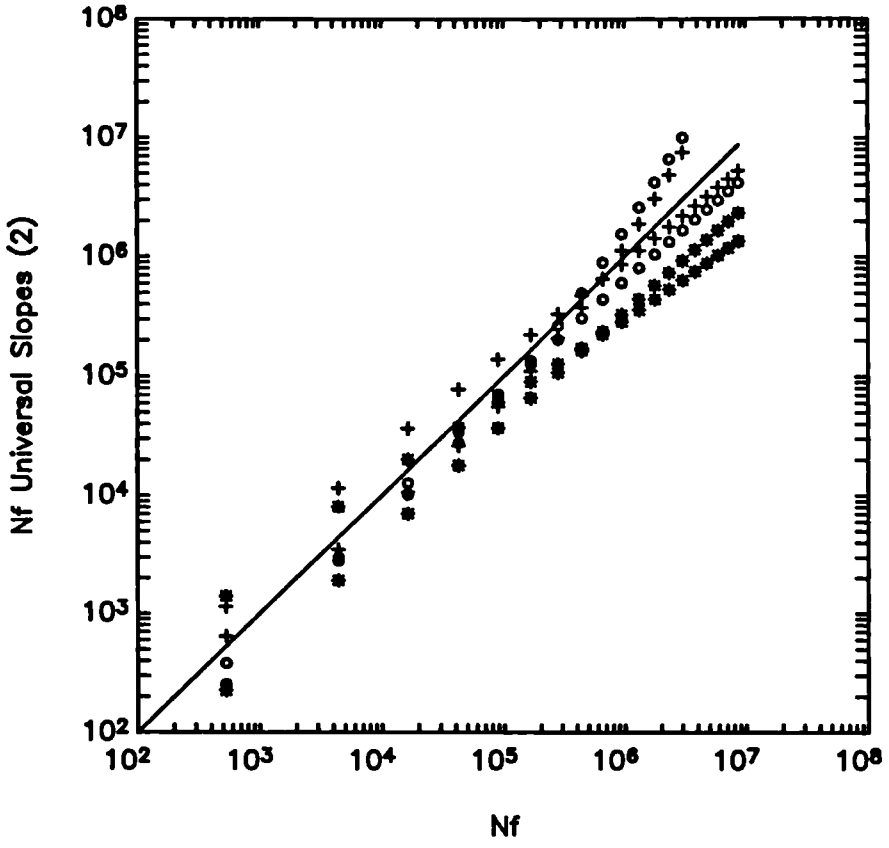

Fig 2.8

Fatigue Life Prediction and Muralidharan-Manson
Universal Slopes Approximation

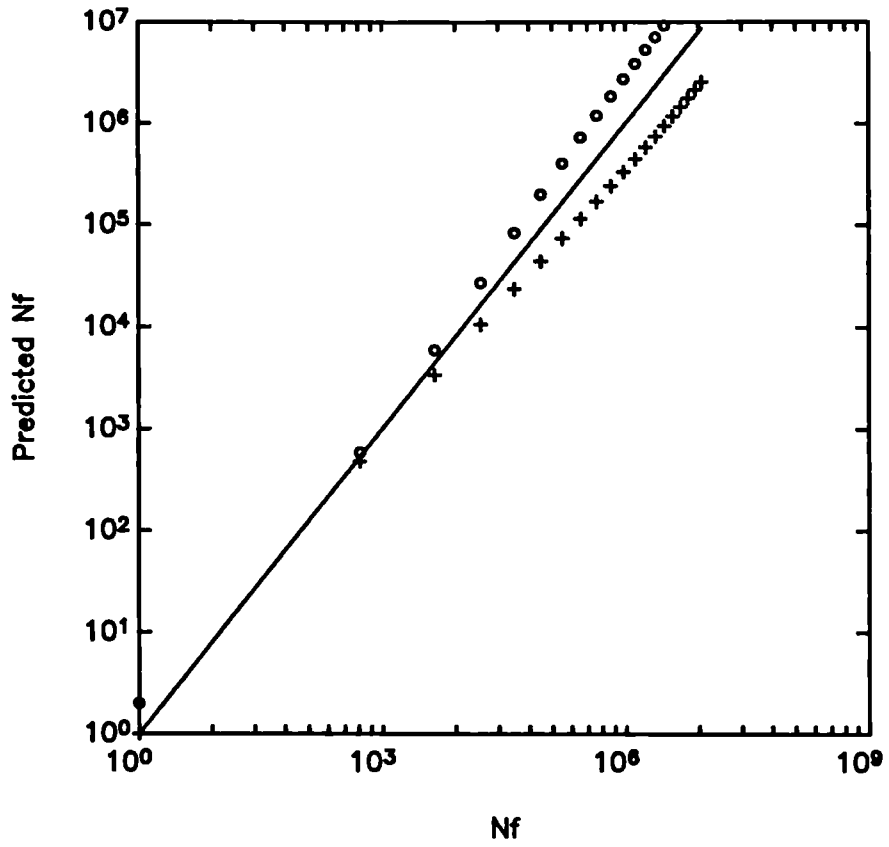

———————— 0% Error in σ'_f

o o o o o o o +10% Error in σ'_f

+ + + + + + + -10% Error in σ'_f

Fig 2.9

Sensitivity of Predicted Fatigue Life to σ'_f

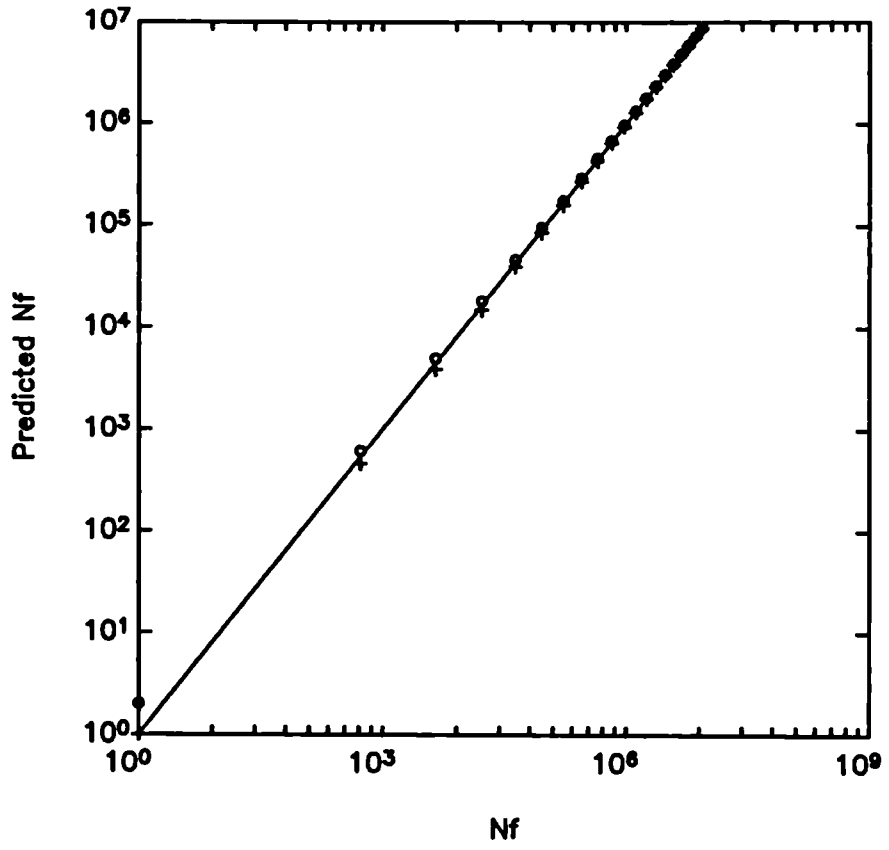

——————— 0% Error in ε'_f

o o o o o o o +10% Error in ε'_f

+ + + + + + + -10% Error in ε'_f

Fig 2.10

Sensitivity of Predicted Fatigue Life to ε'_f

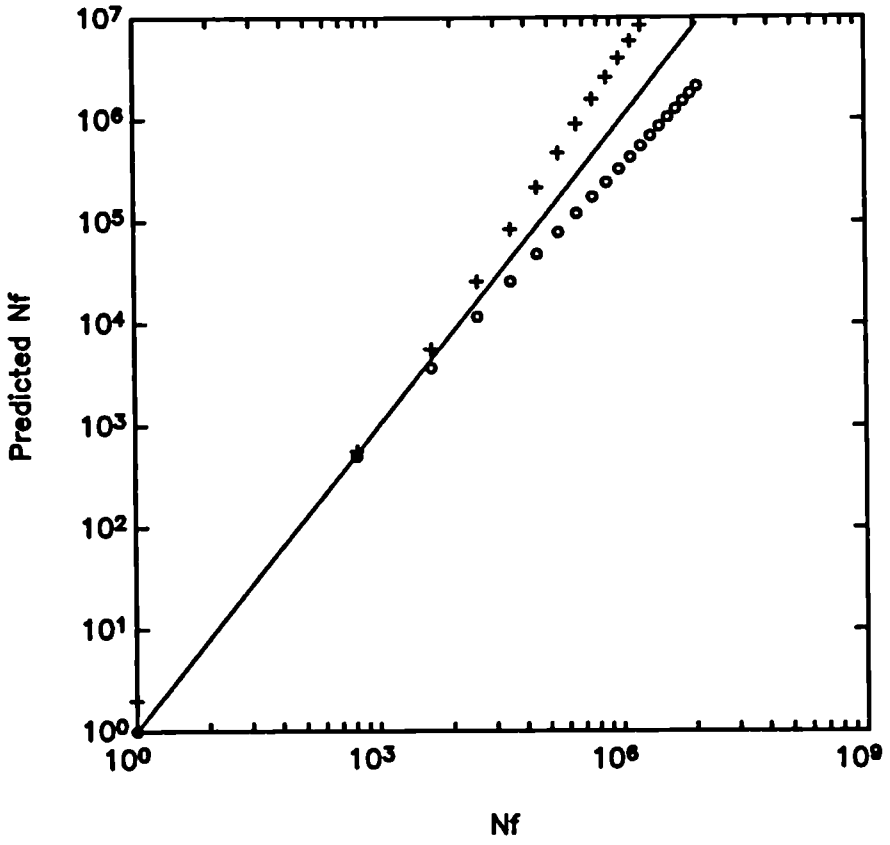

——————— 0% Error in *b*

o o o o o o o +10% Error in *b*

+ + + + + + + -10% Error in *b*

Fig 2.11

Sensitivity of Predicted Fatigue Life to *b*

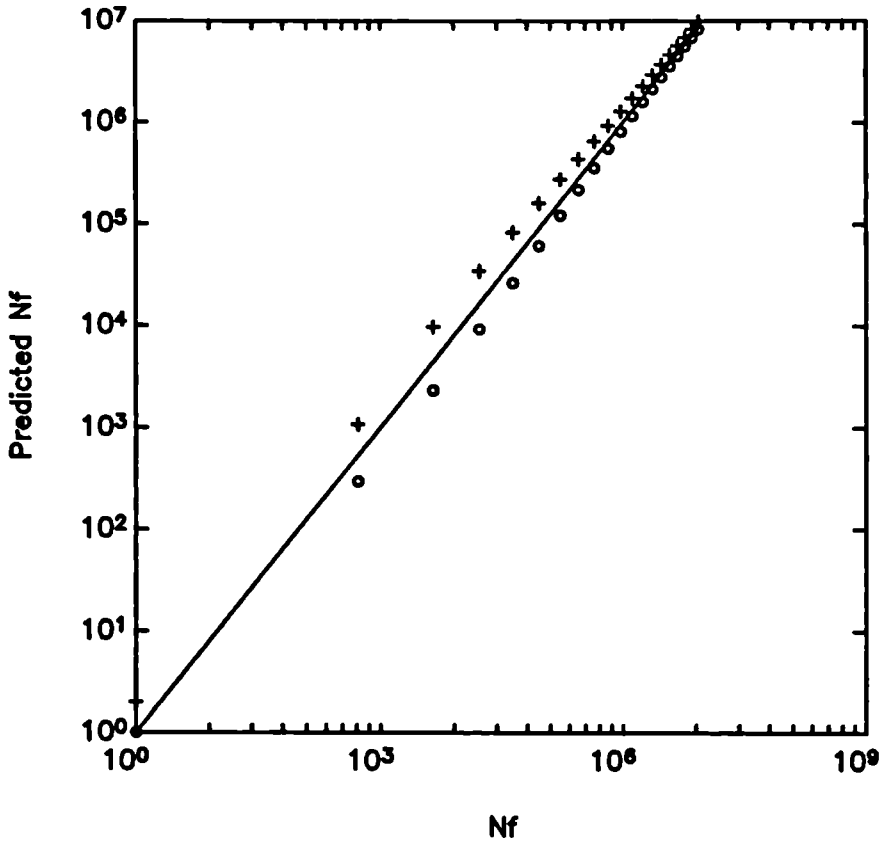

———————	0% Error in *c*
o o o o o o o	+10% Error in *c*
+ + + + + + +	-10% Error in *c*

Fig 2.12

Sensitivity of Predicted Fatigue Life to *c*

CHAPTER THREE - Fatigue Crack Propagation in Threaded Connections

3.1 Introduction

Despite the wide use of threaded fasteners in the assembly of structural and machine components, surprisingly little published material exists addressing fatigue crack growth in screw threads. This is partly due to the complexity of the internal stress mechanics of the system and the enormous variation of connection types, materials, quality of manufacture and maintenance. Observation of fatigue crack growth is also difficult as the crack is practically always hidden within the connection until it emerges as a through crack. Cracks most frequently occur in the thread roots thus giving rise to the analogy of cracks in circumferentially notched bars, and the use of the Harris [3.1] solution for external circumferential cracks in a tube under uniform axial tensile stress or torsion. This is a useful solution, however not directly relevant to threaded connections. Solutions do exist for related geometrical shapes and some SIF solutions have been published for specific threaded connections [3.2, 3.3, 3.4]. James and Mills [3.5] produced probably the most useful, review and innovative synthesis of possible solutions for bolts. This is mainly an assessment of SIF solutions in rods and includes interesting observations on how these cracks grow in reality. However, no conclusive solution is formed, the variations such as thread form, hollow tube and indeed internal cracks are not even considered.

For these reasons, development of a generic solution for the fatigue crack growth from any thread root valid under any symmetrical stress system is attempted in this chapter. The solution excludes a calculation for the load distribution within the entire connection such as those by Sopwith, Patterson or Bluhm and Flanagan [3.6, 3.7, 3.8]. Geometric features remote from the threads (such as Stress Relief Groove Pin and Bore Back Box in drill tools) have become commonplace as stress relief mechanisms in highly critical fatigue areas within connections. For this reason it is considered that the load distribution is best analysed separately using finite element or photoelastic methods, and that once known the SIF solution proposed in this chapter can be implemented.

Weight function solutions (introduced earlier) provide relatively simple stress intensity factor solutions for arbitrary symmetric loading systems. Finite element methods are invariably computationally inefficient, especially where a number of growth scenarios are to be considered. They are, however,when used with full scale test results, useful validation techniques. The weight function method is mathematically exact, errors in a final solution can be solely attributed to inaccurate mechanical interpretation or simplification of the problem being addressed.

The proposed solution uses a recent development in weight function theory which eliminates differentiations in the calculation, making the routine far more stable and computationally efficient. The solution is an amalgam of published solutions each of which themselves weigh the influence of several geometrical features. The solution is structured modularly so that it can evolve easily with the advent of more comprehensive sub solutions. The background, development and details of the SIF solution is described in the following sections.

3.2 Petroski-Achenbach Crack Opening Displacement

The weight function as defined in chapter one is attributed to Bueckner [3.9] who first identified a geometric singularity in a cracked elastic domain as a function of stress intensity at the crack tip, independent of externally impressed forces. Rice [3.10] developed this feature, his derivation of the weight function from first principles is set out in chapter one and gives the weight function as:

$$f_m(s,a) = \frac{H}{2K_m}\frac{\partial u_m(s,a)}{\partial a} \tag{3.1}$$

The significance of this function was not immediately appreciated since the term requiring the crack face displacement is not easily defined. A breakthrough in the usefulness of the weight function for the computation of stress intensity factor was evident with the successful implementation of the Petroski-Achenbach [3.11]

analytical representation of crack opening displacement as a function of a reference stress intensity factor and corresponding stress distribution in the potential crack plane. The approach is to simply use the expression,

$$K = \int_0^a \sigma(x) f(a,x) dx \tag{3.2}$$

'x' is the distance from the notch root

to self substitute into the expression for the weight function itself (3.1). It is apparent that an integral identity results from which a single parameter form for the crack displacement is determined. This means that assuming a one-parameter form for the crack shape leads to an expression for the crack face displacement in terms of the reference variables required for the weight function alone. This can be seen as follows:

$$K^2 = \frac{H}{2} \int_0^a \sigma(x) \frac{\partial u}{\partial a} dx \tag{3.3}$$

since $u(a,x) = 0$, at $x = a$,

$$\int_0^a [K(a)]^2 da = \frac{H}{2} \int_0^a \sigma(x) u(a,x) dx \tag{3.4}$$

A parametric representation of $u(a,x)$ must demonstrate limiting behaviour near the crack tip, i.e. [3.12],

$$u(a,x) = \frac{4K}{H} \left(\frac{a-x}{2\pi} \right)^{\frac{1}{2}} \tag{3.5}$$

It must also demonstrate consistent behaviour for small cracks, i.e.,

$$u(a,x) = f(a,x)$$
$$as\ a \rightarrow 0, f(a,x) = 0$$

These requirements along with the necessity that unknown parameters could be easily determined from a knowledge of 'K' and 'σ' alone, gives the assumed Petroski-Achenbach displacement representation for an edge crack in Mode I as:

$$u(a,x) = \frac{\sigma_o}{H\sqrt{2}}\left[4F\left(\frac{a}{t}\right)\sqrt{a(a-x)} + \frac{G\left(\frac{a}{t}\right)(a-x)^{\frac{3}{2}}}{\sqrt{a}}\right] \tag{3.6}$$

where

$$F\left(\frac{a}{t}\right) = \frac{K}{\sigma_o\sqrt{\pi a}} \tag{3.7}$$

$G\left(\frac{a}{t}\right)$ is determined from a principle of self consistency giving,

$$G\left(\frac{a}{t}\right) = \frac{\left[\frac{\sqrt{2}}{\sigma_o}I_1 - 4F\left(\frac{a}{t}\right)a^{\frac{1}{2}}I_2\right]a^{\frac{1}{2}}}{I_3} \tag{3.8}$$

where,

$$I_1 = \int_0^a [K(a)]^2 da \tag{3.9}$$

$$I_2 = \int_0^a \sigma(x)(a-x)^{\frac{1}{2}} dx \tag{3.10}$$

$$I_3 = \int_0^a \sigma(x)(a-x)^{\frac{3}{2}} dx \tag{3.11}$$

Mattheck *et al.* [3.13] showed that this expression could be used successfully with a weight function solution and corrected to describe the stress intensity factor for a three dimensional semi-elliptical surface crack. Niu and Glinka [3.14] incorporated the COD into a 'Bueckner type' weight function by substituting (3.6) into (3.1) giving,

$$f_m(a,x)=\frac{H}{2K_m}\frac{\partial}{\partial a}\left\{\frac{\sigma_O}{H\sqrt{2}}\left[4F\left(\frac{a}{t}\right)\sqrt{a(a-x)}+\frac{G\left(\frac{a}{t}\right)(a-x)^{\frac{3}{2}}}{\sqrt{a}}\right]\right\} \tag{3.12}$$

differentiating gives the weight function as:

$$\frac{1}{\sqrt{2\pi}(a-x)}\left\{1+\left(\frac{a-x}{a}\right)\left[1+\frac{2F'\left(\frac{a}{t}\right)a}{F\left(\frac{a}{t}\right)}+\frac{3G\left(\frac{a}{t}\right)}{4F\left(\frac{a}{t}\right)}\right]+\left(\frac{a-x}{a}\right)^2\left[\frac{G'\left(\frac{a}{t}\right)a}{2F\left(\frac{a}{t}\right)}-\frac{G\left(\frac{a}{t}\right)}{4F\left(\frac{a}{t}\right)}\right]\right\} \tag{3.13}$$

$$\Rightarrow \qquad f_m(x,a)=\frac{1}{\sqrt{2\pi(a-x)}}\left[1+M_1\left(\frac{a-x}{a}\right)+M_2\left(\frac{a-x}{a}\right)^2\right] \tag{3.14}$$

where,

$$M_1=\frac{4F'\left(\frac{a}{t}\right)a+2F\left(\frac{a}{t}\right)+\frac{3}{2}G\left(\frac{a}{t}\right)}{2F\left(\frac{a}{t}\right)} \tag{3.15}$$

$$M_2=\frac{G'\left(\frac{a}{t}\right)-\frac{1}{2}G\left(\frac{a}{t}\right)}{2F\left(\frac{a}{t}\right)} \tag{3.16}$$

$$F'\left(\frac{a}{t}\right)=\frac{d}{d\left(\frac{a}{t}\right)}\left[F\left(\frac{a}{t}\right)\right] \tag{3.17}$$

$$G'\left(\frac{a}{t}\right)=\frac{d}{d\left(\frac{a}{t}\right)}\left[G\left(\frac{a}{t}\right)\right] \tag{3.18}$$

This is a neat self contained form, but computationally involved. For this reason Niu and Glinka expressed 'M_1' and 'M_2' as parametric equations for a specific reference system. This is quite satisfactory for that particular system but still renders the easy wide use of weight function solutions beyond the ability of average design engineers. To make full use of any design solution, it must be easily incorporated into a computer program. The reference stress state may be defined in a number of ways, so for flexibility reasons it is most likely that a numerical differentiation algorithm will be incorporated into the program to solve for $\partial u/\partial a$. Numerical differentiation is the determination of approximate values of the derivative of a function [3.15]. It should be avoided whenever possible as these results will be less accurate than the function from which they have been derived. It is a much more sensitive process than numerical integration which is essentially a smoothing process, whereas differentiation often involving the subtraction of two large values and division by a small one requires care and perception, especially where the function being differentiated is approximated by a polynomial. It is essentially due to this and the complexity of computation, that the Petroski-Achenbach solution is difficult to implement. Niu [3.16] warned that the solution may break down if the reference loading is not defined by a continuous monotonically varying function, or if the crack surfaces are not fully loaded over the entire crack length.

3.3 Multiple Reference Load States

3.3.1 A Bueckner Representation

Munz *et al.* [3.17] showed that the crack opening displacement could be accurately calculated from known stress intensity factors and corresponding load states and expressed in terms of a power series. This prompted Shen and Glinka [3.18] to derive the 'Bueckner type' function (previous section) independent of the Petroski-Achenbach COD. As before the weight function is expressed in the form:

$$f_m(x,a)=\frac{1}{\sqrt{2\pi(a-x)}}\left[1+M_1\left(\frac{a-x}{a}\right)^{\frac{1}{2}}+M_2\left(\frac{a-x}{a}\right)+M_3\left(\frac{a-x}{a}\right)^{\frac{3}{2}}\right] \quad (3.19)$$

The parameters 'M_1', 'M_2' and 'M_3' for a particular cracked body can be determined from (3.2) knowing at least two reference stress intensity factor solutions and corresponding stress states. These must be linearly independent of each other. Obviously to solve the three unknown weight function parameters, an extra relationship is required. This is supplied by Munz's [3.17] observation that the slope of the crack surface of central through cracks and double edge cracks under symmetrical loading should be zero at $x = 0$, i.e.,

$$\frac{\partial u(x,a)}{\partial x}\Big|_{x=0}=0 \quad (3.20)$$

hence,

$$\frac{\partial f(x,a)}{\partial x}\Big|_{x=0}=0 \quad (3.21)$$

For deep single edge cracks, due to rotation of the cracked section in a finite thickness body, (3.22) is more appropriate.

$$\frac{\partial^2 f(x,a)}{\partial x^2}\Big|_{x=0}=0 \quad (3.22)$$

i.e. the curvature of the crack mouth is zero.

The constitutive equations for determining the weight function parameters are thus:

$$K_{r1} = \int_0^a \sigma_{r1}(x) \frac{1}{\sqrt{2\pi(a-x)}} \left[1 + M_1 \left(\frac{a-x}{a} \right)^{\frac{1}{2}} + M_2 \left(\frac{a-x}{a} \right) + M_3 \left(\frac{a-x}{a} \right)^{\frac{3}{2}} \right] \tag{3.23}$$

$$K_{r2} = \int_0^a \sigma_{r2}(x) \frac{1}{\sqrt{2\pi(a-x)}} \left[1 + M_1 \left(\frac{a-x}{a} \right)^{\frac{1}{2}} + M_2 \left(\frac{a-x}{a} \right) + M_3 \left(\frac{a-x}{a} \right)^{\frac{3}{2}} \right] \tag{3.24}$$

$$\frac{\partial}{\partial x} \left\{ \frac{1}{\sqrt{2\pi(a-x)}} \left[1 + M_1 \left(\frac{a-x}{a} \right)^{\frac{1}{2}} + M_2 \left(\frac{a-x}{a} \right) + M_3 \left(\frac{a-x}{a} \right)^{\frac{3}{2}} \right] \right\} \Big|_{x=0} = 0 \tag{3.25}$$

Solving simultaneously, the three unknowns 'M_1', 'M_2', 'M_3' specific to a particular cracked geometry may be found.

3.3.2 Arithmetic Series Representation of COD Derivative

The weight function approach requires knowledge of the crack profile. The previous sections show how an assumed profile can be used and how knowledge of a second set of reference data can eliminate the necessity of a formal derivation of crack opening displacement. A further approach is to directly define the derivative of crack opening displacement, as it is this, not the actual crack profile that is needed for the weight function. This reduces computational effort significantly and increases accuracy for obvious reasons. Ojdrovic and Petroski [3.19] suggest the derivative of the crack profile with respect to 'a' can be expressed in the form of a series:

$$\frac{\partial u}{\partial a} = \frac{2\sigma}{H} \sqrt{2} \sum_{j=0}^{m} C_j \left(1 - \frac{x}{a} \right)^{j-\frac{1}{2}} \tag{3.26}$$

where,

$$C_0 = \frac{F\left(\frac{a}{t}\right)}{2} \tag{3.27}$$

C_j are unknown co-efficients, m are symmetrical loading states, i.e.,

$$(K_1, K_2, K_3, \ldots\ldots\ldots K_m; \quad m \geq 1)$$

since,

$$\frac{\partial u}{\partial a} = \frac{K_i(a)K(a)}{H\int_0^a \sigma_i(x)dx} \tag{3.28}$$

$$\Rightarrow \qquad 2\sigma\sqrt{2}\left[\frac{F}{2}\left(1-\frac{x}{a}\right)^{-\frac{1}{2}} + C_j\left(1-\frac{x}{a}\right)^{j-\frac{1}{2}}\right] = \frac{K_i(a)K(a)}{\int_0^a \sigma_i(x)dx} \tag{3.29}$$

$$\Rightarrow \qquad C_j = \frac{\frac{K_i(a)K(a)}{2\sqrt{2}\sigma\int_0^a \sigma_i(x)dx} - \frac{F}{2}\left(1-\frac{x}{a}\right)^{-\frac{1}{2}}}{\left(1-\frac{x}{a}\right)^{j-\frac{1}{2}}} \tag{3.30}$$

$$= \qquad \frac{\frac{F}{2}\left[\frac{K_1(a)}{\int_0^a \sigma_i(x)dx}\sqrt{\frac{\pi a}{2}} - \left(1-\frac{x}{a}\right)^{-\frac{1}{2}}\right]}{\left(1-\frac{x}{a}\right)^{j-\frac{1}{2}}} \tag{3.31}$$

$$= \frac{\frac{F}{2}\left[K_i(a)\sqrt{\frac{\pi a}{2}} - \int_0^a \sigma_i(x)\left(1-\frac{x}{a}\right)^{-\frac{1}{2}}dx\right]}{\int_0^a \sigma_i(x)\left(1-\frac{x}{a}\right)^{j-\frac{1}{2}}dx} \tag{3.32}$$

if,

$$C_j = \frac{q_i}{w_{ij}} \tag{3.33}$$

let,

$$w_{ij} = \int_0^a \sigma_i(x)\left(1-\frac{x}{a}\right)^{j-\frac{1}{2}}dx \tag{3.34}$$

$$\Rightarrow \quad q_i = \frac{F}{2}\left[K_i(a)\sqrt{\frac{\pi a}{2}} - w_{i0}\right] \tag{3.35}$$

The weight function can now be expressed in the form:

$$f(a,x) = \frac{H}{K(a)}\frac{\partial u(a,x)}{\partial a} = \frac{2\sigma}{K(a)}\sqrt{2}\sum_{j=0}^{m} C_j\left(1-\frac{x}{a}\right)^{j-\frac{1}{2}} \tag{3.36}$$

$$= \sqrt{\frac{2}{\pi a}}\frac{2}{F}\sum_{j=0}^{m} C_j\left(1-\frac{x}{a}\right)^{j-\frac{1}{2}} \tag{3.37}$$

3.4 Comparison of Models

The previous two sections detailed the approaches available for the calculation of weight functions. By far the simplest expression is that derived from the series representation of the derivative of crack profile i.e. expression (3.37). The effort taken to express the weight function derived from multiple reference states (MRS) in a 'Bueckner form' (3.19) is trivial, a cosmetic exercise at the expense of computational endeavour and accuracy of results. The aim of this section is to highlight that expression (3.37) is not only less troublesome mathematically, but far more accurate and stable than the traditional assumed profile approach characterised by equation (3.14). In order to do this several scenarios involving input-output relations of the two expressions are considered using published 'exact' solutions for simple cracked bodies.

Considering the solutions of Brown and Srawley for an edge crack in a finite width sheet [3.23] using a collocation method, given as:

$$\frac{K}{\sigma\sqrt{\pi a}} = 1.12 - 0.23\left(\frac{a}{t}\right) + 10.6\left(\frac{a}{t}\right)^2 - 21.7\left(\frac{a}{t}\right)^3 + 30.4\left(\frac{a}{t}\right)^4 \tag{3.38}$$

$$\frac{K}{\frac{6M\sqrt{\pi a}}{t^2}} = 1.12 - 1.39\left(\frac{a}{t}\right) + 7.32\left(\frac{a}{t}\right)^2 - 13.1\left(\frac{a}{t}\right)^3 + 14.0\left(\frac{a}{t}\right)^4 \tag{3.39}$$

for tension (ends free to rotate) and pure bending respectively. These claim an accuracy to within 1% for $a/t \leq 0.6$. Giving the assumed profile expression the solution for uniaxial tension (above) and requiring it to calculate the bending

situation returns values overestimating the exact solution by no more than 7%, Fig 3.1. The multiple reference state solution by its definition required both tension and bending solutions as input and returned exactly the given bending solution.

Daoud and Cartwright [3.24] investigated circular arc edge cracks in circular bars using a two-dimensional plane-stress finite element analysis. To represent the curvature of the bar stepped elements were used across the diameter, the thickness of these representing the area left by the intersecting crack. Expressions for uniaxial tension and bending are given as:

$$\frac{K}{\sigma\sqrt{\pi a}} = 0.891 - 5.863\left(\frac{a}{D}\right) + 44.64\left(\frac{a}{D}\right)^2 - 109.0\left(\frac{a}{D}\right)^3 + 98.25\left(\frac{a}{D}\right)^4 \tag{3.40}$$

$$\frac{K}{\frac{6M\sqrt{\pi a}}{t^2}} = 0.677 - 2.982\left(\frac{a}{D}\right) + 19.93\left(\frac{a}{D}\right)^2 - 46.94\left(\frac{a}{D}\right)^3 + 40.37\left(\frac{a}{D}\right)^4 \tag{3.41}$$

Valid for:

$$0.0625 \le \frac{a}{D} \le 0.5625$$

Again giving the assumed profile weight function the tension solution and asking for the bending solution returns values having a maximum error of 9% converging to the exact solution as the change in gradient stabilises (Fig 3.2). This time the multiple reference weight function is only given the tension solution. The maximum error between this and the finite element solution is 0.3%. This displays the innate soundness of the approach which will behave adequately with only one reference state in cases where stress gradients are gentle and monotonic. It can be shown that

'C_I' in equation (3.37) is equal to 'G' in equation (3.6) when only one reference load case is used. However, this is not differentiated whereas it is assuming a crack opening displacement profile.

Finally to compare the two methods where three solutions are available, these being uniform uniaxial tension, pure bending and surface shear loading in an isotropic semifinite strip Figs 3.3, 3.4 and 3.5 respectively, the results of Kaya and Erdogan [3.25] were used. These were evaluated numerically by solving a system of elastic algebraic equations in terms of the limiting boundary identities. Fig 3.6 shows the curve fitted solutions for the three loading conditions in terms of normalised stress intensity factor. The solution for surface shear is shown in Fig 3.7 with approximations by the two weight function methods. The assumed profile method was given the uniaxial tension solution, whereas the multiple reference method was given both tension and bending relations as reference states. Fig 3.8 shows how well both perform in terms of percentage error. The assumed profile method falls off rapidly at any shift in gradient. This may seem tolerable concerning the simple situations considered, however it is of great concern when contemplating the stability of the method regarding large stress gradients such as those associated with tooth loading in threaded connections. On the other hand the development of the multiple reference states weight function expressed as a series is mathematically the least involved and extremely reliable. The main disadvantage of the approach is that it generally requires at least two known solutions where often to know one reference solution is sumptuous.

3.5 Weight Function for Threaded Connections

3.5.1 2-D Solution

The geometry and notation of a loaded thread tooth-root is shown in Fig 3.9. As seen earlier the weight function solution requires the reference stress intensity factor under any Mode I loading system to be known. In this case instead of using an assumed crack profile, two reference stress systems are used, i.e., uniaxial tension and pure bending. By virtue of the definition of the weight function being a unique property of geometry, the influences it represents can be isolated and combined. This was effectively achieved by Niu and Glinka

[3.20] and by Mattheck *et al.* [3.13] after Impellizzeri and Rich [3.26] used what they called *Geometry Correction Factors* for the influence of geometric anomalies on the stress intensity factor. The loading on a tooth is unique in that unlike many solutions dealing with a 'notch-type' geometry, only one face of the 'notch' relays a tensile or crack opening stress '*P1*', see Fig 3.10. This is why the solution can be isolated into the simplified form of Fig 3.9. This ignores any effect of the compressive tooth bending stresses due to load on the preceding tooth. The stress intensity factor solution also ignores the effect of the root radius 'ρ', since any fracture mechanics solution requires that a crack is already present and outside the effect of 'ρ' on the magnitude and position of the maximum root stress has little effect on crack propagation.

The analytical conformal mapping solutions of Hasebe *et al.* [3.21],[3.22] can be used to develop a relationship for stress intensity factor for a two dimensional crack growing from a thread root with respect to flank angle, shank (or tube wall) thickness and tooth height. These solutions are for strips with angular steps. Solutions are available for 'U-notch' and 'V-notch' geometries which may resemble a thread geometry in appearance but as explained above only one face is loaded making the step or shoulder situation more appropriate. Hasebe's solution for a crack originating from an angular corner of a semi-infinite plate with a step [3.22] was analysed as a plane elastic problem, uniform tension being the boundary condition. Stress intensity factors were given in terms of,

$$K_{SF}^{\theta} = F_{1h}\,\sigma_o\sqrt{\pi h} \tag{3.42}$$

To normalise this into a more standard form, 'F_{1h}' was simply multiplied by $\sqrt{h/a}$.

The finite strip SIF solutions of [3.21] were normalised as,

$$K_{FS}^{0} = \frac{F_{1h}(t-a)^{1.5}}{\sqrt{\pi}} \frac{K_I}{t\sigma_o} \tag{3.43}$$

Dividing by,

$$\left(\frac{a}{t}\right)^{\frac{1}{2}} \left(1-\frac{a}{t}\right)^{\frac{3}{2}} \tag{3.44}$$

gives the standard Y factor for tension and,

$$\frac{K}{\frac{6M\sqrt{\pi a}}{t^2}} \tag{3.45}$$

for bending.

Hasebe noted that for short cracks the stress intensity factor was more affected by the decreasing value of the flank angle. However, with increasing crack depth the influence of 'θ' lessens but the existence of the step considerably affects the stress intensity factor to the last.

Assuming that the effect of geometrical features on the stress intensity factors can be weighted or separated,

$$\frac{K_{SF}^{\theta}}{K_{SF}^{0}} = \frac{K_{FS}^{\theta}}{K_{FS}^{0}} \tag{3.46}$$

$$\Rightarrow \qquad K_{FS}^{\theta} = \frac{K_{SF}^{\theta} K_{FS}^{0}}{K_{SF}^{0}} \tag{3.47}$$

The published solutions are tabulated. Curve fitting resulted in the following relations for uniaxial tension:

$$\frac{K_{SF}^{\theta}}{\sigma\sqrt{\pi a}} = 1.325\left(\frac{a}{h}\right)^{\left(-0.1867+0.0223\log_e\left(\frac{a}{h}\right)^2\right)} F$$

$$F = e^{\left(H_0+H_1\log_e\left(\frac{a}{h}\right)+H_2\log_e\left(\frac{a}{h}\right)^2\right)}$$

$$H_0 = -0.138x10^{-6}\theta^3 + 0.0064x10^{-6}\theta^4 - 0.0001x10^{-6}\theta^5$$

$$H_1 = 0.3603x10^{-5}\theta^2 - 0.0275x10^{-5}\theta^3 + 0.0005x10^{-5}\theta^4$$

$$H_2 = 0.1735x10^{-5}\theta^2 - 0.0056x10^{-5}\theta^3 \qquad (3.48)$$

$$\frac{K_{FS}^{0}}{\sigma\sqrt{\pi a}} = 1.4 - 2.4\left(\frac{a}{t}\right) + 10.1\left(\frac{a}{t}\right)^2 + 37.6\left(\frac{a}{t}\right)^3 - 196.3\left(\frac{a}{t}\right)^4$$

$$+280.3\left(\frac{a}{t}\right)^5 - 301.3\left(\frac{a}{t}\right)^8 + 981.7\left(\frac{a}{t}\right)^{13} - 1545.7\left(\frac{a}{t}\right)^{17} + 1140.5\left(\frac{a}{t}\right)^{23} \qquad (3.49)$$

$$\frac{K_{SF}^{0}}{\sigma\sqrt{\pi a}} = 1.325\left(\frac{a}{h}\right)^{\left(-0.1867+0.0223\log_e\left(\frac{a}{h}\right)^2\right)} \qquad (3.50)$$

The bending solutions are assumed the same as the axial for K_{SF}^{θ} and K_{SF}^{0}, since in an infinitely thick plate,

$$\sigma_B = \sigma_O\left(1 - \frac{x}{NA_{\to\infty}}\right) \approx \sigma_O \qquad (3.51)$$

$$\frac{K_{FS}^{0}}{\frac{6M\sqrt{\pi a}}{t^2}} = 46.118\left(\frac{a}{t}\right)^{(16.1883+36.6111\log_e\left(\frac{a}{t}\right)+51.5185\log_e\left(\frac{a}{t}\right)^2+46.8241\log_e\left(\frac{a}{t}\right)^3+}$$

$$27.9993\log_e\left(\frac{a}{t}\right)^4+11.0833\log_e\left(\frac{a}{t}\right)^5+2.8668\log_e\left(\frac{a}{t}\right)^6+0.4646\log_e\left(\frac{a}{t}\right)^7+0.0427\log_e\left(\frac{a}{t}\right)^8+0.0017\log_e\left(\frac{a}{t}\right)^9)$$

(3.52)

Substituting the above solutions into (3.39) gives a reference stress intensity factor for a two dimensional crack growing from a 'thread like' notch. Both axial and bending solutions for K_{FS}^{θ}, into (3.37) yields an accurate simple weight function for that geometry, knowing the stress distribution in the uncracked plane.

3.5.2 3-D Solution

In reality most engineering structures are not thin plate sections but thick flat angular or tubular bodies, where plain strain conditions prevail. However, once the influence of the tooth is known in a two dimensional sense it is common practice to superimpose this influence on to any three dimensional body [3.13],[3.14]. Components of threaded connections are tubular by nature, the male sections can be solid rods or hollow externally threaded pipes. Female sections are always essentially internally threaded pipes. Instead of using the two dimensional solutions from the previous section, only the impact of the projection (tooth) is required. As before the following must hold,

$$\frac{K_{SF}^{\theta}}{K_{SF}} = \frac{K_{Rod}^{\theta}}{K_{Rod}} \tag{3.53}$$

$$\Rightarrow \qquad K_{Rod}^{\theta} = \frac{K_{SF}^{\theta} K_{Rod}}{1.12\sigma\sqrt{\pi a}} \tag{3.54}$$

The significance of normalising to the value of an edge crack in an infinite strip is not only convenient but is essential to maintain the universality of the expression under any load system. It will be shown in the following section that the resulting weight function will only be valid for one stress system if a component of the reference stress intensity factor is specific to that stress system. The stress intensity factor for an edge crack in an infinite strip is the only situation where K_I is identical for any opening mode stress system.

Knowing the stress intensity factor for a semi-elliptical crack in a rod, the stress intensity factor for a crack in a bolt can be evaluated. Figs 3.11 and 3.12 show the notation for an external and internal surface crack in a tube respectively. The appendix gives solutions for cracks in rods, external and internal tubes under tension and bending. These solutions were published in tabular form, after curve fitting families of curves, the solutions may appear cumbersome but when programmed and used as reference states for weight functions, practically every crack in any threaded connection under any symmetrical load system can be evaluated for K_I.

The external stress intensity factors for circumferential surface cracks presented in Appendix III were evaluated by Raju and Newman [3.27] using singularity finite elements along the crack front and linear-strain elements elsewhere. The nodal-force method was employed in the derivation of the stress intensity factors. The part-through internal circumferential crack solutions evaluated by Delale and Erdogan [3.28] used a line-spring model. The results compare favourably with finite element results from various studies. In all cases only the stress intensity factor at the deepest point of the crack was considered.

3.6 Stress Distribution

The preceding sections detailed the formulation of stress intensity factors for threaded connections. Remembering that these solutions are only reference cases intended for weight function calculations, the analysis is not yet complete. In order

that 'C_j' is found for equation (3.37), it is necessary to know '$\sigma(x)$' i.e. the corresponding stress distribution along the potential crack plane to the reference stress intensity factor distribution.

Niu and Glinka [3.20] had the situation:

$$K_2^{\theta} = \frac{K_1^{\theta} K_2^{\alpha}}{K_1^{\alpha}} \tag{3.55}$$

hence

$$K_2^{\theta} = \frac{K_{1norm}^{\theta}}{K_{1norm}^{\alpha}} K_2^{\alpha} \tag{3.56}$$

Replacing by a weight function identity,

$$\int_0^a \sigma_{\theta}(x) f_{2\theta}(a,x,\theta)dx = \frac{K_{1norm}^{\theta}}{K_{1norm}^{\alpha}} \int_0^a \sigma_{\alpha}(x) f_{2\alpha}(a,x,\alpha)dx \tag{3.57}$$

They then claim,

$$f_{2\theta}(a,x,\theta) = \frac{K_{1norm}^{\theta}}{K_{1norm}^{\alpha}} f_{2\alpha}(a,x,\alpha) \tag{3.58}$$

This can only be true if,

$$\sigma_{\theta}(x) = \sigma_{\alpha}(x) \tag{3.59}$$

This cannot be so as the stress fields will be different for differently angled shoulders. Even if this was valid, since the ratio of normalised stress intensity factors representing a correction factor are determined for a particular loading condition, the resulting weight function is not necessarily accurate for other loading conditions

[3.26].There does not appear to be any easy escape from defining the actual stress distribution along the uncracked plane, so a general stress distribution relationship must be found to tally with each reference stress intensity factor. The weight function for a threaded rod is thus:

$$f^{\theta}_{Rod}(a,x)=\frac{f^{\theta}_{SF}f_{Rod}}{f_{edgeSF}} \tag{3.60}$$

3.6.1 Stress Concentration Factors

Referring to (3.60), the only component of the composite weight function that is influenced by a geometric stress concentration is that of the semi-finite strip with an angular projection. Unfortunately the stress intensity factor solutions used for this quantity were published without accompanying stress concentration factors. Niu [3.29] undertook a finite element analysis of such a two dimensional plane strain geometry. Eight-noded isoparametric quadrilateral elements were used in twelve meshes varying flank angle and root radius, however the parameters embraced were not absolute for the specific stress intensity factor solutions. Similar problems were encountered when attempting to use other limiting solutions e.g. [3.30], [3.31]. It was then realised that the most appropriate stress concentration factors would be those derived from the stress intensity factor solutions themselves.

The stress field in the vicinity of a crack tip is described by the relations (1.29) in chapter one. By selecting the origin of the coordinate system at the point 'ρ/2' from the notch tip gives the relations [3.32],

$$\sigma_x=-\frac{K_I}{\sqrt{2\pi r}}\frac{\rho}{2r}\mathrm{Cos}\frac{3\theta}{2}+\frac{K_I}{\sqrt{2\pi r}}\mathrm{Cos}\frac{\theta}{2}\left[1-\mathrm{Sin}\frac{\theta}{2}\mathrm{Sin}\frac{3\theta}{2}\right]+.....$$

$$\sigma_y=\frac{K_I}{\sqrt{2\pi r}}\frac{\rho}{2r}\mathrm{Cos}\frac{3\theta}{2}+\frac{K_I}{\sqrt{2\pi r}}\mathrm{Cos}\frac{\theta}{2}\left[1+\mathrm{Sin}\frac{\theta}{2}\mathrm{Sin}\frac{3\theta}{2}\right]+.....$$

$$\tau_{xy} = -\frac{K_I}{\sqrt{2\pi r}}\frac{\rho}{2r}\mathrm{Cos}\frac{3\theta}{2} + \frac{K_I}{\sqrt{2\pi r}}\mathrm{Sin}\frac{\theta}{2}\mathrm{Cos}\frac{\theta}{2}\mathrm{Cos}\frac{3\theta}{2} + \ldots..$$

(3.62)

For a mode I type loading and configuration, i.e., K_{II} and K_{III} are zero,

$$\sigma_{max} = \sigma_y\big|_{r=\frac{\rho}{2},\theta=0} = \frac{2K_I}{\sqrt{\pi\rho}} \tag{3.62}$$

This shows the close relationship between stress concentration and stress intensity factors. Because all items in equation (3.62) are constants other than the maximum stress and the stress intensity factor, the following must hold for the reference solutions,

$$SCF^{\theta} = SCF^{0}\frac{K_I^{\theta}}{K_I^{0}} \tag{3.63}$$

Extrapolating the reference stress intensity factor solutions to $a/h \rightarrow$ to zero gives the relationship,

$$\frac{K_I^{\theta}}{K_I^{0}} = T_{K_T}(\theta) = F\big|_{\frac{a}{h}\rightarrow 0} \tag{3.64}$$

where F is the expression in equation (3.48).

This leaves only the relatively easy choice of an appropriate stress concentration factor for a step or shouldered two dimensional body. Several studies were considered [3.33] - [3.37], however Wilson and White's [3.37] results seem the most suitable. The chosen relation is shown in Fig 3.13. This together with (3.64) and coupled with the stress distribution expression (following section) satisfies the reference solutions for the weight function.

A universal expression for the stress concentration factor at any thread root was sought. However, after exhaustive delving, it became apparent that no unrelated investigation can be appropriate to the complex loading system in a threaded fastener. Many published finite element meshes appear very similar to a loaded tooth [3.38], [3.39], but invariably the boundary conditions employed depict a very different arrangement, e.g. zero displacement along a plane is representative of the unique situation of symmetry about that plane, as that state will only exist where the net summation of forces is zero. It was shown earlier that a tooth is only loaded on one face making general notch solutions malapropos. For these reasons it is suggested that each tooth geometry is analysed separately in order to evaluate the maximum stress at the critical thread root.

3.6.2 Stress Distribution Due to Notches

The preceding section dealt with stress concentration factors owing to the existence of a geometric discontinuity. The stress concentration factor is just the one value specific to a particular form. The weight function stress intensity factor solution requires that both the reference and the ensuing opening component stress distribution along the potential crack plane is known.

From the relations (3.62) the opening component stress field in the close neighbourhood of the blunt notch tip is,

$$\sigma_y = \frac{K_I}{\sqrt{2\pi r}}\left(1 + \frac{\rho}{2r}\right) \tag{3.65}$$

Glinka [3.40] showed that at $r = \rho/2$,

$$\sigma_y = \frac{2K_I}{\sqrt{\pi\rho}} \tag{3.66}$$

so,

$$K_I = \frac{K_T \sigma_0}{2} \sqrt{\pi \rho} \tag{3.67}$$

Resubstituting into (3.65) gives,

$$\sigma_y = \frac{K_T \sigma_0}{2\sqrt{2}} \left[\left(\frac{\rho}{r} \right)^{\frac{1}{2}} + \frac{1}{2} \left(\frac{\rho}{r} \right)^{\frac{3}{2}} \right] \tag{3.68}$$

Expressing in terms of 'x' the distance from the notch tip, (remembering that relations (3.62) were evaluated with the origin of 'r' a point ρ/2 from the notch tip, i.e. $x = r - \rho/2$)

$$\sigma_y = \frac{K_T \sigma_0}{2} \left[\left(1 + \frac{2x}{\rho} \right)^{-\frac{1}{2}} + \left(1 + \frac{2x}{\rho} \right)^{-\frac{3}{2}} \right] \tag{3.69}$$

The above expression based on the Creager and Paris [3.41] stress - stress intensity factor relationships is only reliable for "mathematically sharp" notches. Glinka and Newport [3.42] found that for notches having stress concentration factors greater than 4.5, expression (3.69) was appropriate. However they proposed the mean value of (3.69) and Usami's [3.43] expression for the case of elliptical notches as the most appropriate description of the stress field due to notches having a stress concentration factor of less than 4.5. This expression seriously underestimates the stress distribution for blunt notches ($K_T < 3$), especially for $x > \rho$.

Kujawski [3.44] concluded that (3.69) gives a good approximation for $x/\rho < 0.2$, independently of K_T. A correction factor was proposed which should increase and decrease with increasing distance, x/ρ, and stress concentration factor, K_T, respectively. He proposed the following,

$$f = 1 + \frac{\mathrm{Tan}\left(\frac{\pi}{2K_T}\right)}{2.8}\left(\frac{x}{\rho} - 0.2\right)$$

$$for \frac{x}{\rho} \geq 0.2 \qquad (3.70)$$

$$f = 1.0$$

$$for \frac{x}{\rho} < 0.2 \qquad (3.71)$$

He noted that the expression was more likely to overestimate rather than to underestimate the stress distribution leading to safe estimations. The results agree well with the published finite element and experimental studies. Figs 3.14 and 3.15 show the distributions compared with those of [3.42], for K_T equal to 3.0 and 7.0 respectively. The Newport - Glinka relationship for σ_y in the case of the blunt notch shows the stress component dropping well below the nominal stress at distances greater than $x>\rho$. The expression (3.69) with the correction factors (3.70), (3.71) were used for the reference and ensuing stress fields under remote uniaxial tension.

The nominal stress is taken as the stress at a cross-section equal to the section from the minor diameter of the thread i.e. the tooth height is not included. In bending, the nominal stress is the maximum bending stress at the minor diameter so the stress distribution must be modified by multiplying by,

$$\left[1 - \frac{2x}{d}\right] \qquad (3.72)$$

for rods and external cracks in pipes, and,

$$\left[1-\frac{2(t-x)}{d}\right] \tag{3.73}$$

for internal cracks in pipes.

3.7 Crack Shape Evolution

It is of little wonder that few studies have rigourously pursued the evolution of surface cracks, considering that to this stage, this chapter has only regarded the stress intensity factor at one point (deepest) under one crack opening mode. Most of these investigations have dealt with crack growth in flat plates under simple loading configurations, despite this we are warned against causally adopting a closed form solution [3.45].

Variation of crack aspect ratio depends on environment, initial defect configuration [3.45], R-ratio [3.46], Paris growth exponent [3.48], mean stress [3.47] and load intensity and mode. The stress intensity factor tends to decrease with increasing values of crack aspect ratio [3.5]. This section whilst not suggesting selection of any particular growth relationship, aims to highlight the relevant analyses and emphasise the important observations of how cracks tend to grow in threaded connections. These will be later examined in chapter five with regard to the experiments carried out as part of this study.

Connolly [3.49] observed that cracks in tension grow towards semi-circles in flat plates, whereas in bending cracks elongate to become long shallow semi-ellipses. Reference [3.45] also agreed that under bending the Holdbrook and Dover [3.50] expression is in agreement with most experimental observations. In tension, the Newman and Raju [3.48] is the most accurate. Scott and Thorpe [3.47] comply with these pointing out that the finite dimension correction factors in reference [3.50] can increase the effective value of stress intensity factor by as much as forty percent.

Most solutions are based on empirical results, beach marking [3.4], [3.51], NDT Methods (e.g. Alternating Current Field Measurement [3.49]) and heat tinting techniques [3.52] are the most common experimental methods. Reference [3.45] used a three-dimensional finite element technique to model a planar defect in a plate, calculating the stress intensity factor around the crack front, interactively using the Paris growth law to define crack extension and automatically regenerate the new crack front. Another approach which is gaining prominence, is the RMS or average stress intensity factor, which is presented as an Influence Function [3.53]. This method isolates the two crack growth directions, instead of computing the stress intensity factor for points along the crack surface, the average stress intensity factor which represents the strain energy release rate is calculated in each degree of freedom. Müller *et al.* [3.54] and Athanassiadis *et al.* [3.55] used the method successfully to predict crack ratio behaviour, however Oore [3.53] suggests the method could lead to unconservative forecasts especially in the event of low cycle fatigue.

Fig 3.16 shows a general overview of possible crack geometries for notched and unnotched cylinders under tension and bending loads [3.56]. It is obvious that crack evolution models will be many and varied. Axial tension, unidirectional, reversed and rotating bending will all have their own distinctive crack evolution peculiarities. Under high local stress, the kinetics of crack development is characterised by the multiple initiation of cracks along the circumference of the first loaded thread, the fast crack growth around the circumference and a decrease of growth rate into the depth of the cross-section [3.57]. At stresses close to the yield limits, the crack length is near to the length of the circumference. With the decrease of maximum cyclic stress, the crack shape becomes ellipsoidal. James and Mills [3.5], looking at other studies concerned with fatigue crack growth in bolts suggest that very early in the growth process, cracks tend to assume a semicircular front and the intersection of the crack with the free surface is almost at right angles. This shape is maintained until close to half the bolt thickness when the front flattens to approach a straight front. Raju and Newman [3.27] and Erjian Si [3.56] assumed a similar progression. Forman and Shivakumar [3.52] again assuming a circular crack front intersecting the rod surface at right angles derived two limiting expressions for a/c. One where

the radius of the circle is the crack depth, the other where the radius falls outside the cross-section of the rod. They postulated that these were upper and lower bound situations for both tension and bending. In hollow cylinders, the fatigue cracks were found to agree accurately with the shape of a transformed semiellipse, but no crack shape development relation is suggested. Crack aspect ratio will be further considered in chapter 5, as will the experimental solutions of Kermani [3.58] and Dale [3.59].

3.8 Discussion

The chapter so far has reported in detail the development of the stress intensity factor solutions for threaded connections. This section will attempt to establish the integrity of the new solutions. As mentioned earlier, very few stress intensity factor solutions for threaded connections have been published. Many of these are unavailing for comparative purposes because of obscure features of analysis or presentation, others use unconventional geometrical notation such as the projection of coordinates on the cylinder surface onto a plane, making the reprojection and subsequent interpretation dubious. The main uncertainty with using published results lies with the exposition of crack aspect ratio.

Fig 3.17 shows the new solution for a threaded M20 UNC bolt plotted against various edge crack solutions in round bars under tension. From geometrical considerations the expression for crack aspect ratio was calculated in terms of the notation given earlier for an external crack (see chapter five). Daoud, Cartwright and Carey's [3.60] two dimensional finite element and compliance results agree excellently with each other. Blackburn's three dimensional finite element results only extend for very small values of a/D but are in keeping with the others. Finally Bush [3.62] calculated dimensionless stress intensity factors for edge cracks in solid bars from experimental compliance (inverse slope of load-displacement curve). The latter are in excellent agreement with the new solution after the effect of the thread has abated. The new solution is slightly on the conservative side of all the results until the crack depth approaches half the diameter of the bar. At this point however, it is considered that crack growth is verging on the realm of unstable crack growth. Again it should

be noted that what the new solution is modelling is a semi-elliptical crack having the major and minor dimensions ofanequivalent edge crack. This model becomes increasingly contradictory as the crack approaches half thickness of the bar.

The same crack aspect ratio model was used in Fig 3.18 where the bending solution is compared to the compliance results of Bush [3.63]. Again the influence of the thread is abnormally high due to the crack aspect ratio. The new solution is once again conservative until the half thickness point is approached.

The previous section quoted the findings of Forman and Shivakumar [3.52] with regard to crack aspect ratio. Fig 3.19 shows the progression of stress intensity factor for a circular-arc surface crack growing in the circumference of a solid rod in tension. The crack aspect ratio for the new solution is defined by Forman and Shivakumar's upper bound relationship for a circular crack. Their stress intensity factor solution is however, not based on experimental results but is basically Tada's rectangular bar solutions multiplied by an arbitrary correction factor thought appropriate. These are clearly over conservative. More substance is given to their crack shape relationships. The finite element results of Daoud and Cartwright [3.24] and the experimental findings of Wilhem *et al.* [3.51] compare favourably with the predicted behaviour of the M20 bolt away from the influence of the thread. Again under bending (Fig 3.20), Daoud and Cartwright's [3.24] results correlate excellently with the new solution, Forman and Shivakumar once more overestimating the event.

Erjian Si [3.56] reviewed many surface crack solutions in round bars. A solution was published averaging the results studied, but was presented as a function of varying crack aspect ratio. The results shown in Fig 3.21 are for a semi-elliptical crack with the stated shape characteristics. These to say the least are extremely vague, however the two constant aspect ratio curves show excellent agreement. Perhaps even more revealing to how Erjian Si's shape expression evolves can be seen when comparing his results with the new solution for bending (Fig 3.22). Maybe $a/c = 0.64$ at some point approaching $D/2$, but the indication is that $a/c = 0.5$ at the point $D/2$. This is a speculative observation, however it must be highly probable considering the nearness of the predictions. In the companion paper [3.64],

graphical representation is made of what the stress intensity factors for threaded bars should look like. This, despite no rigourous experimental or analytical analysis of any particular thread type, shows a behaviour similar to the results of the new solution, i.e. the rapidly dipping stress intensity factor due to the thread and more gradual elevating as the crack grows through the bar.

Perhaps impertinently the new solution was pressed beyond its strict validity limits, however it is important to know how it will behave at extremes. Fig 3.23 shows how it responds when the crack half length is half the circumference of the bar. Compared with the analytical circumferential solution of Benthem and Koiter [3.65], it felicitously over estimates the stress intensity factor by no more than twenty five percent. It is not suggested that the solution be used in such circumstances, but it is encouraging to know that the solution will fail-safe if improperly used.

A Threaded ISO M8 x 1.0 bolt was analysed by Toribio *et al.* [3.2] and [3.66]. Unfortunately the crack length ratio was defined in terms of a length projected onto the horizontal. Instead of trying to equate this to the more conventional notation, which often leads to results being extrapolated outside their validity limits, it was decided to observe them intact in terms of extreme circumstance. Fig 3.24 shows the tension solutions for the ISO M8 x 1.0 (1.0mm pitch) using Forman and Shivakumar's upper and lower bound crack shape relations. Also plotted are the Toribio *et al.* solutions for two extreme crack aspect ratios. James and Mills' [3.5] hypothetical 'threaded' bar is also shown. Again, the upper and lower bounds are impressive. Regrettably, Toribio's finite element results do not cover the all important thread influence sector, James and Mills' fictitious lone point giving the only indication of what the distribution should look like. However, the new solution appears in all senses correct and behaves as expected despite the scenario. Under bending, both limits are again plotted enclosing the James and Mills solution for a circular crack in a round bar, Fig 3.25.

Published stress intensity factor solutions for solid bars are rare, even more scarce are stress intensity factors for internal and externalcircumferentialcracks in tubes. Fig 3.26 plots the new solution for a small crack aspect ratio against three solutions, two for edge cracks the other for a circumferential crack in tension.

Wilkowski and Eiber's [3.67] experimentally derived stress intensity factor solutions for edge cracks have been used in fatigue analysis of threaded connections by Chen [3.68]. Here they are plotted along with the Harris solution for circumferential cracks in hollow tubes [3.1] and Bush's [3.62] edge crack compliance results under tension loading. The Wilkowski and Eiber edge crack results agree better with the Harris circumferential crack than with Bush's edge crack. This exponential behaviour is only explicable if r_i/t is extremely small, whereas the results given by Bush seem more realistic for larger values of r_i/t. The comparison with the new solution is inconclusive because of the low aspect ratio approximation, but again the behaviour is consistent with conjecture.

Fig 3.27 shows the new solution with a very low crack aspect ratio for an internal pipe crack compared with the theoretical internal circumferential pipe solution of Rajab [3.69]. More relevant results are shown in Fig 3.28. These are all semi-elliptical internal tube cracks under tension loading. Poette and Albaladejo's finite element results [3.70] compare favourably with the new solution. The results of Chen [3.71] for a crack emanating from the first engaged thread root of a box in a large diameter threaded connection are surprising. It specifies that the solution is valid for a part-through-thickness crack but does not elaborate on its validity range. The finite element results seem to break down at values of $a/t > 0.6$. Again no influence of the thread is represented.

Figs 3.29 - 3.34 show the new solutions for a unified threaded rod, externally and internally threaded tube under tension and bending respectively, varying crack aspect ratio. Figs 3.35 - 3.38 show the effect of radius to thickness ratio on the externally and internally threaded tube cracks under tension and bending

respectively. These show little effect of the radius to thickness ratio at the thread root but favourable reduction in stress intensity factor with increased ratio. This is less marked in bending.

The new solutions have been shown to be versatile and wide ranging. Only tension and bending cases have been shown here but remembering that the solution is in the form of a weight function, any subsequent loading condition can be solved in terms of opening mode stress intensity factor. Care must be exercised as with any stress intensity factor solution, factors such as size effects [3.72] must be considered when dealing with abnormally large or small components. However, the greatest size effect effects frequently associated with threaded connections are due to the lack of geometric scaling for standard threads. This solution allows input of any thread form on any size rod or tube (within relevant limits).

The curves generated are output from a Fortran program using a numerical integration algorithm [3.73]. Numerical accuracy is not a concern. The stability of the solution as a whole is excellent.

Future development of this solution can take the form of addition of new stress intensity factor modes e.g. [3.74], or even replacement of any of the constitutive equations with the advent of more extensive subsolutions.

3.9 Summary

The chapter began by introducing the weight function and examined various aspects of it. A new approach of expressing the derivative of crack opening displacement in series form is explored and eventually adopted after favourable comparison with traditional and contemporary solutions. A weight function is developed for a two dimensional surface crack in a strip with a thread like projection. From this a full three dimensional surface crack solution evolved, its development is elaborated in detail, mentioning pitfalls and approximations which have been made by other investigators. Stress distributions and concentrations are examined which are all important to the final stress intensity factors.

Crack shape evolution is considered, the findings and observations of other studies are highlighted. A thorough discussion compares the few relevant published solutions available with those of the new weight function. Comparisons are very favourable despite the lack of a fully satisfactory solution for a threaded connection.

Besides being a useful indication of fatigue life for threaded connections, the solution can be used as an optimisation tool in deciding what geometrical characteristics are critically associated with fatigue crack growth from thread roots.

3.10 References

[3.1] Harris, D. O., "Stress Intensity Factors for Hollow Circumferentially Notched Round Bars", Journal of Basic Engineering, ASME, pp 49-54, 1967.

[3.2] Toribio, J., and Sanchez-Gálvez, V., "3D Numerical Computation of the Stress Intensity Factor in a Cracked Bolt with a Nut", ECF 8, Fracture Behaviour and Design of Materials and Structures, pp 1111-1118, 1990.

[3.3] Nord, K. J. and Chung T. J., "Fracture and Surface flaws in Smooth and Threaded Round Bars", Int. J. of Fracture, 30, pp 47-55, 1986.

[3.4] Mackay, T. L. and Alperin, B. J., "Stress Intensity Factors for Fatigue Cracking in High-Strength Bolts", Eng. Fracture Mech., vol 21, no 2, pp 391-397, 1985.

[3.5] James, L. A. and Mills, W. J., "Review and Synthesis of Stress Intensity Factor Solutions Applicable to Cracks in Bolts", Engineering Fracture Mechanics, vol 30, no 5, pp 641-654, 1988.

[3.6] Sopwith, D. G., "The Distribution of Load in Screw Threads", Proceedings Institution of Mechanical Engineers, vol 159, pp 373-383, 1948.

[3.7] Patterson, E. A., and Kenny, B., "A Modification to the Theory for the Load Distribution in Conventional Nuts and Bolts", J. of Strain Analysis, vol 21, pp 17-23, 1986.

[3.8] Bluhm, J. I., and Flanagan, J. H., "A Procedure for the Elastic Stress Analysis of Threaded Connections Including the use of an Electrical Analogue", Expl. Stress Analysis, vol XV, no 1, pp 85-100, 1957.

[3.9] Bueckner, H.F., "A Novel Principle for the Computation of Stress Intensity Factors", Zeitschrift für Angewandte Mathematik und Mechanik, 50, pp 529-546, 1970.

[3.10] Rice, J. R., "Some Remarks on Elastic Crack-Tip Stress Fields", Int. J. Solids Structures, vol 8, pp 751-758, 1972.

[3.11] Petroski, H. J. and Achenbach, J. D., "Computation of the Weight Function from a Stress Intensity Factor", Eng. Fracture Mech., vol 10, pp 257-266, 1978.

[3.12] Paris, P. C. and Sih, G. C., "Stress Analysis of Cracks", ASTM, STP 381, pp 30-83, 1965.

[3.13] Mattheck, C., Munz, D. and Stamm, H., "Stress Intensity Factor for Semi-elliptical Surface Cracks Loaded by Stress Gradients", Eng. Fracture Mech., vol 18, no 3, pp 633-641, 1983.

[3.14] Niu, X., Glinka, G., "Stress Intensity Factors for Semi-Elliptical Surface Cracks in Welded Joints", Int. J. Fracture, vol 40, pp 255-270, 1989.

[3.15] Kreyszig, Erwin, "Advanced Engineering Mathematics", 5th Ed., John Wiley & sons, 1983.

[3.16] Niu, X., "Technical Note: Some Requirements on the Reference Loading with Large Stress Gradient for the Calculation of Weight Functions using the Petroski-Achenbach Method", Eng. Fracture Mech., vol 36, pp 167-172, 1990.

[3.17] Munz, D., Fett, T. and Mattheck, C., "On the Calculation of Crack Opening Displacement from the Stress Intensity Factor", Eng. Fracture Mech., vol 27, no 6, pp 697-715, 1987.

[3.18] Shen, G. and Glinka, G., "Determination of Weight Functions from Reference Stress Intensity Factors", Theoretical and Applied Fracture Mechanics 15, pp 237-245, 1991.

[3.19] Ojdrovic Rasko, P., Petroski, Henry, J., "Weight Functions from Multiple Reference States and Crack Profile Derivatives", Eng. Fracture Mech., vol 39, no 1, pp 105-111, 1991.

[3.20] Niu, X. and Glinka, G., "The Weld Profile Effect on Stress Intensity Factors in Weldments", Int. J. of Fracture, 35, pp 3-20, 1987.

[3.21] Hasebe, N., Matsuura, S. and Kondo, N., "Stress Analysis of a Strip with a Step and a Crack", Eng. Fracture Mech., vol 20, no 3, pp 447-462, 1984.

[3.22] Hasebe, N. and Ueda, M., "A Crack Originating from an Angular Corner of a Semi-Infinite Plate with a Step", Bull. JSME, vol 24, no 189, pp 483-488, March 1981.

[3.23] Rooke, D. P and Cartwright, D. J., "Compendium of Stress Intensity Factors", H M Stationary Office, ISBN 0117713368, 1976.

[3.24] Daoud, O. E. K., Cartwright, D. J., "Strain Energy Release Rate for a Circular-Arc Edge Crack in a Bar Under Tension or Bending", Journal of Strain Analysis, vol 20, no 1, 1985.

[3.25] Kaya, A. C. and Erdogan, F., "Stress Intensity Factors and COD in an Orthotropic Strip", Int. J. Fatigue, vol 16, no 2, pp 171-190, 1980.

[3.26] Impellizzeri, L. F. and Rich, D. L., "Spectrum Fatigue Crack Growth in Lugs", ASTM STP 595, pp 320-336, 1976.

[3.27] Raju, I. S. and Newman, J.C., " Stress Intensity Factors for Circumferential Surface Cracks in Pipes and Rods Under Tension and Bending Loads.", Fracture Mechanics: Seventeenth Volume, ASTM STP 905, pp 789-805, 1986.

[3.28] Delale, F. and Erdogan, F., "Application of the Line-Spring Model to a Cylindrical Shell Containing a Circumferential or Axial Part-Through Crack", Journal of Applied Mechanics, vol 49, pp 97-102, 1982.

[3.29] Niu, Xionan, "Effects of Local Stresses on Fatigue Strength of Tubular Welded Joints", Ph. D. Thesis, University College London, 1987.

[3.30] Francavilla, A., Ramakrishnan, C. V., Zienkiewicz, O. C., "Optimisation of Shape to Minimize Stress Concentration", Journal of Strain Analysis, vol 10, no 2, 1975.

[3.31] Etemad, M. R., "Estimates of Regions of Stress Concentrations in 'T'-Butt Weld Geometries", Journal of Strain Analysis, vol 26, no 2, 1991.

[3.32] Tada, H., "The Stress Analysis of Cracks Handbook", Del Research Corporation, Missouri, 1978.

[3.33] Baratta, F. I., "Comparison of Various Formulae and Experimental Stress-Concentration Factors for Symmetrical U-Notched Plates", Journal of Strain Analysis, vol 7, no 2, 1972.

[3.34] Baratta, F. I., Neal, D. N., "Stress-Concentration Factors in U-Shaped and Semi-Elliptical Edge Notches", Journal of Strain Analysis, vol 5, no 2, 1970.

[3.35] Battenbo, H., Baines, B. H., "Numerical Stress Concentrations for Stepped Shafts in Torsion with Circular and Shaped Fillets", Journal of Strain Analysis, vol 9, no 2, 1974.

[3.36] Matthews, G. J., Hooke, C. J., "Calculation of Stress-Concentration Factors for Grooved Shafts in Bending Using the Point-Matching Technique", Journal of Strain Analysis, vol 8, no 2, 1973.

[3.37] Wilson, I. H., White, D. J., "Stress-Concentration Factors for Shoulder Fillets and Grooves in Plates", Journal of Strain Analysis, vol 8, no 1, 1973.

[3.38] Freese, C. E., Bowie, O. L., "Stress Analysis of Configurations Involving Small Fillets", Journal of Strain Analysis, vol 10, no 1, 1975.

[3.39] Kosmatka, J. B., Fries, R. H., Reinholtz, C. F., "Tension and Bending Stress Concentration Factors in 'U', 'V', and opposed 'U'-'V' Notches", Journal of Strain Analysis, vol 25, no 4, 1990.

[3.40] Glinka, G., "Calculation of Inelastic Notch-Tip Strain-Stress Histories Under Cyclic Loading", Eng. Fracture Mech., vol 22, no 5, pp 839-854, 1985.

[3.41] Creager, M. and Paris, P., "Elastic Field Equations for Blunt Cracks with Reference to Stress Corrosion Cracking", Int. J. Fract. 3, pp 247-252, 1967.

[3.42] Glinka, G. and Newport, A., "Universal Features of Elastic Notch-Tip Stress Fields", Int. J. Fatigue 9, no 3, pp 143-150, 1987.

[3.43] Usami, S., "Short Crack Fatigue Properties and Component Life Estimation", Current Research on Fatigue Cracks, The Soc. Mater Sci., Kyoto, 1985.

[3.44] Kujawski, D., "Estimations of Stress Intensity Factors for Small Cracks at Notches", Fatigue Fract. Engng. Mater. Struct. vol 14, no 10, pp 953-965, 1991.

[3.45] Gilchrist, M. D., Chipalo, M. I. and Smith, R. A., "Shape Development of Surface Defects in Tension Fatigued Finite Thickness Plates", Int. J. Pres. Ves. & Piping 49, pp 121-137, 1992.

[3.46] Scott, P. M. and Thorpe, T. W., "A Critical Review of Crack Tip Stress Intensity Factors for Semi-Elliptic Cracks", Fatigue Engng. Mater. Struct., 4, pp 291-309, 1981.

[3.47] Mahmoud, M. A., "Quantitative Prediction of Growth Patterns of Surface Fatigue Cracks in Tension Plates", Eng. Fract. Mechs., 30, pp 735-746, 1988.

[3.48] Newman, J. C. and Raju, I. S., "An Empirical Stress-Intensity Factor Equation for the Surface Crack", Eng. Fract. Mech. vol 15, no 1-2, pp 185-192, 1981.

[3.49] Connolly, M. P., "A Fracture Mechanics Approach to the Fatigue Assessment of Tubular Welded Y and K Joints" Ph. D. Thesis, University of London, 1986.

[3.50] Holdbrook, S. J. and Dover, W. D., "The Stress Intensity Factor for a Deep Surface Crack in a Finite Plate", Eng. Fract. Mech., 12, pp 347-364, 1979.

[3.51] Wilhem, D., Fitzgerald, J., Carter, J., and Dittmer, D., "An Empirical Approach to Determining K for Surface Cracks", "Advances in Fracture Research", Eds., D. Francois *et al.*, pp 11-21, 1980.

[3.52] Forman, R. G., and Shivakumar, V., "Growth Behaviour of Surface Cracks in the Circumferential Plane of Solid and Hollow Cylinders", Fracture Mechanics: Seventeenth Volume, ASTM STP 905, pp 59-74, 1986.

[3.53] Oore, M., "Assessment of Influence Function for Elliptical Cracks Subjected to Uniform Tension and to Pure Bending", Fracture Mechanics: Twenty-First Symposium, ASTM STP 1074, pp 490-508, 1990.

[3.54] Müller, H. M., Müller, S., Munz, D., and Neumann, J., "Extension of Surface Cracks During Cyclic Loading", Fracture Mechanics: Seventeenth Volume, ASTM STP 905, pp 625-643, 1986.

[3.55] Athanassiadis, A., Boissenot, J. M., Brevet, P., Francois, D., and Raharinaivo, A., "Linear Elastic Fracture Mechanics Computations of Cracked Cylindrical Tensioned Bodies", Int. J. of Fracture, vol 17, no 6, pp 553-566, 1981.

[3.56] Si, E., "Stress Intensity Factors for Edge Cracks in Round Bars", Eng. Fract. Mech., vol 37, no 4, pp 805-812, 1990.

[3.57] Makhutov, N., Zatsarinny, V., Kagan, V., "Initiation and Propagation Mechanics of Low Cycle Fatigue Cracks in Bolts", Advances in Fracture Research, ICF 5, Eds., D. Francois *et al.*, 2, pp 605-612, 1981.

[3.58] Kermani, B., "Drill String Threaded Connection Failure Analysis and Case Studies", EMAS, 1989.

[3.59] Dale, B. A., "An Experimental Investigation of Fatigue Crack Growth in Drill String Tubulars", SPE 1559, 1986.

[3.60] Daoud, O. E. K., Cartwright, D. J., Carey, M., "Strain Energy Release Rate for a Single Edge Cracked Circular Bar in Tension", Journal of Strain Analysis, vol 13, no 2, pp 83-89, 1978.

[3.61] Blackburn, W. S., "Calculation of Stress Intensity Factors for Straight Cracks in Grooved and Ungrooved Shafts", Engineering Fracture Mechanics, vol 8, pp 731-736, 1976.

[3.62] Bush, A. J., "Stress Intensity Factors for Single-Edge-Crack Solid and Hollow Round Bars Loaded in Tension", Journal of Testing and Evaluation, vol 9, no 4, pp 216-223, July 1981.

[3.63] Bush, A. J., "Experimentally Determined Stress Intensity Factors for Single-Edge-Crack Round Bars Loaded in Bending", Experimental Mechanics, pp 249-257, 1975.

[3.64] Si, E., "Stress Intensity Factors for Surface Cracks Emanating from the Circumferential Notch Root in Notched Round Bars", Engineering Fracture Mechanics, vol 37, no 4, pp 813-816, 1990.

[3.65] Benthem, J. P., and Koiter, W. T., "Asympototic Approximations to Crack Problems", Chapter 3, "Methods of Analysis of Crack Problems", Ed. G. C. Sih, 1972.

[3.66] Toribio, J., Sanchez-Gálvez, V., and Astiz, M. A., "Stress Intensification in Cracked Shank of Tightened Bolt", Theoretical and Applied Fracture Mechanics, 15, pp 85-97, 1991.

[3.67] Wilkowski, G. M. and Eiber, R. J., "Evaluation of Tensile Failure of Girth Weld Repair Grooves in Pipe Subjected to Offshore Laying Stresses", Trans. of ASME, J. of Energy Resources Technology, vol 103, pp 48-55, March 1981.

[3.68] Chen, W. C., "Fracture Control Strategy for TLP Tethers", Proceedings of the 6th International Offshore Mechanics and Arctic Engineering Symposium, vol 1, 1987.

[3.69] Rajab, M. D., "Fracture Analysis for Pipes Containing full Circumference Internal Part - Throughwall Flaw", Int. J. Pres. Ves. Piping, 41, pp 11-23, 1990.

[3.70] Poette, C. and Albaladejo, S., "Stress Intensity Factors and Influence Functions for Circumferential Surface Cracks in Pipes", Engineering Fracture Mechanics, vol 39, no 4, pp 641-650, 1991.

[3.71] Chen, W. C., "Fatigue - Life Predictions for Threaded TLP Tether Connector", OTC 5938, May 1989.

[3.72] Haagensen, P. J., Slind, T., and Orjasaeter, O., "Size Effects in Machine Components and Welded Joints", OMAE, pp 367-377, 1988.

[3.73] Patterson, T. N. C., "The Optimum Addition of Points to Quadrature Formulae", Math. Comp. 22, pp 847-856, 1968.

[3.74] Jordan, E. H., Kim, B. K., "Approximate Weight Functions for Externally Cracked Cylinders in Mode I and Mode III", Engineering Fracture Mechanics, vol 41, no 3, pp 411-416, 1992.

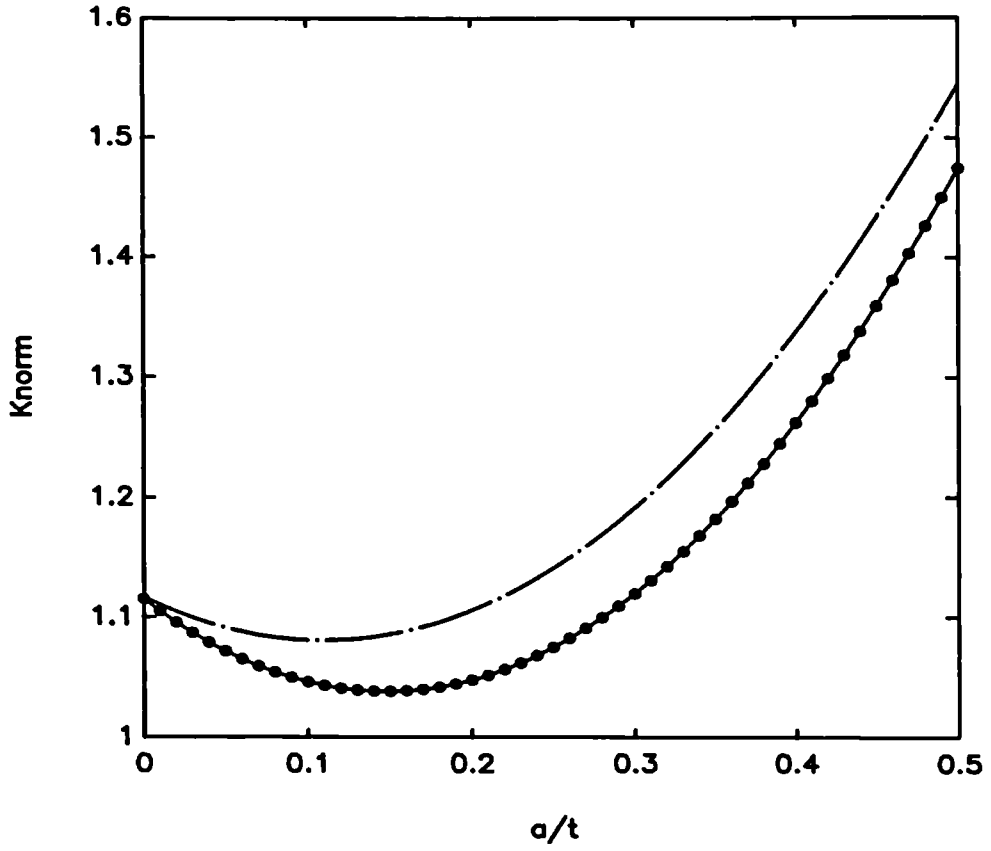

——·——	Weight Function using Petroski-Achenbach COD
oooooo	Weight Function using Multiple Reference States
————	Brown & Srawley

Fig 3.1

Bending of an Edge Crack in a Finite Width Sheet

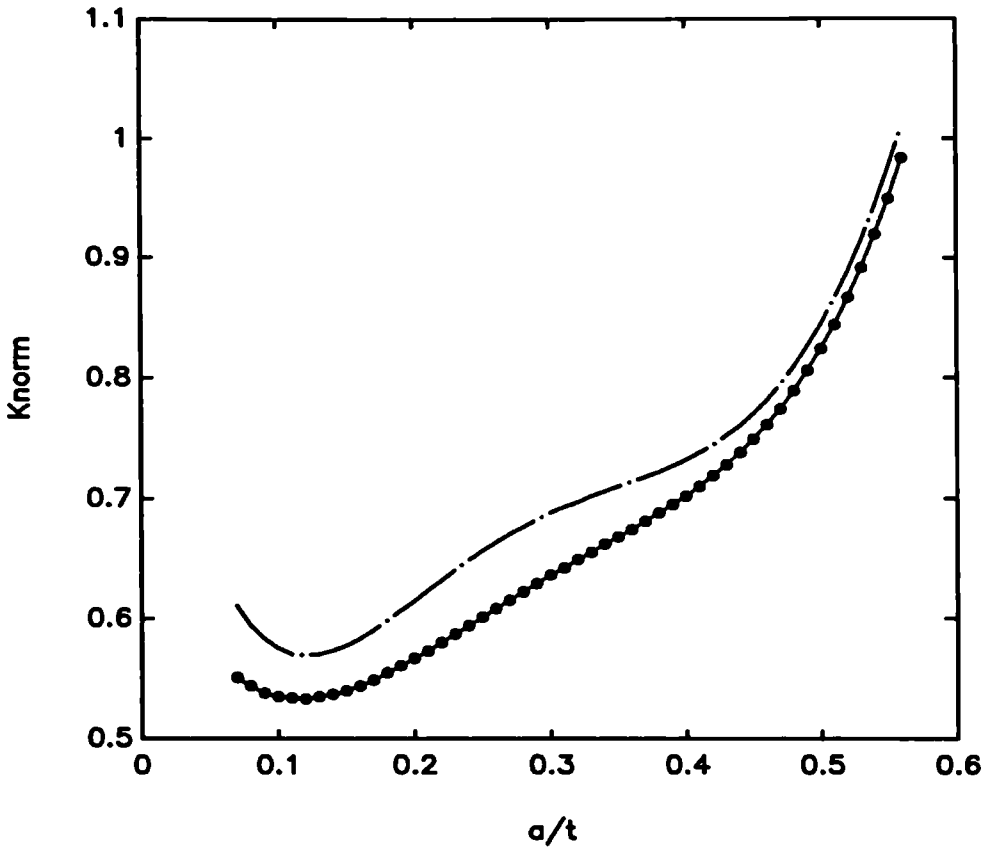

——·—— Weight Function using Petroski-Achenbach COD

oooooo Weight Function using Multiple Reference States

———— Daoud & Cartwright

Fig 3.2

Bending of a Circular Arc Edge Crack in a Circular Bar

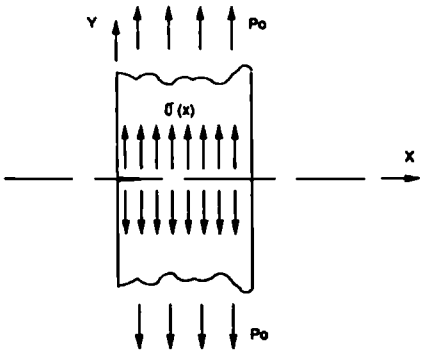

Fig 3.3 Uniform Uniaxial Tension

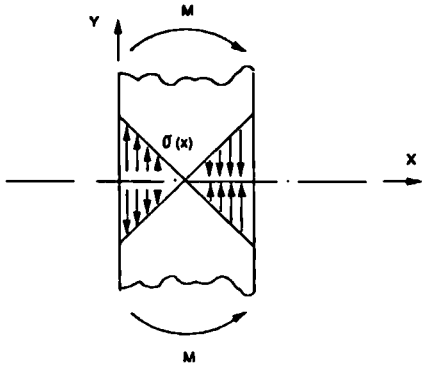

Fig 3.4 Pure Bending

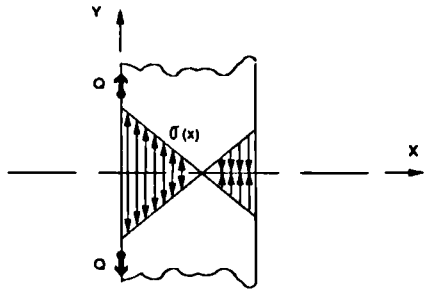

Fig 3.5 Surface Shear

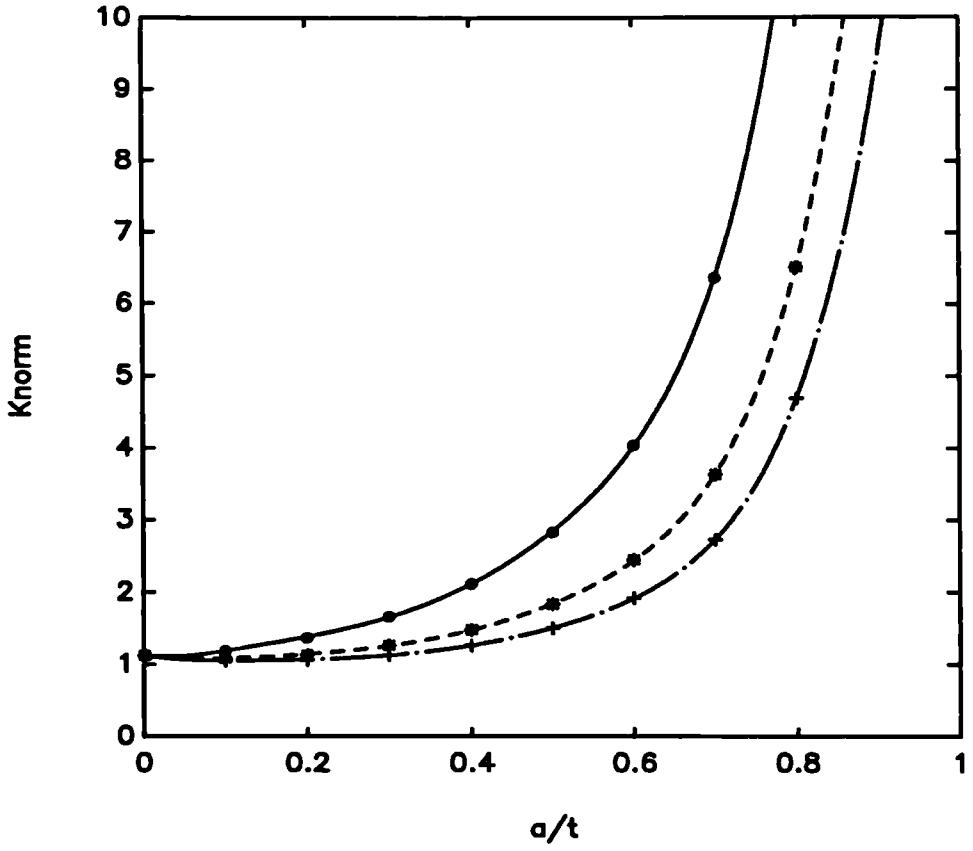

Pure Bending

Surface Shear

Uniform Uniaxial Tension

Fig 3.6

SIFs under Three Loading Conditions

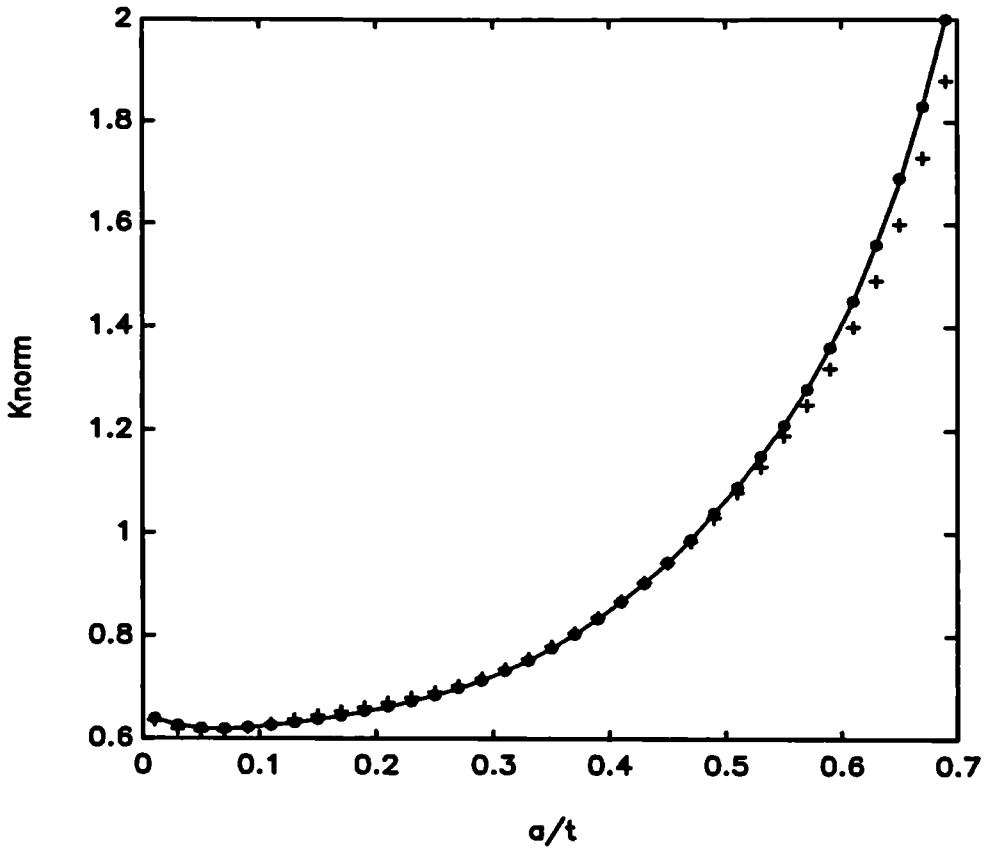

++++++	Weight Function using Petroski-Achenbach COD
oooooo	Weight Function using Multiple Reference States
————	Exact Solution

Fig 3.7

Weight Function SIF Solutions for an Edge Crack under Shear Loading

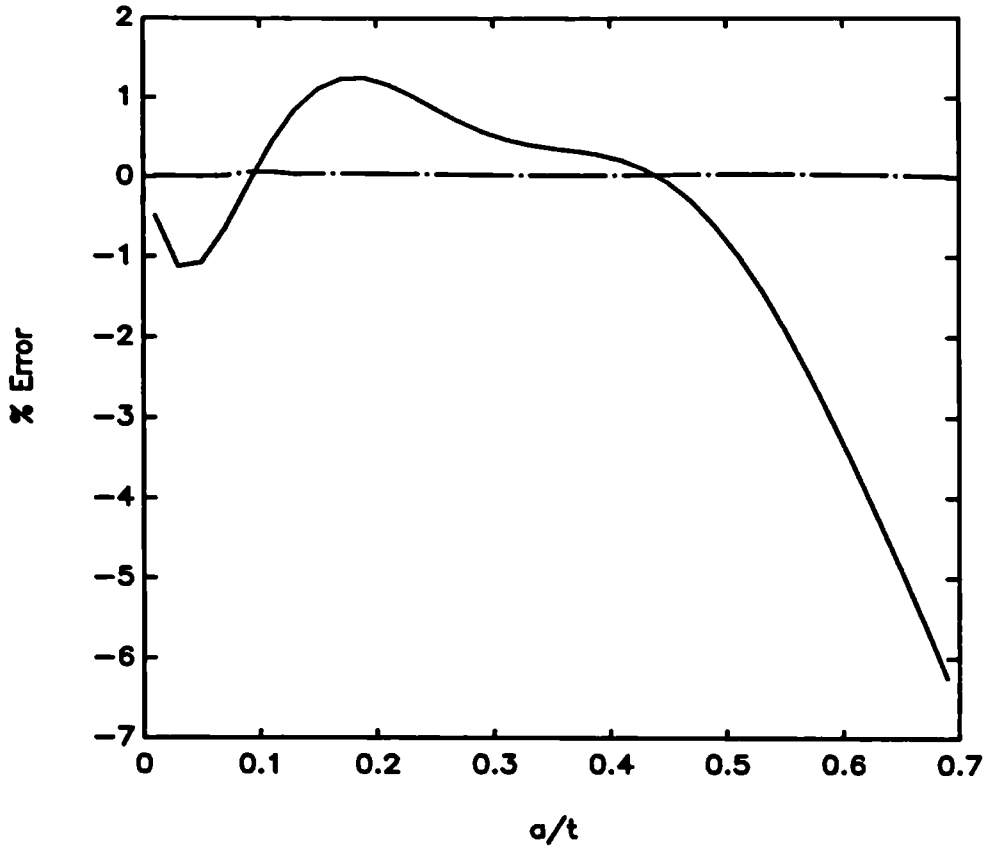

Weight Function using Petroski-Achenbach COD

Weight Function using Multiple Reference States

Fig 3.8

Assumed Profile SIF Versus Multiple Reference States Approach

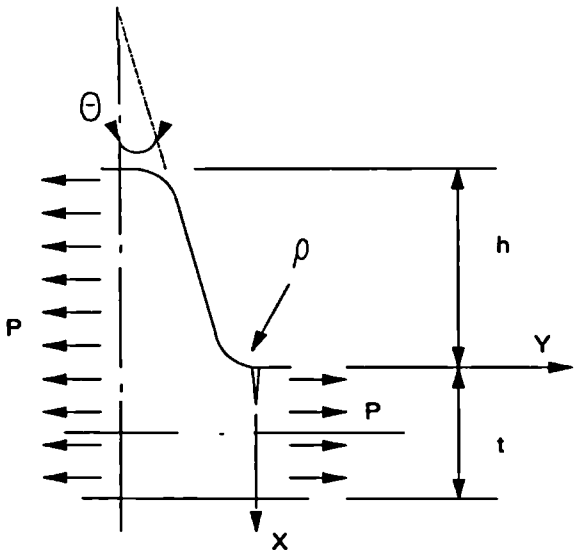

Fig 3.9 Edge Crack in a Thread Root

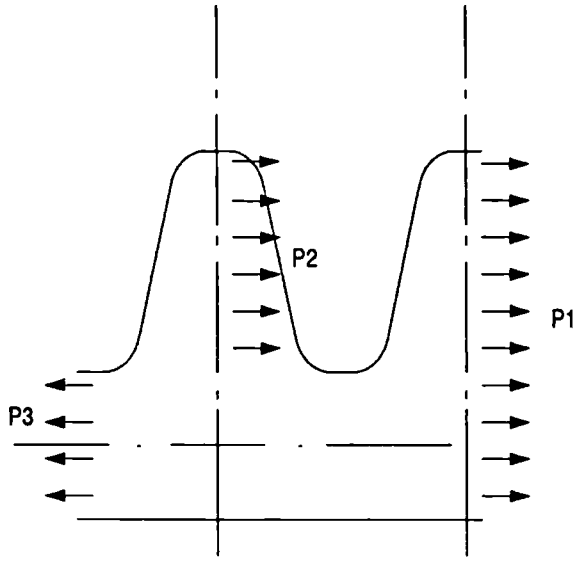

Fig 3.10 Applied Loads Contributing to Thread Root Stress

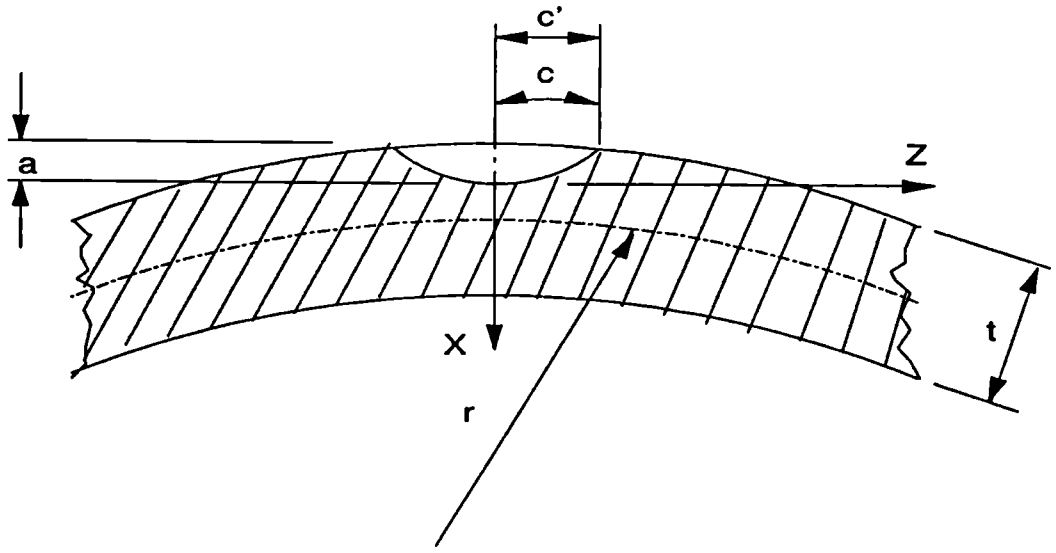

Fig 3.11 External Surface Crack in a Tube

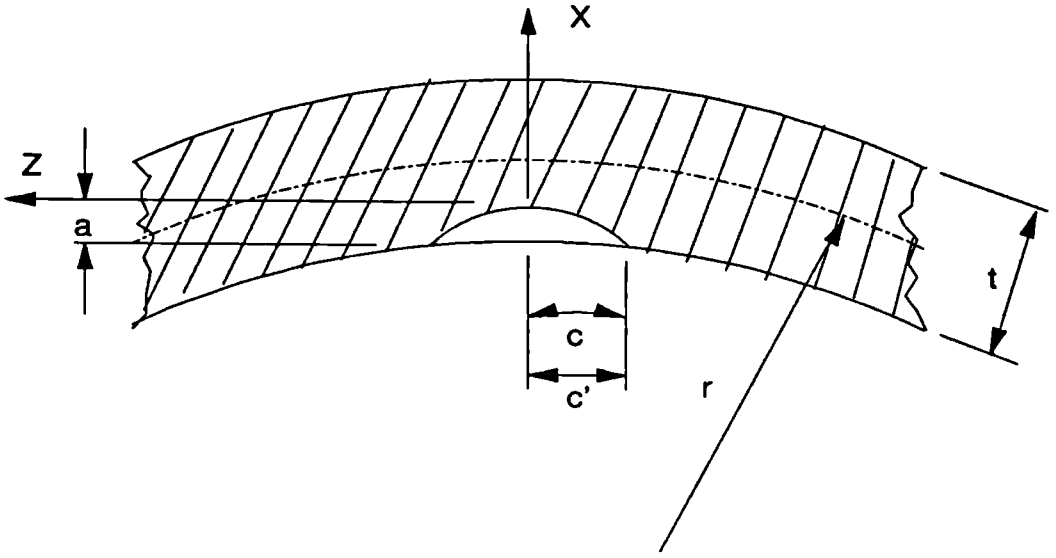

Fig 3.12 Internal Surface Crack in a Tube

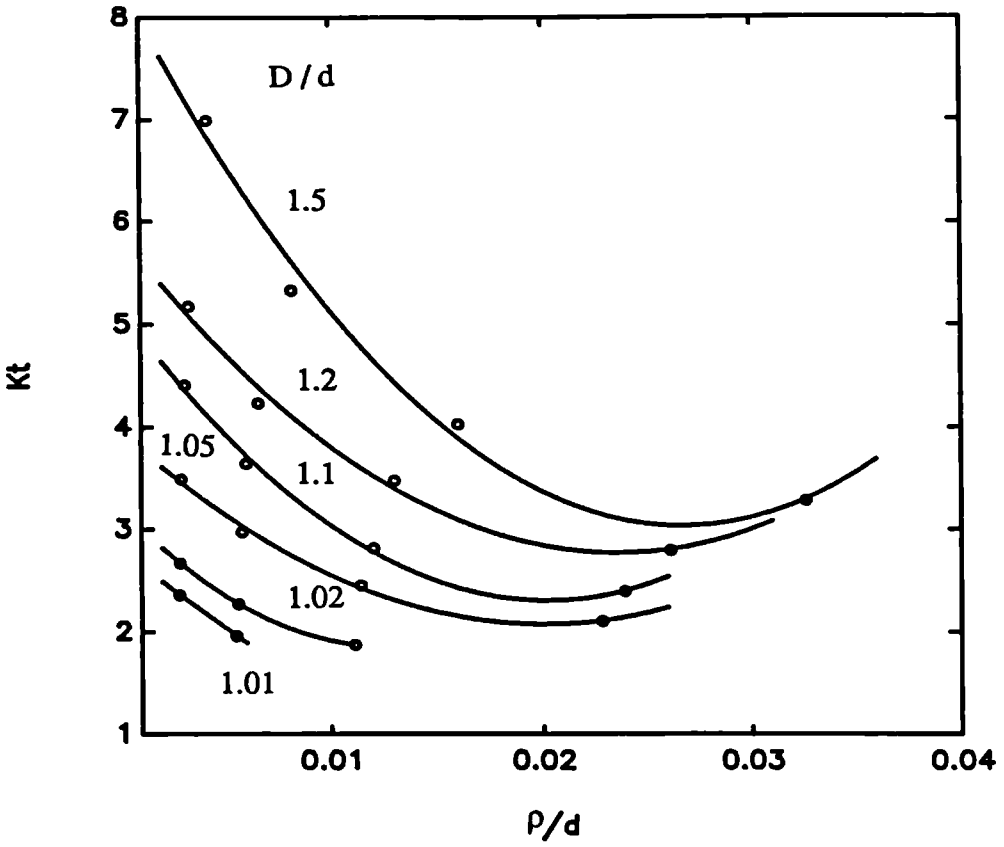

Fig 3.13

Stress Concentration Factors for a Shoulder in a Strip [3.37]

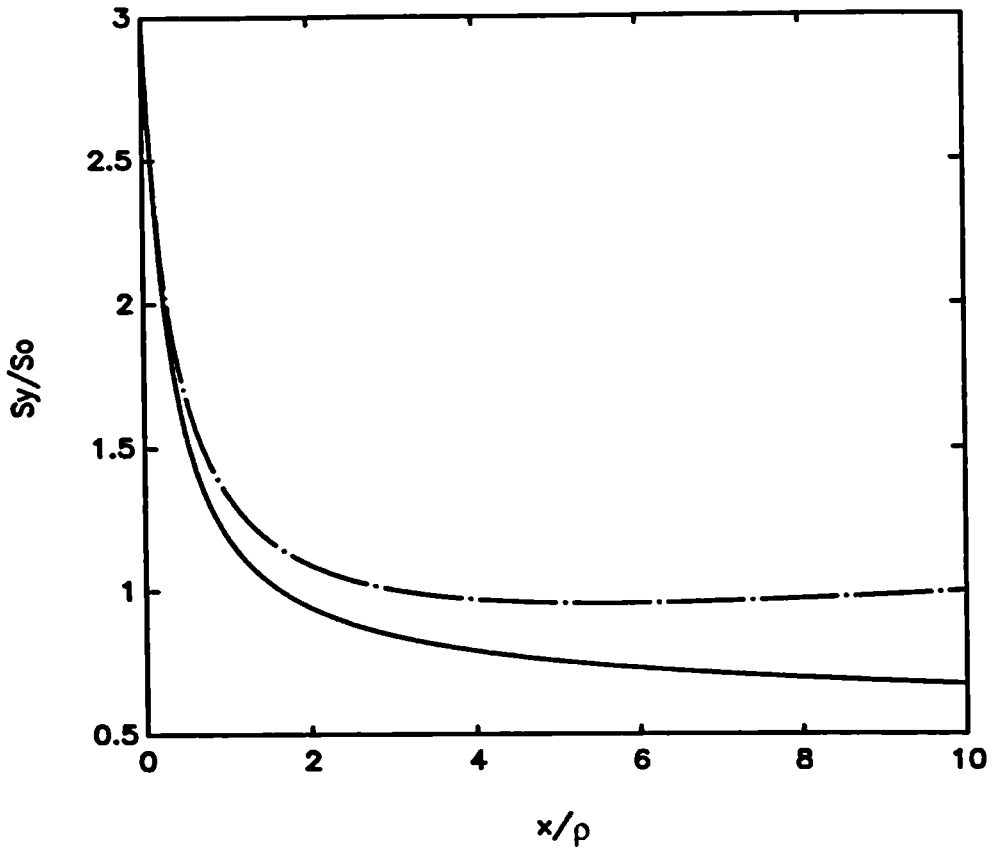

Newport-Glinka

Kujawski

Fig 3.14

Stress Distribution Through a Section due to a Notch: $K_T = 3.0$

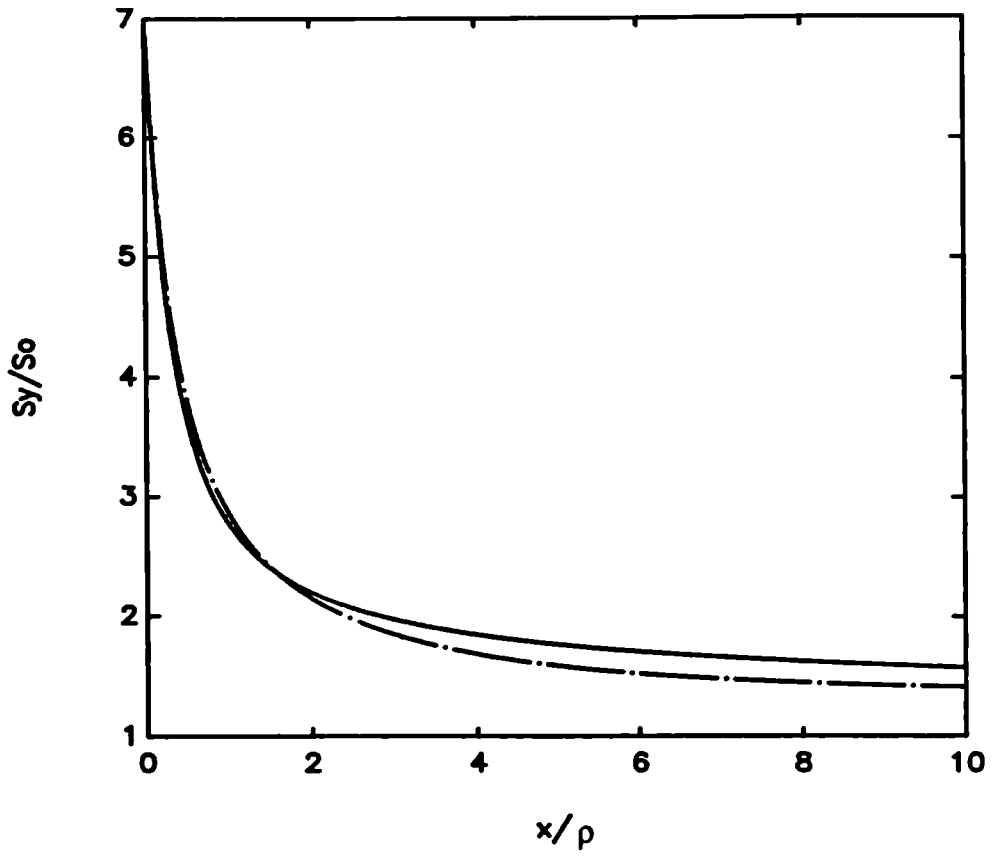

Newport-Glinka

Kujawski

Fig 3.15

Stress Distribution Through a Section due to a Notch: $K_T = 7.0$

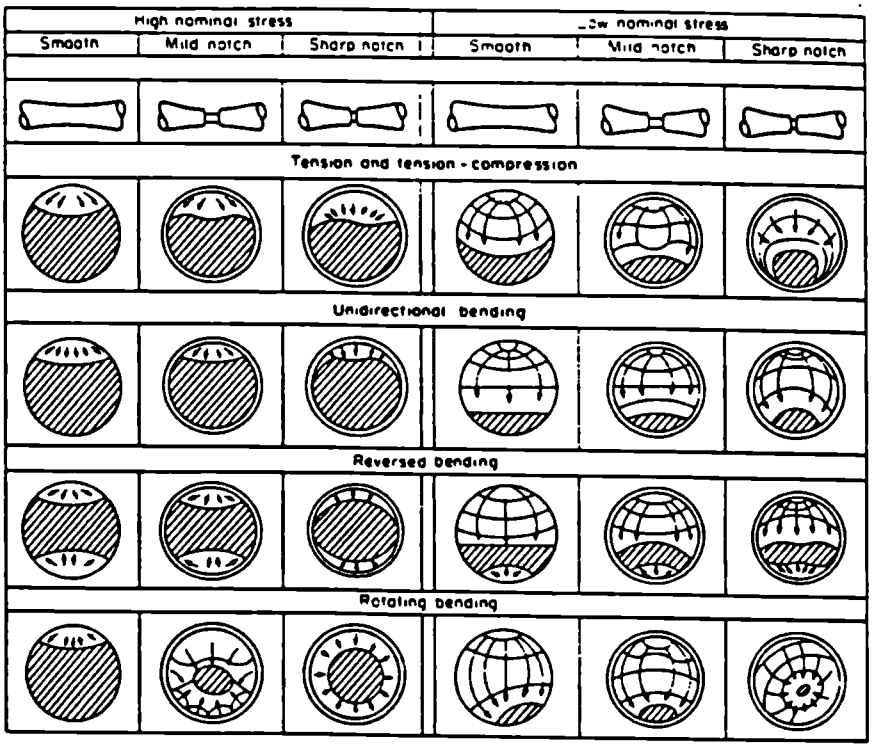

Fig 3.16

Schematic Fatigue Fracture Surfaces for Round Bars
under Tension and Bending Loads [3.56]

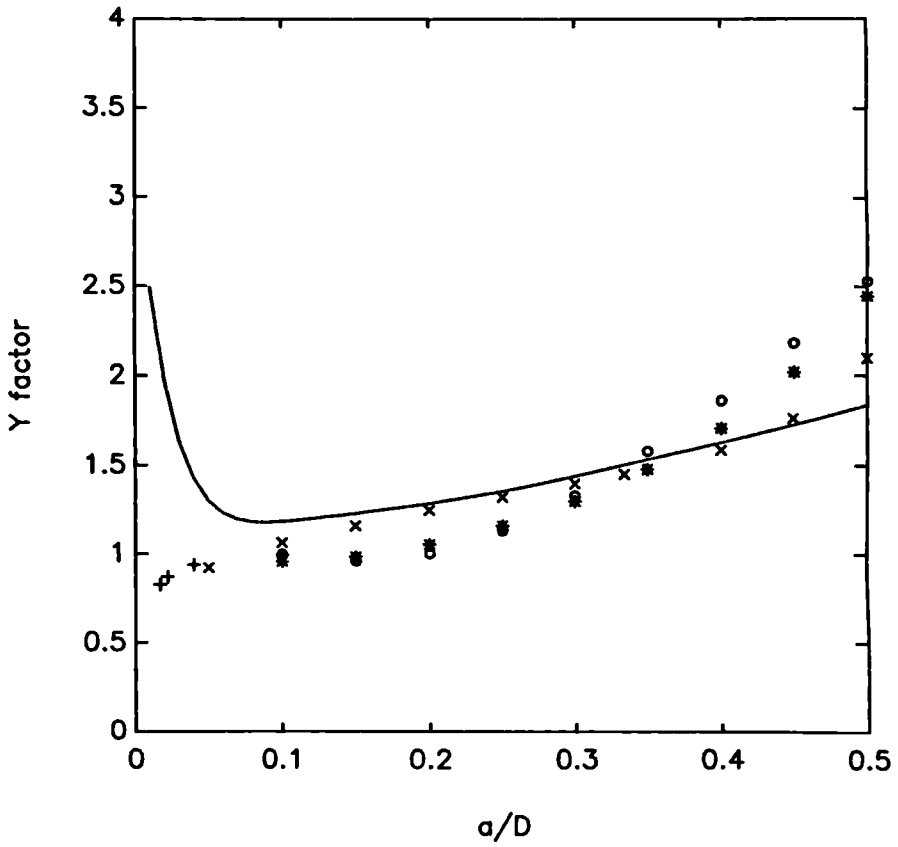

———	M20 UNC
$\frac{a}{c}=\frac{2a}{D\,\mathrm{Cos}^{-1}\left(1-2\frac{a}{D}\right)}$	Edge Crack
o	Daoud, Cartwright & Carey (Compliance)
*	Daoud, Cartwright & Carey (FE)
+	Blackburn
x	Bush

Fig 3.17

Edge Crack in a Round Bar under Tension

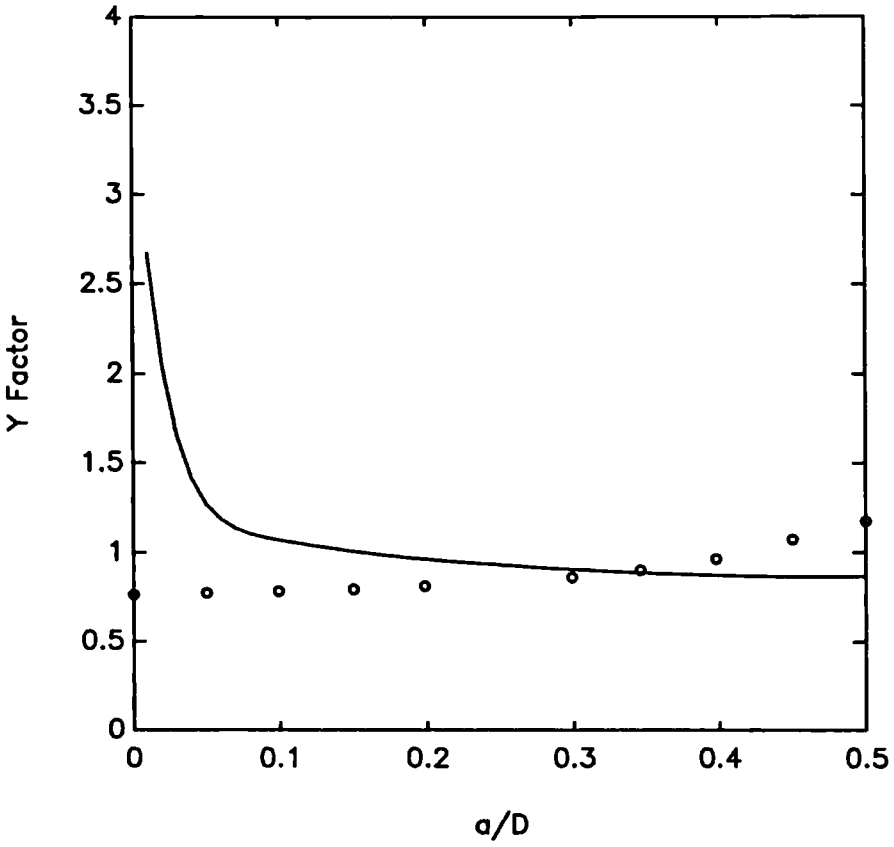

———	M20 UNC
$\frac{a}{c}=\frac{2a}{D\,\mathrm{Cos}^{-1}\left(1-2\frac{a}{D}\right)}$	Edge Crack
o	Bush

Fig 3.18

Edge Crack in a Round Bar under Bending

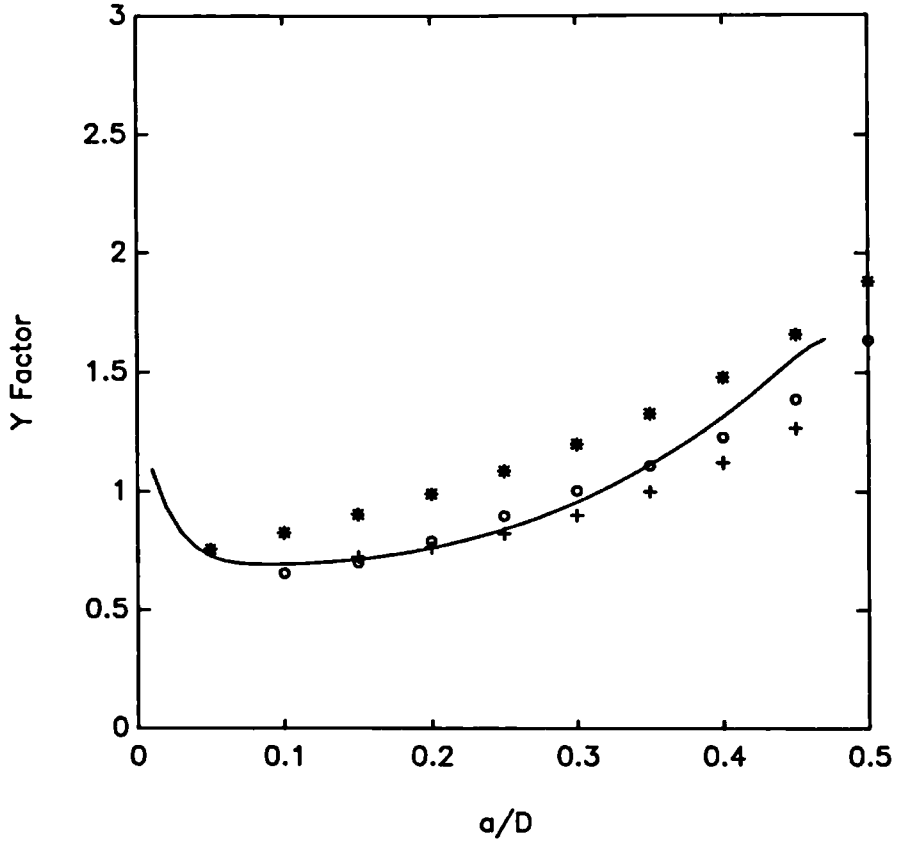

———— M20 UNC

$\frac{a}{c} = \frac{2\frac{a}{D}}{\text{Tan}^{-1}\left[2\frac{a}{D}\left(\frac{1-\frac{a}{D}}{1-\frac{2a}{D}}\right)\right]}$ Circular Crack

o Daoud & Cartwright

\+ Wilhem

* Forman & Schivakumar

Fig 3.19

Circular-Arc Surface Crack in a Round Bar under Tension

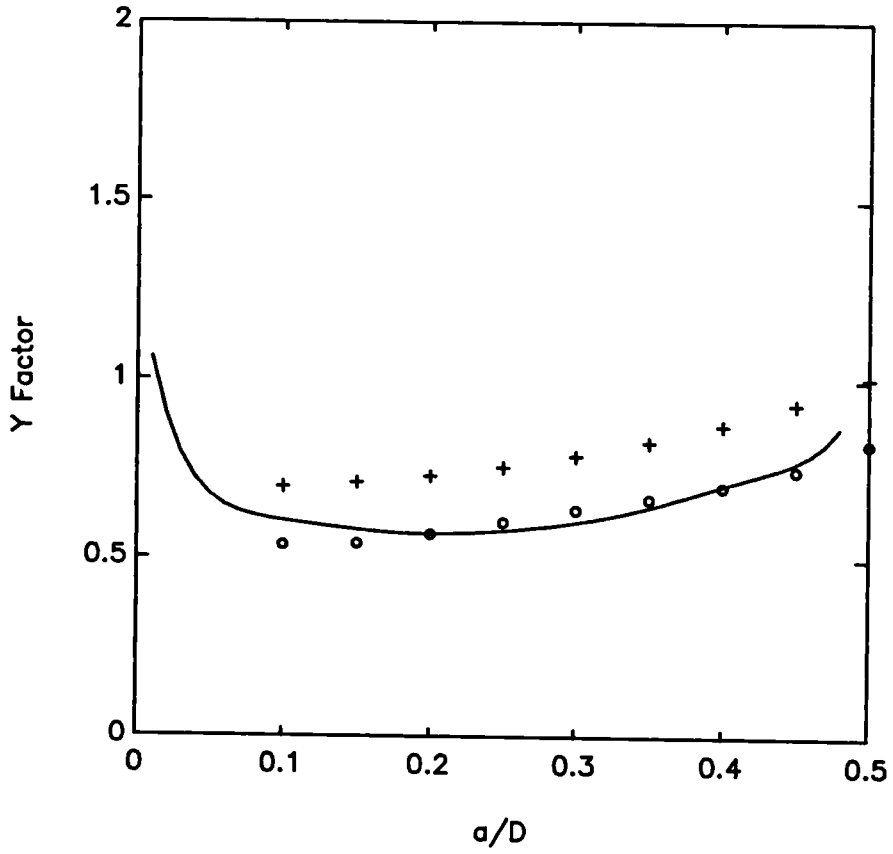

——————— M20 UNC

$\frac{a}{c} = \frac{2\frac{a}{D}}{\mathrm{Tan}^{-1}\left[2\frac{a}{D}\left(1-\frac{a}{D}\right)\Big/\left(1-\frac{2a}{D}\right)\right]}$ Circular Crack

o Daoud & Cartwright

\+ Forman & Schivakumar

Fig 3.20

Circular-Arc Surface Crack in a Round Bar under Bending

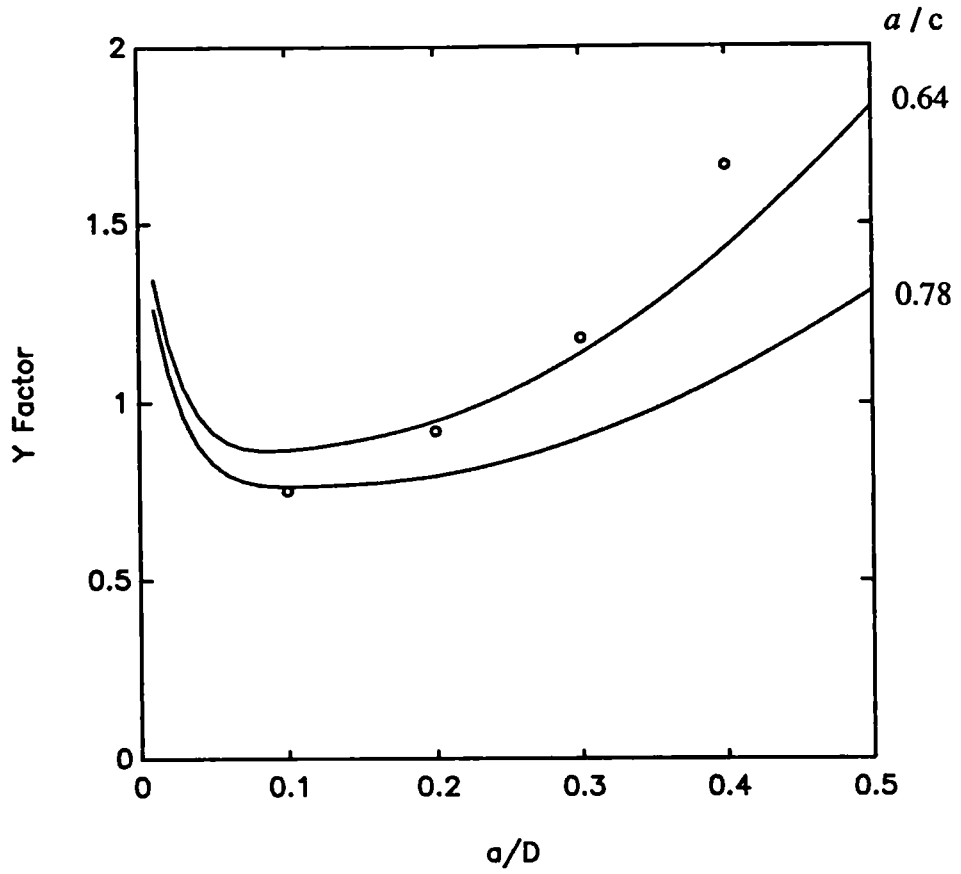

—————— M20 UNC

o Erjian Si

$\frac{a}{c} \sim 0.78, \quad a < \frac{D}{2}$

$\frac{a}{c} \sim 0.64, \quad a \to \frac{D}{2}$

Fig 3.21

Semi-elliptical Surface Crack in a Round Bar under Tension

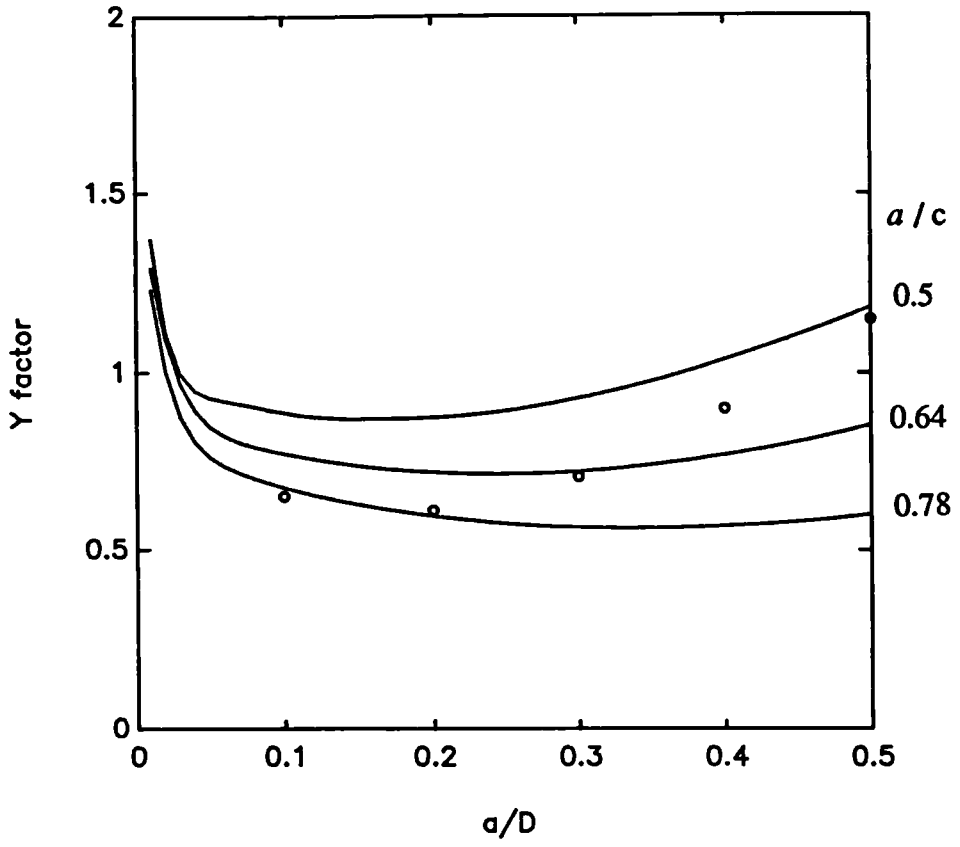

—————— M20 UNC

o Erjian Si

$\frac{a}{c} \sim 0.78, \quad a < \frac{D}{2}$

$\frac{a}{c} \sim 0.64, \quad a \to \frac{D}{2}$

Fig 3.22

Semi-elliptical Surface Crack in a Round Bar under Bending

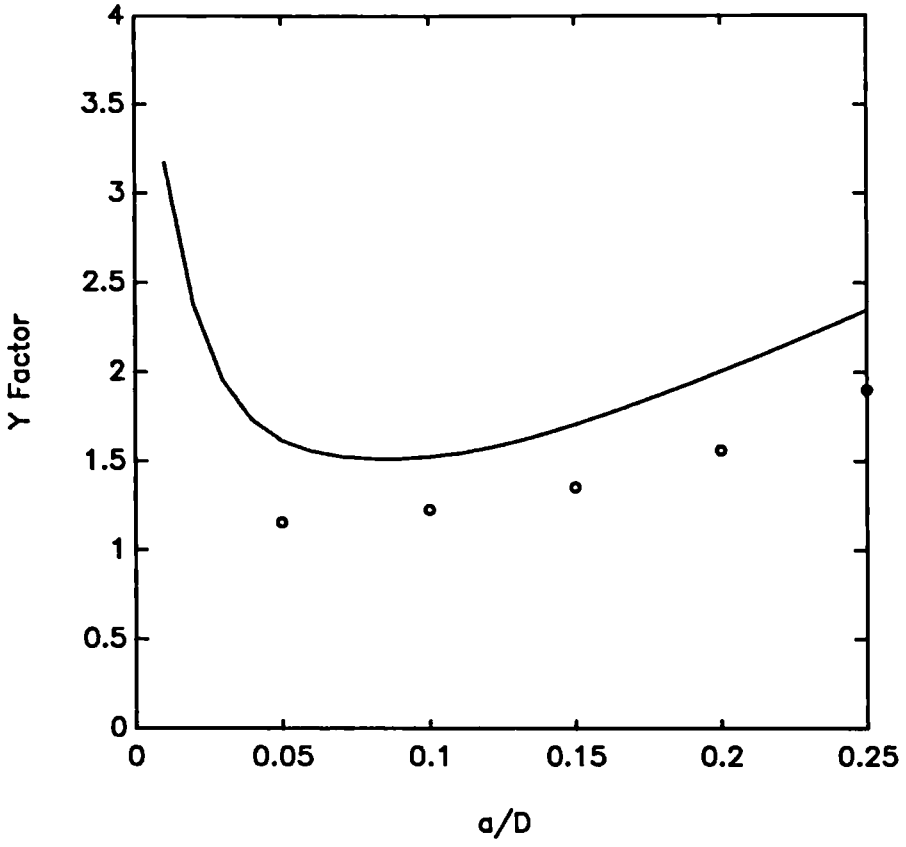

—————— M20 UNC

$\frac{a}{c} = \frac{2a}{\pi D}$

o Benthem & Koiter

Fig 3.23

Circumferential Crack in a Round Bar under Tension

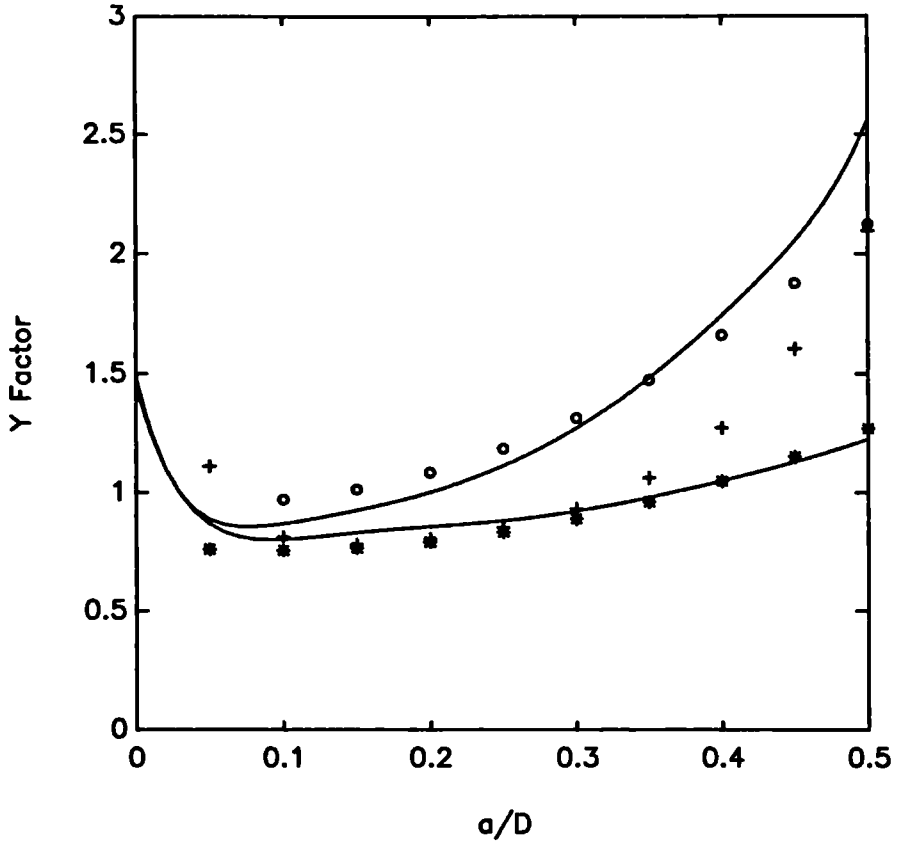

———— ISO M8 x 1.0

$\frac{a}{c} = \frac{2\frac{a}{D}}{\text{Tan}^{-1}\left[2\frac{a}{D}\left(1-\frac{a}{D}\right)\right]}$ Upper Bound Circular Crack

$\frac{a}{c} = \frac{\frac{a}{D}}{\text{Sin}^{-1}\left(\frac{a}{D}\right)}$ Lower Bound Circular Crack

* Toribio $\frac{a}{b} = 1.0$

o Toribio $\frac{a}{b} = 0.2$

\+ James & Mills

Fig 3.24

Crack in an ISO M8 x 1.0 Bolt under Tension

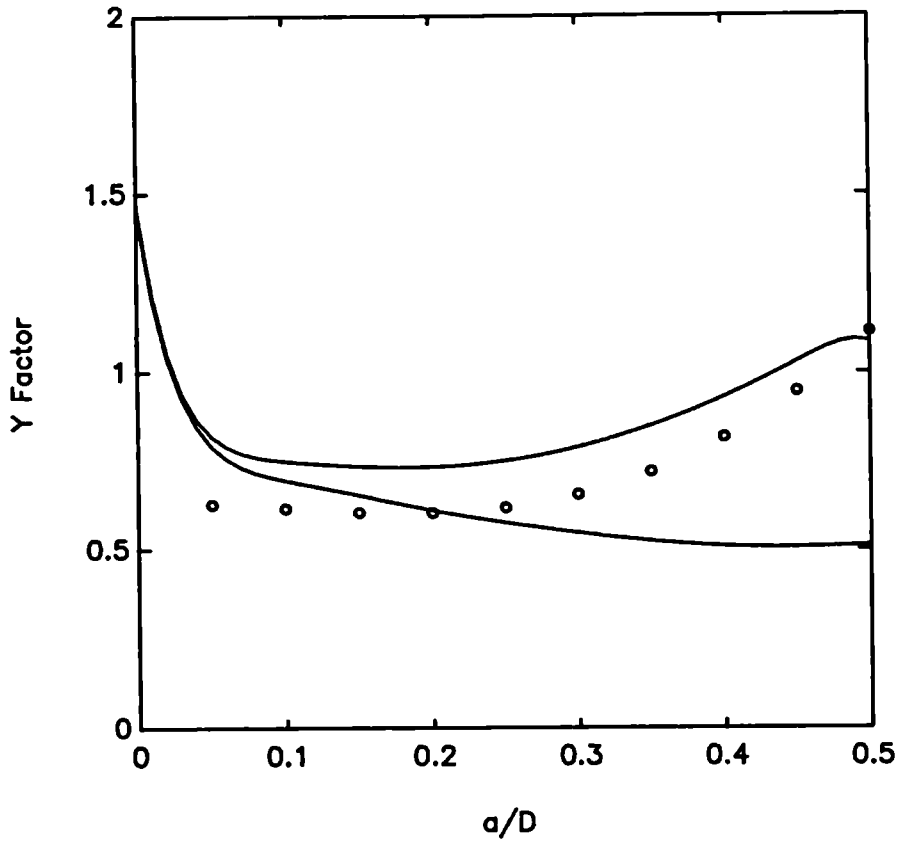

———— ISO M8 x 1.0

$\frac{a}{c} = \frac{2\frac{a}{D}}{\text{Tan}^{-1}\left[2\frac{a}{D}\frac{\left(1-\frac{a}{D}\right)}{\left(1-\frac{2a}{D}\right)}\right]}$ Upper Bound Circular Crack

$\frac{a}{c} = \frac{\frac{a}{D}}{\text{Sin}^{-1}\left(\frac{a}{D}\right)}$ Lower Bound Circular Crack

o James & Mills

Fig 3.25

Crack in an ISO M8 x 1.0 Bolt under Bending

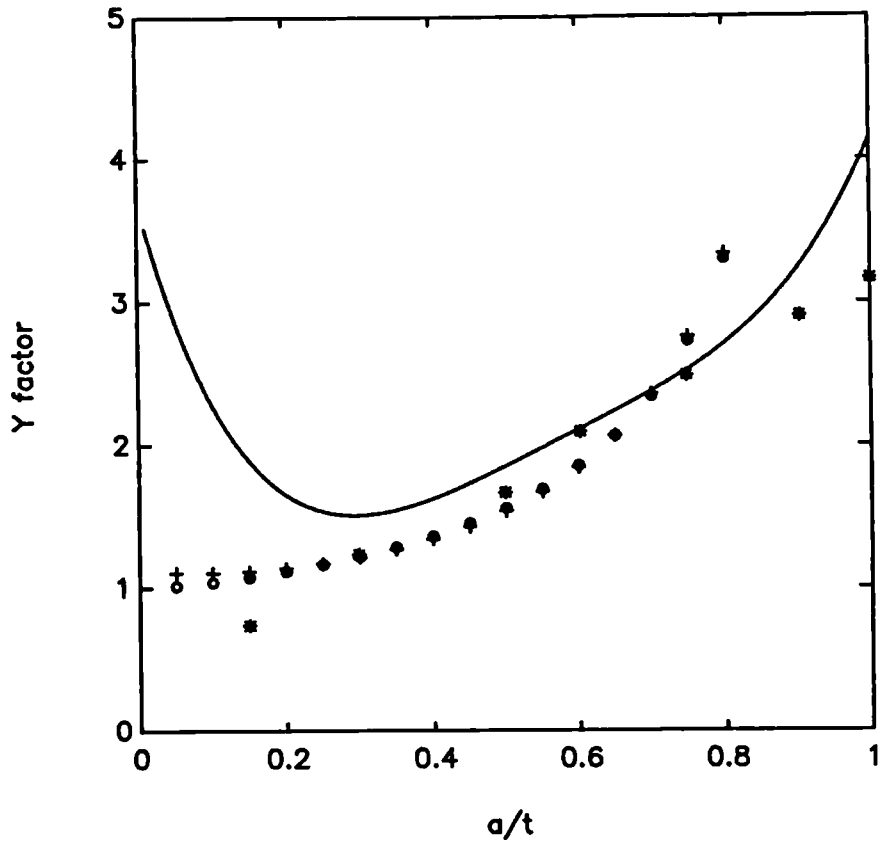

———— ISO M8 x 1.0

$\frac{a}{c} = 0.2$

o Wilkowski & Eiber (Edge)

\+ Harris (Circumferential)

* Bush (Edge)

Fig 3.26

External Tube Crack under Tension

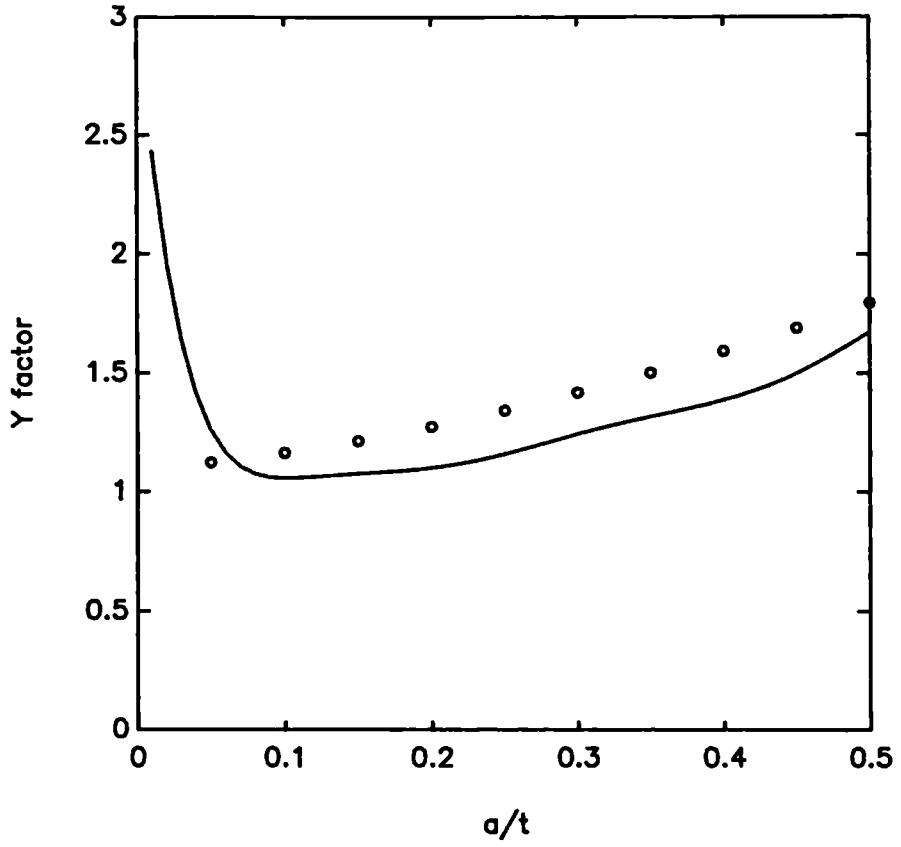

———————— ISO M8 x 1.0

$\frac{a}{c} = 0.1$

$\frac{r_i}{t} = 9.5$

o Rajab (Circumferential)
$\frac{r_i}{t} = 9.5$

Fig 3.27

Internal Circumferential Tube Crack under Tension

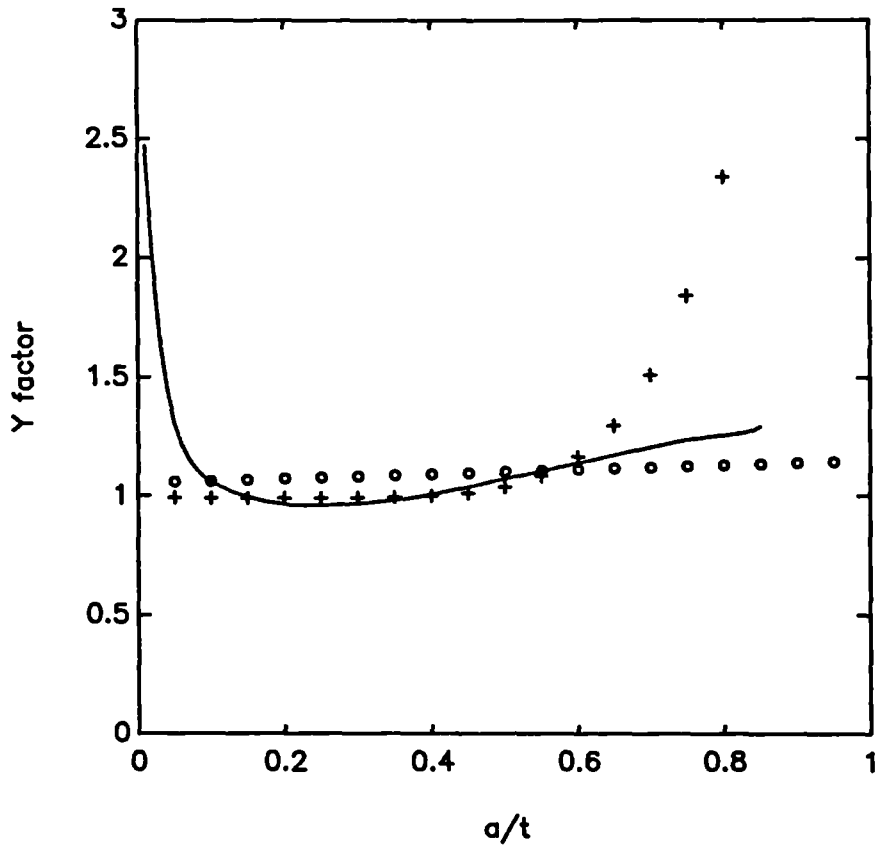

———— ISO M8 x 1.0

$\frac{a}{c} = 0.4$

$\frac{r_i}{t} = 9.5$

o Poette & Albaladejo
$\frac{r_i}{t} = 9.5$

\+ Chen

Fig 3.28

Internal Semi-elliptical Tube Crack under Tension

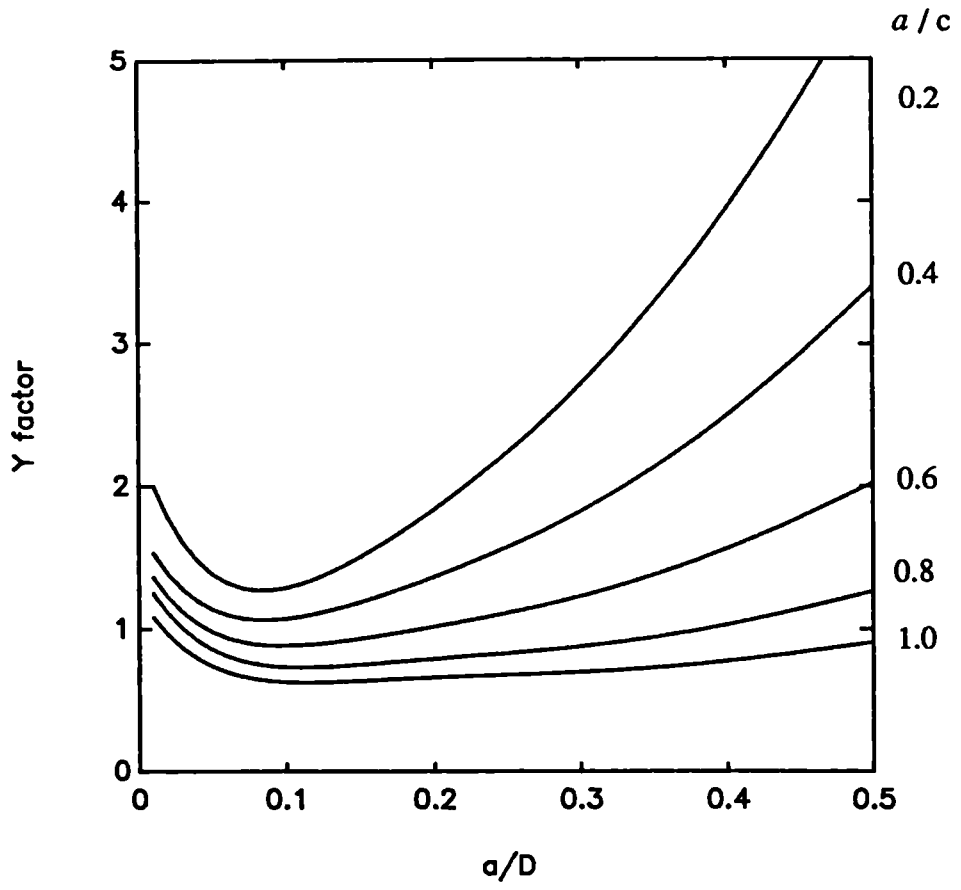

θ	30°
h	1.353 mm
D	20 mm
ρ	0.2 mm
K_T	4.5

Fig 3.29

Semi-elliptical Crack in a Threaded Bar under Tension

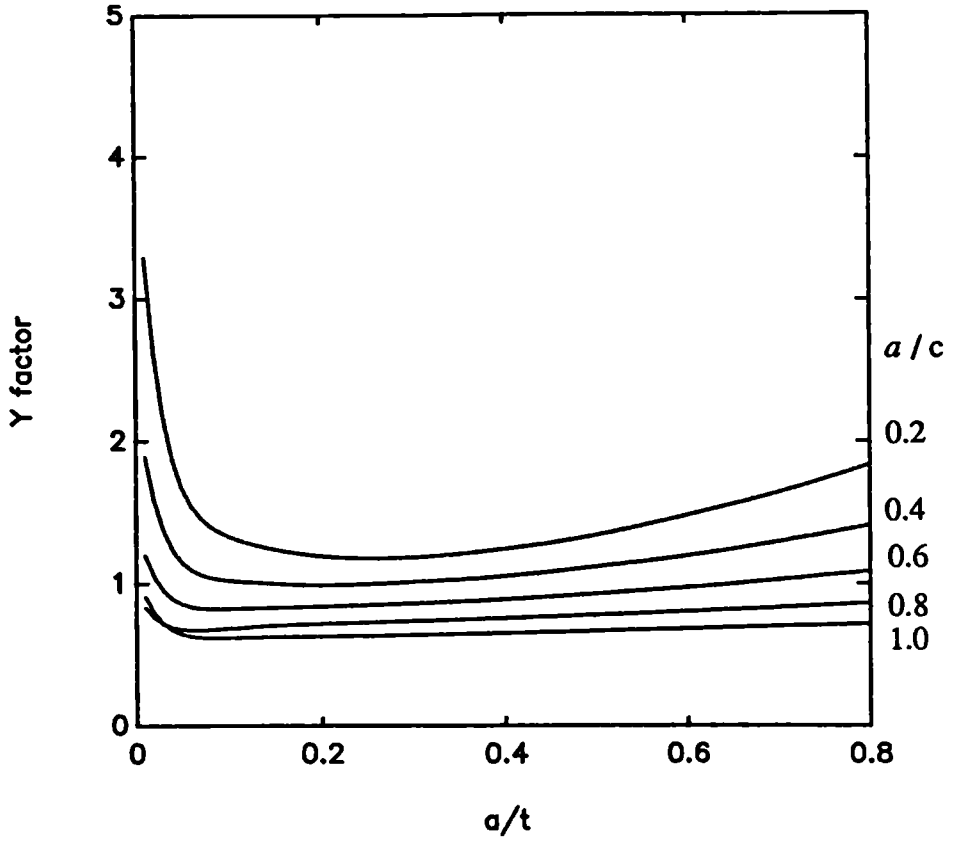

$\frac{r_i}{t} = 2.0$

θ	30°
h	1.353 mm
t	20 mm
ρ	0.2 mm
K_T	4.5

Fig 3.30

Semi-elliptical External Crack in a Threaded Tube under Tension

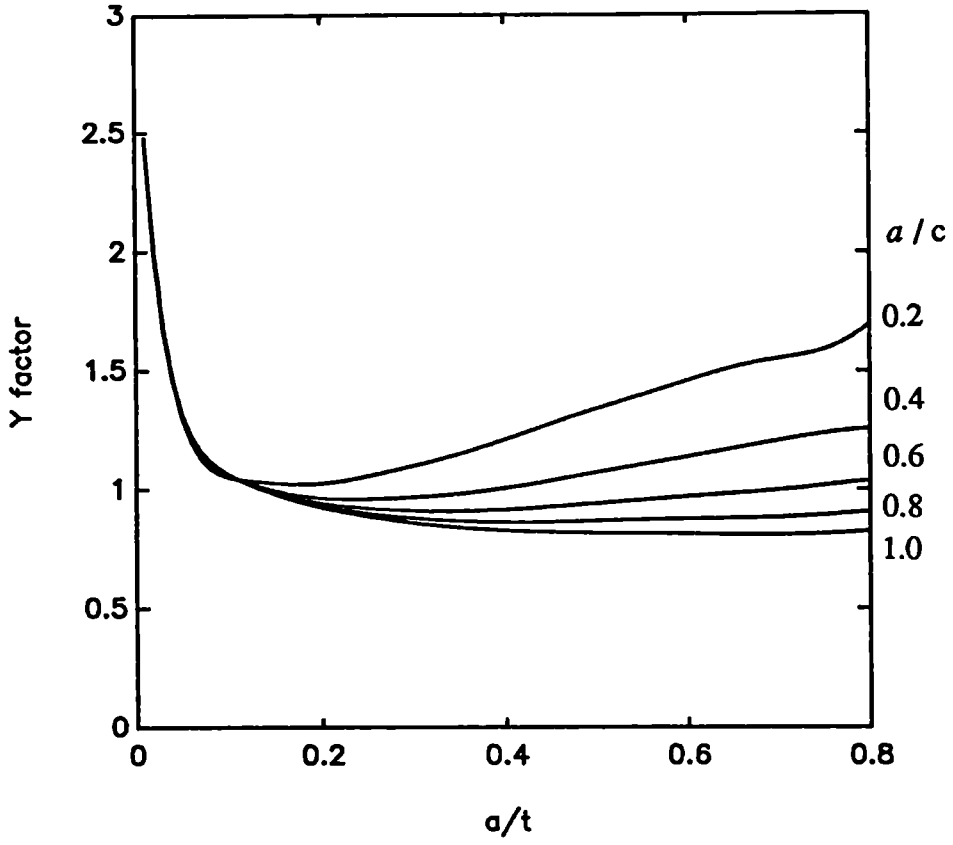

$\frac{r}{t} = 9.5$	
θ	30°
h	1.353 mm
t	20 mm
ρ	0.2 mm
K_T	4.5

Fig 3.31

Semi-elliptical Internal Crack in a Threaded Tube under Tension

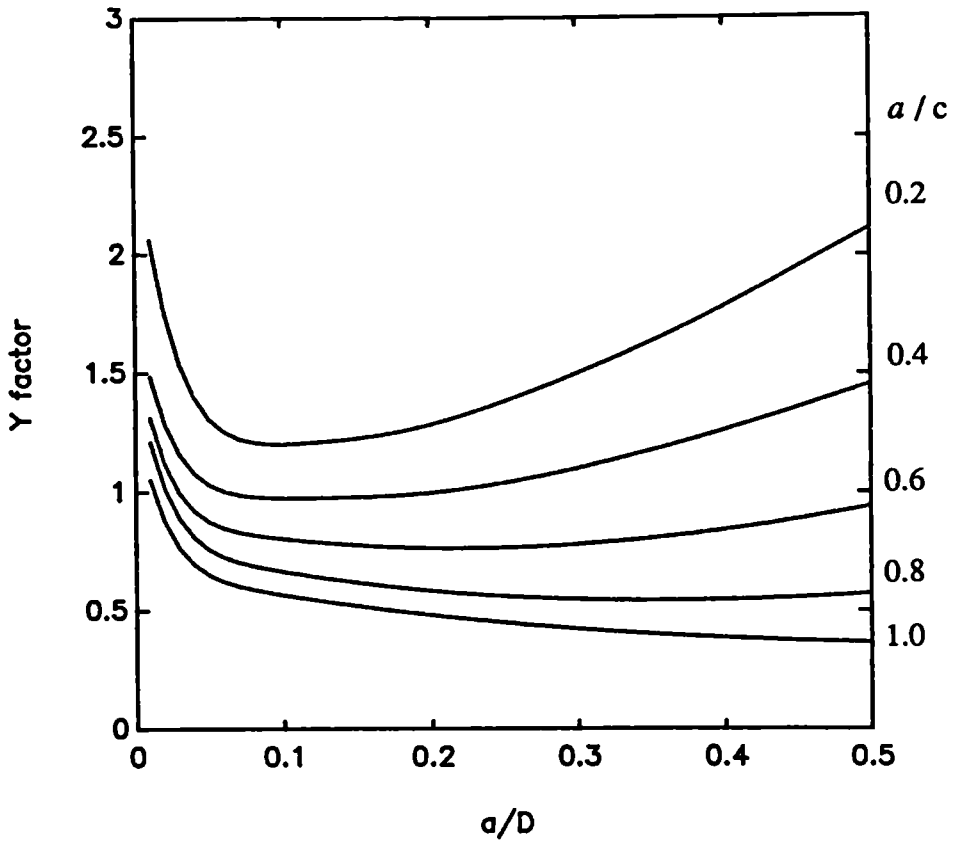

θ	30°
h	1.353 mm
D	20 mm
ρ	0.2 mm
K_T	4.5

Fig 3.32

Semi-elliptical Crack in a Threaded Bar under Bending

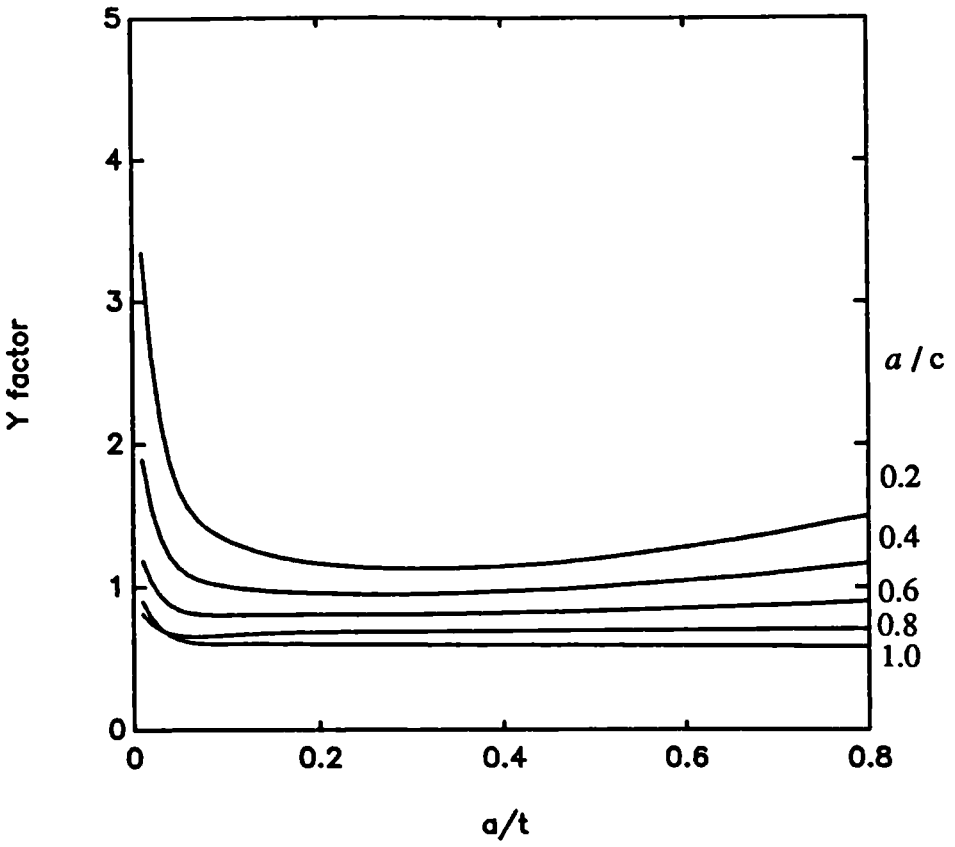

$\frac{r_i}{t} = 2.0$

θ	30°
h	1.353 mm
t	20 mm
ρ	0.2 mm
K_T	4.5

Fig 3.33

Semi-elliptical External Crack in a Threaded Tube under Bending

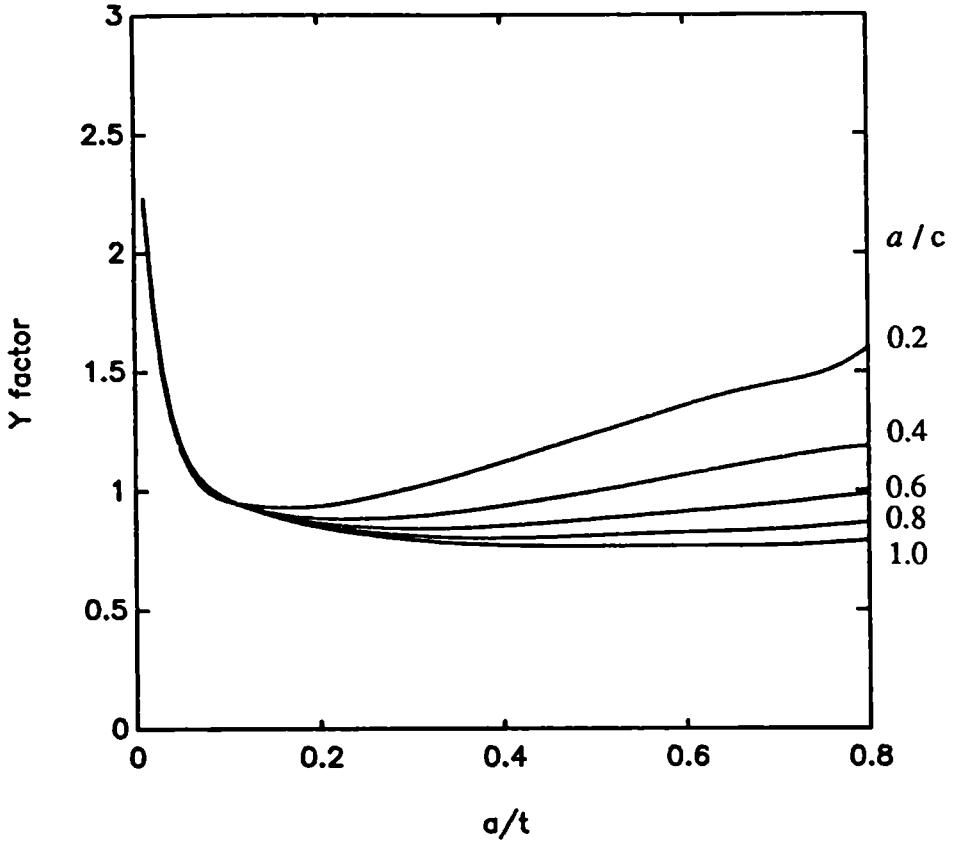

$\frac{r}{t} = 9.5$

θ	30°
h	1.353 mm
t	20 mm
ρ	0.2 mm
K_T	4.5

Fig 3.34

Semi-elliptical Internal Crack in a Threaded Tube under Bending

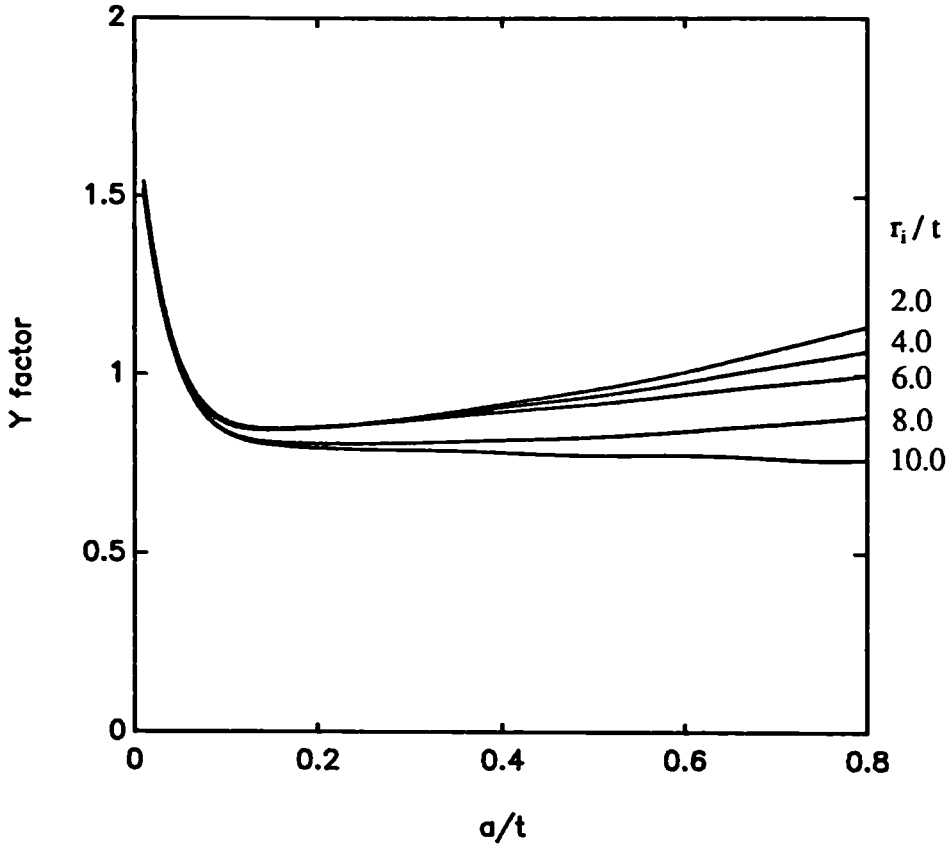

$\frac{a}{c} = 0.5$

θ	30°
h	1.353 mm
t	20 mm
ρ	0.2 mm
K_T	4.5

Fig 3.35

Semi-elliptical External Crack in a Threaded Tube under Tension

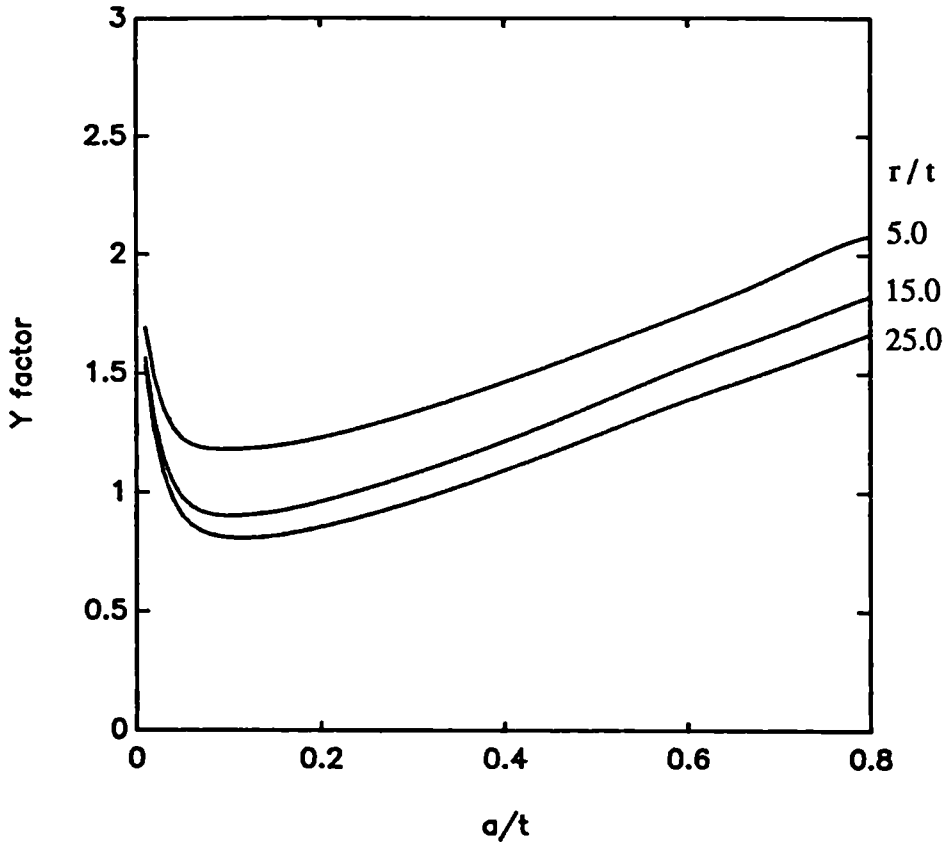

$\frac{a}{c} = 0.5$

θ	30°
h	1.353 mm
t	20 mm
ρ	0.2 mm
K_T	4.5

Fig 3.36

Semi-elliptical Internal Crack in a Threaded Tube under Tension

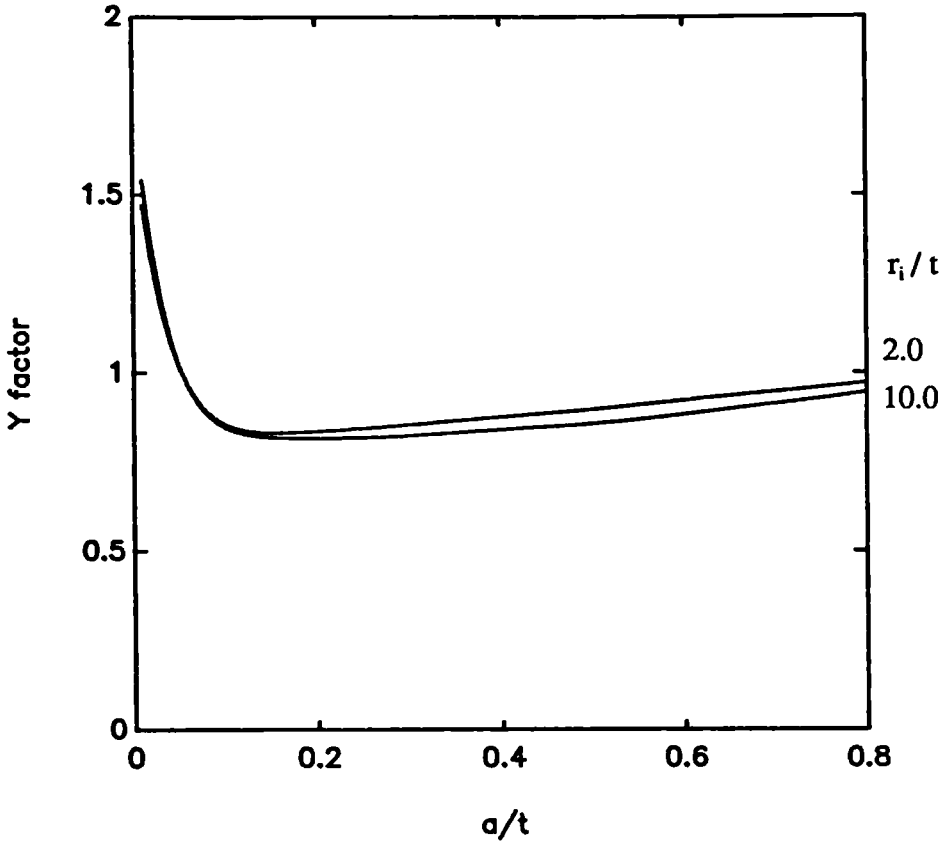

$\frac{a}{c} = 0.5$

θ	30°
h	1.353 mm
t	20 mm
ρ	0.2 mm
K_T	4.5

Fig 3.37

Semi-elliptical External Crack in a Threaded Tube under Bending

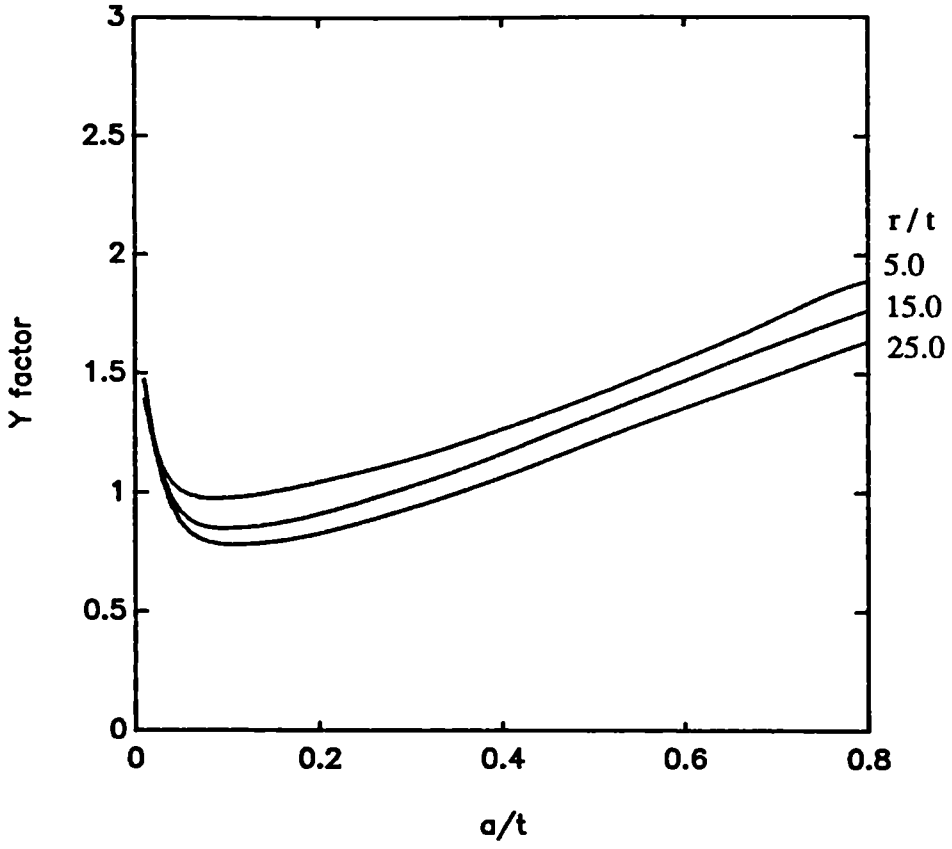

$\frac{a}{c} = 0.5$

θ	30°
h	1.353 mm
t	20 mm
ρ	0.2 mm
K_T	4.5

Fig 3.38

Semi-elliptical Internal Crack in a Threaded Tube under Bending

CHAPTER FOUR - Experimental Work

4.1 Introduction

The theoretical models described in the previous chapters remain abstract until they can be utilised in a practical manner to indicate the fatigue resistance of various threaded connections. The experimental tests used to validate the initiation and propagation models are reported in the form of two engineering case studies. The background to these, the experimental details and unprocessed fatigue test results are described in the following sections. Interpretation of the results, comparison with the prediction models and discussion of these in the context of the respective case studies will follow in the succeeding chapter. The case studies considered involve situations where threaded fasteners are fundamental to each operation, and are distress regions with regard to fatigue failure. The loading and environment is quite different for both circumstances, even the typical connections examined are diverse contributing examples of male as well as female component failures. Full scale fatigue tests were conducted in each situation, every effort was made (within reason) to keep the characteristics of each test as near as possible to those in reality.

4.2 Fatigue Tests of Tethers for Tension Leg Platforms

A Tension Leg Platform (TLP), or Tension Buoyant Platform (TBP), is a floating structure having a novel mooring system. The platform is held against its natural buoyancy by a number of vertical risers fixed to the sea bed. These risers consist of clusters of tethers which are generally loaded axially in tension. Wave and wind loading on the installation cause the tethers to be randomly stressed. The degrees of freedom of such a structure are shown in Fig 4.1. There are to date only two TLPs in operation as drilling/production oil platforms; Conoco's Hutton TLP (1984), and the Jolliet Field Tension Leg Well Platform (1990). However, Hutton is the only platform having its tether segments connected by threaded fasteners. This pioneering project raised many technical problems requiring innovative solutions. Service data of how successful these have been is only now becoming available and much analysis is required to understand the service load mechanisms acting on the structural components of the platform.

The requirements of a high strength steel (high carbon equivalent) to resist the axial stressing of the tethers made it necessary to join the individual lengths of each tether with a threaded connection, rather than by welding. It is this threaded connection which is of interest from the fatigue point of view, as high stress concentrations occur due to the load distribution and geometrical discontinuities within the connection. Work has been done on stress analysis of screw threads (e.g. [4.1]), however, the mechanisms of fatigue and effects of torque in these are little understood.

Constant amplitude tests have been carried out on similar connections [4.2]. However, it is generally accepted that it is necessary to examine the effects of overloading and variable frequency stressing on components which are subject to random loading in practice. The tests completed as part of this study were designed to be as realistic as possible. The Hutton platform was taken as a model and an attempt was made to try to simulate similar load sequences on the test connections to those that might exist in service.

4.2.1 Determination of Load Response Spectrum

The predominant load excitation on an offshore installation is due to wave elevation. Such loading is thus a function of wave frequency and directionality. In the northern North Sea, established oceanographic measurements have resulted in the adoption of the Pierson-Moskowitz wave elevation spectrum (or modifications to this) as the most appropriate expression of water surface behaviour, for a fully developed sea.

The concept of a fully developed sea, is a proposal that such a state exists where the wind induced energy on the water surface is equal to the loss of energy due to wave breaking.

The spectrum is based on the assumption that the dominant part of a wind generated sea is a function of five parameters: frequency, gravity, friction, velocity and fetch [4.3].

The original Pierson-Moskowitz spectrum is given by:

$$S_{yy}(\omega)d\omega = \left[\alpha \frac{g^2}{\omega^5}\right] e^{-\beta\left(\frac{\omega_o}{\omega}\right)^4} d\omega \qquad (4.1)$$

where:

$\omega_o = g/U$
$\alpha = 8.10 \times 10^{-3}$
$\beta = 0.74$

U is the wind speed

The model describes the fully developed sea determined by one parameter, namely, wind speed or significant wave height. The fetch and duration are assumed to be infinite.

Det Norske Veritas adopted a modified version of (4.1), which expresses the power spectral density function '$S_{yy}(\omega)$' in terms of significant wave height, 'H_s' and mean zero crossing period 'T_z'. This is given as:

$$S_{yy}(\omega) = \frac{H_s^2 T_z}{8\pi^2}\left(\frac{\omega T_z}{2\pi}\right)^{-5} e^{\left[-\frac{1}{\pi}\left(\frac{\omega T_z}{2\pi}\right)^{-4}\right]} \qquad (4.2)$$

The above form of the equation is used in this analysis. Constant significant wave height, zero crossing period and direction for a reasonable duration (about three hours) constitutes a sea state. A wave scatter diagram represents the occurrence of sea states over a period of time. The sample wave scatter diagram

shown in Fig 4.2 shows the occurrence of sea states in terms of wave height and period at the Hutton site from December 1985 to February 1986 [4.4]. Three sea states were considered for the analysis. These are:

Sea State	H_s (m)	T_z (sec)
1	2.25	6
2	2.75	7
3	3.75	8

The reasons these were considered are that they are the most probable occurring states out of the one thousand occurrences monitored, they also correspond to frequencies for which the most reliable structure response data is available. The power spectral density function of wave elevation, '$S_{yy}(\omega)$' versus frequency for the three sea states are shown in Fig 4.3. The predominant frequency and frequency distribution of each state is different and will thus excite a different structural response.

The basic equation of motion for a TLP is given as:

$$F(t) = M\ddot{x} + (K_h + K_t)x + B\dot{x} \tag{4.3}$$

where:

$F(t)$ is the wave excitation vector
M is the total mass matrix, i.e. physical mass + added mass

K_h is the hydrostatic stiffness matrix
K_t is the tether stiffness matrix
B is a linearised damping matrix

$\ddot{x}$, $\dot{x}$ and x are the acceleration, velocity and displacement vectors respectively, in the various degrees of freedom

The concept of an added mass arises from the fact that a body moving through a fluid imparts an acceleration to some of the surrounding fluid. The force required by the body to cause this acceleration can be equated to the body having an added mass to its physical mass.

In a study on a six column TLP (similar to the Hutton TLP) [4.5], Response Amplitude Operators (RAOs) were presented for the structure in head, bow and quarter seas. The RAO is a transfer function which describes the structure's response over a range of frequencies. For the purposes of this study the RAO shown in Fig 4.4 [4.6] for a six column TLP port bow tether tension in head seas was used. It should be noted however, equation (4.3) is a rigid body equation of motion and is based on a Morrison formulation which assumes:

(a) The structure is an assembly of cylindrical, rectangular elements and non-elongated members. The cylindrical columns and rectangular pontoons have large length to breadth ratios. The non-elongated members' dimensions are small relative to incident wave lengths.

(b) No hydrodynamic interference exists between members.

(c) The sinusoidal wave motions induce the same forces regardless of the absolute motions of the structure.

(d) Negligibly small damping as a result of wave radiation effects.

Also as linear wave theory is used, it is assumed the motion amplitudes of the platform are very small.

The cable pretension was 4000 tonnes and the natural period was found to be two seconds. The strange behaviour of the structure at low periods is due to cancellations of one (e.g. pitch) or more of the various modes of freedom. Fig 4.5 shows the same RAO in terms of frequency in rad/sec. The relationship between the transfer function '$H(\omega)$', wave excitation power spectral density function '$S_{yy}(\omega)$', and the structural response spectrum '$G_{yy}(\omega)$' is given by:

$$G_{yy}(\omega) = |H(\omega)|^2 S_{yy}(\omega) \tag{4.4}$$

$H(\omega)$ is shown superimposed on a wave elevation spectrum in Fig 4.6, and Fig 4.7 shows the final tether loading spectra for the three sea states.

Returning to the question as to which sea state spectrum should be chosen, it should be noted that the lower the mean zero crossing period the closer the excitation is to the resonant frequency of the structure. In practice these excitations do occur, however, as this study is concerned with the effect of variable amplitude loading on tether connections, it was decided to choose a spectrum having the widest range of spectral data. The large peaks due to resonance tend to diminish the significance of the low amplitude - higher frequency cycles. Such spectra (single peaked, narrow band) are similar to constant amplitude load spectra, work on which has been done earlier. The spectrum chosen is the sea state:

$H_s = 2.25$ m, $T_z = 6$ sec.

The corresponding load spectrum is shown in Fig 4.8.

4.2.2 Experimental Procedure

Having the desired spectrum, a time series was generated to give a similar amplitude - frequency distribution. The routine, previously used to generate Wave Action Standard History (WASH) [4.7], was used to create the sequence. A discrete random number generator, e.g. shift register is used as a white noise source which is weighted using a filter function to amplify required frequencies thus diminishing to insignificance the remaining noise. Input of the spectrum was in the form of thirty two discrete values at equidistant points over the frequency domain, starting at zero hertz.

Table 4.1, shows the characteristics of the load spectrum and its corresponding time series. The time series consists of a sequence of numbers which are designed to be output periodically on a Digital to Analogue Converter (DAC). As the proposed tests were air tests, the frequency of loading was not important. The dominant period of the chosen sea state is about nine seconds (~ 0.11 Hz). In order to speed up the tests, the time series was output to the DAC at intervals around ten times quicker that the WASH routine's output, thus maintaining the progression of load amplitude whilst accelerating the process of crack growth.

The length of the time series was considered to be adequately long before repetition, as work done by Kam [4.8] shows that after 10,000 cycles or 40,000 seconds (which ever is greater), all the statistical characteristics associated with the spectrum will have been realised, i.e. clipping ratio etc., will have stabilized.

The threaded connections tested were $5^1/_2$" x 17 lbs/ft C75 VAM joints [4.9]. This coupling was designed as a casing joint. It has a Buttress-type thread, providing a double metal-to-metal seal at the pin end, energised by a reverse angle internal shoulder. The advantage of this is not structural but is reaped in the provision of non-turbulent flow within the pipe. The pipe itself is a wrought steel tubular without a welded seam. The steel grade C75 used is termed a restricted yield strength grade by API Specification 5Ac. This grade is

recommended for use in sour gas service (or H_2S). Sulphide stress cracking is likely when high strength/hardness steels are exposed to such an environment. It is for this reason that the yield strength is restricted (Chapter 6).

The chemical composition and mechanical properties of the C75 steel are given in Table 4.2. Fig 4.9 shows the main dimensions of the joint [4.2]. In order that the assembled pipe could be fixed to the Instron 1000 kN hydraulic test rig, flanges which would be bolted to the load actuator and load cell were welded to the pin ends.

To weld the En24 (flange) steel to the C75 (pipe) steel (Carbon equivalent of ~0.533%), 5mm Philips 565 electrodes (baked two hours at 250°C prior to welding) were used. Preparation of the pipe end consisted of machining a 30° bevel angle to the intended weld surface. Preheat temperature was 300°C at a rate of 2000°C/Hr. The weld area was then post heat stress relieved and the pipe - flange intersection ground to a smooth transition. Holes were then drilled into the flange so that the pipe could be bolted to the test rig.

The connection is a tapered screw that forces the pin and box shoulders together to form a seal and acts as a structural member, making the pin as strong as the box in bending and tension. It is essential for this reason that the correct torque (as specified by the manufacturers) is used to optimise the local preload.

If the connection is under torqued, "Galling" could also occur, i.e. the working out of the lubricant (hence welding of adjacent surfaces) due to wobbling and alternating separation and closure of thread surfaces [4.10].

The optimum make-up torque for the joint used is 7445 Nm, this was applied by holding the box in a purpose made jig, rotating the pin using a lever arm attached to the pin end and pulled using a chain block. A 250 kN load ring was put in series between the lever arm and the applied force so that the correct torque could be evaluated and applied to the joint. An example of the make-up details of one

of the connections is given in Fig 4.10. The torques given in this figure are expressed in ft.lbs. American Petroleum Institute (API) and the oil industry as a whole quote this imperial unit in their standards and assembly tables.

The joints were inspected before fatigue testing using Magnetic Particle Inspection (MPI). They were then assembled, the lubricant being "Shell Alvania EP2" grease as recommended by the manufacturers. The intention was to apply the advised optimum torque, however, when applying such high torques it is difficult to attain an accuracy of greater than $\pm 5\%$ unless sophisticated specialist machinery is used. The assembled joint was loaded axially in tension on a Servo-Hydraulic test machine, and inspected regularly using an automated Alternating Current Field Measurement (ACPD) test apparatus [4.2]. In order to do this inspection, the joint was removed from the fatigue test rig and the pins unscrewed from the box coupling. The original positions of the pins relative to the coupling were stamp marked on their surfaces to ensure that the joint could be reassembled exactly as it had been. Before inspection, the pins were cleaned with methylated spirit to remove any lubricant on the threads. It was found that for the ACPD testing, the process had to be slowed down from the previous rate used, as the U8 crack microgauge [4.11] needs at least 1.5 sec. to settle before giving a steady reading each time the probes are moved. A Hewlett-Packard Spectrum Analyser (model 3582A) was used to compare the input load spectrum (into the hydraulic controller) with the actual spectrum as measured by the load cell on the test rig.

The output load cycles were also counted on line by a program running on an independent satellite of the PDP-11 computer system. This program utilised an algorithm for rainflow cycle counting [4.12], which defines individual cycles as closed stress/strain hysteresis loops. The cumulative frequency distribution of the time series as counted by the on line program is shown in Fig 4.11.

4.2.3 Experimental Results

The results of five large scale fatigue tests on VAM joints are considered. The first three were under constant amplitude loading (carried out by Newport [4.2]). Tests 4 and 5 were variable amplitude tests carried out as part of this study.

The manufacturers had recommended the high torque levels but later revised these to an optimum value of 7445 Nm. All five connections failed at the first engaged (critical) tooth of the pin, the fatigue crack growth data is shown in Figs 4.12, 4.13, 4.14. It should be noted that due to a fault in the hydraulic test rig the large initiation life for test No 1, may not be correct [4.2].

Tests 1 and 3 were examined destructively in order to validate the crack growth measurement technique [4.2]. Here it was shown that the ACPD predicted the shape and length of the crack accurately, but underpredicted the depth by 15%. A correction was therefore applied to give the crack growth data.

Fig 4.14 shows the crack growth data for tests 4 and 5. For test 4 the first point was obtained using ACPD, the others being the beach marks caused by the making and breaking of the joint. The data points for test 5 were all obtained from ACPD and the correction applied. Table 4.3 summarises the fatigue test details. The nominal stress range is simply the applied axial load divided by the remote cross-sectional area of the tube. In the case of the two variable amplitude tests, the stress is the nominal weighted average stress range (chapter two) obtained by normalisation of the spectral data (Table 4.1) to the applied nominal stress range.

Experimental tests were also done on Compact Tension (CT) specimens in order to obtain fatigue material properties of the C75 steel, from which the joints were manufactured. The details of these tests are set out in Appendix I.

As previously mentioned, it is important that the correct make-up torque is applied to the threaded connection. As shown in Fig 4.15, the application of a torque on the VAM joint will impose a mean compressive stress in the region of the critically

loaded teeth of the box, thus protecting it from tensile loading. The pin therefore becomes the weakest member. It was decided to try to assess the extent of the applied torque on the pin, by strain gauging the inside circumference. The gauges measure the strains due to the torque induced preload within the pin as it forces itself against the shoulder of the box.

Six "Three-Element Rectangular Rosette" strain gauges were put on the inside surface of the pin, the positions and orientations of which are shown in Fig 4.16. Several strain scans were made during the make-up torquing. The intervals at which strain measurements were taken are shown in Fig 4.17 as torque versus pin revolutions (the box being held) from the point where the connection was "hand tight".

For every scan of each gauge, principal strains ε_x and ε_y were calculated from a Mohr's strain circle. The strains ε_x and ε_y correspond to longitudinal (Fig 4.18) and circumferential (Fig 4.19) strains respectively.

It can be clearly seen from these results that the effect of preload is negligible in the vicinity of the sixteenth thread, contrary to the relatively high strain values recorded at the second thread from the free end of the pin. It can be concluded therefore that the direct effect of preload in the pin's critical tooth can be neglected for this joint, providing the correct torque is applied, i.e. preload will effect the overall load distribution within the connection and is taken account of by the overall stress analysis. However, it is assumed that this is its only effect on the critical pin tooth.

From the longitudinal strain results, axial stress hence load was calculated. These are compared in Fig 4.20 with the theoretical solution given by the equation (4.5), the derivation of which is set out in Appendix II.

$$P_t = \frac{2M_t}{d_m}\left(\frac{l + \pi\mu d_m \sec\theta}{\pi d_m - \mu l \sec\theta} + \frac{\mu_c d_c}{d_m}\right)^{-1} \qquad (4.5)$$

where:

P_t = Induced Preload
M_t = Make-up Torque
d_m = Mean diameter of thread
d_c = Mean diameter of pin face
μ = Coefficient of friction between threads
μ_c = Coefficient of friction at the pin and box shoulder
l = Pitch
θ = Flank angle

4.3 Fatigue Tests of Drill String Connections

Drill strings are another engineering application where threaded fasteners are used under dynamic loading conditions. These strings are continuous assemblies of pipes, collars, ancillary equipment and a drill bit. The drill pipes and collars are normally supplied in approximately thirty foot lengths, tools in series can often be much shorter. It is not uncommon for onshore oil and gas drilled wells to exceed ten thousand feet deep, implying more than four hundred threaded connections in the entire string assemblage for each well. Offshore drilling platforms can be over one thousand feet above the sedimentary basin, increasing the number of connections required to penetrate the reservoirs.

Normal tools used in a typical string other than the end drilling bit are hole enlargers, reamers and stabilisers for directional drilling. Drilling muds are continuously pumped through the string at pressures of three to four thousand pounds per square inch. These travel through the drill bit and carry up the bored rock and silt material to the surface via the outside of the assembly. After a certain depth is drilled (depending upon boring medium), the hole is encased with a steel and cement liner. A drilling liner is another casing string which accompanies the drill string down the hole as drilling is preformed. Its function is to provide isolation of the injected mud from porous media. For shallow wells the entire string is driven (rotated) at the surface, however for deeper wells it is usually advantageous to deploy down hole motors to prevent "wind up" contributing to torsional failure. The speed of rotation

again depends upon the drilling medium and drill bits. At low speeds (less than sixty RPM) the string may stick to the hole sides (slip sticking) producing a rapid unwinding. Normal rotating speeds range between eighty and two hundred RPM.

Axial compressive cyclic loads are normally induced by the manually operated tensioners which maintain the required weight on the bit (WOB). For floating drilling vessels, wave motion may cause substantial fluctuations in cyclic and bending loads along the string, however these are normally mechanically compensated. During the drilling process, the entire string may be removed and disassembled for various reasons. This will induce relatively low cyclic large tensile stresses due to the sheer weight of the string.

To summarise, the main loading modes on the threaded fasteners are:

(i) Compressive axial (high cycle)
(ii) Tensile axial (low cycle)
(iii) Bending (high cycle)
(iv) Torsional (high cycle)
(v) Pressure (high cycle)
(vi) Preload due to make-up torque (low cycle)

Material used for the string depends upon a variety of factors. Usually a high strength steel is used. Drill pipes have friction welded threaded connections thus limiting the maximum permissible carbon equivalent. However, for fatigue resistance a certain amount of ductility is advantageous. The material should be able to resist the corrosive drilling mud and in the case of sour wells, stress corrosion cracking. Another criterion is that for directional drilling, the various gyro and directional probes used require a non-magnetic material for accurate results. These are generally austenitic stainless steels.

There are many problems associated with predicting the fatigue endurance of drill string connections. These primarily result from the inability to define the actual loading conditions as each drilling process is unique in terms of drilling medium, direction and manual involvement.

Lubinski [4.14] defined the maximum permissible Dog-Legs in rotary boreholes to prevent static failure and [4.15] described a cumulative fatigue damage approach using S-N curves and a Miner's rule. However he did not identify the threaded fastener as being a critical section, his whole analysis was concerned with drill pipe. He later extended his analysis to maximum permissible horizontal motions of floating drilling vessels [4.16]. Zeren [4.17] did a similar analysis but took the distance between joints into account and found that by adding "protectors" (thickening sections) between joints, decreased the fatigue damage at Dog-Legs . Chen [4.18] used a finite element analysis to compare published fatigue threaded fastener results and recommended the use of microalloyed steels to resist fatigue initiation. Burgess *et al.* [4.19] carried out a useful study of Drill String vibration and pointed out that in deviated well drilling, less fatigue failures occurred due to damping of vibrations at stabilisers. Dale [4.20] conducted several full scale rotating-bending fatigue tests and derived parametric equations for fatigue propagation of different connection types. He suggested that fatigue propagation accounted for fifty percent of the total fatigue life. However he does not state what quantitative non-destructive method he used to detect the initial cracks of depth 0.05".

Gensmer [4.21] identified the proximity of the internal taper and its length to the tool joint as a critical fatigue failure region. Tsukano *et al.* [4.22] again looked at the internal upset and conducted extensive rotating bending fatigue tests and finite element analyses on drill pipe. The object of the fatigue tests was to identify the crack initiation sites and not to provide quantitative fatigue test results. Specimens failed in the pipe body and at the pipe-tool joint transition.

This brief review shows how limited the fatigue analysis has been in the area of drill string failure. Dale [4.23] reported that inspection techniques had never

conclusively found fatigue cracks in a study of thirty-three drill pipe fatigue failures over a fifteen month period. This points to the need for comprehensive fatigue evaluation of drill strings and improved inspection methods and philosophy.

The following sections report the fatigue tests of drill collar threaded connections.

4.3.1 Test and Specimen Details

The joints tested were of two different materials and two different thread forms. The materials used were non-magnetic "Staballoy AG 17" [4.24] steel and AISI 4145H steel. Typical compositions and mechanical properties of these steels are set out in Tables 4.4 and 4.5. Both thread forms API NC50 and API $6^{5}/_{8}$" Reg are modified 'V' form threads with truncated crests and rounded roots (Fig 4.21 and Table 4.6). Pressure seals are not made on the threads as these are designed to accommodate excess thread compound (dope), foreign matter and thread wear. These rotary shoulder connections make a pressure seal by screwing the shoulders together to the recommended torque, making the pin as strong as the box under static bending loads.

The AISI 4145H threads were treated with an anti-gall solution of iron manganese phosphate. This acts as a lubricant separating the metal surfaces during initial make-up and assists in holding the dope in position whilst torquing-up the connection. The non-magnetic AG 17 steel joints were treated with a solution of phosphoric acid and a catalyst, a process known as bondarising, to provide an anti-gall coating to the threads. The lubricant (dope) used was "Koper-kote" [4.25], a commercially available powdered copper-zinc compound. Before the joints were made-up, the connections were steam cleaned, degreased using solvents and rough edges deburred using a fine round file.

All joints tested were newly manufactured, therefore the connections were "walked in" as recommended by the manufacturers [4.26]. This involves making-up the connection to the recommended torque, breaking-out and inspecting for damage, finally when satisfied the threads are without blemish,

the joint is relubricated and made-up to the approved torque. The connections were inspected using MPI (not the AG17) then transported to a commercial drilling service yard, where they were cleaned, gauged and made-up. Gauging was in accordance with API specification 7 [4.27].

The make-up torque was applied by restraining the pin or box section in a pneumatically activated cradle and applying the torque to its mating section. This torque was achieved by engaging a hydraulic jack (mounted in a trunnion) to the end of the tong which was self locking to the drill collar. This perpendicular force multiplied by the effective tong arm length applies an accurate and controllable torque. Joint break-out was achieved in a similar manner.

Two types of fatigue tests were conducted, i.e. cyclic axial tension tests and rotating bend tests. The axial tests were conducted on an Instron Servo-hydraulic $\pm$ 2.5 MN test machine (Fig 4.22). This had a built in load cell connected to the servo control loop which maintained constant amplitude loading, regardless of the axial displacement. Cycle counting was carried out on line with the built in sinusoidal function generator. However, a back-up electro-mechanical counter was also used. The rotating bend tests were conducted on a specially built test rig shown in Fig 4.23. The collar lay in the bearings of the two end mountings which were structurally fixed to the floor. The centre two bearings applied upward normal forces to the collar via two 100 kN hydraulic jacks acting on the bearing mountings and restrained against the floor. This created a four point bending situation, where the collar between the centre bearings was subjected to a constant bending moment. The collar was connected via a universal coupling to a 14 kW variable frequency electric motor which provided fully reversed cyclic stressing of the collar connection (R ratio of -1).

The hydraulic jacks were calibrated against the load cell from the commercial fatigue test rig used for the axial tests, the results of which can be seen in Fig 4.24.

The crack propagation was monitored using a beach marking technique [4.28], which could be evaluated on inspection of the fracture surface.

4.3.2 Experimental Stress Analysis of Test Specimens

Experimental stress analysis of threaded connections is difficult and limited as the main areas of interest (thread fillet radii) are inaccessible once the connection is made. A useful method of evaluating the magnitude of the surface stress in a member is to measure the local strain or deformation. The most common type of strain gauge used is based on the electrical resistance method. This works on the principle that the change in electrical resistance of a wire is directly proportional to its extension. Strains in different planes can be measured and analysed using Mohr's strain circle to give principal strains, hence principal stresses. However, it is possible to strain gauge areas of the pipe wall opposite the connection. For this study it was decided to apply electrical resistance strain gauges at various positions on the outside surface of the drill collar. Because the bores of the test specimens were so small, application of strain gauges on the inside surface is a highly specialised operation and was considered futile as the pin wall thicknesses were relatively large. Two test specimens were analysed:

a) axial test: API $6^{5}/_{8}$" Reg, OD $7^{1}/_{2}$", Bore $3^{1}/_{4}$" with bore back box and stress relief groove pin.

b) rotating bend test: API $6^{5}/_{8}$" Reg, OD $7^{1}/_{2}$", Bore $3^{1}/_{4}$" with bore back box and stress relief groove pin.

The aims of the axial test stress analysis were:

(i) To validate axiality of the loading and calibration of the load cell.

(ii) To detect any opening at the rotary shoulder faces (i.e. overcoming of the preload / applied torque).

(iii) To provide remote values of stress for possible future comparison with the finite element analysis results of the load distribution within the box.

The aim of the rotating bend test stress analysis was purely to validate the calibration of the fatigue test rig. Sixteen "Three-Element Rectangular Rosette" strain gauges were fixed to the outside surface of the axial test specimen. The positions of these are shown in Fig 4.25. The two pairs of eight gauges were placed directly opposite each other (0° and 180°) in order to test the axiality of the applied load through the fixing grips.

Gauges [1, 8, 9, 16] were remote control sensors. Gauges [2, 3, 10, 11] were placed so as to give the membrane stress opposite points in the box wall. Gauges [4, 5, 6, 7, 12, 13, 14, 15] were designed to give an indication into the behaviour of the rotary shoulder interface under applied axial loading.

The positions of the eight strain gauges fixed to the outside surface of the rotating bending test specimen are shown in Fig 4.26. In both cases the specimens were loaded to the maximum fatigue test load pausing at suitable intervals to measure strains at each channel. The strain gauges were connected to a 192 channel solatron integrated measurement system controlled by a PDP 11-23 computer. The strain results were collected and stored on disk. These strains were then analysed giving principal and shear stresses using Mohr's stress circle. In all cases the results that follow show the maximum and minimum principal stresses corresponding to longitudinal and circumferential stresses respectively. Also dashed lines are the best fit lines in a least-squares sense and solid lines are these corrected to intersect at zero strain (stress) corresponding to zero applied load.

Figs 4.27-4.30 show the results of the axial test. Fig 4.27 plots the maximum principal stress of the remote gauges [1, 8, 9, 16] against the applied axial load. The corrected results are within 4% of those expected from theory. Fig 4.28 shows the results of intermediate box gauges [2, 3, 10]. These show expectedly higher stresses due to the reduction in section thickness, however results from

gauges [2, 10] are indistinguishable from gauge [3] indicating the insensitivity of strain measurement along the connection through the wall thickness. Gauge [11] gave inconsistent unstable strains and its results were disregarded. Figs 4.29 and 4.30 show the strain results of gauges [5, 12, 13, 14, 15] at the shoulder interface. Stress is sustained throughout, indicating no opening of shoulder faces, however, Fig 4.30 shows an equally high negative circumferential stress on loading in this region, suggesting perhaps relief of a bulging due to the high make-up torque. All results indicate the load was being applied axially. Fig 4.31 shows the results of the rotating bend test. These are consistent with theoretical predictions from simple beam theory, but besides verification of the test rig calibration, they reveal little.

4.3.3 Axial Test Results

Axial Test 1: **API NC50, OD $6^1/_2$", Bore $2^1/_2$", standard pin & box. AISI 4145H steel.**

This specimen was tested with the joint being hand tight. No make-up torque was applied at any stage of the joint's life. The applied load range was initially 698 kN, R ratio being 0.02, at a frequency of 4 Hz.

The cycling was interrupted periodically and beach marked at a load range of 180 kN, R ratio of 0.58, and frequency of 8 Hz. It was possible during this test (being untorqued) to inspect the pin using MPI. This was carried out twice during testing. Circumferential cracks were apparent in the thread root of the last fully engaged threads and with the second inspection indications were also seen at the first and second engaged threads. The applied cyclic load was then (after 4.67×10^6 cycles) raised to 1043 kN, R ratio of 0.03 and frequency of 2.5 Hz. At this elevated load some of the bolts holding the specimen into the test rig failed. This would have effected the axiality of loading. The specimen failed at the first box thread after 5.4×10^5 cycles at the higher loading. Failure for all tests was defined as a through crack. The box was sectioned and split open after cooling in liquid

nitrogen. Three beach marks could be clearly seen. The two occasions where the joint was split for inspection could be identified, also the point where bolt failure occurred nearing the end of the test produced a bench mark. Three other intended marks were found after a microscopic inspection.

The cracks on the mating pin thread at the box failure site could be explained by the above normal deformation of the corresponding box threads due to the presence of the fatal crack. The crack growth data is shown in Fig 4.32.

Axial Test 2: **API NC50, OD $6^1/_2$", Bore $3^1/_4$", standard pin & box. AISI 4145H steel.**

This specimen was walked-in and torqued to its recommended optimum value of 28,000 ft lbs. The cyclic load range was 776 kN, R ratio of 0.05, and frequency 4 Hz throughout the test. Beach marking was made periodically at a load range of 155 kN, R ratio of 0.8 and a frequency of 8 Hz. The connection was not broken-out at any stage during fatigue testing. The box failed once more at the first engaged thread after 4.13×10^6 cycles. Fig 4.33 shows the crack growth data.

Axial Test 3(a): **API $6^5/_8$" Reg, OD $7^1/_2$", Bore $2^{13}/_{16}$", bore back box & stress relief groove pin. AISI 4145H steel.**

The joint was made to a torque of 60,000 ft lbs and the applied nominal stress range was 34 MPa. The test was conducted at an R ratio of 0.062 and a frequency of 2.64 Hz. The cycling was interrupted periodically and beach marked. The testing was continued for seven million cycles without apparent cracking.

The torque on the joint was broken and the pin and box were steam cleaned and degreased. An inspection was conducted on the pin using the magnetic particle

inspection (MPI) technique. The pin was inspected using the Ardrox AC electromagnetic yoke with fluorescent magnetic ink. No evidence of fatigue cracking was found. The box was inspected using the DC electromagnetic yoke with fluorescent magnetic ink. Again no evidence of fatigue cracking was found.

A further inspection method was employed to investigate possible fatigue cracking in the box side of the connection. The Alternating Current Field Measurement Method (ACFM) was used. The inspection system is based on the principle of non-contacting ACFM. This method has been developed from the Alternating Current Potential Difference (ACPD) technique, an inspection method capable of both crack detection and sizing which has been used extensively on a wide variety of geometries. In particular it has proved successful for the inspection of threads in the aircraft and nuclear industries. The ACFM technique relies on the fact that when an alternating current is passed through a conductor, the electric current flows in a thin skin within the surface region of the component, with an associated magnetic field just outside that component, the current flow is disturbed by the presence of the defect leading to a corresponding disturbance of the magnetic field adjacent to the component. The inspection technique relies on the detection of magnetic field disturbances at the thread root, flank or crown and the theoretical interpretation of the data in terms of defect size. The probes used in the inspection process have been designed to fit the thread form. The system requires no prior calibration. The complete system comprises of an IBM PC, crack microgauge [4.11] and a hand held probe with the correct thread form. A $6^{5}/_{8}$" Reg box probe was used to scan the threads. No crack indications were found. The fatigue result of the test was deemed a runout.

Axial Test 3(b): **API $6^5/_8$" Reg, OD $7^1/_2$", Bore $2^{13}/_{16}$", bore back box & stress relief groove pin. AISI 4145H steel.**

This specimen (deemed a runout in test 3(a)) was fatigue tested with the joint hand tight and no applied torque. The applied nominal stress range was 49 MPa. The test was conducted at an R ratio of 0.04 and a frequency of 1.5 Hz. Beach marking was at intervals of 3.0×10^5 cycles. The box failed after 9.47×10^5. The through crack surface was revealed after sectioning the failed region and breaking open the crack whilst cooled below brittle transition using liquid nitrogen. The crack had grown from the 7th thread root and started at a right angle to the thread flank, i.e. 30° to the taper. All the loaded flanks were badly pitted, suggesting perhaps a degree of fretting occurred. Several crest cracks were clearly visible on non critical teeth. The beach mark due to untorquing the joint was clearly apparent, showing that a 7mm deep crack had grown during test 3(a). An MPI inspection on the pin shows two cracks on the second thread root 58mm and 47mm long respectively. These are separated by a 49mm length. The cracks were preserved intact as they are excellent examples for inspection validation purposes. The crack growth data is shown plotted in Fig 4.34.

Axial Test 4(a): **API $6^5/_8$" Reg, OD $7^1/_2$", Bore $3^1/_4$", bore back box & stress relief groove pin. AISI 4145H steel.**

The specimen was walked-in and torqued to its recommended optimum value of 48,000 ft lbs. The cyclic nominal stress range was 44.8 MPa. The R ratio was 0.066 and the test frequency was 2.0 Hz. This test was stopped as the joint fractured at the pin connection to the test frame after cycling for 6.3 million cycles. The result of this test is also a runout.

Axial Test 4(b): **API $6^5/_8$" Reg, OD $7^1/_2$", Bore $3^1/_4$", bore back box & stress relief groove pin. AISI 4145H steel.**

The specimen which was tested and deemed a runout in test 4(a) had its end connection remachined without breaking the makeup torque and was replaced into the fatigue test rig. The cyclic load applied was 1340 kN giving a nominal stress of 57.9 MPa. The test lasted for 4.2×10^5 cycles before the customised end connection failed. The joint was broken and inspected using the non-contacting ACFM technique. This revealed nothing but a small machining score was noted during a visual inspection. The box was sectioned, cooled and subjected to sharp impacts in order that any flaws present be exposed. No cracks were found. An MPI inspection on the pin was negative.

Axial Test 5: **API NC50, OD $6^1/_2$", Bore $2^{13}/_{16}$", bore back box & stress relief groove pin. Staballoy AG17 steel.**

This non-magnetic specimen was walked-in and torqued to 30,000 ft lbs using the same procedure as for the magnetic steel specimens. The test was conducted at 1.84 Hz, with an applied load range of 1000kN. Beach marking was at intervals of 3.0×10^5 cycles. A through crack was detected having grown from the 11^{th} tooth root in the box after 1.55×10^6 cycles. Dye Penetrant inspection on the pin showed no apparent cracking. Fig 4.35 shows the fatigue crack growth data.

Axial Test 6: **API NC50, OD $6^1/_2$", Bore $3^1/_4$", standard pin & box. Staballoy AG17 steel.**

The second non-magnetic specimen was torqued to 28,000 ft lbs. The nominal stress range was 40.5 MPa. Beach marking was carried out at intervals of 3.0×10^5 cycles. Testing continued for five million cycles without cracking. This result can be regarded as a runout. The test was restarted assuming no damage,

at an applied load range of 1061kN. Testing continued for 1.96 x 10^6 cycles at which stage a fixing connection failed. Dye Penetrant inspection on the pin revealed nothing. The box was inspected using ACFM which revealed possible defects on teeth 11 and 12, and clearly cracks on teeth 13 and 14. This was then sectioned as before, however, the AG17 steel specimens were not cooled in liquid nitrogen as it is a face centred cubic crystalline structure which does not display brittle temperature transition behaviour. No cracks were found.

4.3.4 Rotating Bend Test Results

Rotating Bend Test 1: API NC50, OD $6^1/_2$", Bore $2^1/_2$", standard pin & box. AISI 4145H steel.

Applied torque was 30,000 ft lbs, after walking-in. The applied bending moment was 19.7 kNm at a rotational speed of 240 RPM. Beach marking was carried out periodically for 2.5 x 10^4 cycles at a bending moment of 22.4 kNm. Failure occurred rapidly after 5.78 x 10^6 cycles, the crack "ripping" around the entire box circumference in one revolution. The crack growth data is shown in Fig 4.36.

Rotating Bend Test 2: API NC50, OD $6^1/_2$", Bore $3^1/_4$", standard pin & box. AISI 4145H steel.

This specimen was again walked-in and torqued to 28,000 ft lbs. The applied bending moment was 25.5 kNm at 240 RPM. Beach marking was conducted at 22.39 kNm for 4.4 x 10^5 cycles at 190 RPM. Again failure resulted in the total fracture of the box after 1.24 x 10^6 cycles. Fig 4.37 shows the crack growth curve.

Rotating Bend Test 3: API NC50, OD $6^{1}/_{2}$", Bore $2^{13}/_{16}$", bore back box & stress relief groove pin. Staballoy AG17 steel.

The specimen was made-up to a torque level of 32,000 ft lbs. The fatigue test was carried out at a moment amplitude of 27.8 kNm. The test frequency was 2.75 Hz. Beach marking was conducted at a moment amplitude of 21.2 kNm and a frequency of 4.0 Hz. Failure resulted in the total fracture of the box after 1.33 million cycles. Crack initiation occurred in the 11^{th} root of the bore back box region. Fig 4.38 shows the crack growth results.

Rotating Bend Test 4: API NC50, OD $6^{1}/_{2}$", Bore $3^{1}/_{4}$", standard pin & box connection. Staballoy AG17 steel.

This specimen was walked-in and torqued to 30,000 ft lbs. It was anticipated that the standard pin and box connection in this test would have a higher SCF value than for bend test 3 which featured a connection with bore back box and stress relief groove pin. Therefore, the fatigue test was conducted at a lower moment amplitude of 21.2 kNm. Beach marking was conducted at a moment amplitude of 18.4 kNm. The test was stopped after 2.4×10^{6} cycles due to the test rig becoming unstable. This was found to be due to a substantial crack in the pin. The connection still maintained a high residual torque level and required 15,000 ft lbs to break it open. The crack was through wall, initiated at the first loaded thread. The crack growth is shown plotted in Fig 4.39.

Rotating Bend Test 5: API $6^{5}/_{8}$" Reg, OD $7^{1}/_{2}$", Bore $3^{1}/_{4}$", bore back box & stress relief groove pin. AISI 4145H steel.

This specimen was walked-in and torqued to a level of 48,000 ft lbs. The test rig had to be modified to accommodate the larger outside diameters of the remaining two connections. The fatigue testing was carried out at a moment

level of 38.8 kNm. The frequency for this test was increased to 3.94 Hz. Beach marking was carried out at approximately 24 hour intervals at a moment amplitude of 21.2 kNm. After 4.92 x 10^6 cycles no evidence of crack growth was visible and the test rig continued to function in a stable manner. The moment amplitude was therefore increased to 53.5 kNm with the beach marking procedure continued as before. The test was stopped after 6.7 x 10^6 cycles as a sizeable crack in the pin had made the test unstable. The connection was broken open, the breaking torque required was 22,000 ft lbs. Initiation had occurred at the first root and a through wall crack was evident. The crack growth data is plotted in Fig 4.40.

Rotating Bend Test 6: API $6^5/_8$" Reg, OD $7^1/_2$", Bore $3^1/_4$", bore back box & stress relief groove pin. AISI 4145H steel.

The pin and box were made up to a torque level of 48,000 ft lbs. In view of the longer than expected fatigue life for the 7 $^1/_2$" x 3 $^1/_4$" connection, the moment amplitude was increased to a level aimed to produce a fatigue life of around two million cycles. The test was therefore carried out at a moment amplitude of 46.7 kNm. The test frequency was maintained at 3.94 Hz and beach marking was conducted at 21.2 kNm. A through wall crack was evident on the box side of the connection after approximately one million cycles. Initiation had occurred in the 12th root in the bore back box region. The crack appears to have progressed to the 11th root before breaking through the outside wall of the box. Fig 4.41 shows the fatigue crack growth data.

4.4 Discussion

Tables 4.7 and 4.8 summarises the axial and rotating bend test details described in the previous sections. Since the development of the tether load spectrum for this study, service data for the Hutton TLP has become available [4.13]. The tether load spectrum used for the variable amplitude tests appears to be representative of tether response for Hutton. The RAO used had slightly higher amplitudes than those

measured in service, however as the actual wave excitation spectra had higher peaks than those modelled by Pierson-Moskowitz spectra, the effect cancelled to produce quite a realistic load spectrum.

The fatigue crack growth data will be considered in the following chapter. The stress analysis results are quite interesting showing the critical dependence of preload on the coefficient of friction. Both studies showed the significant presence of circumferential stresses at the pin-box interface due to applied torque, despite the differing connection types. It is apparent that a grave area of uncertainty with threaded connections is that associated with preload. No clear consequence of the level of applied torque can be drawn from the experiments described, despite the different test scenarios where preload levels differed. A minimum preload level is most often quoted in terms of prevention of opening during service. Sometimes the critical component can be switched from pin to box (or vice versa) due to the application of preload, however, no reference has been found that associates this mechanism with a threshold level of preload. Certainly the upper bound torque level recommendations by manufacturers would appear the most concerning. Fatigue crack initiation is far more likely if high opening residual stresses exist in thread roots. These can result from over torquing and bad fitting connections. The high mean stress levels associated with over torquing may however, only become critical in corrosive environments (chapter six).

Beach marking proved highly successful in this series of tests. It must be noted that it is an alien loading sequence to most common applications in reality, and may be responsible for a degree of variation to the crack growth behaviour. Another inaccuracy of the test programme where compared to reality is the number of times a joint is made up and broken. Beach marks are quite clear on the fracture surfaces due to the breaking-making operations. Opening and making a threaded joint has an effect on crack propagation. It is well beyond the scope of this study but for future reference, fatigue tests on threaded connections under making-breaking loading solely, would give valuable insight into this grey area.

Another problem which arose during the tests was non destructive evaluation of crack depth. Most components for examination can be inspected in service or some form of crack opening load applied during inspection. Unfortunately the mean opening stress is lost when a threaded fastener is broken for inspection purposes. This makes crack detection and measurement significantly more difficult. One resolution would be an in-service inspection system where the ensuing crack can be detected and quantified from inside or outside the tube. A "thick skin", Direct Current Potential Difference (DCPD) approach may be appropriate.

4.5 Summary

Two case studies are reported. The first is the development and implementation of a typical variable amplitude load sequence on tethers for a tension leg platform. Two full scale fatigue tests were carried out on suitable connections yielding valuable crack growth data. An experimental stress analysis study was also undertaken, observing the relationship of applied torque to internal stresses within the connection.

The second application considered was that of the fatigue of threaded connections used in drill strings. A concise background to the relevant analyses and practices in the industry was reported. Six axial and six full scale rotating bend tests are reported on typical connections. Again experimental stress analysis results are discussed. The fatigue test results will be considered in the following chapter.

4.6 References

[4.1] Sopwith, D. G., "The Distribution of Load in Screw Threads", Proceedings Institution of Mechanical Engineers, vol 159, pp 373 - 383, 1948.

[4.2] Newport, A., "Stress and Fatigue Analysis of Threaded Tether Connections", Ph. D. Thesis, University College London, 1989.

[4.3] Pierson, W. J., Moskowitz, L., "A Proposed Spectral Form for Fully Developed Wind Seas Based on the Similarity Theory of SA Kitaigorodskii", J. of Geophys. Res., vol 69, no 24, 1964.

[4.4] Hutton Unit Parties, "Design and Operation of the Hutton Tension Leg Platform and Licensing of Hutton TLP Technology", Seminar October 1986.

[4.5] Patel, M. H., Witz, J. A., "On Improvements to the Design of Tension Buoyant Platforms", Proceedings of the 4th International Conference on the Behaviour of Offshore Structures, July 1985.

[4.6] Witz, J. A., University College London, Private Communication.

[4.7] Pook, L. P., Dover, W. D., "Progress in the Development of a Wave Action Standard History (WASH) for Fatigue Testing Relevant to Tubular Structures in the North Sea", ASTM Symposium on the Development of Standard Load Spectrum, 29 April 1987.

[4.8] Kam, J. C. P., "Structural Integrity of Offshore Tubular Joints Subject to Fatigue", Ph. D. Thesis, University College London, 1989.

[4.9] VAM joint, supplied by Hunting Oil-Field Services LTD, Aberdeen. (VAM is a registered Trade Mark of Vallourec.)

[4.10] Drilco Midland, Texas, "Shoulder Galling in Drill Collars", Engineering Newsletter no 1017, 5 December 1967.

[4.11] Dover, W. D., Collins, R., "Recent Advances in the Detection and Sizing of Cracks using Alternating Current Field Measurements (A.C.F.M.)", British Journal of NDT, pp 291-295, November 1980.

[4.12] Glinka, G., Kam, J. C. P., "Rainflow Counting Algorithm for Very Long Stress Histories", International Journal of Fatigue 9, no 3, pp 223-228, 1987.

[4.13] Jefferys, E. R., Conoco Inc., Private Communication.

[4.14] Lubinski, A., "Maximum Permissible Dog-Legs in Rotary Boreholes", Journal of Petroleum Technology, vol 13, 1961.

[4.15] Hansford, J. E., Lubinski, A., "Cumulative Fatigue Damage of Drill Pipe in Dog-Legs", Journal of Petroleum Technology, March 1966.

[4.16] Hansford, J. E., Lubinski, A., "Analysis of Some Factors Related to Permissible Horizontal Motions of a Floating Drilling Vessel", Society of Petroleum Engineers Journal, September 1970.

[4.17] Zeren, F., "Fatigue Limits Analysed for Drill Pipe in a Dogleg", Oil and Gas Journal, 1986.

[4.18] Chen, W-C., "Drill String Fatigue Performance", SPE/IADC, 1987.

[4.19] Burgess, T. M., McDaniel, G. L., Das, P. K., "Improving BHA Tool Reliability with Drill String Vibration Models - Field Experience and Limitations", SPE/IADC, 1987.

[4.20] Dale, B. A., "Inspection Interval Guide-lines to Reduce Drill String Failures", IADC/SPE 17207, 1988.

[4.21] Gensmer, R. P., "Field Correlation Between Internal Taper Length and Tube Failures in 4.5-in. 16.60E, IEU Drill Pipe", IADC/SPE, 1988.

[4.22] Tsukano, Y., Nishi, S., Miyoshi, H. and Sogo, Y., "Appropriate Design of Drill Pipe Internal Upset Geometry Focusing on Fatigue Property", IADC/SPE, 1988.

[4.23] Dale, B. A., Moyer, M.C., "Sensitivity and Reliability of Commercial Drill-String Inspection Services", Seventh Offshore South East Asia Conference, 1988.

[4.24] "Jessop Saville Limited" Hawke Street, Sheffield.

[4.25] Koper-kote, Product code A10195, Jet Lube UK Inc., Aberdeen.

[4.26] "Drilling Assembly Handbook", Smith International Inc., P.O. Box 60068, Houston, Texas 77205.

[4.27] API Specification 7, American Petroleum Institute, 1220 L Street, Northwest Washington, DC 20005, 37th Ed, 1990.

[4.28] Mackay, T. L. and Alperin, B. J., "Stress Intensity Factors for Fatigue Cracking in High-Strength Bolts", Eng. Fracture Mechanics, vol 21, no 2, pp 391-397, 1985.

Zeroth Moment 'M_0'	2.869 x 10^4
Second Moment 'M_2'	6.148 x 10^2
Irregularity Factor 'I'	0.8218
RMS (Zero Mean)	0.204 x 10^2
Zero Crossing Frequency	0.1464 Hz
Number of Peaks	24743
Clipping Ratio	3.44
Equivalent Stress (M = 3)	0.563 x 10^3

Table 4.1

Characteristics of the Tether Load Spectrum and its Corresponding Time Series

Chemical Composition	
Carbon	0.32%
Silicon	0.27%
Manganese	1.28%
Phosphorus	0.008%
Sulphur	0.011%
Mechanical Properties	
Yield Strength	549 MPa
Tensile Strength	686 MPa
% Elongation after Fracture (2" $\sqrt{S_0}$)	30%

Table 4.2

Chemical Composition and Mechanical Properties of API Grade 5A C75 Steel

VAM Connection No	Nominal Stress range MPa	Applied Torque kNm	R Ratio	Freq Hz	No. of cycles x 10^6
1	185.0	11.60	0.1	1.0	1.65
2	185.0	10.20	0.1	1.0	0.23
3	185.0	9.60	0.1	1.0	0.22
4	78.2	9.94[1] 7.95[2]	-	-	2.7
5	78.2	7.66	-	-	3.2

[1]Initial makeup torque

[2]Subsequent makeup torque after 0.4 x 10^6 cycles

Table 4.3

Tether Fatigue Test Details

Element	AISI 4145H	AG 17
C	0.45%	0.03%
Mn	1.01%	20.00%
Si	0.26%	0.5%
S	0.019%	0.002%
P	0.020%	0.02%
Cr	1.08%	16.50%
Ni	0.12%	0.50%
Mo	0.30%	-
N_2	-	0.5%

Table 4.4

Typical Chemical Composition of
AISI 4145H and AG17 Steels

Property	AISI 4145H	AG 17
0.2% Proof Stress	865 MPa	687.5 MPa
Tensile Strength	1005 MPa	825.0 MPa
Elongation %	16.0	20.0
Izod Impact J	87.0	60.0
Brinell Hardness	-	277
Vickers Hardness	336	-
Magnetic Permeability	-	1.005

Table 4.5

Typical Mechanical Properties of
AISI 4145H and AG17 Steels

	NC50	6 5/8" Reg
D_{cb}	4.625	5.281
D_{rG}	4.75	6.406
f_{cn}	0.056161	0.043201
F_{cn}	0.065	0.05
f_{cs}	0.056161	0.043201
F_{cs}	0.065	0.05
H	0.216005	0.216005
h_n	0.121844	0.147804
h_s	0.121844	0.147804
L_x	4.0	4.5
P	0.25	0.25
r	0.015	0.015
r_{rn}	0.038	0.025
r_{rs}	0.038	0.025
S_{rn}	0.038	0.025
S_{rs}	0.038	0.025
TPF	2.0	3.0

Dimensions are in inches

Table 4.6

Geometrical Dimensions of Drill Tool Joints
(Fig 4.21)

Test no	Connection Type	Collar Size	Applied Load Range kN	Applied Torque kNm	R Ratio	Freq Hz	No. of cycles x 10^6 /Failure	Steel
1	NC50 Standard	$6^1/_2$" x $2^1/_2$"	698 1043	0	0.02 0.03	4.0 2.5	4.67 Box 0.54	4145H
2	NC50 Standard	$6^1/_2$" x $3^1/_4$"	776	37.96	0.05	4.0	4.13 Box	4145H
3 (a)	$6^5/_8$" Reg BB & SR	$7^1/_2$" x $2^{13}/_{16}$"	835	81.35	0.062	2.64	7.0 Runout	4145H
3 (b)	$6^5/_8$" Reg BB & SR	$7^1/_2$" x $2^{13}/_{16}$"	1200	0	0.040	1.5	0.95 Box	4145H
4 (a)	$6^5/_8$" Reg BB & SR	$7^1/_2$" x $3^1/_4$"	1037	65.1	0.066	2.0	6.3 Runout	4145H
4 (b)	$6^5/_8$" Reg BB & SR	$7^1/_2$" x $3^1/_4$"	1340	65.1	0.023	1.5	0.42 none	4145H
5	NC50 BB & SR	$6^1/_2$" x $2^{13}/_{16}$"	1000	40.67	0.021	1.84	1.55 Box	AG17
6	NC50 Standard	$6^1/_2$" x $3^1/_4$"	650 1061	37.96	0.029 0.017	2.7 1.35	Runout 1.96 none	AG17

BB Bore Back

SR Stress Relief

Table 4.7

Axial Load Fatigue Test Details

Test no	Connection Type	Collar Size	Moment Amplitude kNm	Applied Torque kNm	R Ratio	Freq Hz	No. of cycles x 10^6 /Failure	Steel
1	NC50 Standard	$6^1/_2$" x $2^1/_2$"	19.73 22.39*	40.67	-1	4.0	5.78 Box	4145H
2	NC50 Standard	$6^1/_2$" x $3^1/_4$"	25.46 22.39*	37.96	-1	4.0	1.24 Box	4145H
3	NC50 BB & SR	$6^1/_2$" x $2^{13}/_{16}$"	27.8 21.2*	43.39	-1	2.75	1.3 Box	AG17
4	NC50 Standard	$6^1/_2$" x $3^1/_4$"	21.2 18.4*	40.67	-1	2.75	2.4 Pin	AG17
5	$6^5/_8$" Reg BB & SR	$7^1/_2$" x $3^1/_4$"	38.8 21.2* 53.5	65.1	-1	3.94	4.92 1.79 Pin	4145H
6	$6^5/_8$" Reg BB & SR	$7^1/_2$" x $3^1/_4$"	46.7 21.2*	65.1	-1	3.94	0.992 Box	4145H

BB Bore Back

SR Stress Relief

*Value used for beach marking

Table 4.8

Rotating Bend Fatigue Test Details

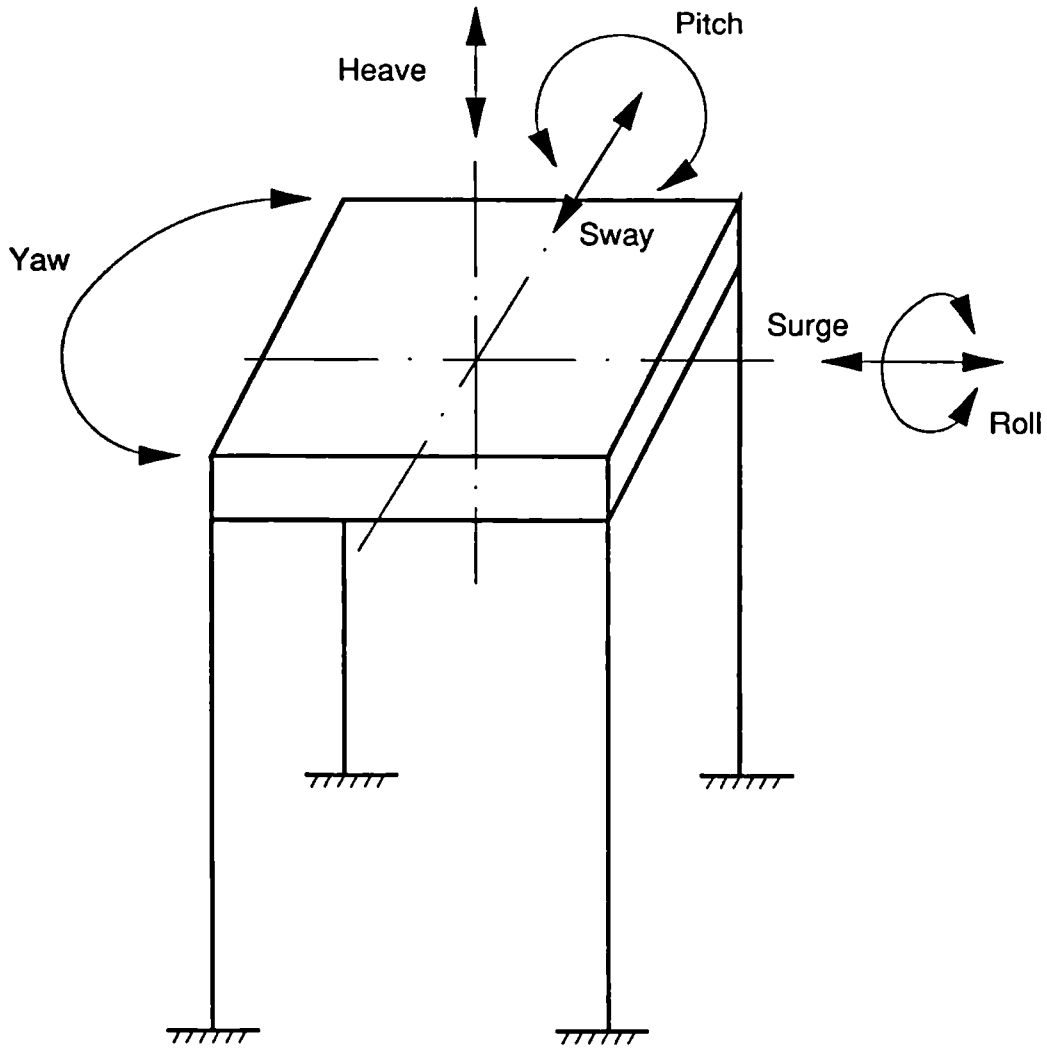

Fig 4.1

TLP Degrees of Freedom

Hourly Significant Wave Height (m)	Mean Zero Crossing Period (Sec)									
	3	4	5	6	7	8	9	10	11	12
12.0 - Max	•	•	•	•	•	•	•	•	1	•
11.5 - 12.0	•	•	•	•	•	•	•	•	•	•
11.0 - 11.5	•	•	•	•	•	•	•	0	0	•
10.5 - 11.0	•	•	•	•	•	•	•	•	•	•
10.0 - 10.5	•	•	•	•	•	•	•	•	2	•
9.5 - 10.0	•	•	•	•	0	•	•	0	1	•
9.0 - 9.5	•	•	•	•	•	•	•	1	1	•
8.5 - 9.0	•	•	•	0	•	•	0	2	•	•
8.0 - 8.5	•	•	•	•	•	•	0	1	•	•
7.5 - 8.0	•	•	•	•	0	•	1	2	•	•
7.0 - 7.5	•	•	•	0	•	0	6	1	•	•
6.5 - 7.0	•	•	•	•	0	•	7	2	1	1
6.0 - 6.5	•	•	•	•	•	1	8	2	•	•
5.5 - 6.0	•	•	0	1	1	6	7	0	•	•
5.0 - 5.5	•	•	•	1	2	14	5	4	0	•
4.5 - 5.0	•	•	•	•	4	30	13	2	•	•
4.0 - 4.5	•	•	•	0	13	30	8	2	•	•
3.5 - 4.0	•	0	0	0	32	33	8	0	•	•
3.0 - 3.5	•	•	1	8	48	26	6	•	•	•
2.5 - 3.0	•	0	9	39	58	21	•	•	•	•
2.0 - 2.5	•	0	16	122	42	2	•	•	•	•
1.5 - 2.0	•	1	58	80	23	1	•	•	•	•
1.0 - 1.5	•	12	84	39	4	•	•	•	•	•
0.5 - 1.0	0	7	19	2	•	•	•	•	•	•
0.0 - 0.5	•	•	•	•	•	•	•	•	•	•
Min - 0.0	•	•	•	•	•	•	•	•	•	•

Fig 4.2

Sample Wave Scatter Diagram
(Hutton Site from December 1985 - February 1986)

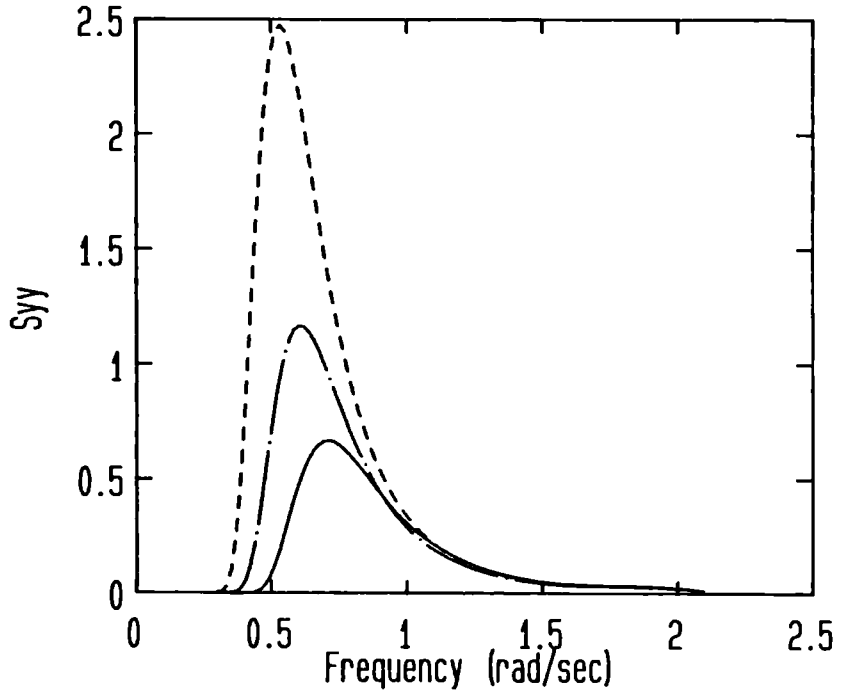

- - - - - - - - - H_s 3.75m, T_z 8sec

——·—— H_s 2.75m, T_z 7sec

———— H_s 2.25m, T_z 6sec

Fig 4.3

Pierson-Moskowitz Spectra for Different Sea States

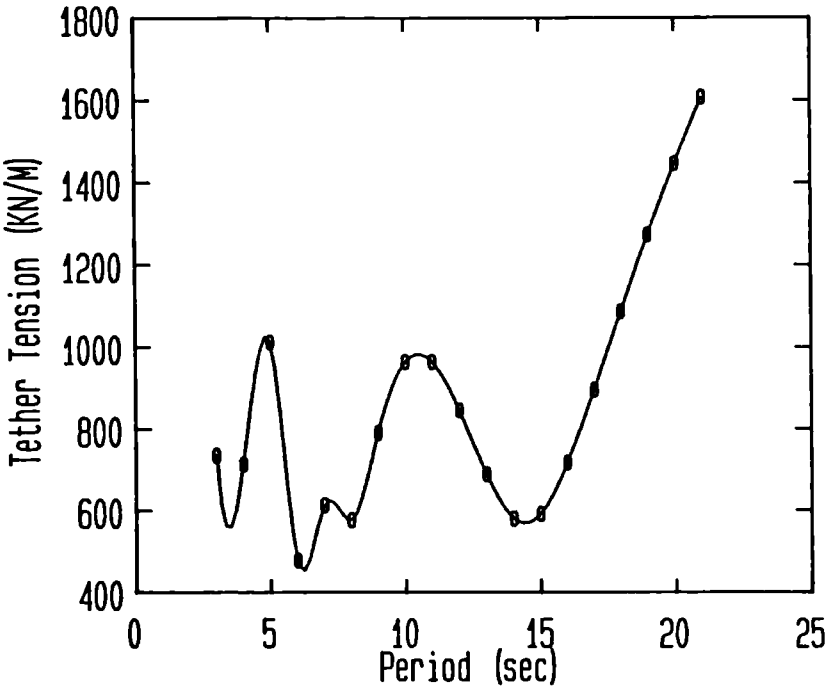

Fig 4.4

Response Amplitude Operator (RAO) in Terms of Period
for a Six Column TLP Port Bow Tether in Head Seas

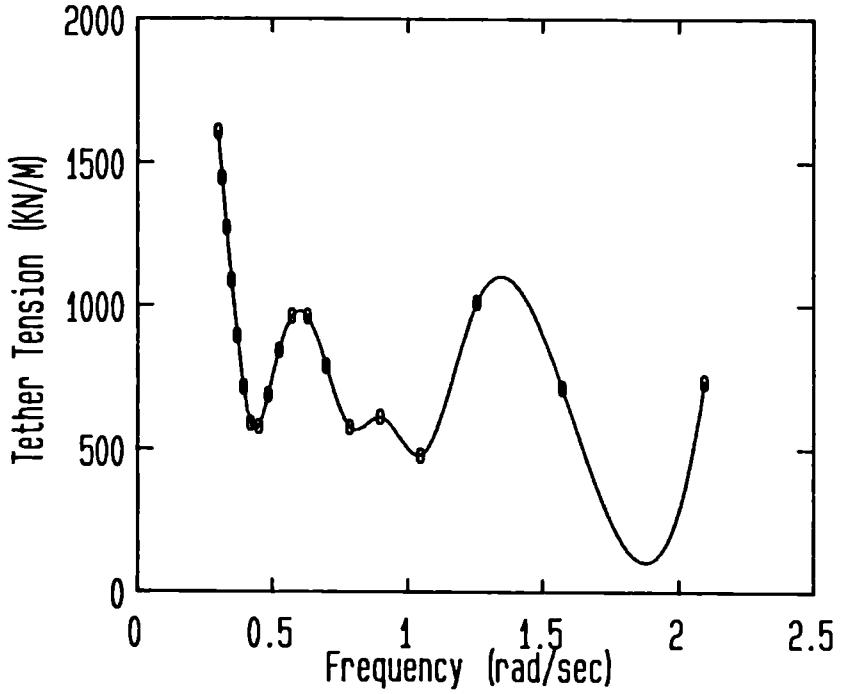

Fig 4.5

RAO in Terms of Frequency for a Six Column TLP
Port Bow Tether in Head Seas

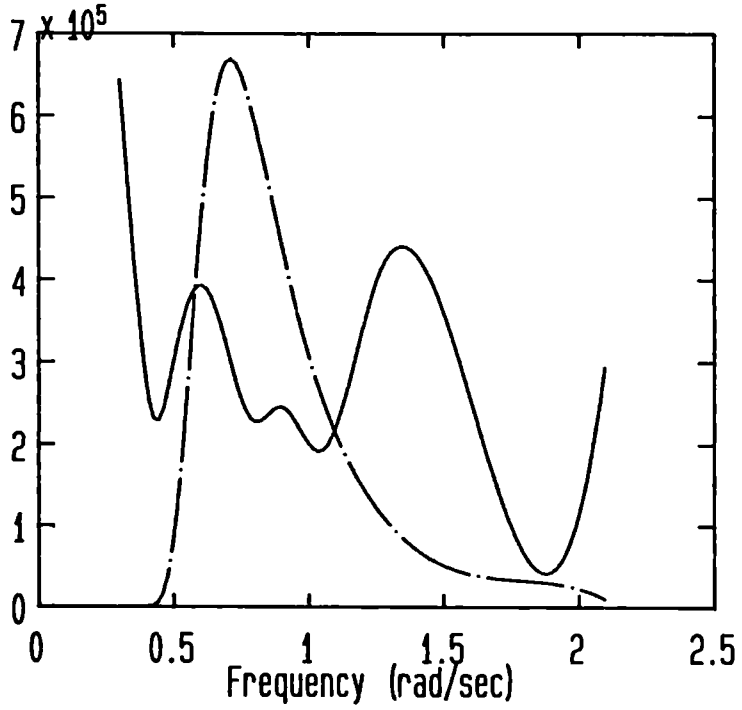

RAO

S_{yy}

Fig 4.6

RAO Superimposed on Wave Elevation Spectrum

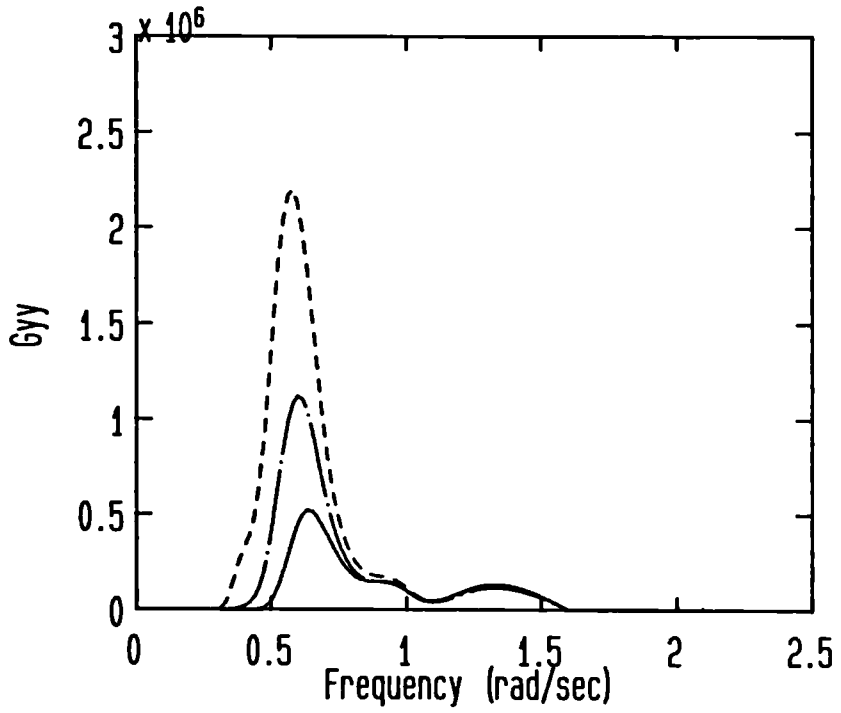

- - - - - - - - - H_s 3.75m, T_z 8sec

——·—— H_s 2.75m, T_z 7sec

———— H_s 2.25m, T_z 6sec

Fig 4.7

Load Response Spectra Excited by Different Sea States

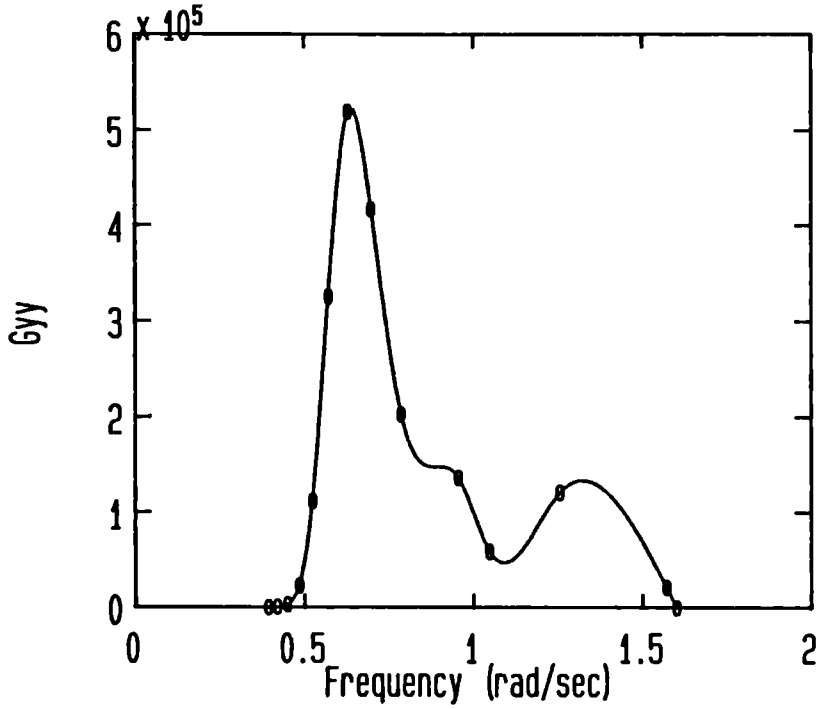

Fig 4.8

Load Response Spectrum - Excitation Sea State: H_s = 2.25m, T_z = 6 Sec

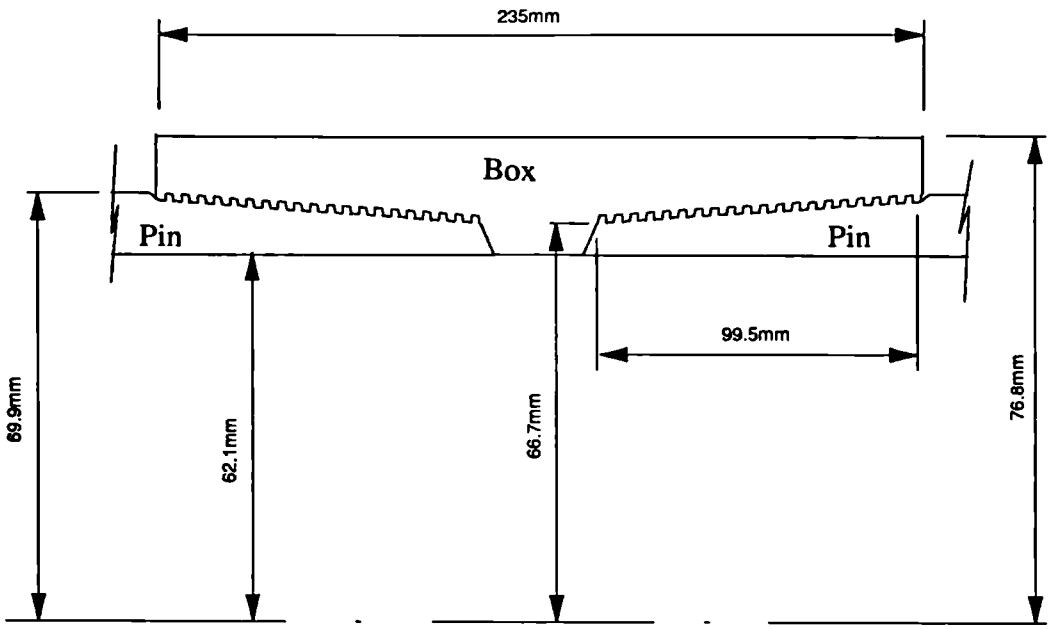

Taper	1" TPF
Pitch	5 TPI
Root Radius	0.203mm
Tooth Height	1.6mm
Tooth Flank Angle	10°

Fig 4.9

Dimensions of VAM Joint

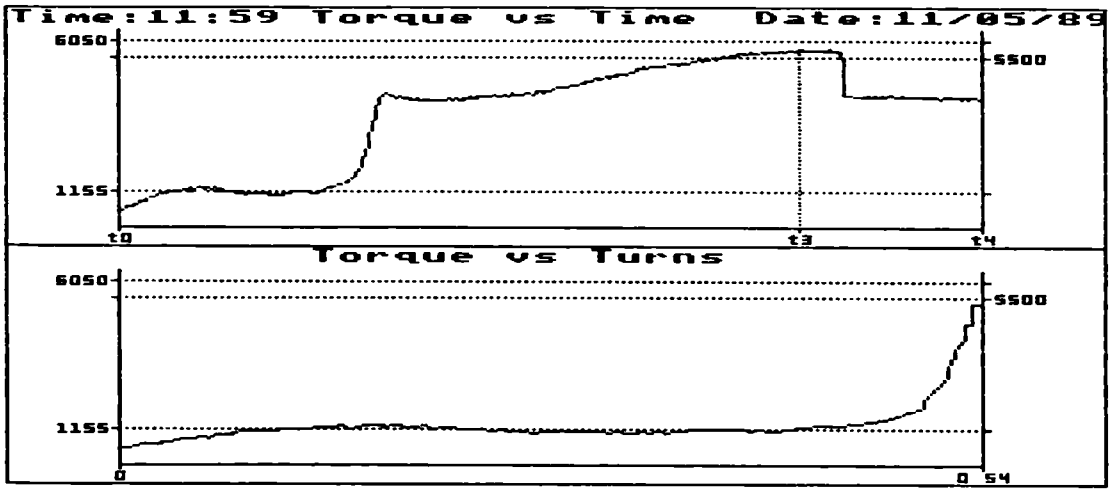

DATE: 11/05/89 TIME: 11:59
CUSTOMER: SHELL PUP/JOINTS

ORDER NO/JOB NO: 405,093
PIPE SIZE: 5.5(17)L80 N/VAM PIPE NO: 2
THREAD COMPOUND: SHELL GREASE:ALVANIA EP2

COMMENT: OPERATOR E.YEATS

MAX TORQUE: 6050 MIN TORQUE: 5500 REF TORQUE: 1155
PEAK TORQUE: 5771 MAX CLAMP PRESSURE: 6071
NO. OF TURNS FROM REF TO OPT TORQUE: 0.442
TIME RUN STARTED: 11:59:55 TIME REF REACHED: 11:59:56
TIME OPT REACHED (t3): 12:00:12 TIME RUN ENDED (t4): 12:00:17
TIME GRAPH STARTS (t0): 11:59:55

Fig 4.10

Make-up Torque Details

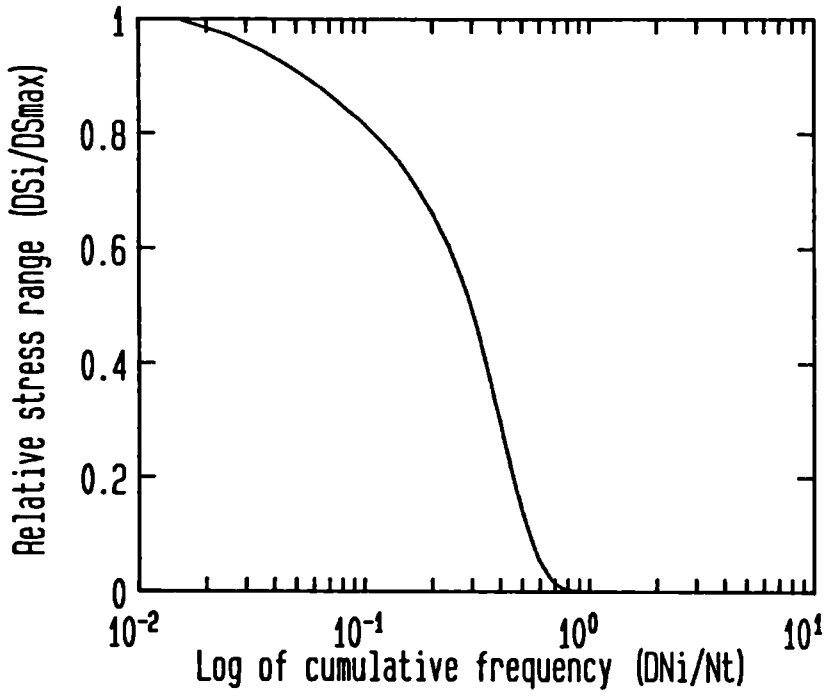

Fig 4.11

Time Series Cumulative Frequency Distribution

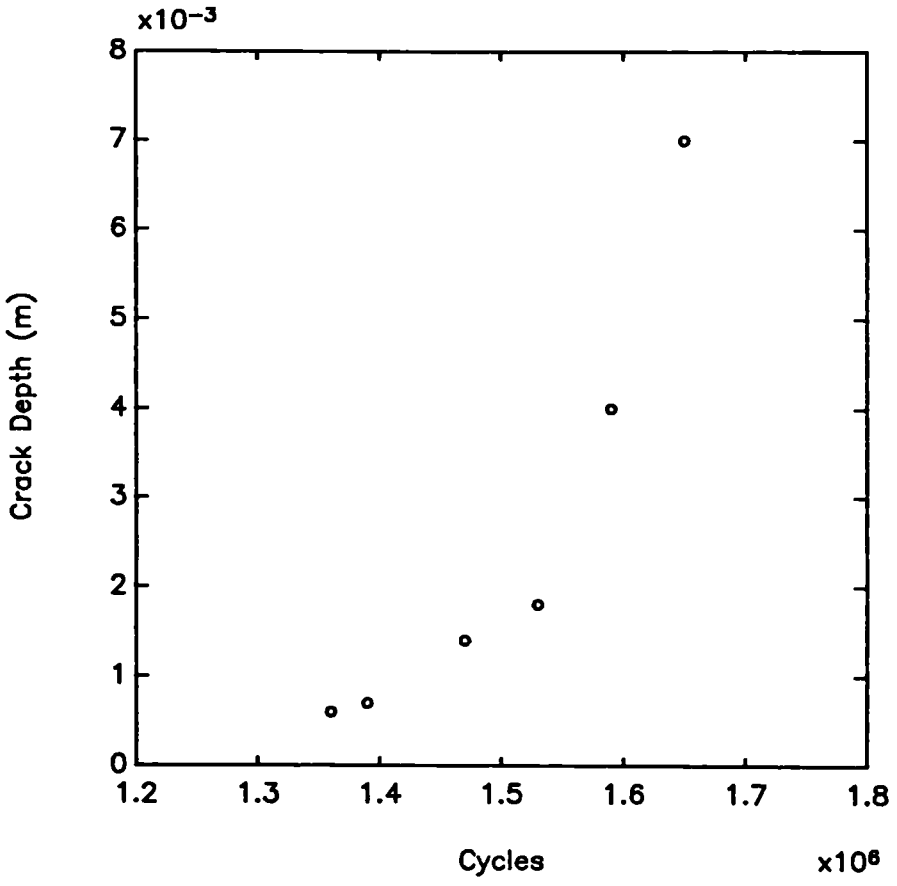

Fig 4.12

Crack Growth Data For Tether Test 1

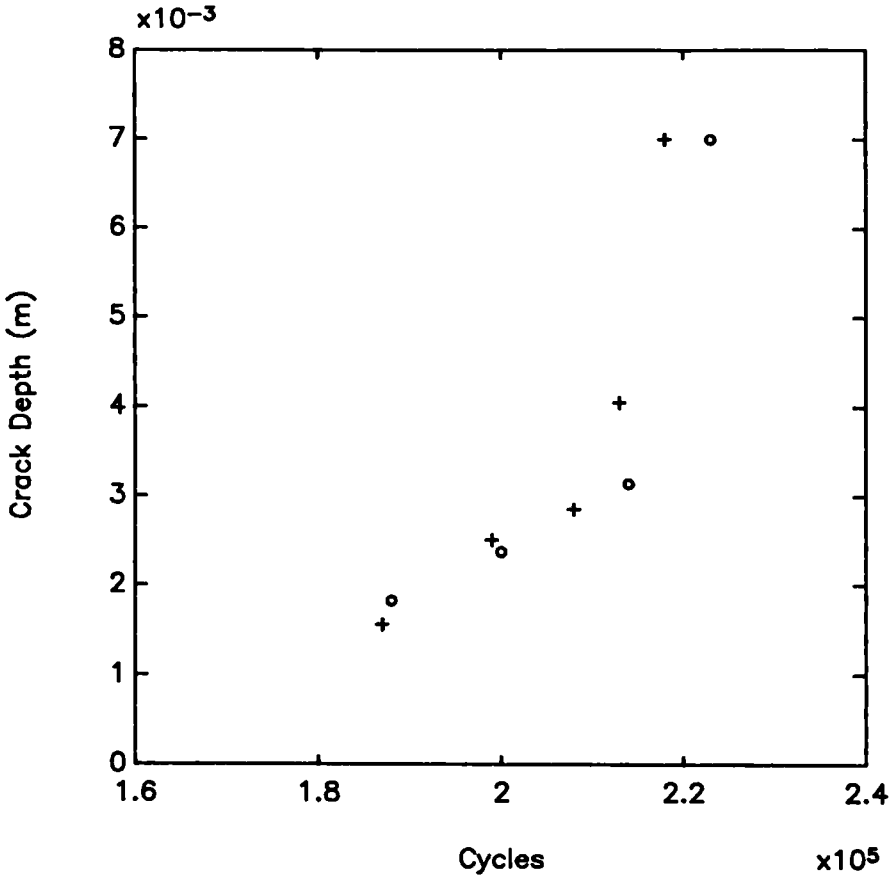

o VAM Test 2

\+ VAM Test 3

Fig 4.13

Crack Growth Data For Tether Tests 2 and 3

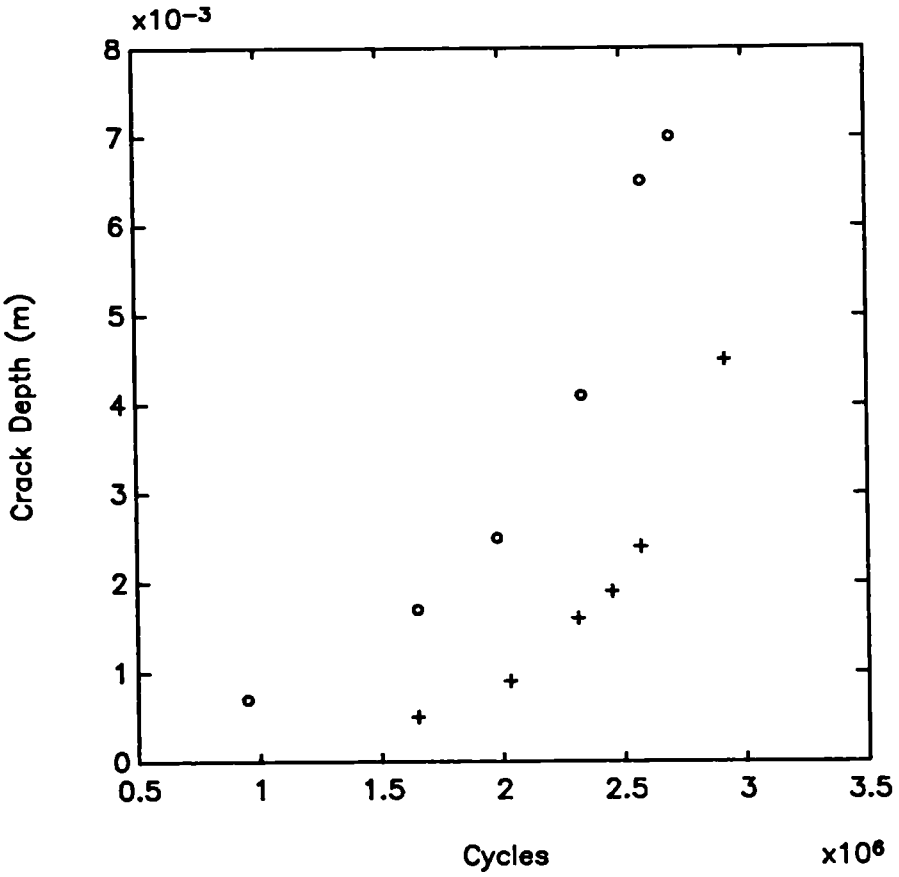

o VAM Test 4

\+ VAM Test 5

Fig 4.14

Crack Growth Data For Tether Tests 4 and 5

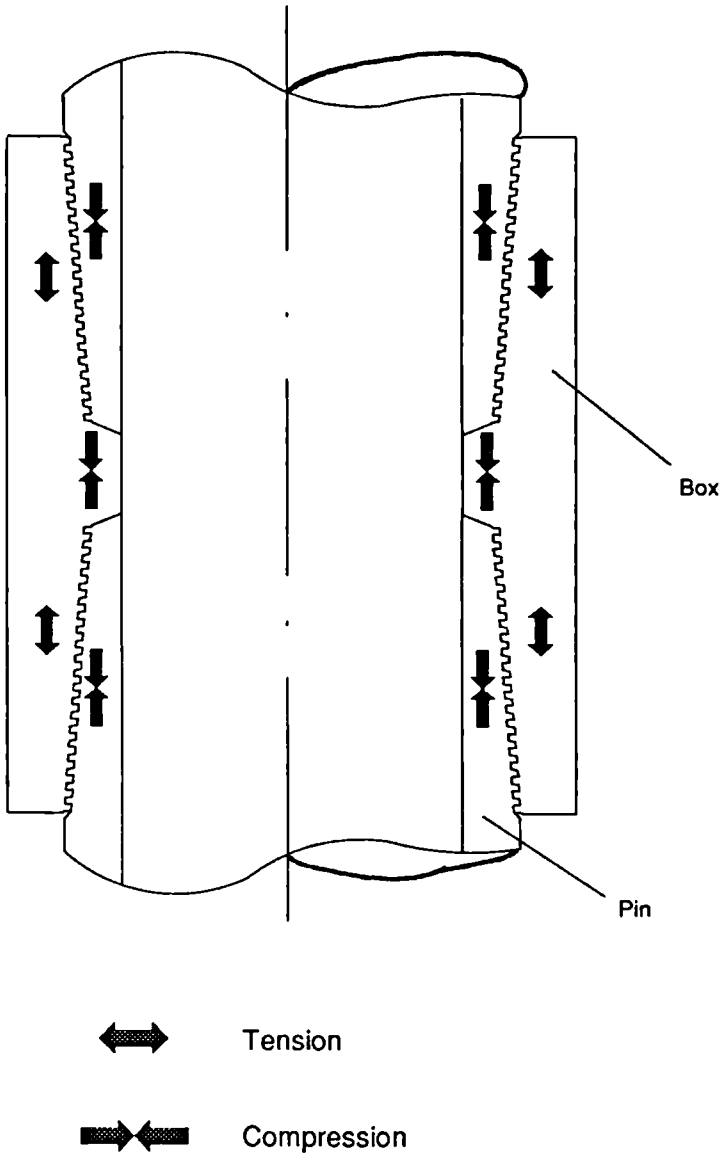

Fig 4.15

Stresses Induced in VAM Joint due to Make-up Torque

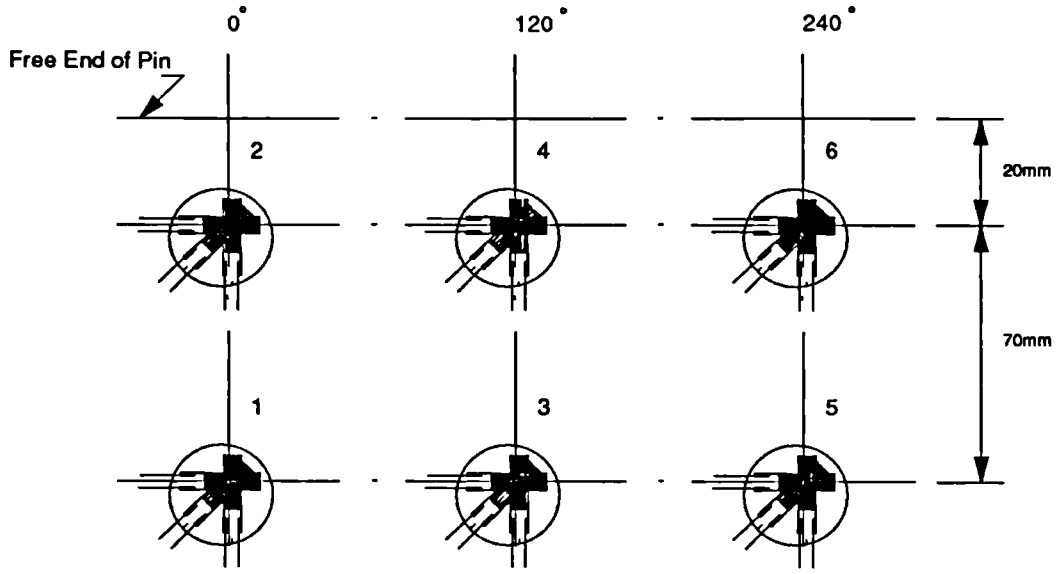

Fig 4.16

Positions of Strain Gauges

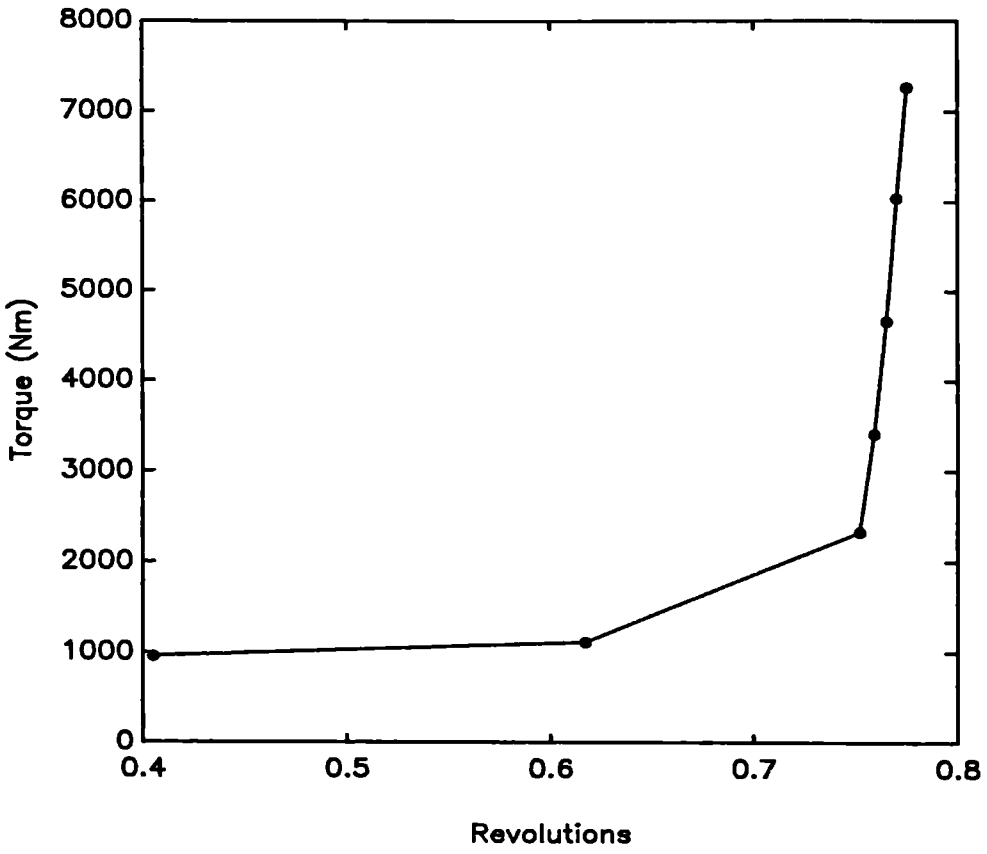

Fig 4.17

Torque Versus Revolutions Plot

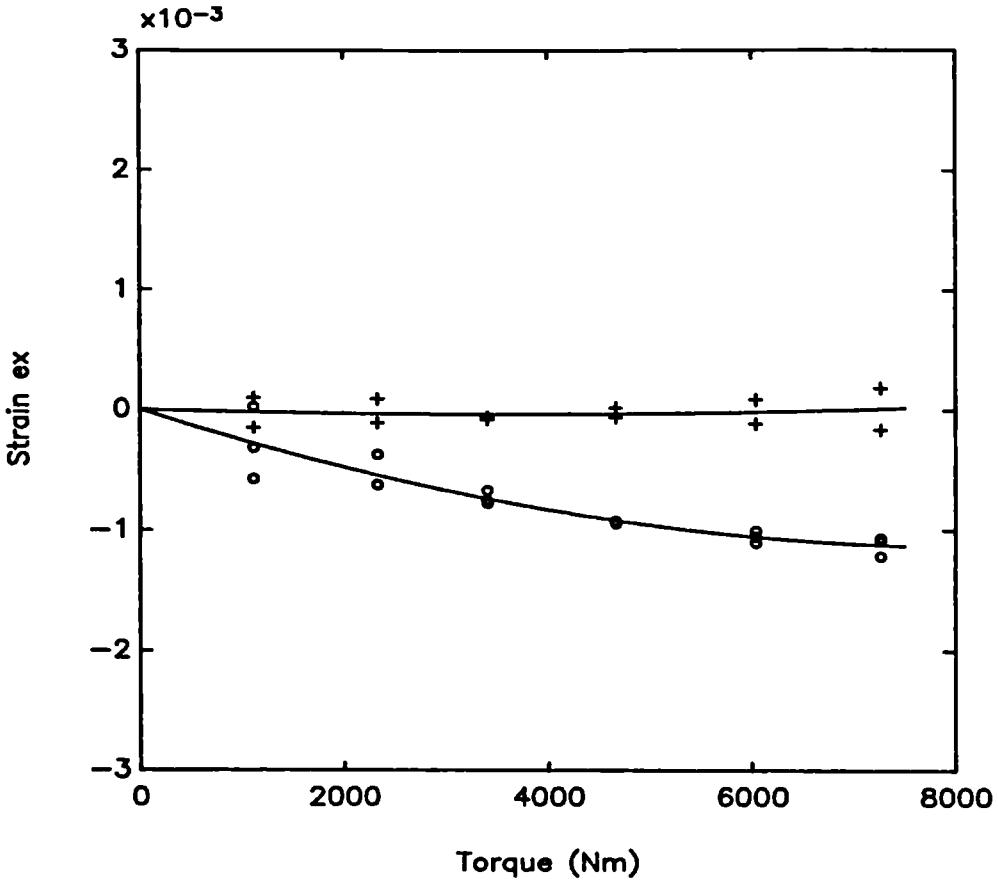

+	Gauges 3,5
o	Gauges 2,4,6

Fig 4.18

Longitudinal Strain Versus Torque

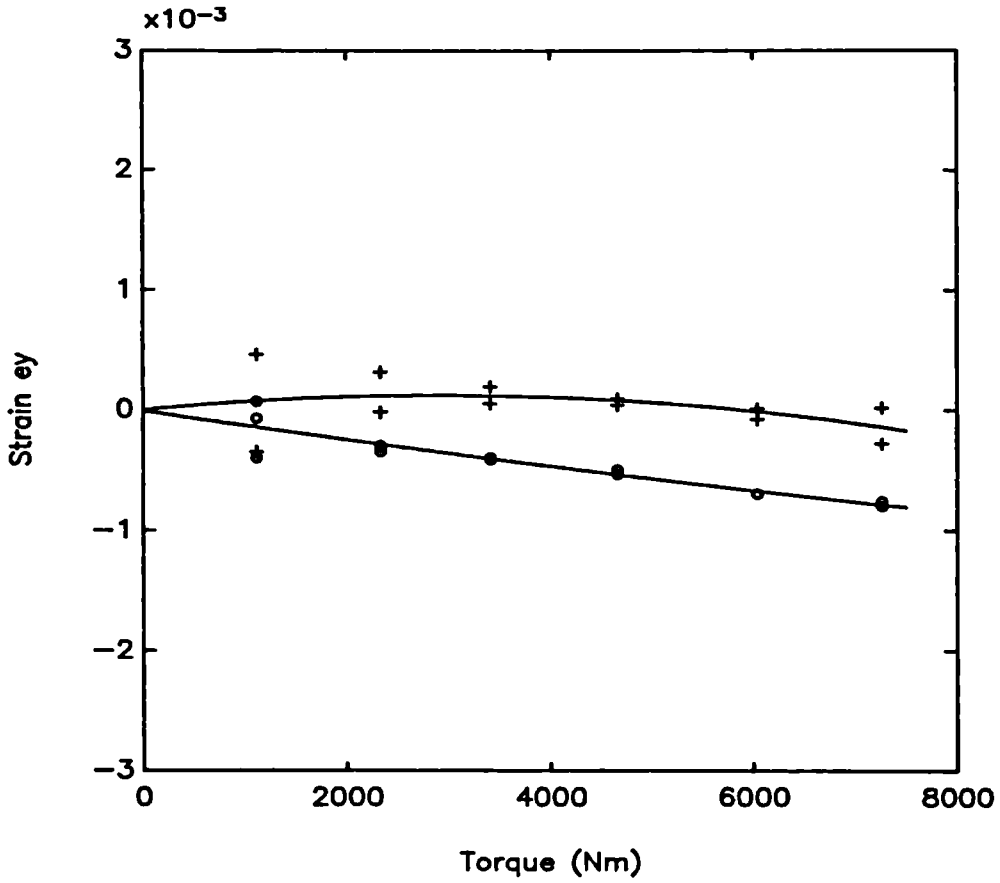

+	Gauges 3,5
o	Gauges 2,4,6

Fig 4.19

Circumferential Strain Versus Torque

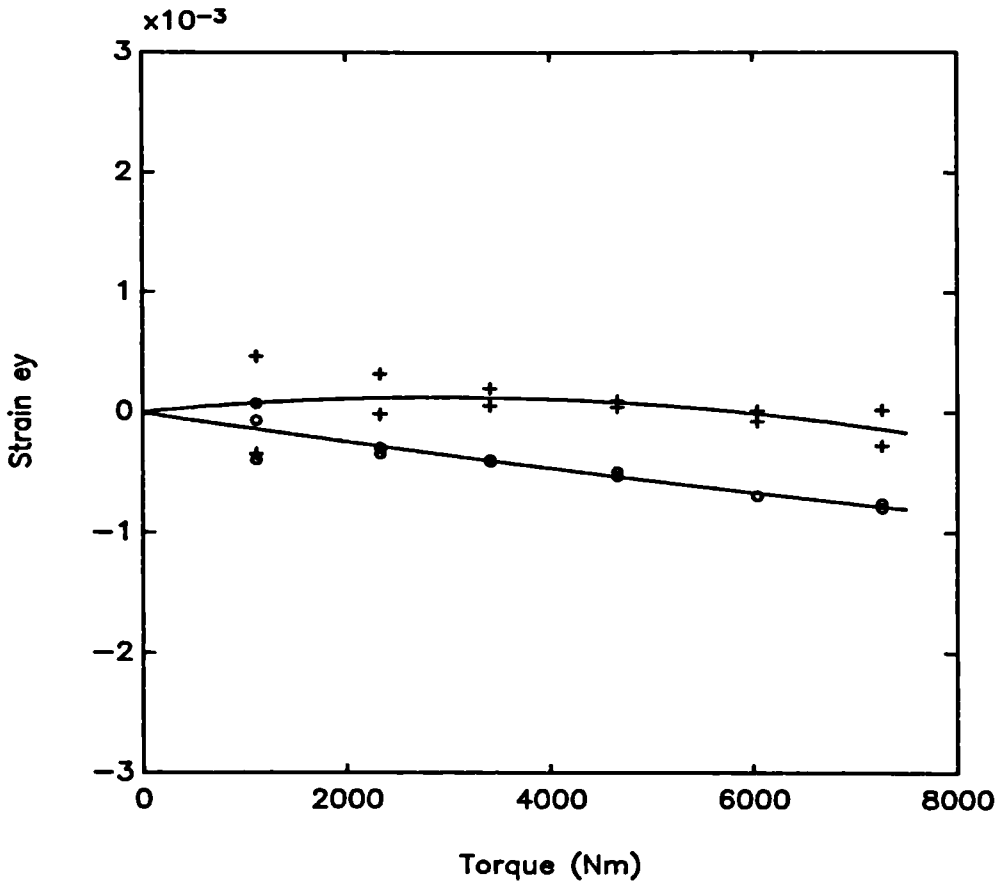

+	Gauges 3,5
o	Gauges 2,4,6

Fig 4.19

Circumferential Strain Versus Torque

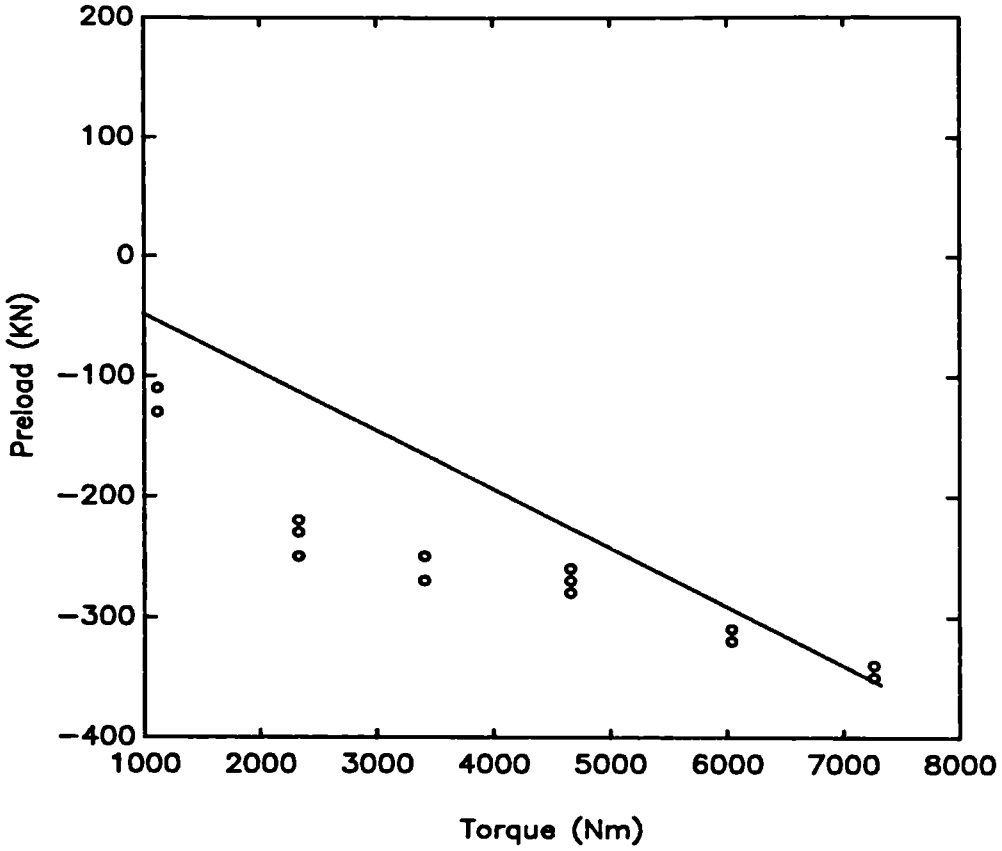

Fig 4.20

Predicted and Experimental Values of Preload

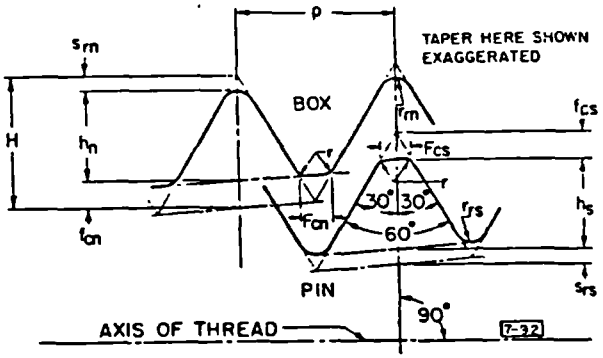

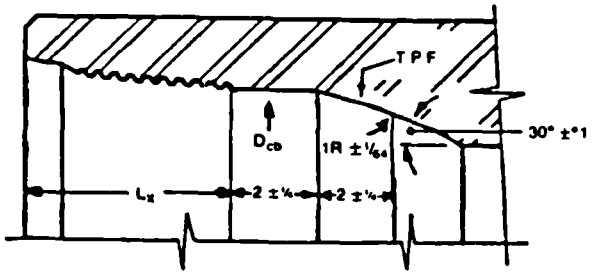

BOREBACK BOX STRESS-RELIEF FEATURE

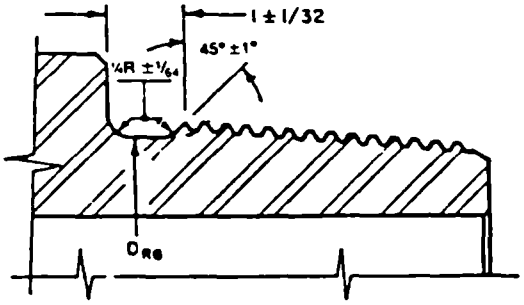

PIN STRESS-RELIEF FEATURE

Fig 4.21

API NC5O and API 6 $^{5}/_{8}$ " Reg Thread Forms

Drill String Axial Load Test	
1	Load Cell
2	Top Flange 1 (ϕ 500 x 100)
3	Top Flange 2 (ϕ 500 x 100)
4	ϕ 100 x 400 Pin
5	Cradle Block (400 x 300 x 100)
6	Drill Collar
7	Bottom Flange 2 (ϕ 540 x 100)
8	Bottom Flange 1 (ϕ 540 x 100)
9	Hydraulic Actuator

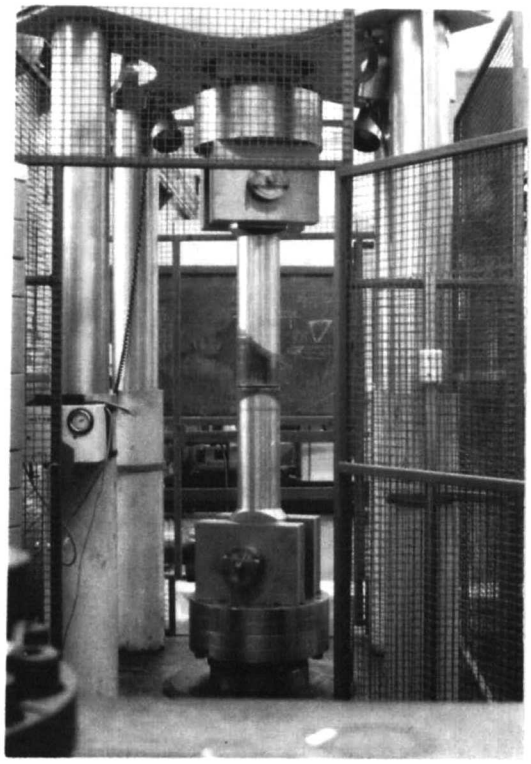

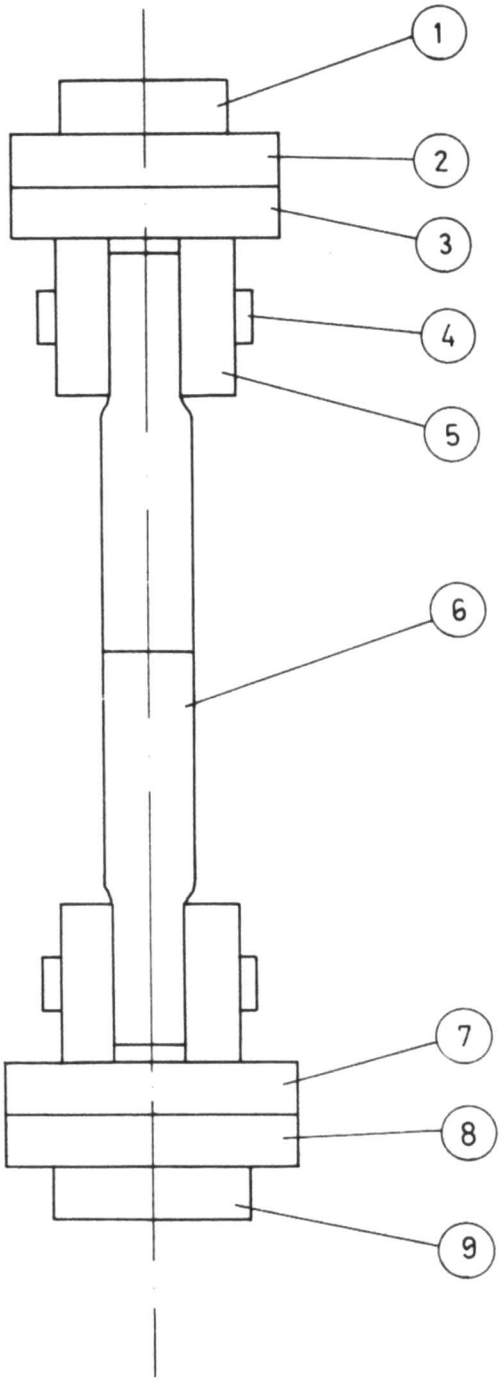

Fig 4.22

Axial Tension Fatigue Test Rig

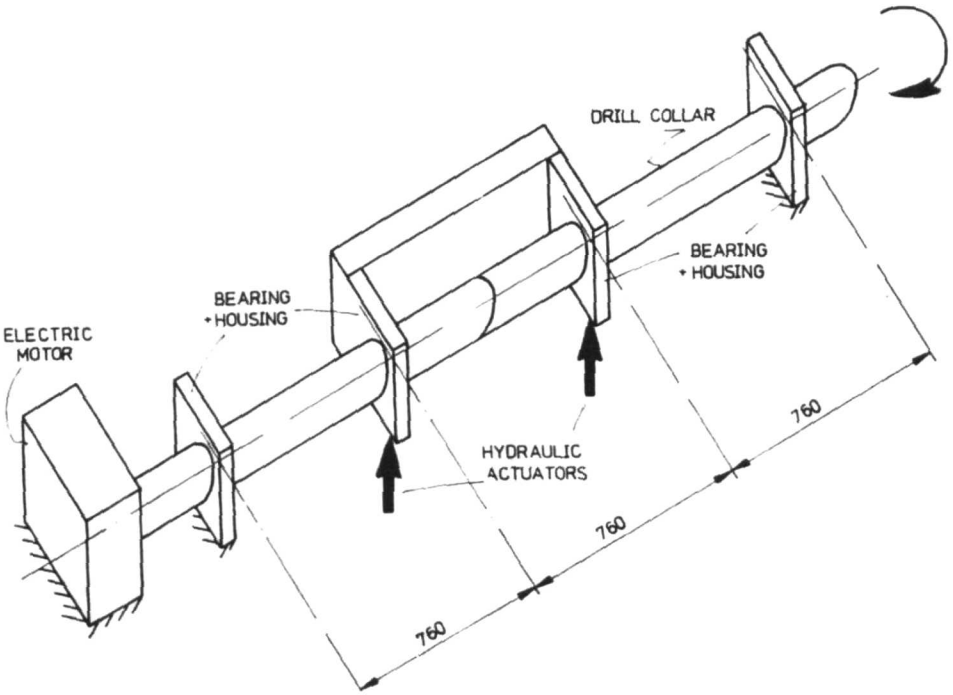

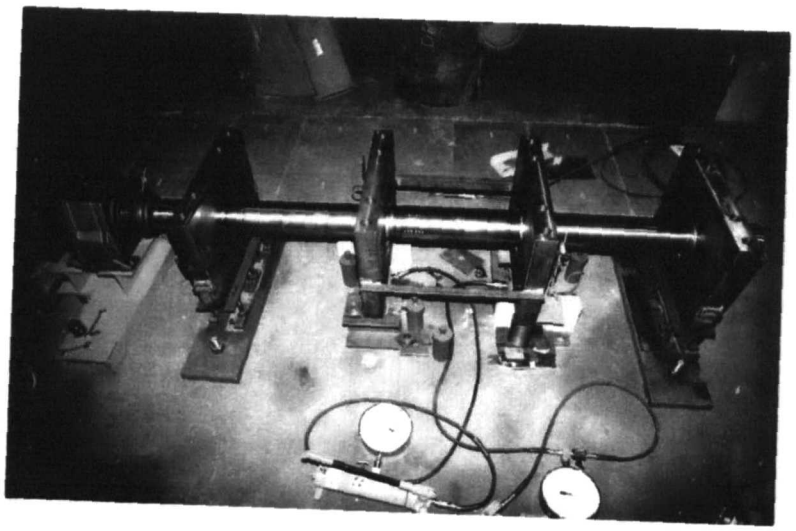

Fig 4.23

Rotating Bend Fatigue Test Rig

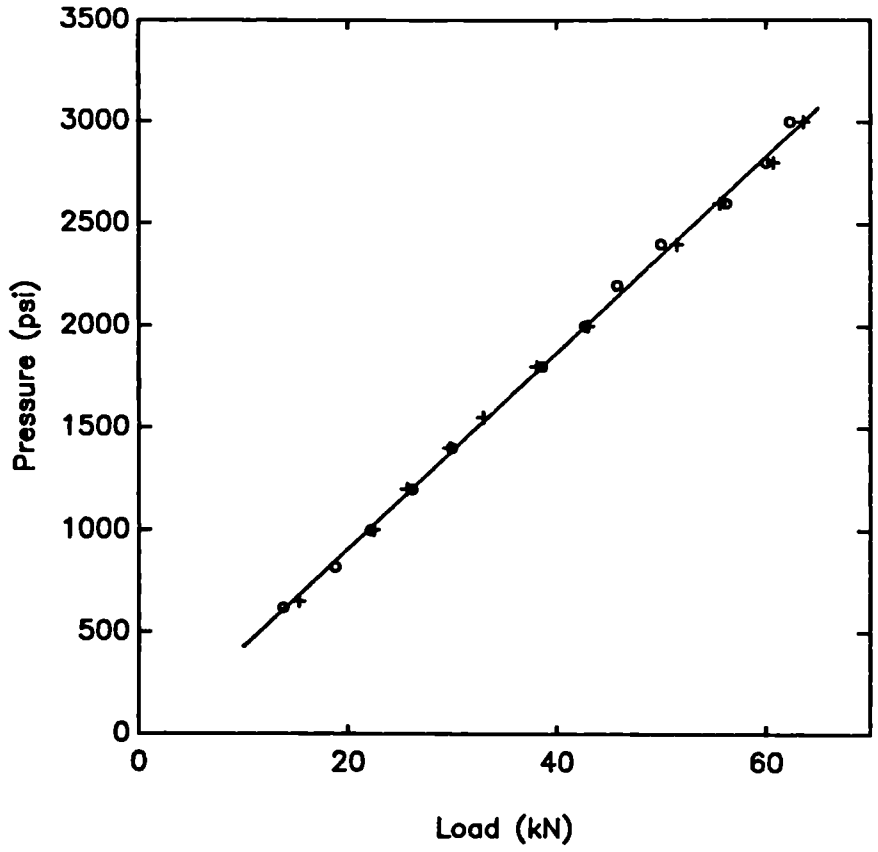

o Jack 1

\+ Jack 2

Fig 4.24

Hydraulic Jack Calibration

Strain Gauge Distances from Pin-Box Shoulder

Gauges 1,8,9,16	250mm
Gauges 2,10	60mm
Gauges 3,11	40mm
Gauges 4,12,7,15	4mm
Gauges 5,6,13,14	2mm

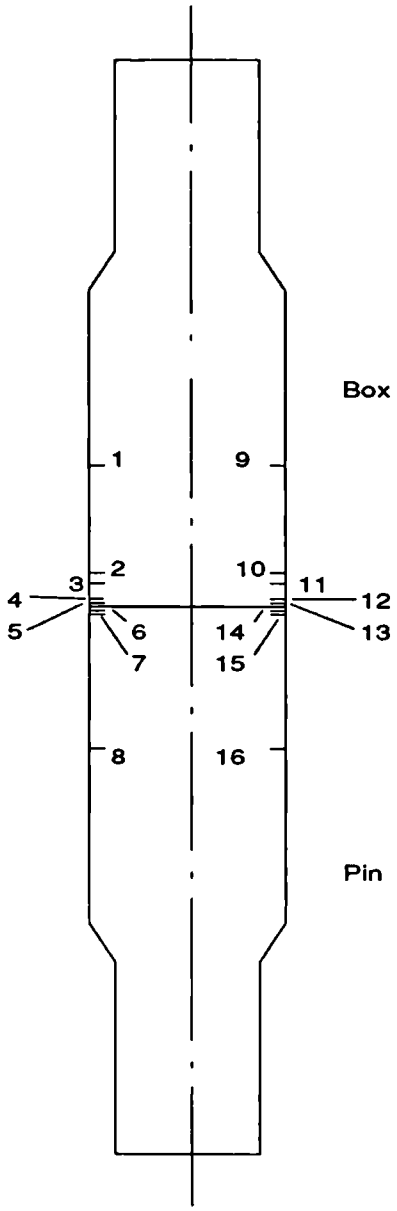

Fig 4.25

Position of the Axial Test Strain Gauges

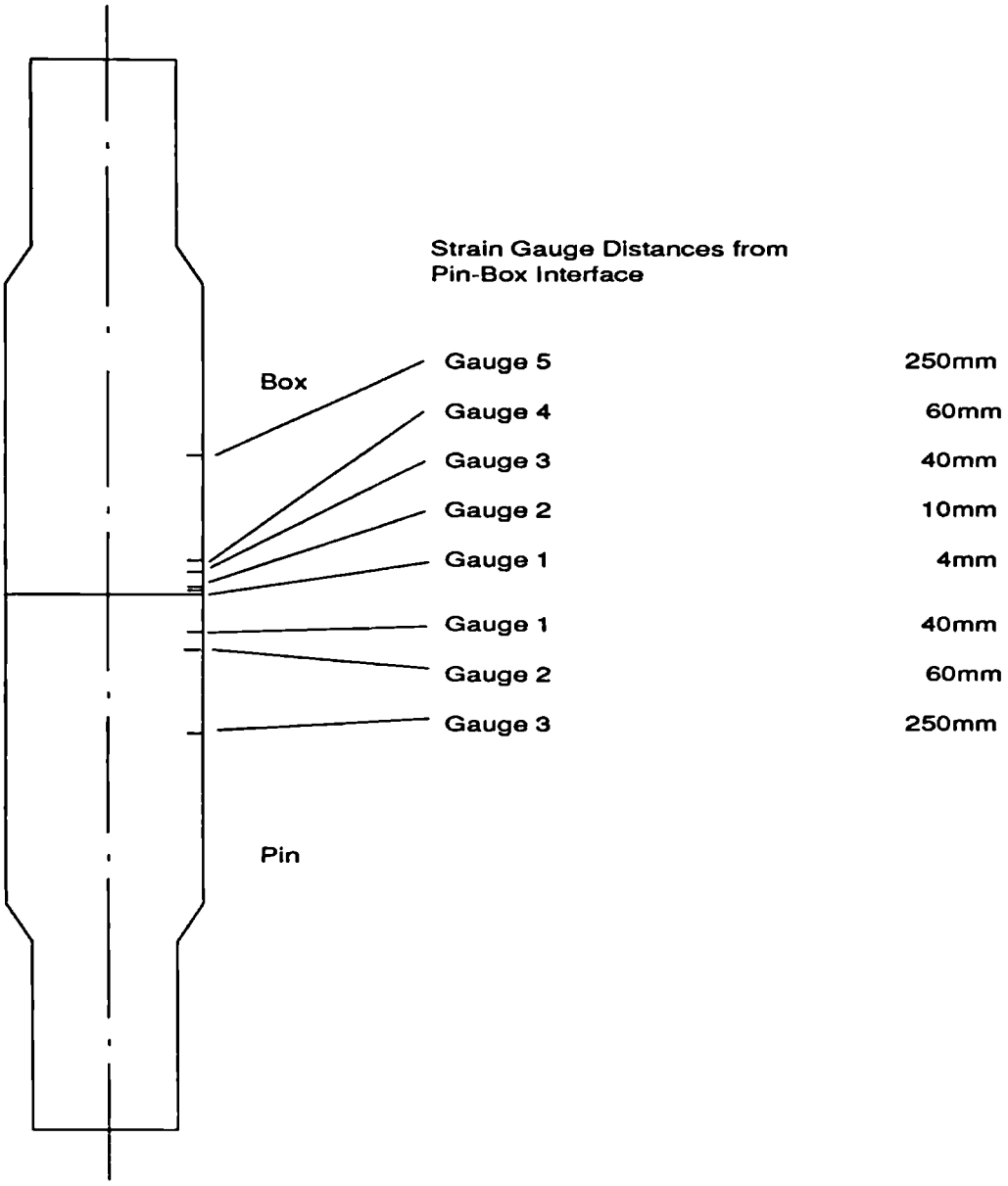

Fig 4.26

Position of the Rotating Bend Test Strain Gauges

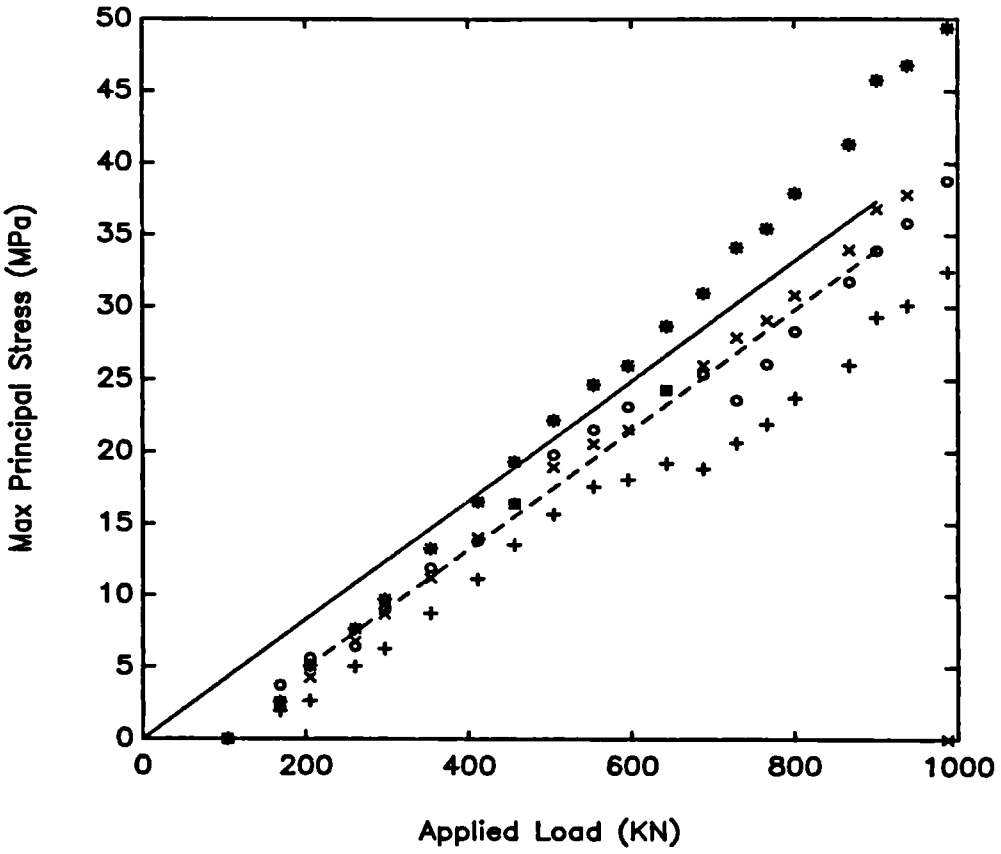

o	Gauge 1
+	Gauge 8
*	Gauge 9
x	Gauge 16

Fig 4.27

Results of the Remote Axial Strain Gauges

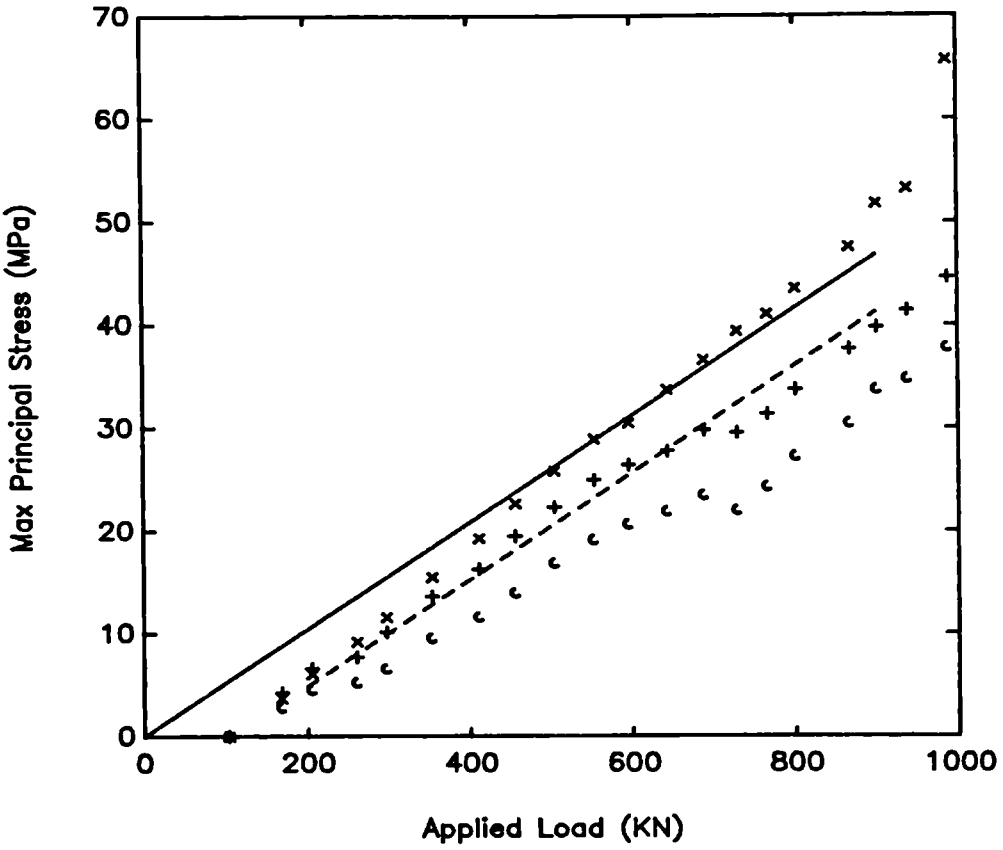

o	Gauge 2
+	Gauge 3
x	Gauge 10

Fig 4.28

Results of the Intermediate Axial Box Strain Gauges

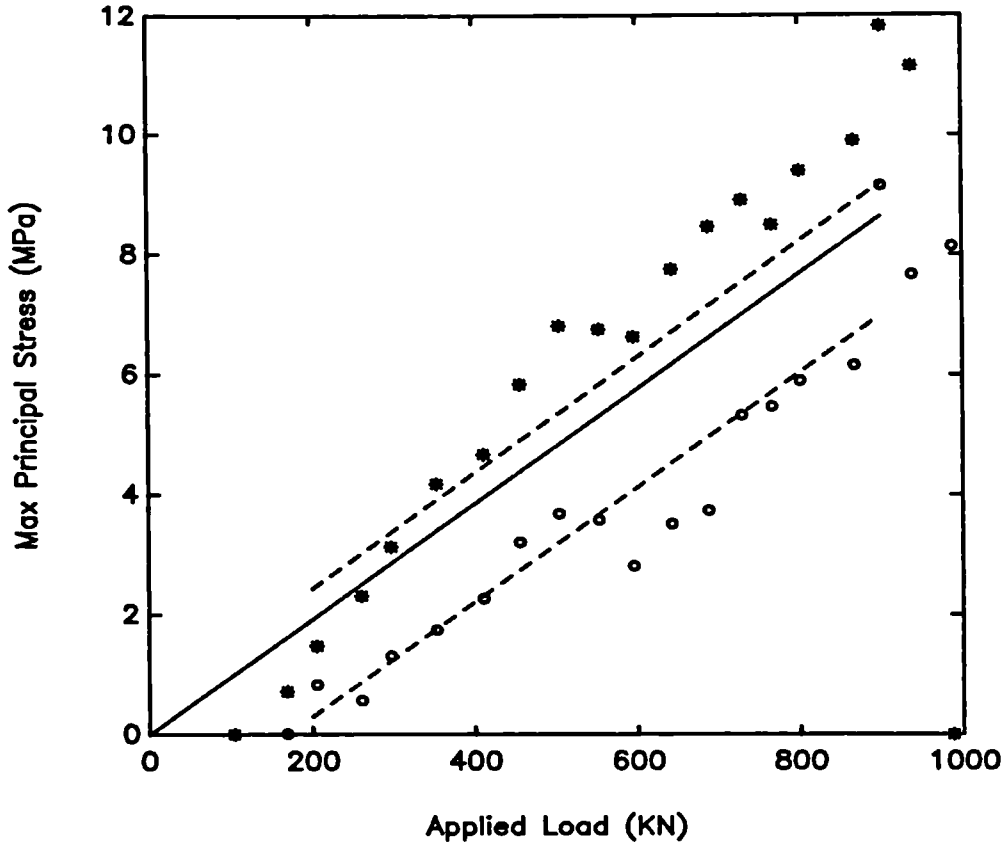

o Gauge 14

* Gauge 12

Fig 4.29

Longitudinal Principal Stresses at the Shoulder Interface

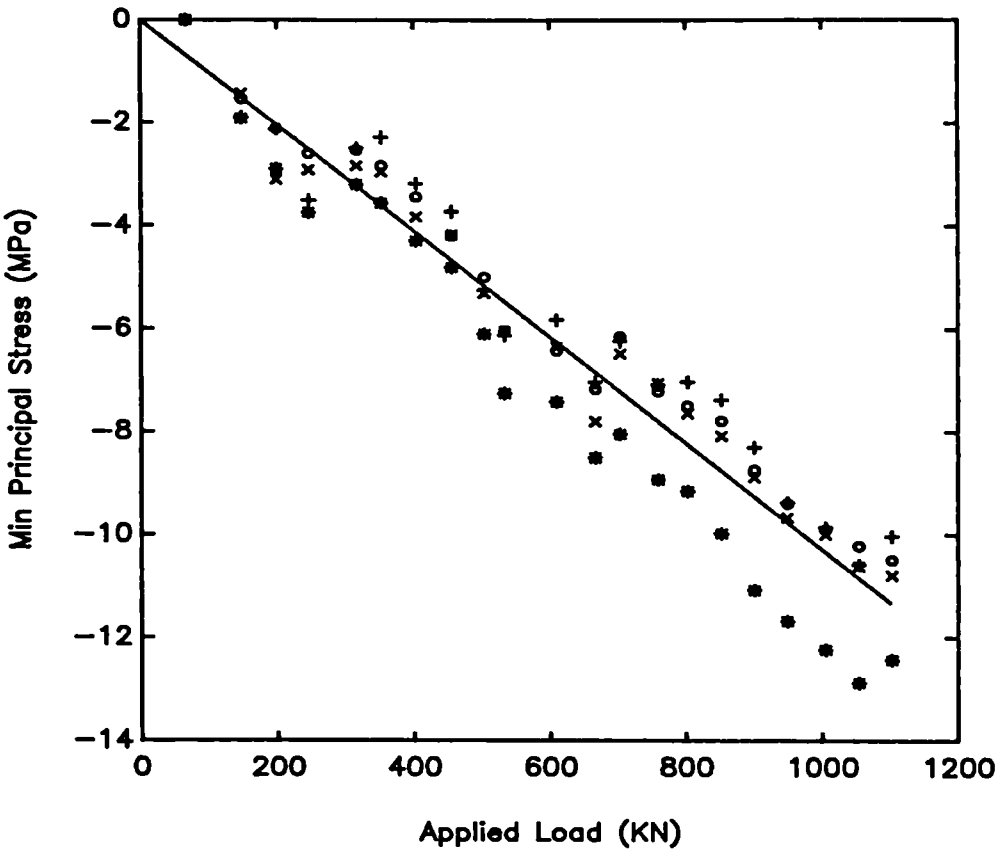

*	Gauge 5
o	Gauge 13
+	Gauge 14
x	Gauge 15

Fig 4.30

Circumferential Principal Stresses at the Shoulder Interface

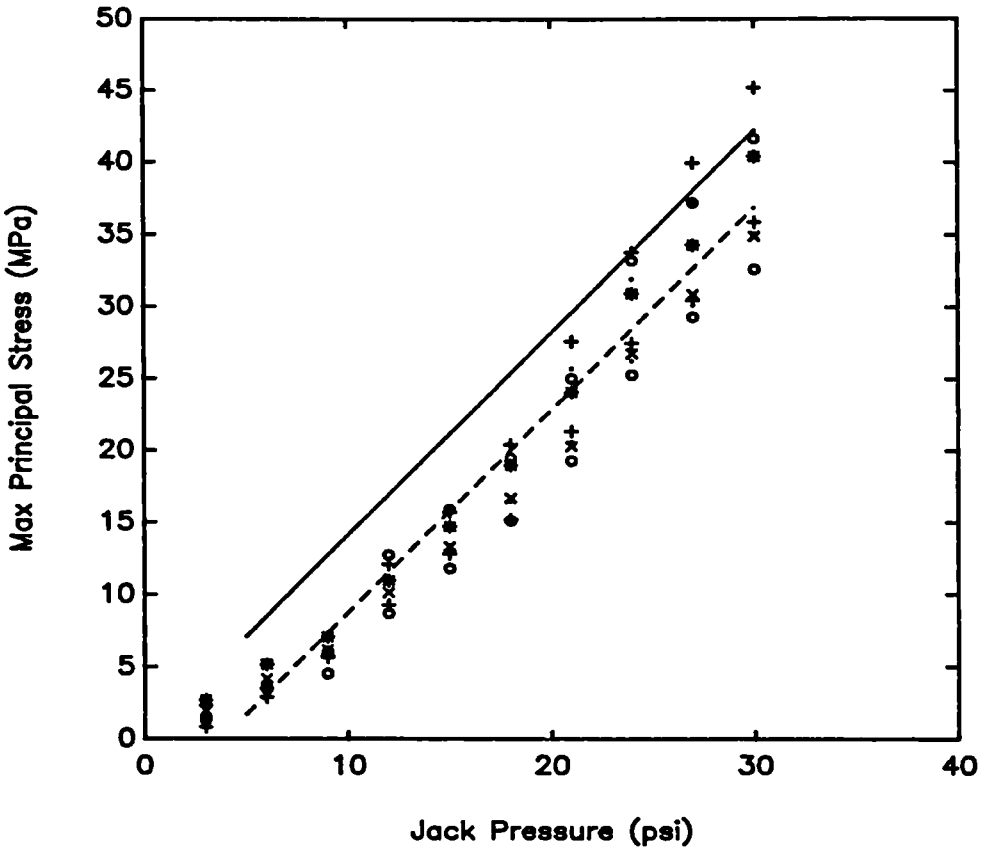

Fig 4.31

Results of the Rotating Bend Strain Gauges

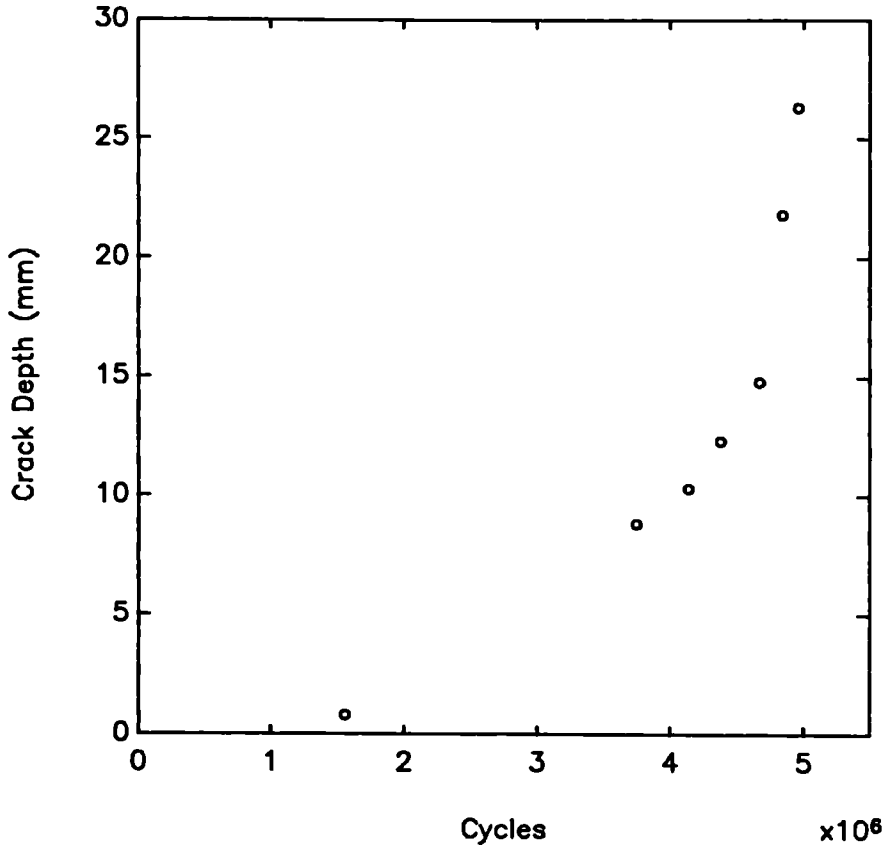

Fig 4.32

Crack Growth Data for Axial Test 1

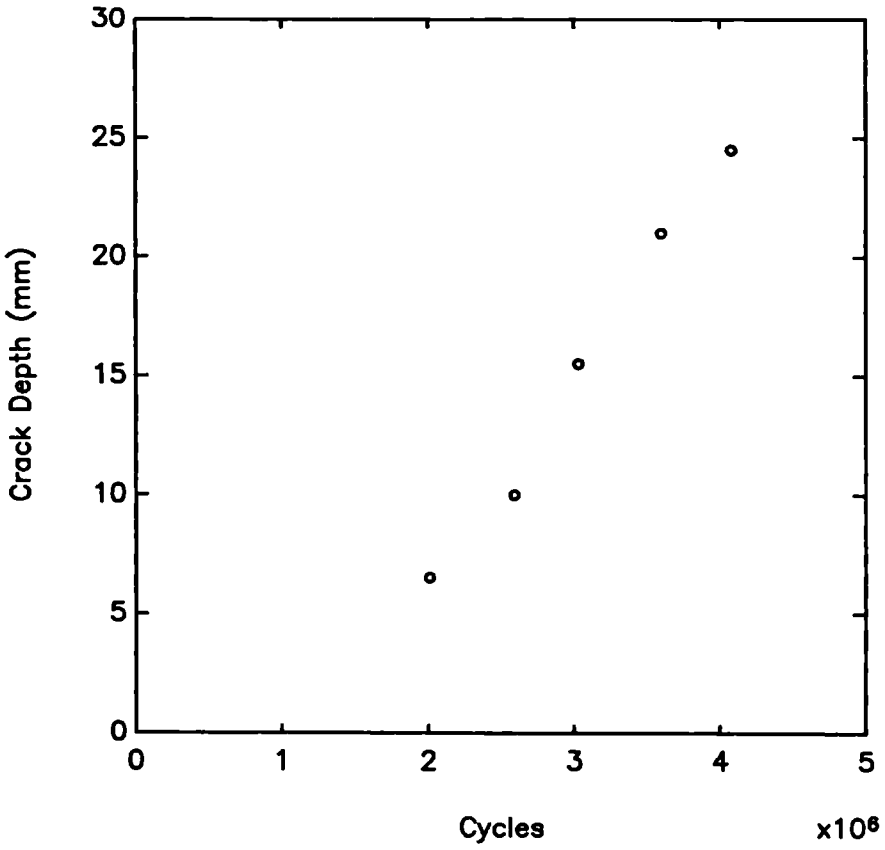

Fig 4.33

Crack Growth Data for Axial Test 2

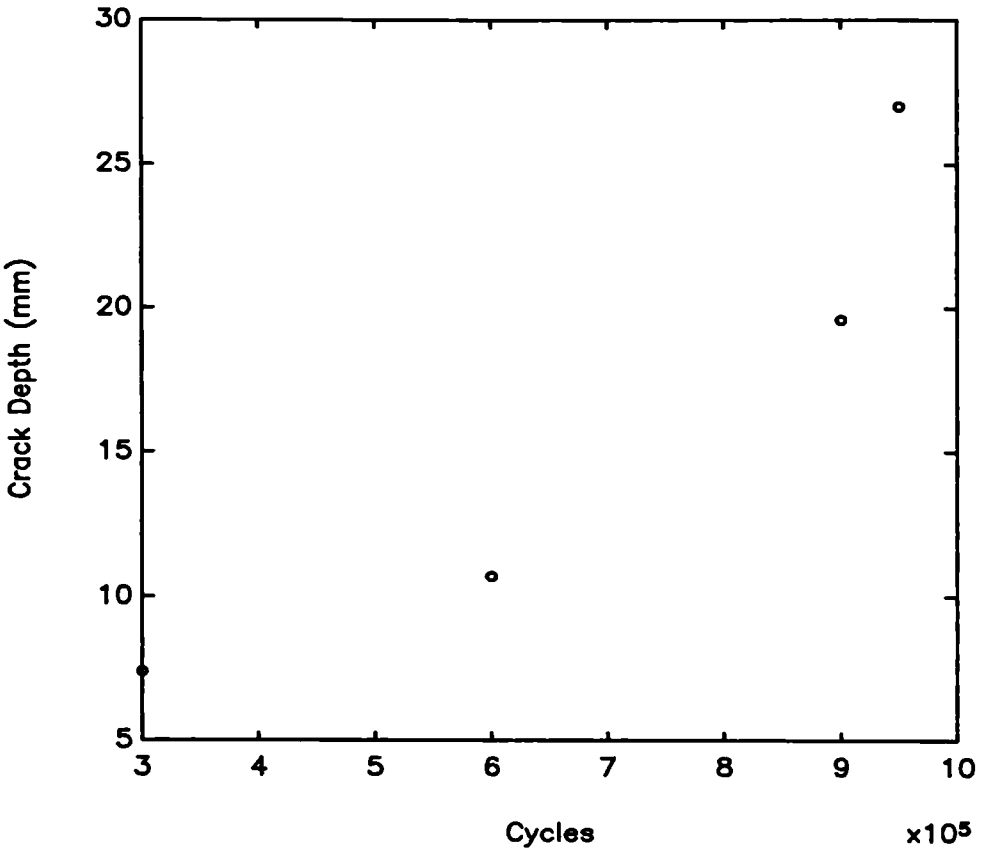

Fig 4.34

Crack Growth Data for Axial Test 3(b)

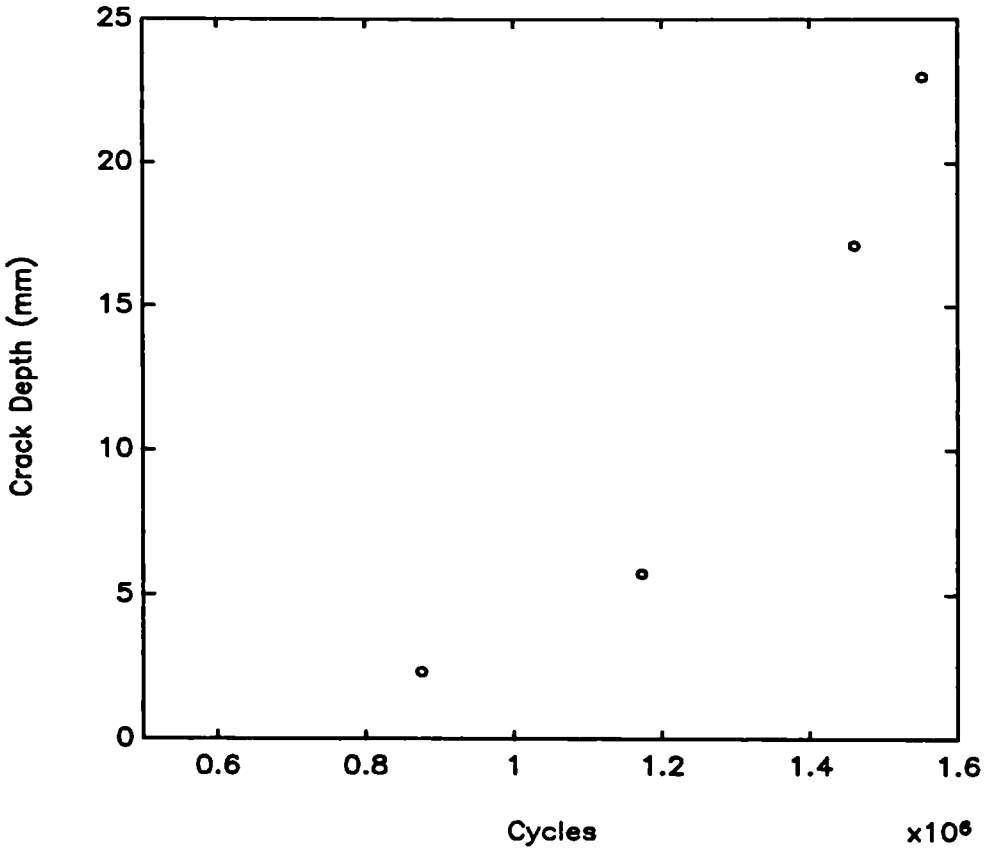

Fig 4.35

Crack Growth Data for Axial Test 5

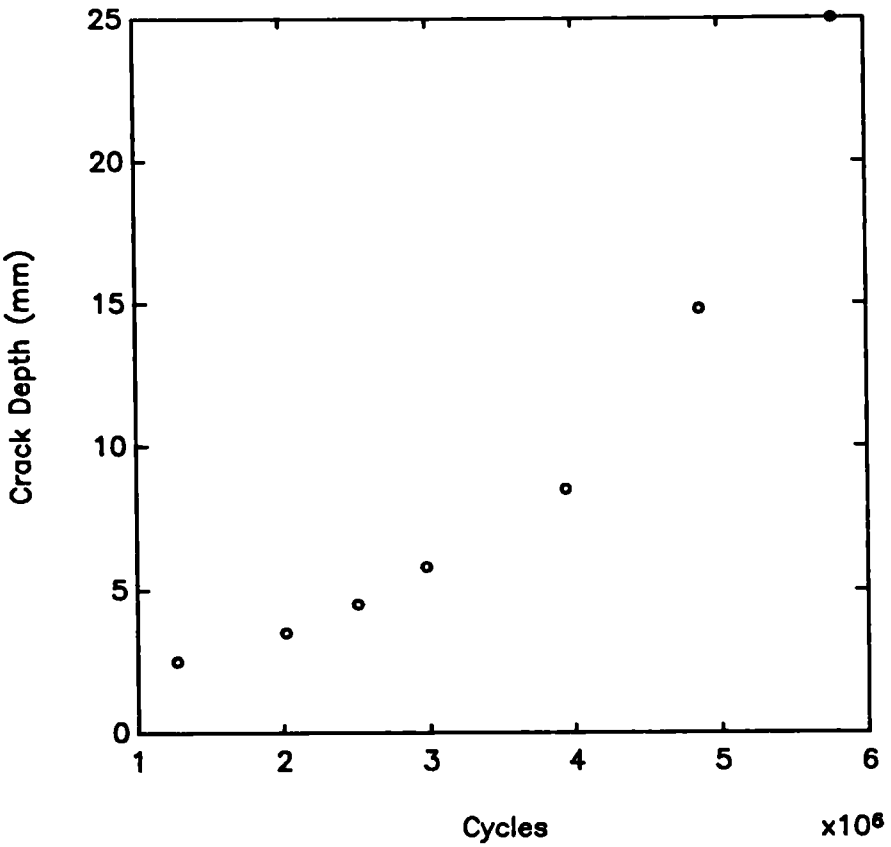

Fig 4.36

Crack Growth Data for Rotating Bend Test 1

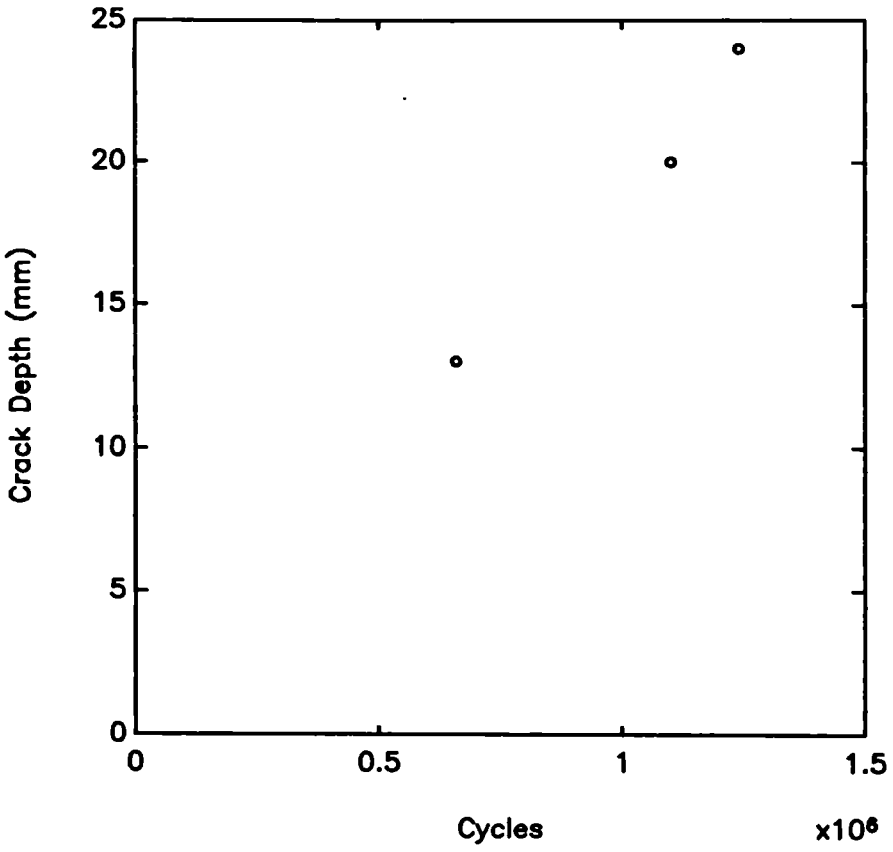

Fig 4.37

Crack Growth Data for Rotating Bend Test 2

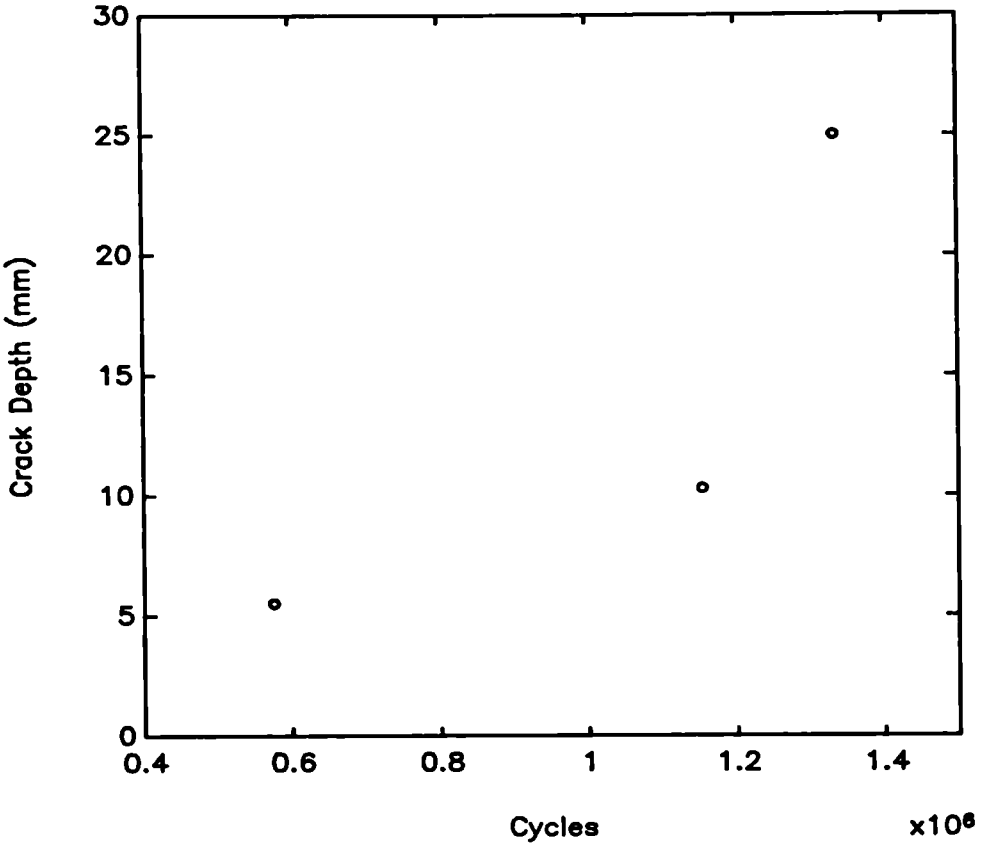

Fig 4.38

Crack Growth Data for Rotating Bend Test 3

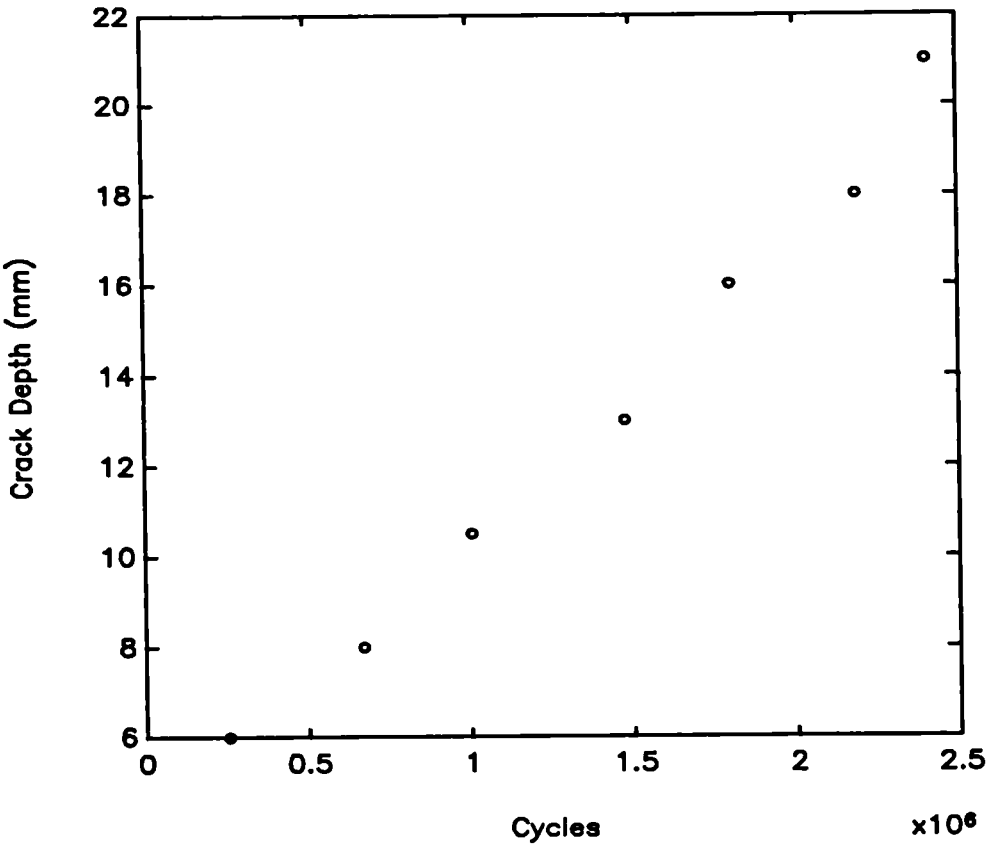

Fig 4.39

Crack Growth Data for Rotating Bend Test 4

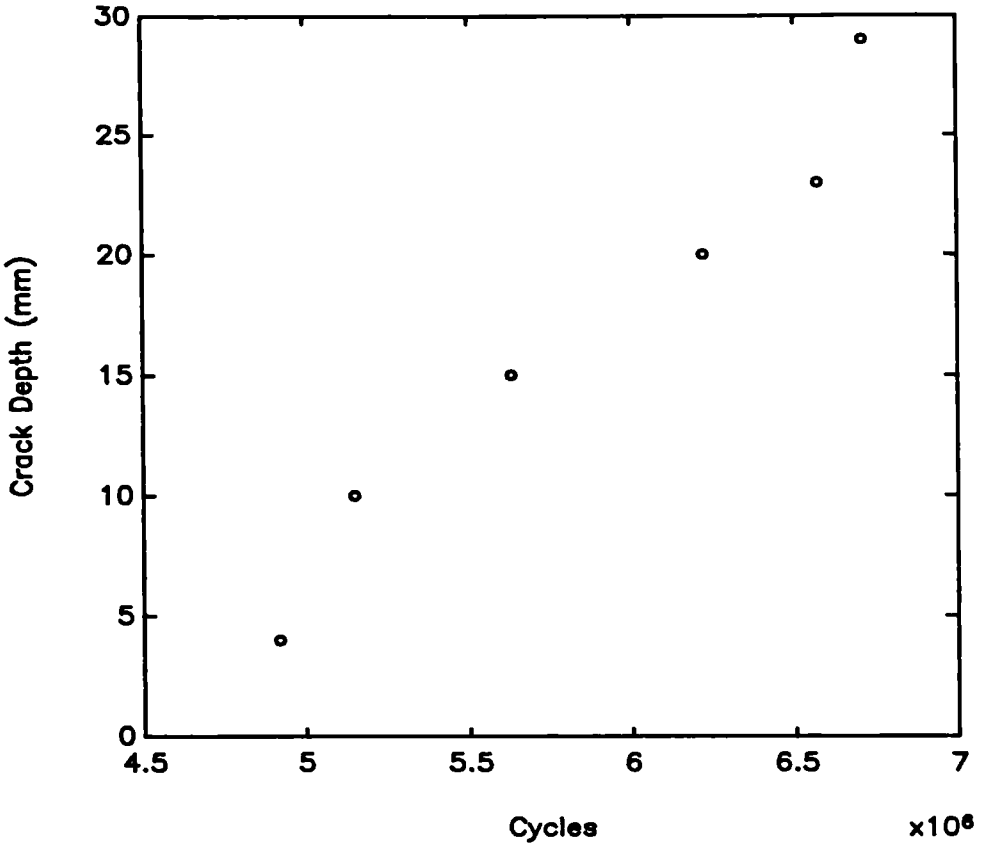

Fig 4.40

Crack Growth Data for Rotating Bend Test 5

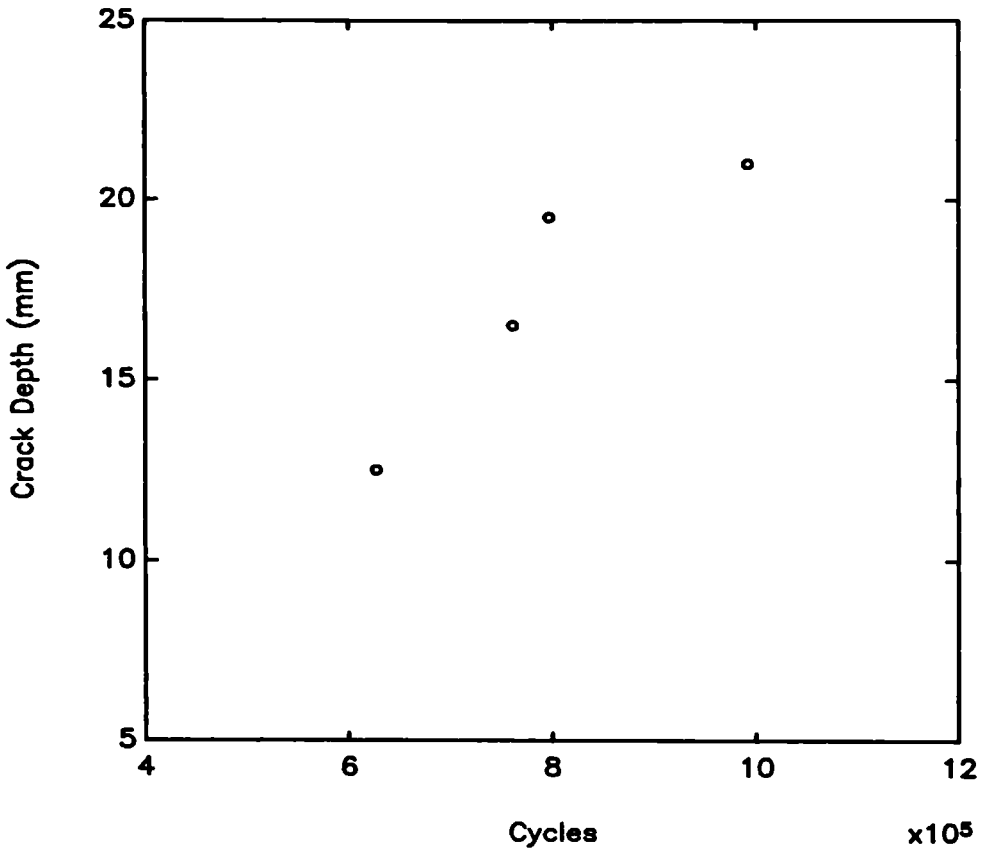

Fig 4.41

Crack Growth Data for Rotating Bend Test 6

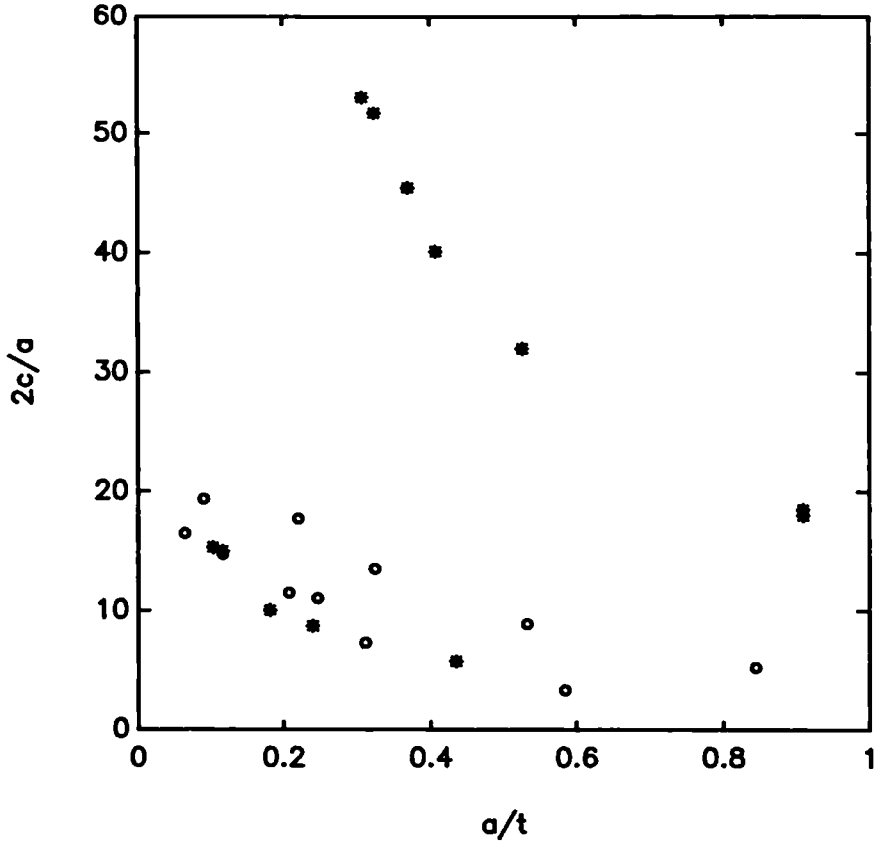

* Constant Amplitude Tests

o Variable Ampitude Tests

Fig 4.42

Crack Aspect Ratios for the Tether Tests

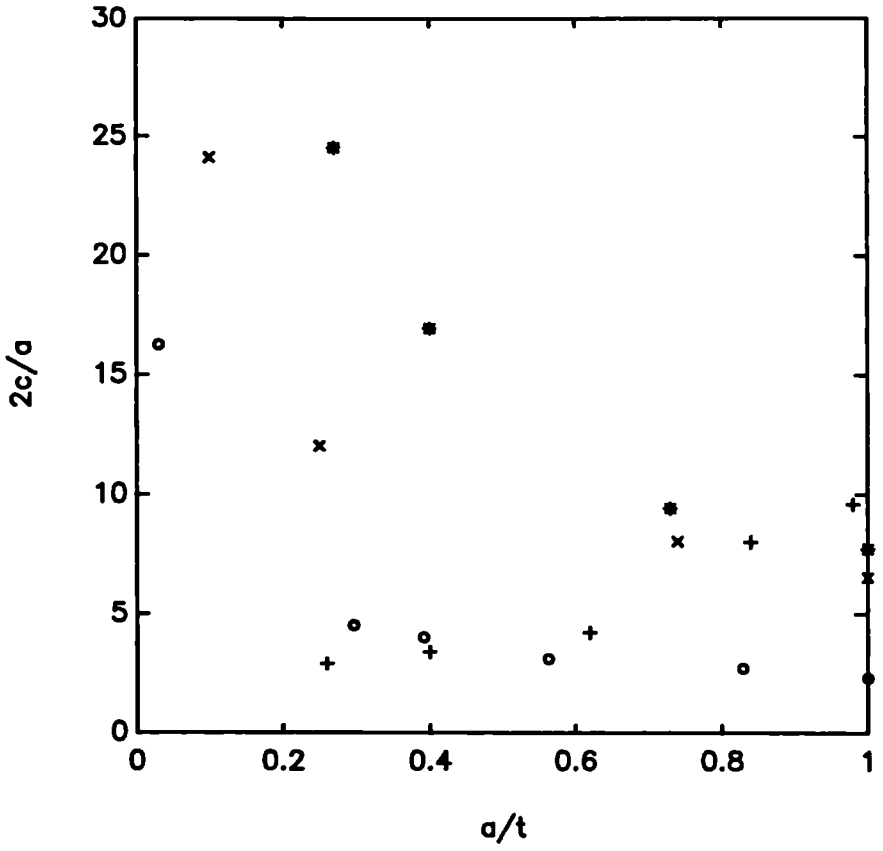

o	Axial 1
+	Axial 2
*	Axial 3(b)
x	Axial 5

Fig 4.43

Crack Aspect Ratios for the Axial Tests

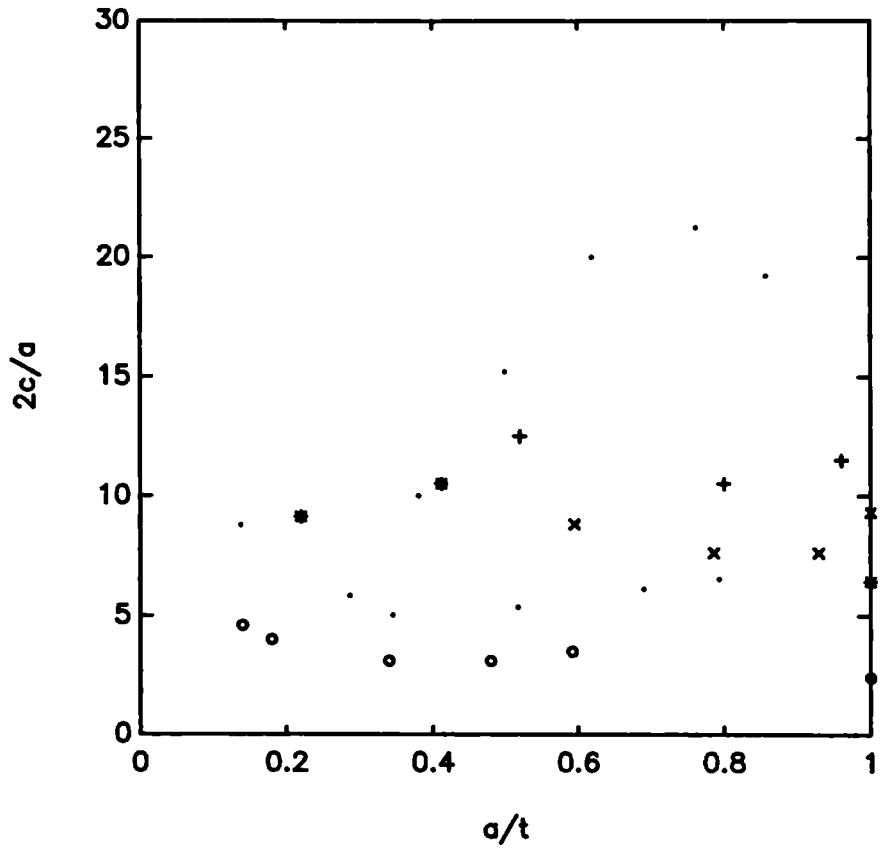

o	Rotating Bend 1
+	Rotating Bend 2
*	Rotating Bend 3
.	Rotating Bend 4,5
x	Rotating Bend 6

Fig 4.44

Crack Aspect Ratios for the Rotating Bend Tests

CHAPTER FIVE - Failure Appraisal of Threaded Connections

5.1 Introduction

This chapter will interpret the results of the fatigue tests reported in the previous chapter in terms of the crack initiation, and propagation models from chapters two and three respectively. Such a post-mortem examination of the test findings and observations is a useful way of identifying the various failure mechanisms participating in the overall degradation of a structural component. These aid in the adaptation of existing solutions or may suggest regions of validity for the analysed models. An independent stress analysis of the joints tested was not undertaken as it requires a thorough study. Sufficient details of stress analyses of the joints are available from other sources to enable an adequate use of the fatigue prediction models.

An attempt is made to characterise crack aspect ratio development which is essential for a blind fatigue crack propagation prediction. The comparisons of prediction and experimental results have the benefit of hindsight where crack shape and location are known. But this has the advantage of eliminating certain variables from calculations so the inadequacies or otherwise of the models can be seen more clearly. It must be reiterated once more that the solutions presented earlier are by no means complete. However, these are structured in a manner that allow the introduction of more comprehensive sub-solutions as they arise, or may accommodate new mechanisms which contribute to the failure process once initiated.

5.2 Stress Analysis of the Joint Geometries

In the case of the VAM joints, a hybrid electric analogue - finite element technique was used to determine the local stress at the critically loaded tooth from which all failures were initiated. This technique was introduced in chapter one. Newport [5.1] carried out finite element analyses on a number of thread forms of various geometries and under different load conditions. From these a parametric equation for the critical VAM tooth root stress concentration factor 'K_T' was derived. This is given as:

$$\log_e K_T = -3.64 + 4.47\frac{P_i}{\Sigma P_i} + 6.96\frac{h}{P} + 0.0195\frac{P}{\rho} - 0.270\frac{t}{h} + 1.79\sqrt{\frac{t}{h}}$$

$$-4.36\left(\frac{P_i}{\Sigma P_i}\right)^2 - 6.82\left(\frac{h}{p}\right)^2 + 1.80\left(\frac{P_i}{\Sigma P_i}\right)^3 + 0.0113\left(\frac{t}{h}\right)^{\frac{3}{2}} \qquad (5.1)$$

The equation is valid for the ranges:

$0.04 < P_i/\Sigma P_i < 1.0$
$0.20 < h/P < 0.5$
$4.20 < P/\rho < 25.4$
$1.60 < t/h < 14.0$

It can be seen from the above expression, that the value of 'K_T' is dependent upon the ratio of axial stress to tooth bending stress, $\Sigma P_i/P_i$. This ratio is obtained from an electrical analogue model of the type developed by Topp [5.2] assuming (as for the finite element model) an axi-symmetric coupling, and is easily run as a Fortran program. The model initially considered the connection as a mechanical system represented by rigid levers joined by springs. These springs represent the stiffness of the pin, box and teeth. The electrical analogue technique arose making an analogy between applied load and electric current through a resistor. Voltage drop across the resistor is equivalent to the deflection of the spring and thus the stiffness is analogous to the inverse of resistance. Once the critical tooth in the connection, and its corresponding value of $\Sigma P_i/P_i$, is known, K_T for the critical section, and hence the critical local stress can be found. The SCF given in Appendix IV is the ratio of the critical tooth root stress to the remote nominal stress in the pipe body, whereas K_T is a local stress concentration factor defined as the ratio of the critical tooth root stress to the stress in the pin wall immediately before the critical tooth root, i.e. K_T is a measure of stress concentration due to the tooth notch.

The electrical analogue model gave $\Sigma P_i/P_i$ for the critical seventeenth pin tooth as 7.7 yielding a value of K_T of 4.62 from equation (5.1). To obtain the SCF from this value i.e. relate the maximum local stress to remote nominal stress in the pin body, K_T is multiplied by S_c, where,

$$S_c = \frac{\left[1+\frac{t}{D_i}\right]^2 - 1}{\left[\left(\frac{D_o}{D_i}\right)^2 - 1\right]} \tag{5.2}$$

S_c is the section correction factor
D_o is the outer diameter of the pin
D_i is the inner diameter of the pin

Stress analysis of the drill collars was carried out entirely using finite element analysis. The loading through these thick walled tubulars is more complex than the thin walled VAM joints. The critical VAM tooth was not considered to be affected by preload (as found by the experimental and electrical analogue stress analyses), whereas the drill collar joints all showed considerable sensitivity to preload from the finite element analyses. Although SCF data was available from the finite element analysis, the weight function prediction requires the stress distribution along the uncracked plane to be known. The stress distribution was assumed to behave like a simple notch using the relations in chapter three. However, this may be a possible area for investigation. In contrast, the stress distribution was not considered to be a significant feature in the thin walled VAM joints, as the affect of the notch was expected to be apparent right through the pipe section. Another assumption for both connection types is that no local or global load redistribution occurs as a result of the propagating surface crack.

The SCF values used in the analysis and quoted in Appendix IV came from a parametric fit of results obtained from a series of finite element runs on threads varying loading and geometrical characteristics [5.3]. The finite element models were two dimensional, axi-symmetric idealisations, loaded axially. For the preloaded model, the shoulders were connected, permitting transmission of axial

load across the intersection. The unpreloaded model had the pin and box shoulders disconnected. The meshes were generated automatically using a purpose designed mesh generator producing about three thousand parabolic quadrilateral axi-symmetric elements having about ten thousand nodes. Node to node gap elements were used for the compressive surfaces between teeth.

The stress concentration factors were derived only for the axial load case. In order to use these results in the prediction analyses for the bending experiments, a modification was made to the stress analysis. The notation given in chapter three and in Appendix IV defined the nominal bending stress as the stress in the outermost fibre of the remote pipe body. The local stress range is defined as:

$$\Delta\sigma_{local} = \sigma_{nom} \, x \, 2 \, x \, SCF \, x \, C_B \tag{5.3}$$

The factor of two, converts the stress amplitude into a stress range under reversed bending. The term C_B is the bending correction given as:

$$C_B = \left[\frac{r \; \overset{+}{-} \; \frac{t}{2}}{R_{max}} \right] \tag{5.4}$$

+ for the pin

- for the box

r is the mean tube radius (see also Appendix IV)

This is simply the linear decay of stress, under bending, to zero at the neutral axis.

5.3 Crack Initiation Lives

Appendix IV summarises the details of all the fatigue tests carried out. This includes an initiation life for each fatigue crack. These lives are defined as the fraction of life taken to produce a crack having an arbitrary depth of 0.2mm, and were obtained by extrapolating the fatigue crack growth data to that depth. Tables 5.1-5.3 show

these lives with ascending values of local stress range for the three materials. These do not take values of preload into account nor do they reflect variations in mean stress or initial surface state.

It is beyond the scope of this study to derive fatigue strength and ductility properties for the individual materials, measurement of surface roughness and residual stress was also considered to be unrealistic within the bounds of this investigation. For these reasons it was thought that the use of a consistent and reliable set of materials data for a representative steel was the most appropriate method of comparing the prediction analysis with the experimental findings. One steel was chosen to represent all three connector steels, this was a version of AISI 4340, its mechanical properties are given as material '5' in Table 2.1 of chapter two. Using the relation:

$$\frac{\Delta\varepsilon}{2}=\frac{\Delta\sigma}{2}+\left[\frac{\Delta\sigma}{2K'}\right]^{\frac{1}{n'}} \tag{5.5}$$

the local cyclic strain range for each test could be evaluated. From this, three predictions of stress range to fatigue crack initiation life were made. These were the method using fatigue strength and ductility properties and the two universal slopes predictions set out in chapter two. Fig 5.1 shows these compared with all experimental crack initiation lives. This with Tables 5.1-5.3 may at first appear to contain an unacceptable amount of scatter, however examination of the experimental details explains some of the scatter points. The constant amplitude VAM results cannot be verified by the author as they were part of an independent study. The first of these was reported to be unreliable, the other two were torqued to such unrecommended values that they must be treated with scepticism and not to be representative of normal loading behaviour. Dismissing these three asterisks (two practically superimposed on each other) at the 762 MPa point leaves two significantly deviated points at 292 MPa and 562 MPa. These are rotating bend tests four and one respectively. Rotating bend test four is a pin failure in an NC5O thread. The critical tooth according to the finite element analysis and all the other experimental results on this geometry was in the box section. The critical local

stress in the box was predicted to be 254.1 MPa whereas it failed in the pin at a position predicted to have a local stress of 145.9 MPa. It is clear that the pin must have been damaged for a crack to have initiated from this position. The other significant deviated point in Fig 5.1 at the 562 MPa stress range is rotating bend test one. This was the first test carried out on the purpose built rig, and although it was not reported in the previous chapter for reasons of clarity, some teething problems were encountered as might be expected. The most notable was leaking hydraulic seals on the jacks, resulting in unsustainable pressure. This problem was rectified after about 1×10^5 cycles which may explain the slightly longer than anticipated crack initiation life. Overall the results are reasonable considering the assumptions made. The universal slopes predictions in this case seem to provide convenient upper and lower bounds, however a lot more experimental points are required before any concrete conclusions can be made.

5.4 Fatigue Crack Growth

The weight function stress intensity factor solution for threaded connections developed in chapter three is used in this section to predict the experimental fatigue crack growth rates. Stress intensity factors are functions of crack geometry. This aspect ratio development would not be known before a crack develops, but might be predicted by an appropriate model. Each test was analysed separately to determine stress intensity factors for every individual crack, taking into account local stress, geometry and crack aspect ratio. Experimental nominal geometric correction (Y) factors are presented in Appendix IV for each test, however these are not directly compared with predicted Y factors. The nominal Y factor is simply the stress intensity factor normalised to the nominal stress in the remote pipe body, i.e., from chapter one,

$$\Delta K = \left(\frac{1}{C} \frac{da}{dn} \right)^{\frac{1}{m}} \tag{5.6}$$

$$Y_{exp} = \frac{\Delta K}{\Delta\sigma_{nom}\sqrt{\pi a}} \tag{5.7}$$

$$\Rightarrow \quad Y_{exp} = \frac{1}{\Delta\sigma_{nom}\sqrt{\pi a}}\left(\frac{1}{C}\frac{da}{dn}\right)^{\frac{1}{m}} \tag{5.8}$$

The Paris law constants '*C*' and '*m*' were obtained for C75 steel using an experimental technique (Appendix I). The values for AISI 4145H and Staballoy AG17 steels were taken as those derived in a similar manner in Reference [5.4] and [5.3] respectively.

A problem arises however, when calculating *da/dn* if there are very few experimental points in the crack growth curve. The experimental nominal *Y* factors quoted in Appendix IV were derived by calculating *da/dn*, the crack growth rate, as a simple linear relationship between adjacent data points. The crack depth '*a*', being the mid point value between data points. It is easy to see how this can lead to erroneous results, especially where there are relatively few data points available. Another alternative is to curve fit the crack growth rates, effectively providing sufficient extra data points to make calculation of *da/dn* a simple exercise of determining the gradient of the tangent to the curve at any point. However all the experimental data did not support one consistent curve definition, and the exercise was deemed too subjective for scientific analysis. Instead the raw crack growth data was compared directly with the prediction. The Paris law,

$$n_2 - n_1 = \frac{1}{C\Delta\sigma^m\pi^{\frac{m}{2}}}\int_{a1}^{a2}\frac{da}{Y^m a^{\frac{m}{2}}} \tag{5.9}$$

can if *Y* is assumed constant be expressed:

$$n_2 - n_1 = \frac{1}{C\Delta\sigma^m \pi^{\frac{m}{2}} Y^m \left(1 - \frac{m}{2}\right)} \left(a_2^{1-\frac{m}{2}} - a_1^{1-\frac{m}{2}} \right) \qquad (5.10)$$

Y can be assumed constant if the crack depth increments are small. Fig 5.2 shows the predicted nominal Y factors for a crack emanating from the critical pin tooth in the VAM joint, for different crack aspect ratios. The individual experimental crack aspect ratios lend themselves better to a consistent curve fit than the crack growth rates. Each crack aspect ratio was fitted with a cubic spline.

The resulting Y factor behaviour for constant amplitude test '1' and the two variable amplitude tests are shown in Fig 5.3. Unfortunately the crack aspect ratios reported for constant amplitude tests '2' and '3' were not in any sense semi-elliptical and were outside the validity range for the weight function solution. These are the only two tests to exhibit such uncharacteristic growth behaviour and cannot be analysed further. The final prediction compared with the experimental results for the remaining VAM joints are shown in Fig 5.4. The prediction in this case like all to follow, takes the first experimental data point as a datum, so that errors in crack initiation prediction cannot influence the crack growth comparisons. The predictions are excellent for constant amplitude test '1' and variable amplitude test '1', an over prediction of seventeen percent in life is calculated for variable amplitude test '2'. It should be noted that accuracy of the comparisons is sensitive to the first experimental point being correct, thus the interpretation of the beach marks is critical. However in view of the assumptions made, namely no load shedding and no influence of the breaking - making of the joint on the fatigue crack growth, the predictions are extremely good.

Essentially the same analysis procedure was followed in order to compare the crack growth predictions with the drill collar experimental results. One difference in the presentation is that local Y factors are used rather than nominal geometric correction factors. The stress intensity factor is normalised to the uniform stress in the pipe body immediately before the first engaged tooth. The first engaged tooth is defined as the first fully formed engaged tooth. This is important as examination of Appendix IV reveals that only the unpreloaded and standard geometry specimens

failed at the first fully formed engaged tooth, the preloaded modified joints all failed at positions on the thread runout with the exception of the two pin failures. The finite element stress analysis did not identify this phenomenon with the modified bore back box, i.e. axial test '3(b)'. The critical local stress was assumed to be the maximum local stress according to the finite element analysis which corresponded to the actual failure site in all cases except for axial test 3(b), which may have failed at this position because of fretting as observed in chapter four. Another aspect worth noting is that some of the crack growth data showed cracks deeper than the pipe wall thickness. This is due to the fact that the beach marks were measured linearly along the crack surfaces, which were not always in a perpendicular plane to the tube axis. This is really only noticeable for the two unpreloaded tests, and would suggest a certain degree of mode II cracking. This is ignored by the prediction analysis.

Figs 5.5-5.8 show the *Y* factors for an NC50 box in tension and bending and a $6^{5}/_{8}$" Reg box in tension and bending respectively. Fig 5.9 compares the prediction with the results of axial test '1'. The prediction appears better than it really is as only the lower stress state is used in deriving the weight function stress intensity factors. The final two experimental points in the life of the specimen are due to a higher stress range (Appendix IV). In reality the prediction is conservative, showing an accelerated rate of crack growth towards the end of the joint's life. This same phenomenon is apparent in most cases. Figs 5.10-5.12 show axial tests '2', '3(b)' and '5'. Tests '2' and '3(b)' again show excellent agreement up until about half the specimen thickness, test '5' shows good agreement between prediction and experiment, any deviation can easily be accounted by small errors in measurement of beach marks.

The rotating bend experimental results show mixed agreement with the predictions. Fig 5.13 (test '1'), 5.14 (test '2'), 5.15 (test '4'), and 5.18 (test '6') show that once more the predictions are in good agreement with the experimental results in the early stages of crack growth, and over predicting crack growth rates after the half thickness point. Fig 5.15 (test '3') shows a dramatic over prediction of life, which may be

experimental scatter. Finally, although the final life of the prediction of test '5' (Fig 5.17) is favourable, the curve bears little relationship to the experimental data. The latter is not consistent with the other test results.

Overall, predictions are very good in the first half of fatigue crack propagation, and are over conservative in the latter stages. This may suggest a certain amount of load shedding or indeed gross plasticity as a long circumferential crack is approached. A clear inadequacy in the above prediction was the lack of a calculated stress field through the uncracked plane. It would appear that this along with a study on load redistribution within threaded connections in the wake of a propagating crack, is essential in order to make the best use of the weight function solution.

5.5 Crack Aspect Ratio

In chapter three reference was made to several crack aspect ratio development relations. The most detailed investigation was by Forman and Shivakumar [5.5] who derived two limiting conditions for crack shape in round bars. The studies of Kermani [5.6] and Dale [5.7] can also be investigated with regard to the present experimental data in this chapter.

An initial check showed that the previously published crack aspect ratio expressions inadequately described the experimental results. For this reason two new limiting expressions were derived. Figs 5.19 and 5.20 show the derivation of two simple idealised cracks, i.e. an edge crack in a circular rod and a circular crack of radius '$D/2 + a$' in a circular rod. Fig 5.21 shows the various prediction models compared with the experimental data from the VAM tests 1, 4 and 5. Forman and Schivakumar's equations do not predict the behaviour in large diameter - thin walled tubes. Both upper and lower bounds are superimposed on each other, clearly use of these should be restricted to their designed application i.e. solid rods. Kermani's study of several failed drill collars yielded the aspect ratio evolution behaviour shown in Fig 5.21 as an initially nearly circular crack growing in length rapidly with the aspect ratio stabilising before the depth reaches half the tube thickness. Although this behaviour bears little resemblance to the experimental data, it should be noted

that Kermani's study was of actual service cracks where there may have been numerous making-up and breaking of the connection. This may indicate a discrepancy between laboratory and service fatigue behaviour. Dale's study of crack growth behaviour, although designed for use in thick walled tubes, is again unrepresentative of the experimental results obtained here. The two newly derived simple edge and circular behavioural relations, by comparison, define the experimental results reasonably well.

Unfortunately an edge and circular crack of radius '$D/2 + a$' do not have any physical meaning for internal cracks in the box section of threaded connections. However, the expression for the edge crack and a modified version of the circular crack, show a surprisingly good description of the drill collar box cracks. Fig 5.22 shows the aspect ratio results of all the box cracks. These can be considered to be split into two categories, (a) short cracks and, (b) long cracks. The short cracks are defined between the bounds of Dale's and edge crack behaviour, i.e. axial test '1', axial test '2' and rotating bend test '1'. These all have relatively long crack growth lives as indicated. The long cracks can be defined between the bounds of the edge crack and modified circular crack behaviour. The crack propagation lives in this case as indicated, are all relatively short. The long cracks can be explained by multiple initiation associated with high stress - low cycle fatigue. Similarly the short cracks can be a result of a single crack initiation often associated with low stress - high cycle fatigue. Clearly there will be a region where both categories overlap, however with more comprehensive experimental fatigue data in the future, this behaviour may be defined as a function of local stress. Finally Fig 5.23 shows the results of the pin failures compared with the prediction models. Rotating bend test '5' is described well by the edge and circular crack bounds, however, rotating bend test '4' (initially damaged) shows Kermani type growth behaviour.

5.6 Summary and Conclusions

Considering the experimental particulars, many scatter points and seemingly erratic crack initiation results reorganised into much more understandable patterns. The assumed representative material cyclic properties gave a good description of the experimental initiation behaviour. The universal slopes approximations gave

convenient upper and lower bounds for the test data. It is important to note that the cyclic properties used were not deemed appropriate individually but were internally consistent properties of an appropriate material.

The generic weight function solution produced consistent stable predictions of fatigue crack growth without the need for any modification to the solution or curve fitting, despite some growth scenarios being outside the validity limits of the constitutive relations. This again shows the stability of the MRS weight function approach. Growth predictions were generally very good but it is suggested these would be further improved with a full definition of stress distribution through the tube wall thickness and a load shedding model as a function of crack geometry.

Three new crack aspect ratio models were derived from simple geometric considerations. These describe the experimental results well. A basis for a future more universal solution as a function of local stress is presented.

5.7 References

[5.1] Newport, A., "Stress and Fatigue Analysis of Threaded Tether Connections", Ph. D. Thesis, University College London, 1989.

[5.2] Glinka, G., Dover, W. D. and Topp, D. A., "Fatigue Assessment of Tethers", Proc. Int. Conf. on Fatigue and Crack Growth in Offshore Structures, I. Mech. E., pp 187-198, 1986.

[5.3] "Prevention of Downhole Failure", Final Report, NDE Centre, University College London, March 1992.

[5.4] "Fatigue Analysis of Drill Strings", Final Report, NDE Centre, University College London, 1990.

[5.5] Forman, R. G., and Shivakumar, V., "Growth Behaviour of Surface Cracks in the Circumferential Plane of Solid and Hollow Cylinders", Fracture Mechanics: Seventeenth Volume, ASTM STP 905, pp 59-74, 1986.

[5.6] Kermani, B., "Drill String Threaded Connection Failure Analysis and Case Studies", EMAS, 1989.

[5.7] Dale, B. A., "An Experimental Investigation of Fatigue Crack Growth in Drill String Tubulars", SPE 1559, 1986.

Test No	$\Delta\sigma_{local}$	N	Comments
VAM 4	322	0.40×10^6	
VAM 5	322	1.20×10^6	
VAM 1	762	1.20×10^6	Not Trustworthy
VAM 2	762	1.15×10^5	
VAM 3	762	1.25×10^5	

Table 5.1

Fatigue Crack Initiation Lives for C75 Steel Specimens

Test No	$\Delta\sigma_{local}$	N	Comments
Axial 3(a)	314.2	6.0×10^6	
Axial 2	342.7	0.5×10^6	Damage ?
RB 5	379.1	3.8×10^6	
Axial 4(a)	380.8	Runout	
Axial 1	421.3	0.8×10^6	No Preload
RB 1	562.0	0.8×10^6	Load Sustained ?
RB 2	608.4	0	
RB 6	933.4	0	

Table 5.2

Fatigue Crack Initiation Lives for AISI 4145H Steel Specimens

Test No	$\Delta\sigma_{local}$	N	Comments
Axial 6	287.2	Runout	
RB 4	291.8	0	Damaged Pin
Axial 5	418.8	0.5×10^6	
RB 3	700.6	0	

Table 5.3

Fatigue Crack Initiation Lives for AG17 Steel Specimens

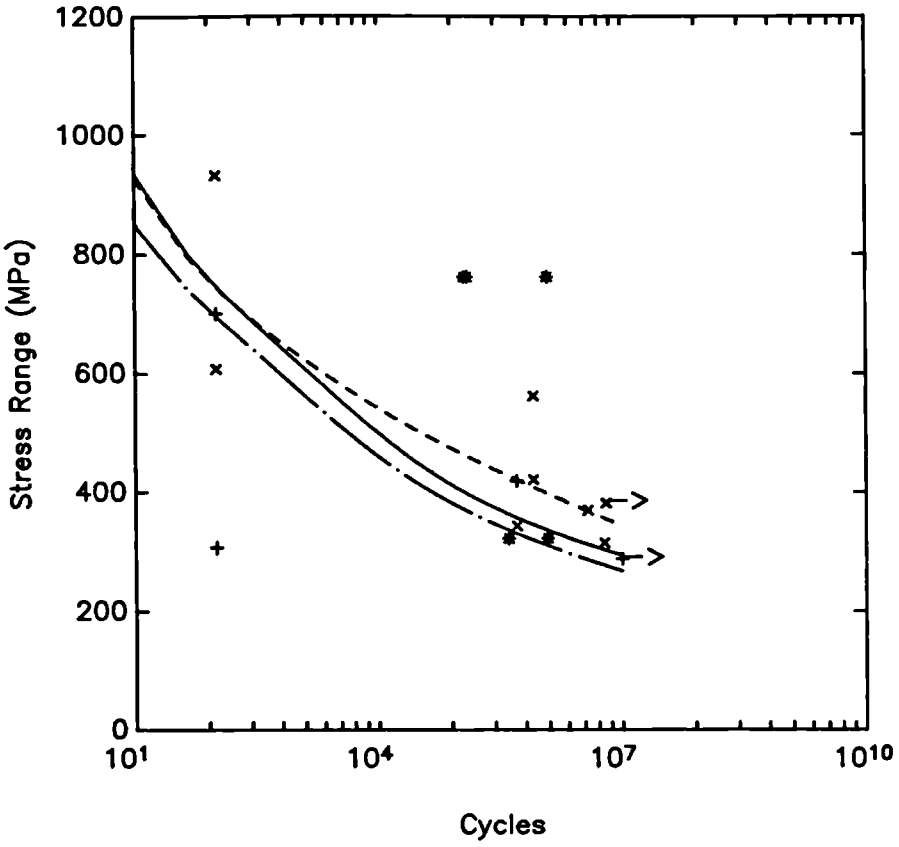

x	4145H
+	AG17
*	VAM
———	Prediction
——·——	Manson-Hirschberg Universal Slopes
– – – –	Muralidharan-Manson Universal Slopes

Fig 5.1

Fatigue Crack Initiation Lives

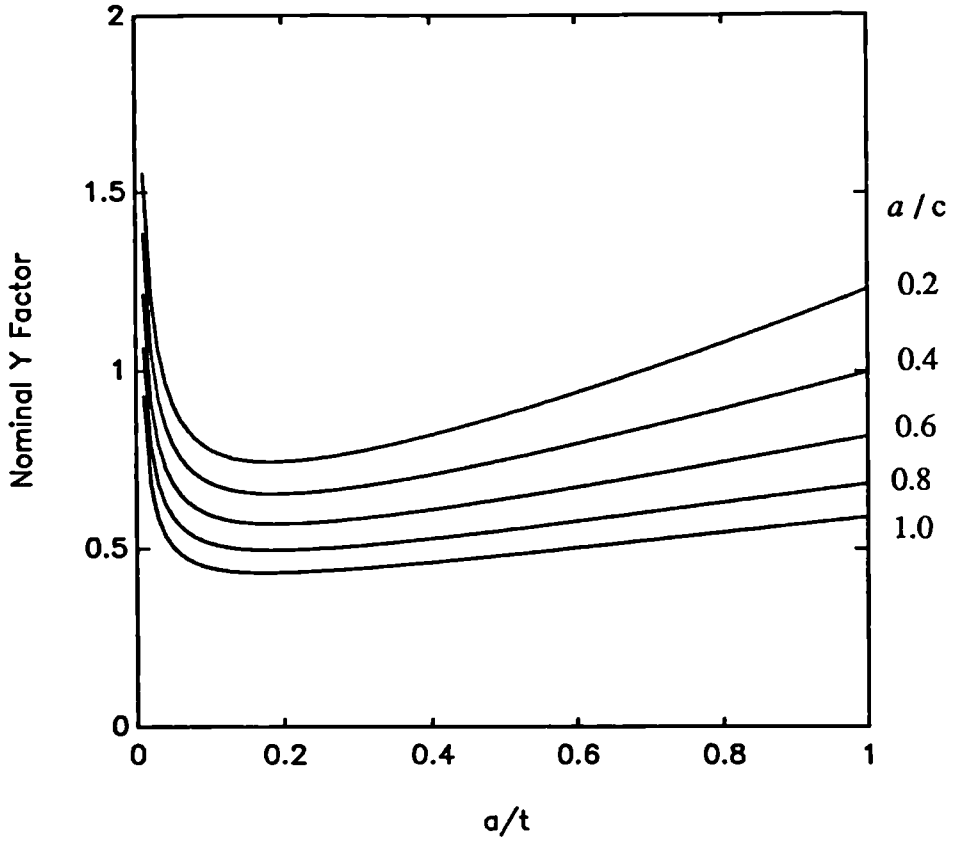

Fig 5.2

Nominal Y factors for VAM Joints

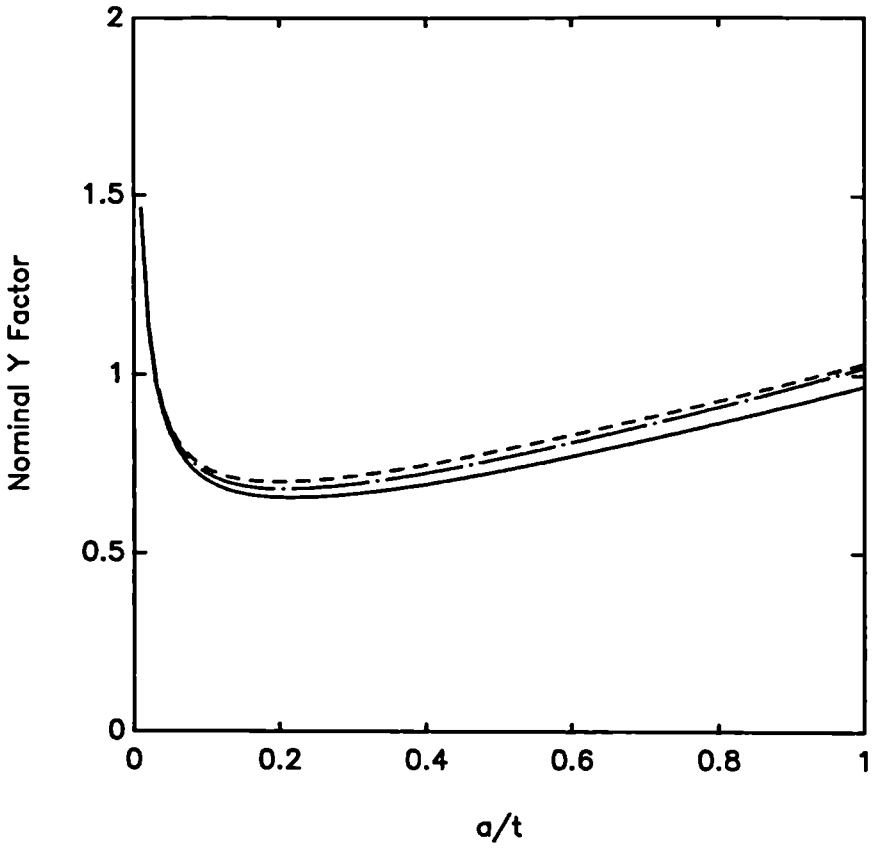

Constant Amplitude Test 1

Variable Amplitude Test 1

Variable Amplitude Test 2

Fig 5.3

Nominal Y Factors for VAM Tests 1, 4 and 5

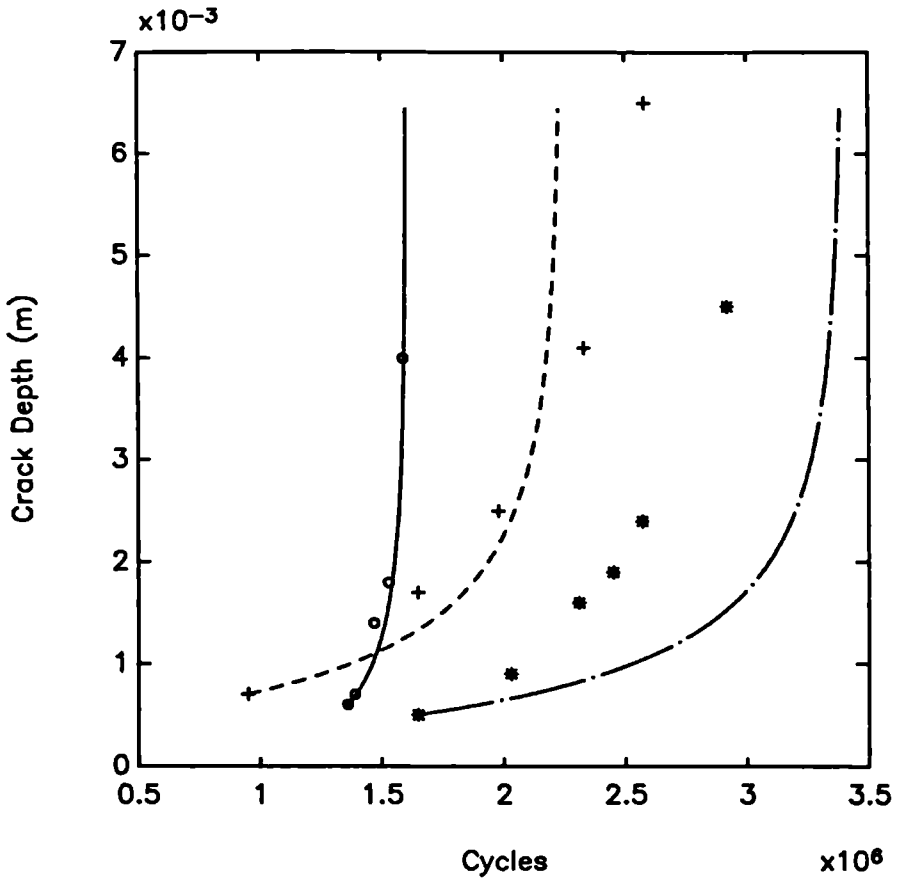

o, ——————— Constant Amplitude Test 1

+, – – – – – Variable Amplitude Test 1 (4)

*, ——·—— Variable Amplitude Test 2 (5)

Fig 5.4

VAM Joint Fatigue Predictions and Experimental Results

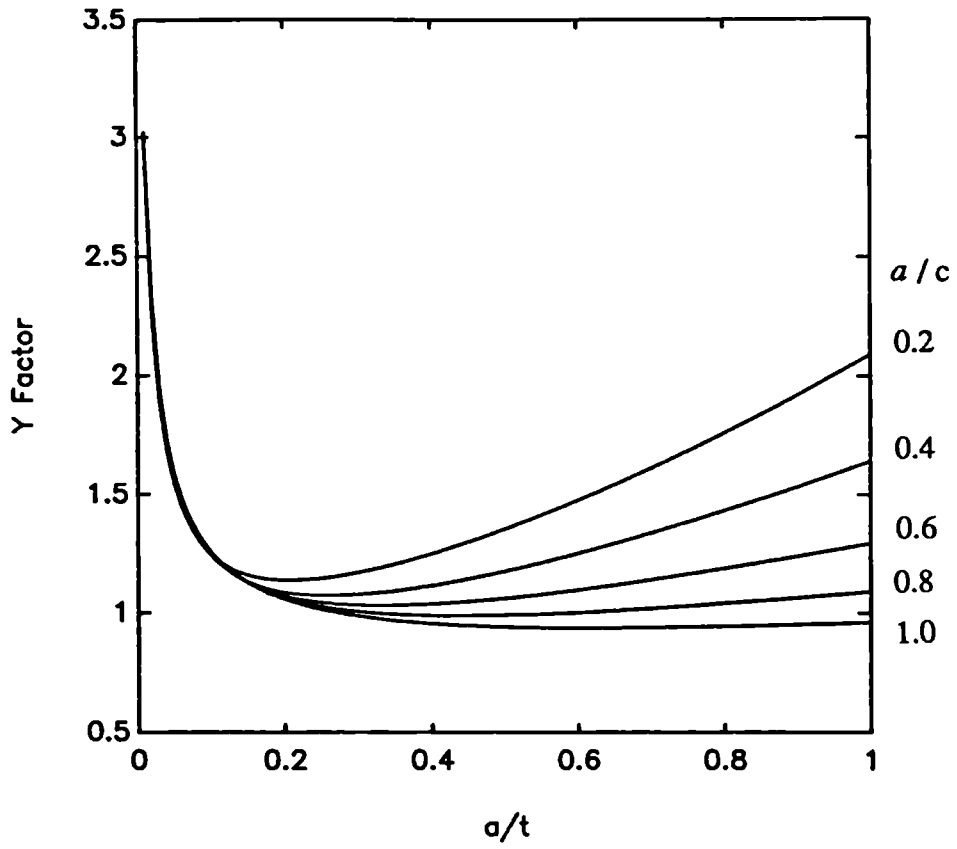

Fig 5.5

Y factors for Cracks in an NC50 Box under Tension

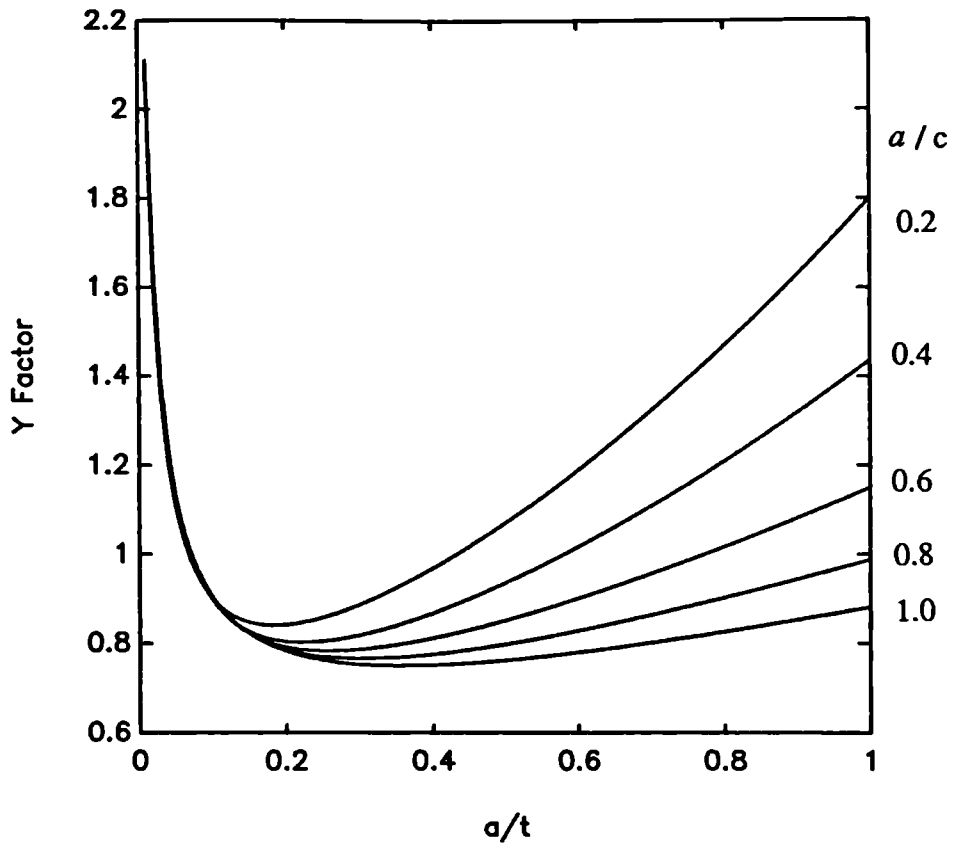

Fig 5.6

Y factors for Cracks in an NC50 Box under Bending

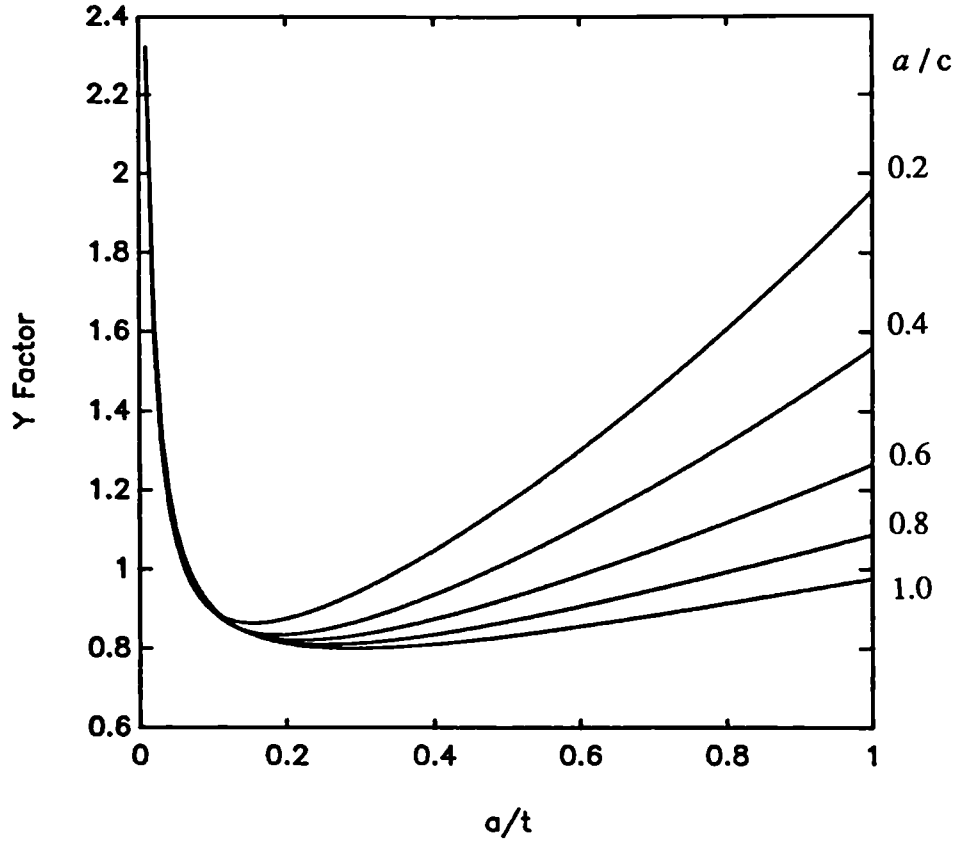

Fig 5.7

Y factors for Cracks in an $6^{5}/_{8}$" Reg Box under Tension

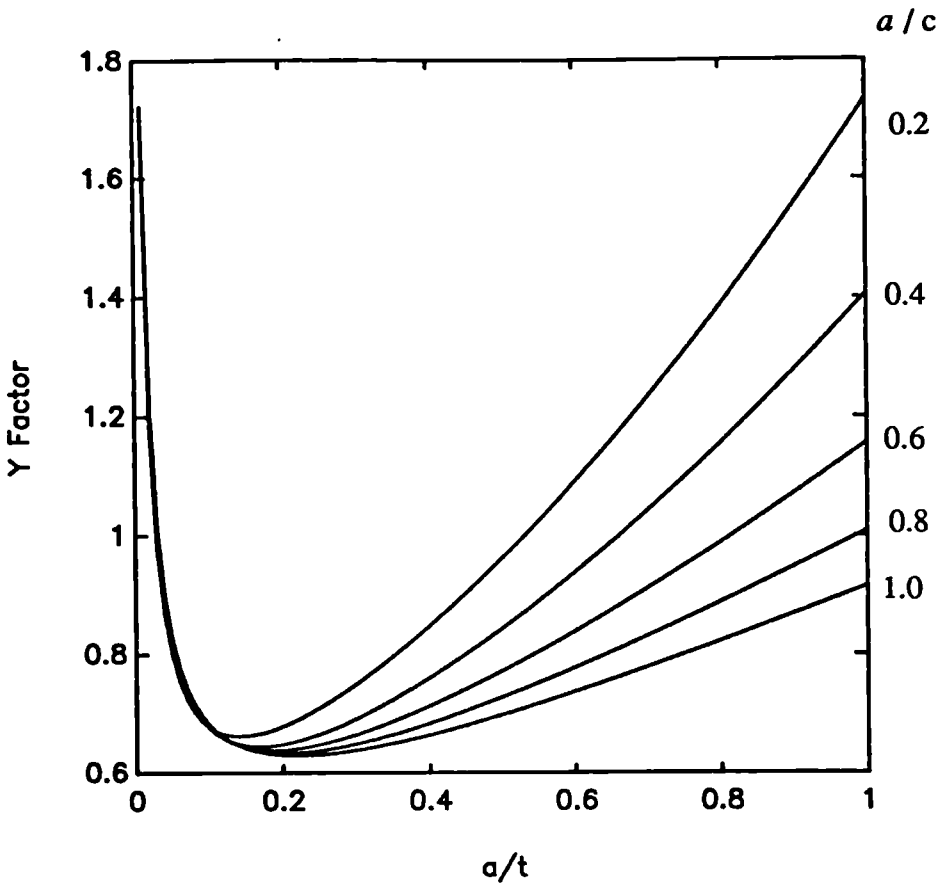

Fig 5.8

Y factors for Cracks in an $6^{5}/_{8}$" Reg Box under Bending

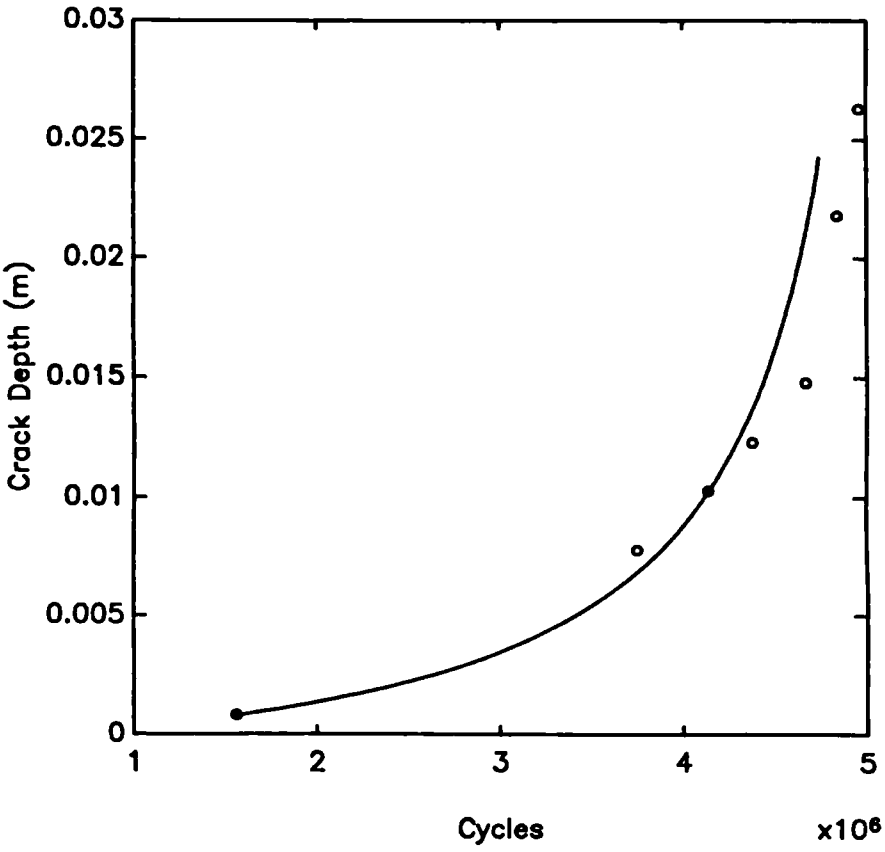

Fig 5.9

Prediction and Experimental Crack Growth Rates for Axial Test 1

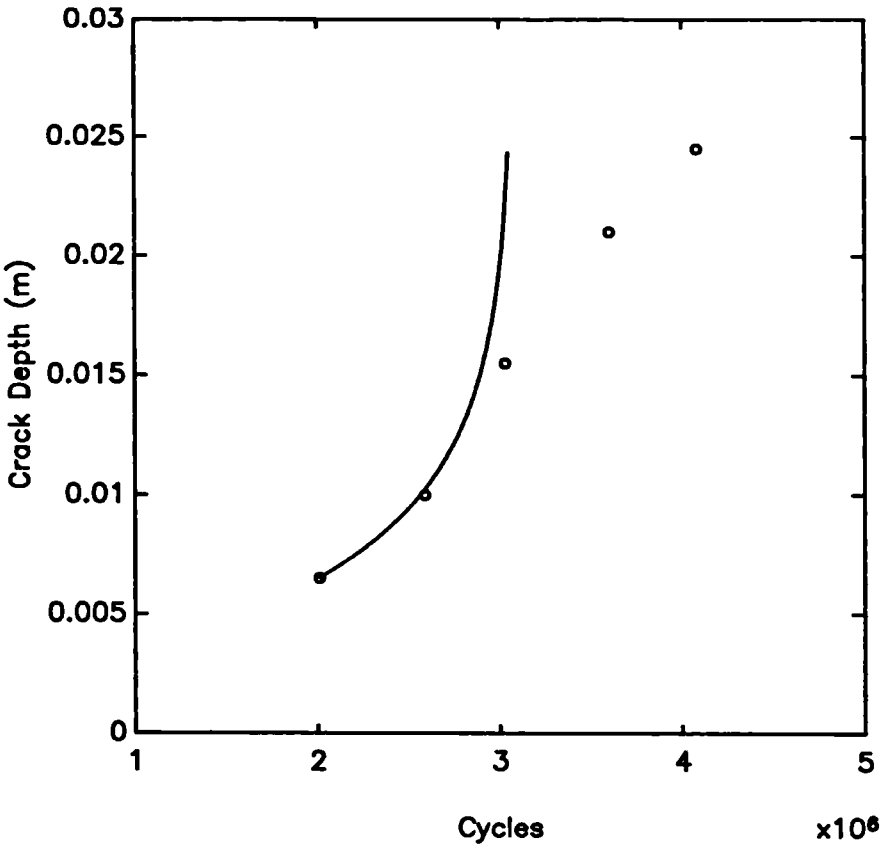

Fig 5.10

Prediction and Experimental Crack Growth Rates for Axial Test 2

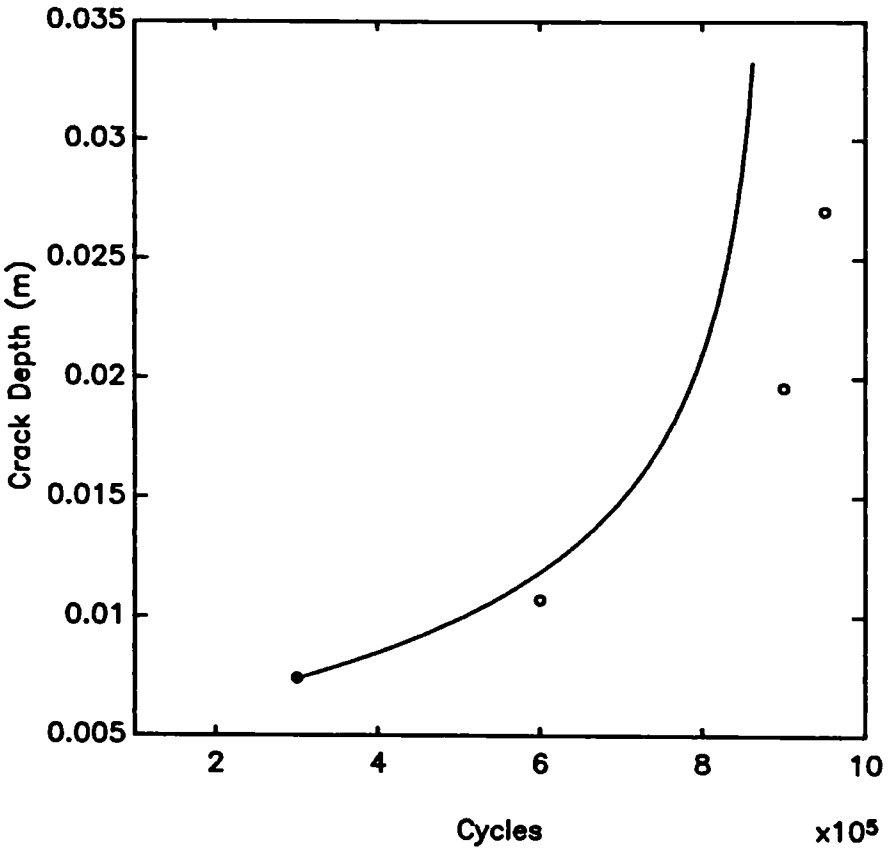

Fig 5.11

Prediction and Experimental Crack Growth Rates for Axial Test 3(b)

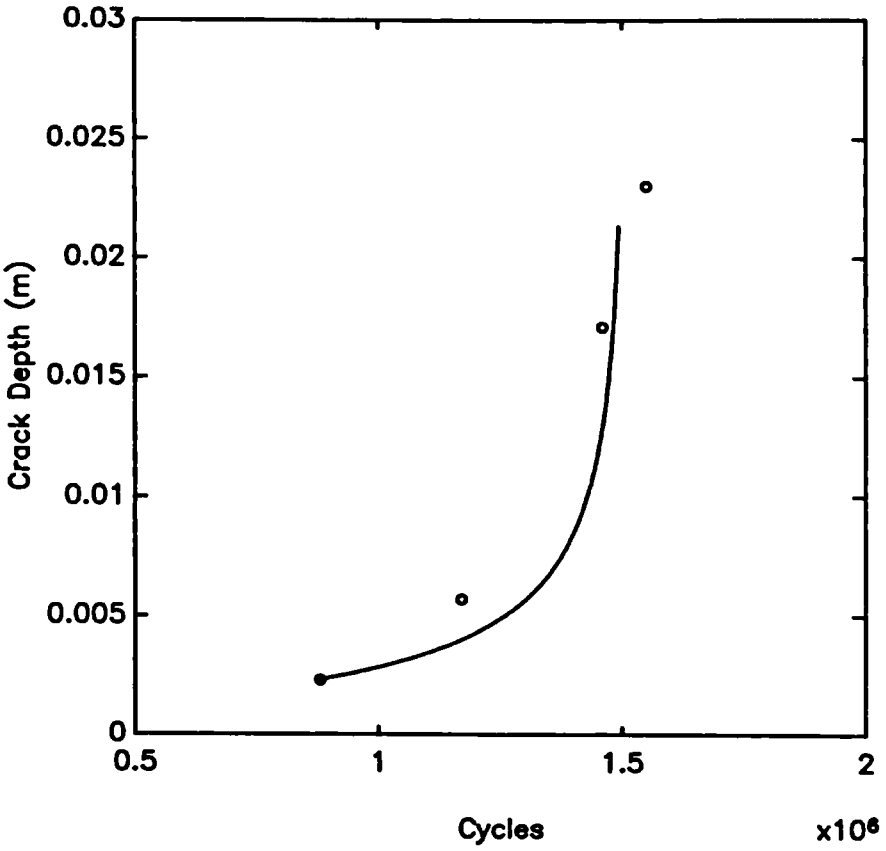

Fig 5.12

Prediction and Experimental Crack Growth Rates for Axial Test 5

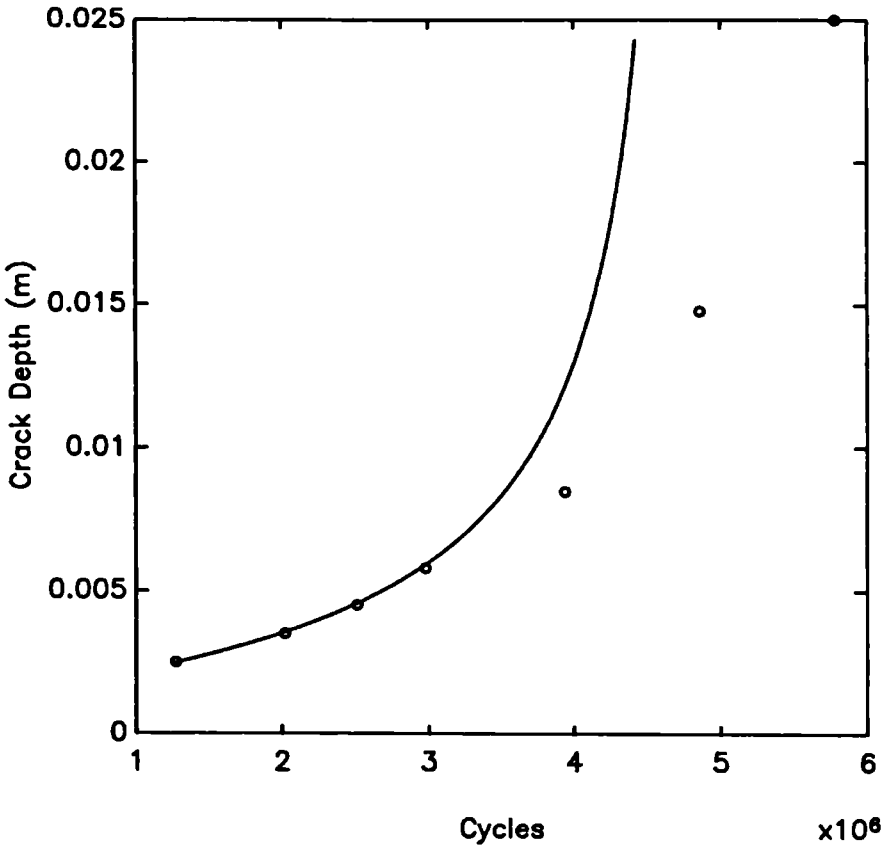

Fig 5.13

Prediction and Experimental Crack Growth Rates for Rotating Bend Test 1

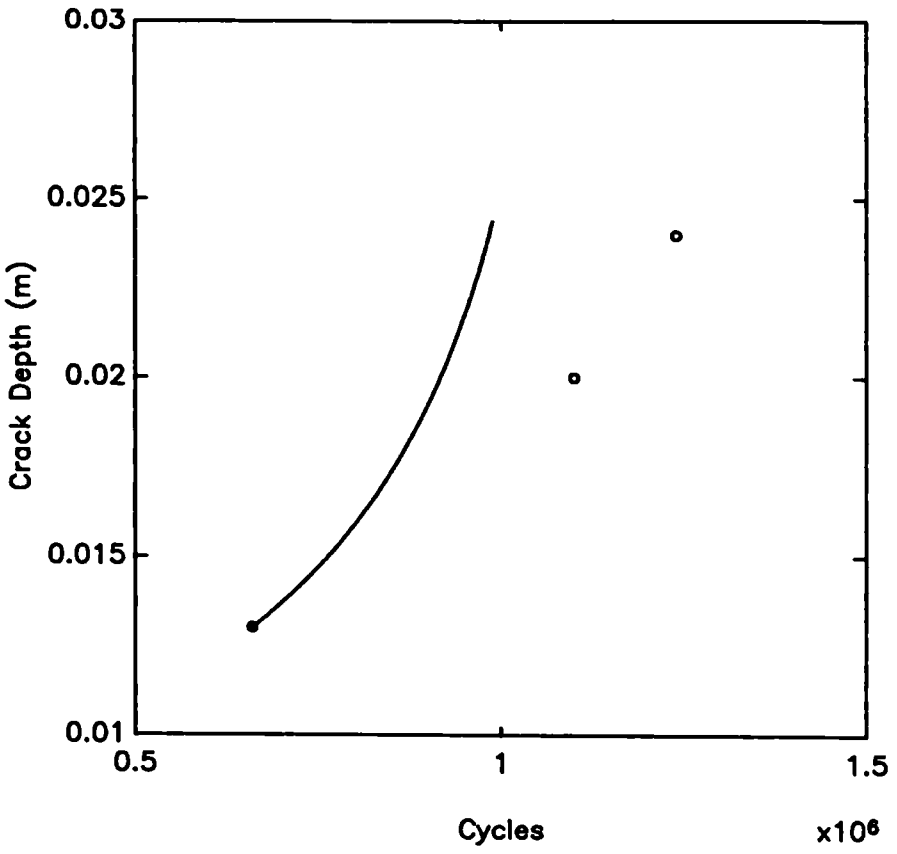

Fig 5.14

Prediction and Experimental Crack Growth Rates for Rotating Bend Test 2

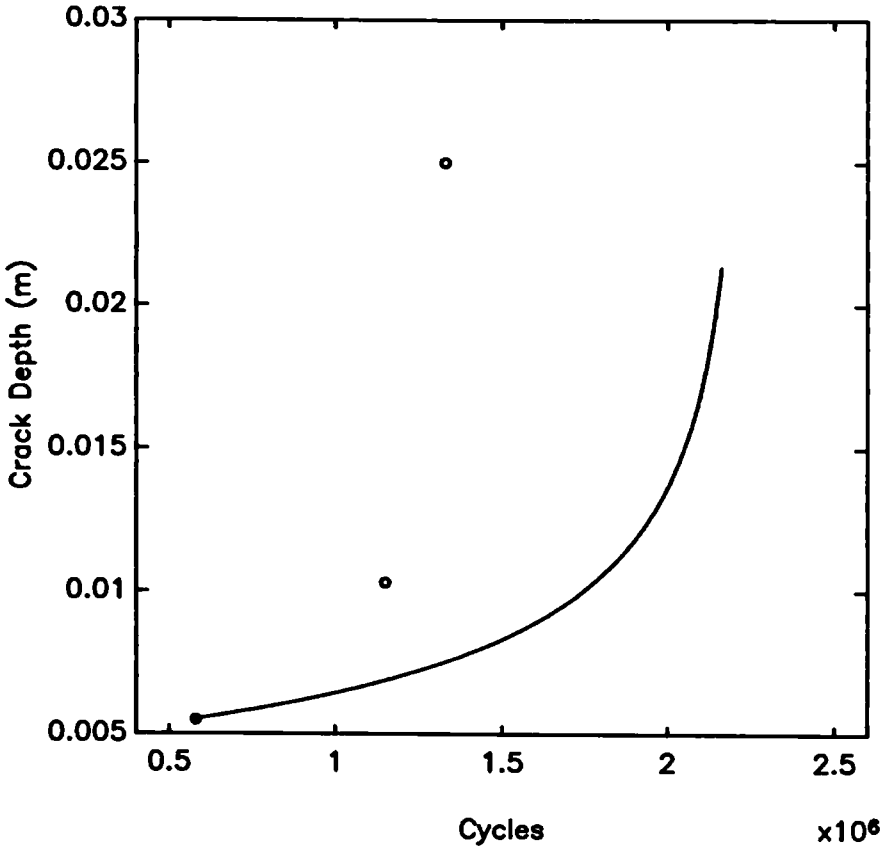

Fig 5.15

Prediction and Experimental Crack Growth Rates for Rotating Bend Test 3

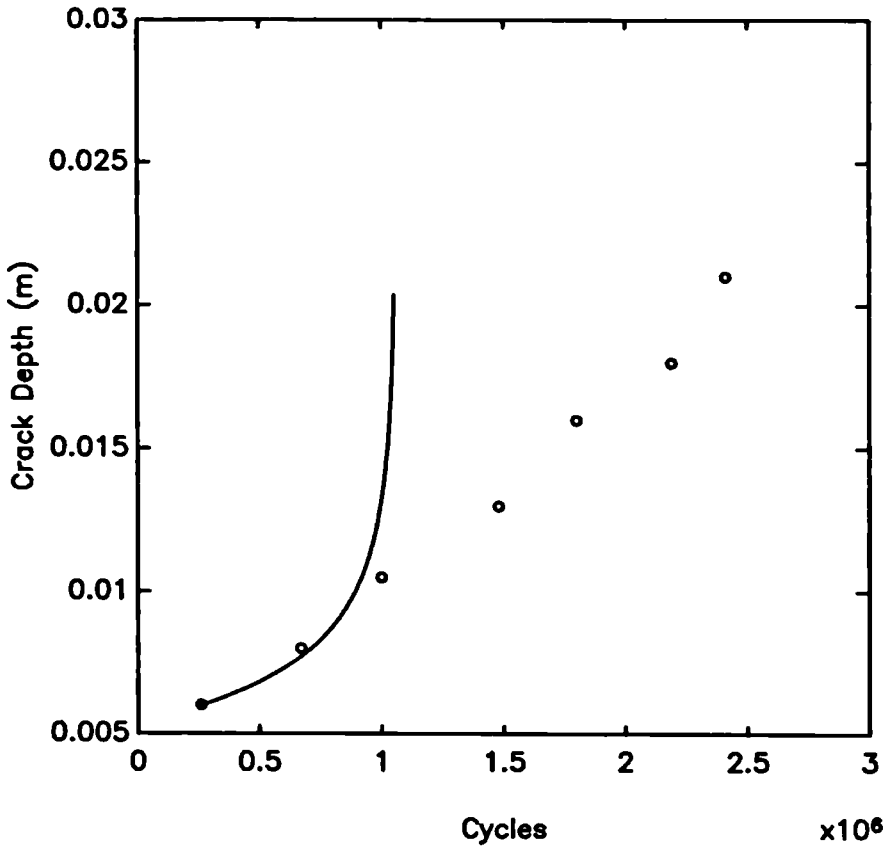

Fig 5.16

Prediction and Experimental Crack Growth Rates for Rotating Bend Test 4

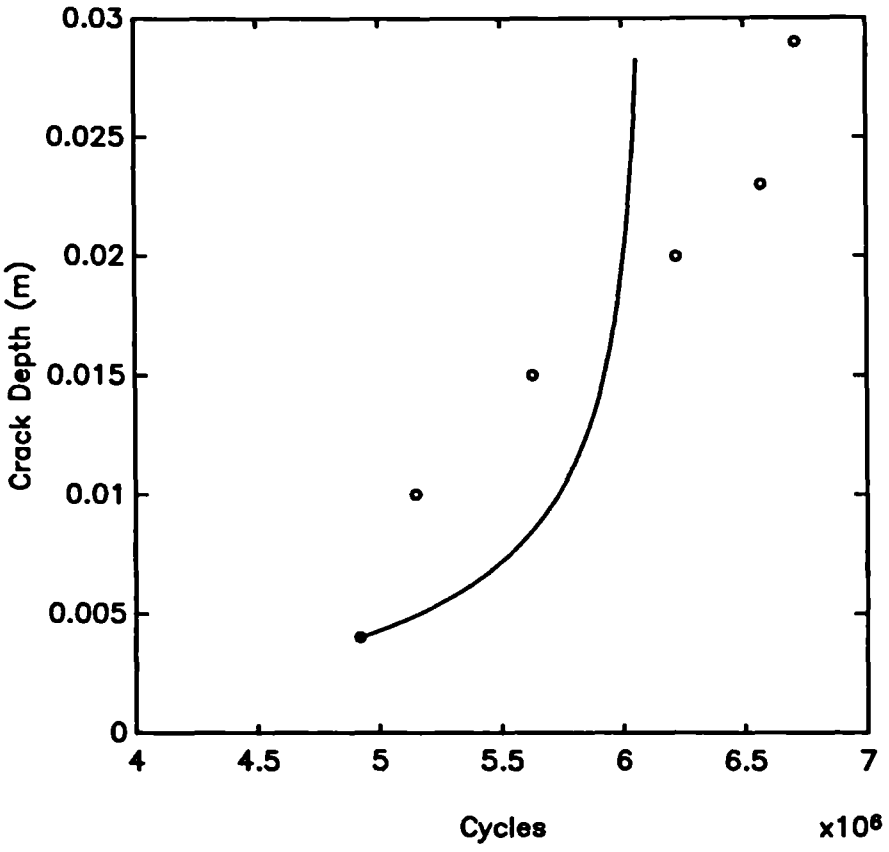

Fig 5.17

Prediction and Experimental Crack Growth Rates for Rotating Bend Test 5

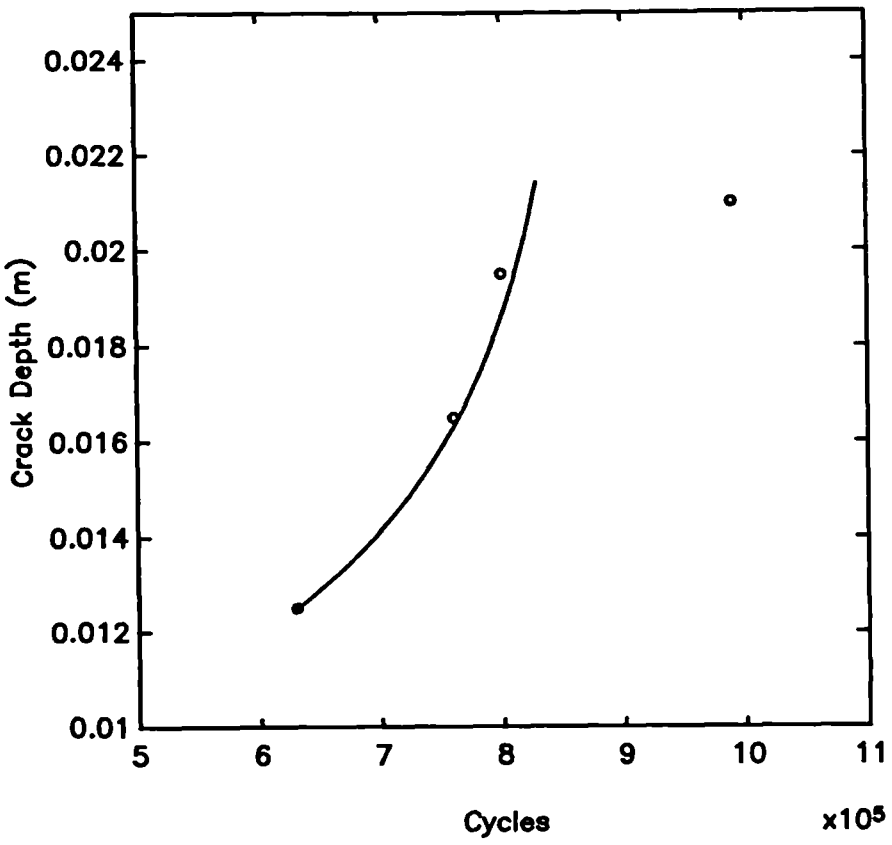

Fig 5.18

Prediction and Experimental Crack Growth Rates for Rotating Bend Test 6

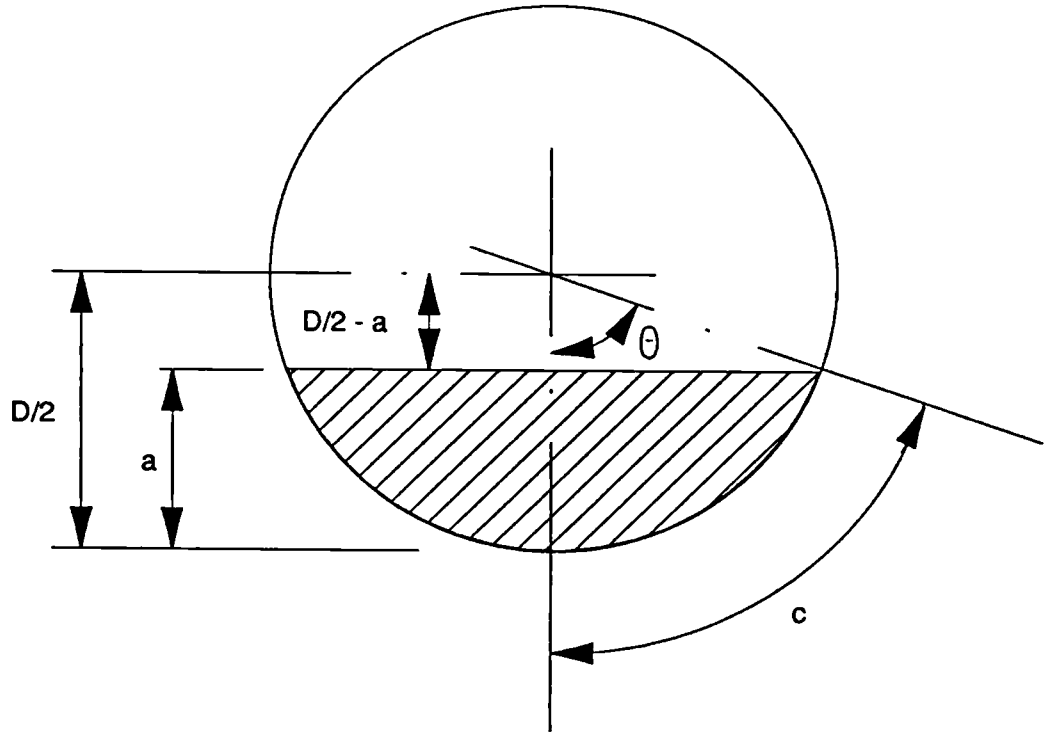

$$\theta = \mathrm{Cos}^{-1}\left[\frac{\frac{D}{2}-a}{\frac{D}{2}}\right]$$

$$i.e. \quad c = \frac{D}{2}\mathrm{Cos}^{-1}\left[1-\frac{2a}{D}\right]$$

Fig 5.19

Edge Crack in a Circular Rod

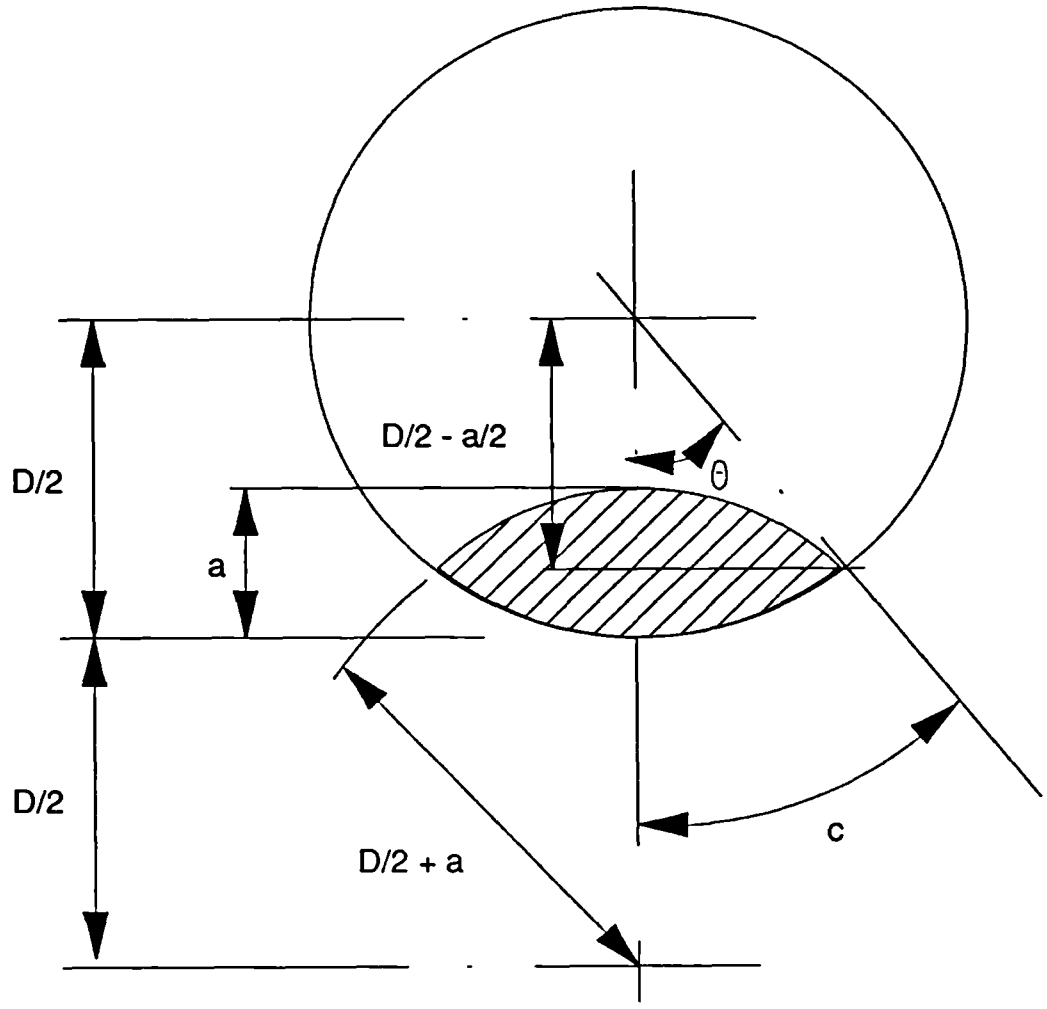

$$\theta = \mathrm{Cos}^{-1}\left[\frac{\frac{D}{2}-\frac{a}{2}}{\frac{D}{2}}\right]$$

$$i.e. \quad c = \frac{D}{2}\mathrm{Cos}^{-1}\left[1-\frac{a}{D}\right]$$

Fig 5.20

Circular Crack in a Circular Rod

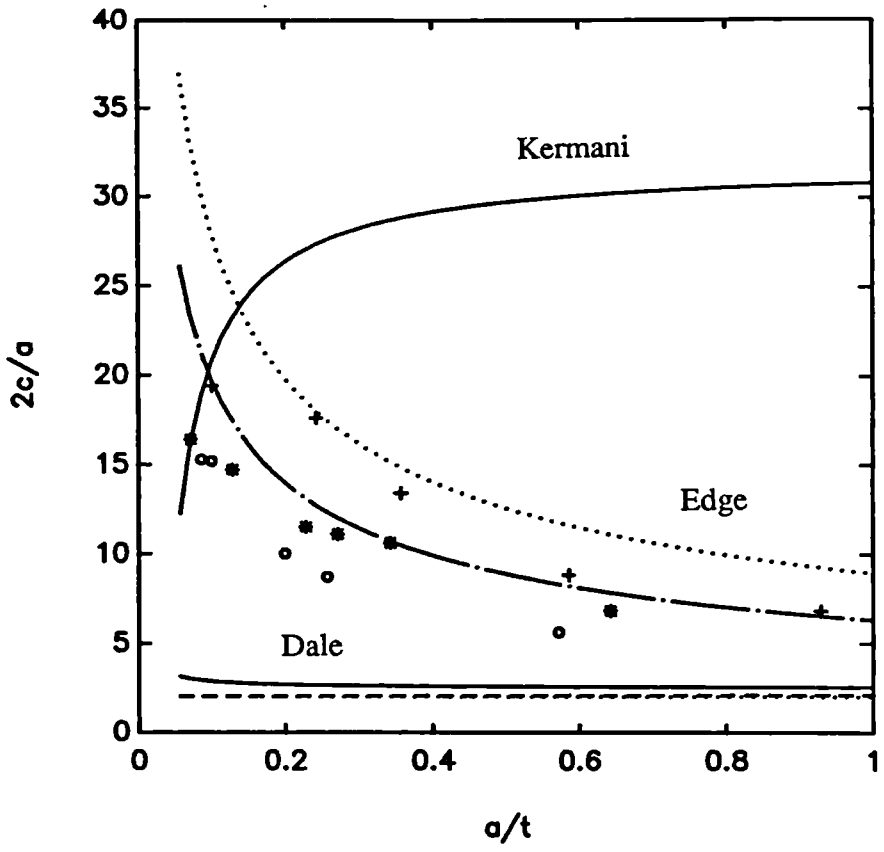

————	Kermani
.....	Edge: $c = \frac{D}{2}\text{Cos}^{-1}\left(1-2\frac{a}{D}\right)$
——·——	Circular: $c = \frac{D}{2}\text{Cos}^{-1}\left(1-\frac{a}{D}\right)$
————	Dale
– – – – –	Forman &
.....	Schivakumar

Fig 5.21

VAM Joint Crack Aspect Ratio

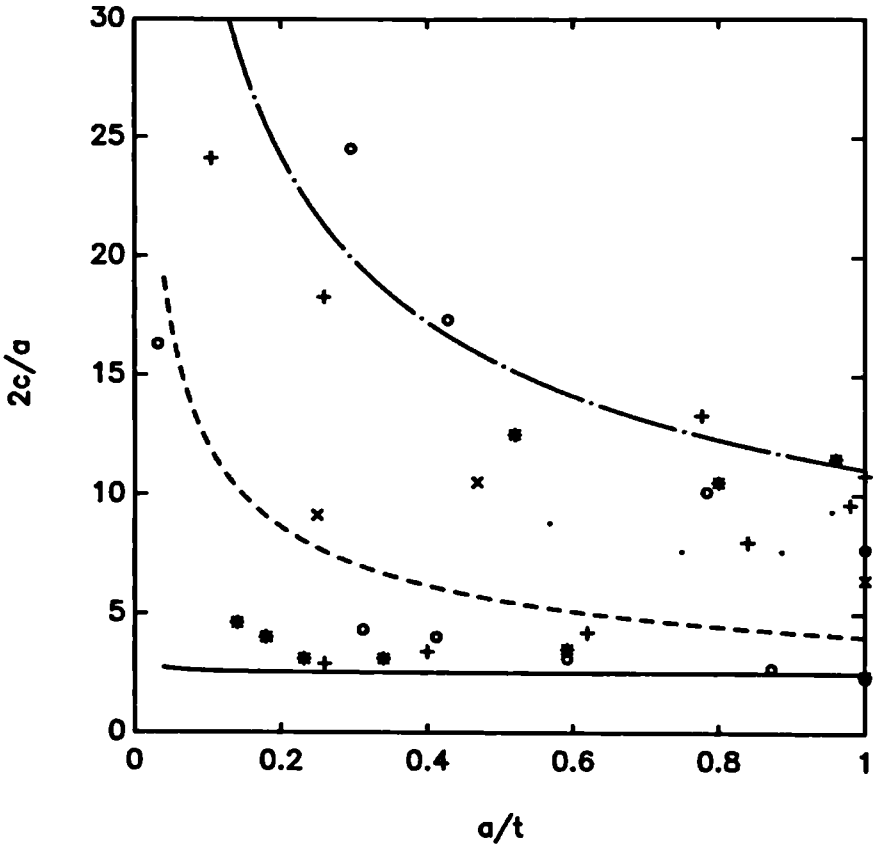

——————— Dale

– – – – – $c = \frac{D_i}{2}\text{Cos}^{-1}\left(1 - 2\frac{a}{D_i}\right)$

——·—— $c = 2D_i\,\text{Cos}^{-1}\left(1 - \frac{a}{D_i}\right)$

High Cycle - Propagation Life

o Axial Test 1 - 4.41 x 10^6
\+ Axial Test 2 - 3.63 x 10^6
* Rotating Bend Test 1 - 4.98 x 10^6

Low Cycle - Propagation Life

o Axial Test 3(b) - 0.95 x 10^6
\+ Axial Test 5 - 1.05 x 10^6
* Rotating Bend Test 2 - 1.24 x 10^6
x Rotating Bend Test 3 - 1.33 x 10^6
. Rotating Bend Test 6 - 0.99 x 10^6

Fig 5.22

Drill Collar Box Crack Aspect Ratio

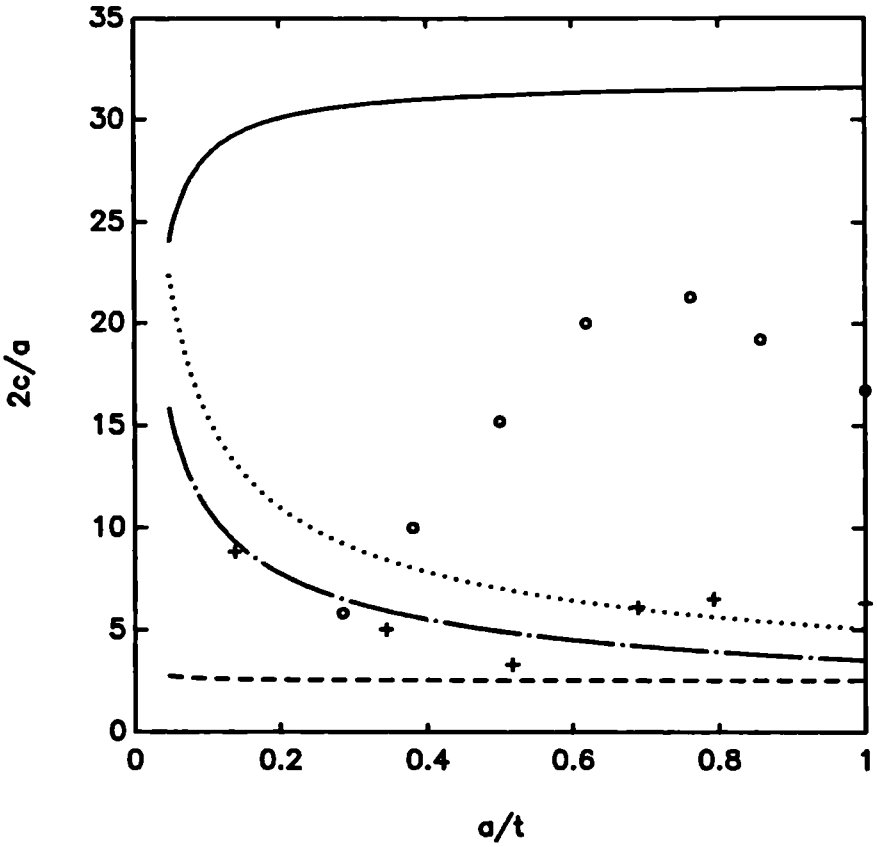

———————	Kermani
.....	Edge: $c = \frac{D}{2}\text{Cos}^{-1}\left(1-2\frac{a}{D}\right)$
——·——	Circular: $c = \frac{D}{2}\text{Cos}^{-1}\left(1-\frac{a}{D}\right)$
– – – – –	Dale
	Propagation Life
o	Rotating Bend Test 4 - 2.41 x 10^6
+	Rotating Bend Test 5 - 2.91 x 10^6

Fig 5.23

Drill Collar Pin Crack Aspect Ratio

CHAPTER SIX - Degradation of Threaded Connections: Factors Associated with their Locale

6.1 Introduction

The fatigue crack growth prediction models developed in this thesis are idealised designs. As with most text book solutions, the structural material is assumed to be uniform, homogeneous, isotropic and chemically inert. Stresses and subsequent strains result solely from the applied loads without any provision for environmental degradation of the material, or material inconsistencies due to forming and succeeding fabrication processes. There are two approaches that may be applied to overcome these discrepancies between theory and reality. The first is to eliminate, control or counteract the inexpedient mechanism. When this is not appropriate or is impossible, the next approach is to quantify the influence of the hostile system and apply an apposite correction to the theoretical solution. In order to do this, the situation must be defined and understood as best possible.

This chapter studies the commoner types of high strength steels encountered in threaded connections, with specific regard to their vulnerability to corrosive attack. Common engineering practices such as plating threads, and the use of lubricants are examined in terms of influencing fatigue performance. The mechanisms of corrosion are investigated and their relevance to threaded connections explored. Implementation of the corrosion fatigue data presented is discussed with respect to the fatigue crack initiation and propagation models developed for threaded connections.

6.2 Threaded Fasteners: Steels, Coatings and Lubricants

The chemical composition of steel is an important characteristic particularly where applications require elevated temperature service, corrosion resistance or toughness. However, classification of steels for threaded fasteners is primarily through strength levels. Modern metallurgy is a highly competitive industry especially in the field of high strength steel alloys. For this reason and because many application industries have their own specifications and standards, there is a confusing variety of codes

describing mechanical properties of steels. The most widely quoted specifications of steel strength or performance level for threaded fasteners are those of the Society of Automotive Engineers (SAE), the International Organisation for Standardisation (ISO), the American Society for Testing and Materials (ASTM), the Industrial Fasteners Institute (IFI) and the American Petroleum Institute (API). The British Standards Institute (BSI) uses the ISO strength grade designation, examples of which are shown in Tables 6.1 and 6.2 [6.1]. The number following the decimal point in a class number for a bolt or stud indicates the ratio of the yield strength to the tensile strength. Any steel which satisfies the characteristics of a property class may be used to comply with that standard. The hardenability of the steels used for threaded fasteners is important when selecting the chemical composition of the steel. As the strength requirements and section size increase, achieving hardenability becomes more difficult [6.2]. For this reason, strength classes may only be valid for certain section sizes. For the purpose of this study, high strength steels having the American Iron and Steel Institute (AISI) classification and used for threaded couplings are reviewed with regard to corrosion fatigue characteristics. Table 6.3 [6.2] shows the composition of typical high strength low alloy (HSLA) threaded connection steels according to their AISI designation. Table 6.4 [6.2] shows their equivalent international classification codes. Most of those steels are hardenable, their mechanical properties varying depending on post solidification heat treatments.

Threads are often coated to protect against corrosion, to hold lubricant (hence prevent galling) or to lower the coefficient of friction. Gall resistant compounds are usually iron-manganese or zinc phosphate coatings. These are applied by dipping the threaded section into the hot coating solution. Zinc coatings are the most common form of corrosion protection for steels. These can be applied by electroplating, zinc phosphating, hot dipping or mechanical plating. Zinc coatings are rarely used on high strength connectors that demand a high life expectancy. Cadmium coatings are quite common on high strength structural fasteners ("black bolts"). Besides their greater resistance to corrosion in marine environments the electroplated coatings enhance torque-preload relationships by providing low coefficients of friction. Aluminium coatings are by far the best against atmospheric, marine and high temperature corrosion. These coatings are applied by hot dipping. In elevated

temperature applications they also protect against galling. High strength fasteners (usually high carbon content) are susceptible to hydrogen embrittlement when being acid cleaned, electrocleaned or electroplated. They should be treated after these processes or fatigue resistance could be severely reduced. Chromium and nickel platings also reduce fatigue strength. Brittle coatings or cases such as carburizing or carbon nitriding are not recommended where fatigue endurance is required.

Lubricants are used in making up threaded joints to enhance torque-preload performance (hence strengthening the joint) and ensuring the joint can be broken, for this reason the lubricant must remain inert under applied stressing. Threaded fasteners fabricated from high strength steels are normally expected to withstand high applied loads implying high internal stresses in the connection. Breakdown of the lubricant in such situations invariably results in fretting on the contact flanks of loaded teeth. High pressure compounds are usually lead based greases containing molybdenum disulphide as a binding agent. However, for very high pressure applications a powdered metallic zinc base is preferred.

6.3 Corrosion Mechanisms

Corrosion is an electrochemical reaction therefore there must always be an electrolyte present to supply free positively charged iron atoms with electrons. Oxygen is generally required, and corrosive action is also temperature dependant. Atmospheric corrosion is perhaps the most common form. Rates of corrosion vary widely with relative humidity and the presence of contaminants such as sulphur and chlorides. Only rarely does corrosion result in a uniform loss of section over the entire surface of engineering structures. More often corrosion results in a localised attack, producing pits, blisters, cracks and crevices which can lead to a catastrophic failure, particularly if mechanical stresses are present. Galvanic corrosion is especially relevant to connectors. Dissimilar metals will have different electrical potentials relative to a standard hydrogen electrode as defined by the electromotive series. If a material is anodic when electrically connected to another metal it will corrode. Galvanic coupling can arise between male and female components of threaded connections. However, it can also arise on a microscopic scale in a two phase alloy. If one phase is anodic relative to the other, attack will be concentrated

on that particular phase. The microstructure of an alloy is very important in determining the morphology of corrosive attack. Generally anything which leads to inhomogeneity in the structure of a metal or alloy is a potential source to corrosive attack. Even single crystals are not immune to localised corrosion. Attack can take place at dislocations, point defects and grain boundaries producing etch pits.

Generally localised corrosive attack results from the spatial separation of anodic and cathodic sites. However, the intensity of attack can vary considerably from system to system. One of the most important factors leading to an increased intensity of localised attack is the relative areas of anodic and cathodic sites. Since the anodic current must equal the cathodic current, then if the anode has a small area relative to the cathode, the anodic current density can be extremely large. Metals immersed in marine water are severely threatened by corrosion. Besides salt water being a better electrolyte than fresh water, chloride ions present break down protective oxide films on metal surfaces. Again availability of oxygen is important, making steels in the proximity of the water line or splash zone particularly vulnerable. Bolted connections are susceptible to crevice corrosion where oxygen differentials make oxygen depleted areas anodic relative to areas having higher oxygen concentrations.

Stress Corrosion Cracking (SCC) is the general term given to environment assisted cracking under sustained or repeated tensile stressing. It is an intergranular fracture mechanism and is therefore dependant on grain orientation, making some materials more susceptible. Hydrogen embrittlement is understood to be the main mechanism contributing to the degradation of steel under SCC. Free hydrogen ions form on wet metal surfaces due to corrosion. These can enter the steel interstitially making the steel less ductile, causing it to fail in a brittle manner. This loss in ductility is attributed to the combining of the hydrogen atoms with impurities such as oxide or sulphide inclusions in the steel, to produce gas pockets within the metal. This internal hydrogen generates significant internal pressure which can result in the formation of blisters and cracks or just provide more obstacles to dislocation movement. In the presence of H_2S (abundant in sour gas wells) the rate at which free hydrogen ions can combine is greatly reduced leaving more free hydrogen ions available to enter the steel. This is known as sulphide stress cracking. API restricts the higher

strength steel grades from operation in such environments [6.3]. In general the susceptibility of steels to SCC increases with increasing yield strength. Gases containing less than 0.0035atm. of H_2S are considered sweet. Sweet corrosion is a type of corrosion often associated with gas well tubing, and is caused by the presence of CO_2. The CO_2 dissolves in water to form carbonic acid, the acidity depending upon the partial pressure of CO_2 gas. The acid reacts with the steel to form iron carbonate. At low velocities the film is protective. At areas of high turbulence, the film breaks down locally producing large deep pits.

Corrosion rates of steel in water are relatively constant between pH 4.5 and 9.5, but increases rapidly at lower pH values and decreases slowly with higher pH solutions (alkaline). This becomes important when dealing with pipe connectors where the conveyed medium can be controlled. Increased velocity of an electrolyte also severely increases corrosive action by removing protective oxide layers. Preferential corrosion occurs at areas of high turbulence. In field oil and gas pipelines, flow in the pipe is generally turbulent. However, locations of geometric discontinuity give rise to very high turbulence, and these often become areas having the highest corrosion rates. Susceptible areas on main transmission lines are at low spots where water can collect. In drill pipes and collars, corrosion can be minimised by using oil based rather than water based muds. However, with the latter, oxygen scavengers and control of pH can limit corrosion damage [6.4]. Care must be taken when choosing mud pH for high temperature applications, as some muds such as lignosulphonates, can break down producing sulphides [6.5].

Chung [6.6], identified high preload levels as being a main contributing factor to SCC in high strength steel bolts. Most standards traditionally recommend preload levels of seventy to one hundred percent of the minimum bolt proof load. Fig 6.1 shows the threshold stresses (defined by σ_{scc}) for HSLA steels with respect to hardness. This shows the need to reduce hardness especially for larger bolts and also raises the concern for an upper bound on preload.

Cathodic Protection (CP) is often used to inhibit corrosion. This is performed by coating with a sacrificial anode or by using an impressed current system where a

d.c. supply is used to satisfy the electron "gobbling" action of the corrosion process. However, the magnitude of the current is critical, and over protection often results in accelerated crack growth. Brown [6.7], in his review on CP of structural and line pipe steels observed that a moderate degree of CP can improve fatigue resistance of these steels. At lower stresses their behaviour can often approach that expected of an air environment. Understanding the specific corrosion mechanism acting on a particular system is important in order to implement corrosion fatigue crack growth rate data to that system [6.8]. Factors such as R - ratio, corrosive medium (chemistry, velocity, pressure, temperature etc.,) and specimen thickness must all be considered. Crack growth data is usually interpretated in terms of Paris coefficients as functions of stress intensity factor. In the case of prediction of crack initiation in a corrosive environment, an S-N approach is usually the most realistic technique.

6.4 Fatigue Behaviour of Connector Steels

As mentioned earlier, these steels are hardenable, meaning that there are many "customised" versions of the steels having similar chemical compositions but their mechanical properties differing widely. An example of this is shown in Fig 6.2 [6.9], which shows the fatigue behaviour of AISI 4140 steel in air, but with varying hardness levels. Rockwell hardness number 20 was achieved by stress relieving at 550 °C for one hour and furnace cooling. An oil quench from 850 °C, tempering for one hour at 625°C and air cooling gave a Rockwell hardness of 28. The same quench but tempering at 515 °C gave a hardness of 37. The steel having a hardness number of 44 was tempered at 415 °C, and finally the hardest steel resulted from a straight oil quench. The variation in fatigue behaviour is dramatic as the steel becomes progressively more hard and brittle showing an increase in fatigue strength. More striking is the rate at which the harder steels degrade in corrosive environments. Fig 6.3 shows the same steels in a solution of deaerated 3% NaCl. There is no apparent change in behaviour of the less hard steels, but the high stress - low cycle regime is considerably different with escalating steel hardness and subsequent strength. Aerating the 3% NaCl solution (Fig 6.4) sees the endurance limits disappear altogether as the corrosion mechanism becomes a prime influence on the fatigue resistance of the steel. Again the change is more marked for the higher

strength versions of the 4140 steel. Fig 6.5 plots together the behaviour of the 44 hardness steel in the three environments. All the tests were conducted at 25 °C, however the important cycling frequency for the corrosion tests was not reported.

S-N behaviour of a selection of thread steels is reported in reference [6.10]. Their chemical compositions and mechanical properties are given in Table 6.5. Figs 6.6-6.8 show the behaviour of these steels in sea water. Each steel is represented by two curves, one displaying an endurance limit which is its manner when cathodically protected, the other curve demonstrates behaviour under free corrosion conditions. All experiments were at a frequency of 1.0 Hz and an R ratio of 0.5. Cathodic polarization was at -1.1 V. Seven of the nine steels represent relatively new strengthening technology namely, precipitation hardening, microalloying - quenching - tempering, control rolling and thermomechanical control processing (TMCP). The published results were given in terms of stress intensity factor divided by the square root of notch radius, these are corrected to give S-N plots in this study, in the interest of consistency. Again it is apparent that the higher yield strength steels are more affected by corrosion action. Fig 6.9 [6.11] summarises the endurance data with respect to tensile strength. Reference [6.12] studying AISI 4340 steels with varying strength levels concluded that the increase in fatigue crack growth rate for 4340 steel exposed to a H_2S gas environment is directly dependent on material yield strength.

A key influencing variable in corrosion fatigue is cyclic frequency. In freely corroding conditions, the rate of crack growth is inversely related to cyclic frequency. Fig 6.10 [6.13] shows the increased crack growth rate with decreasing frequency of 4340 steel in distilled water at 23 °C. The dominance of frequency is directly related to the time dependence of the atomic transport and chemical reactions required for environmental cracking. A stress corrosion frequency threshold always exists. Above this value no change in crack growth rate is identifiable between air and corrosive environments. Higher critical frequencies are associated with more aggressive environments and sensitive microstructures. A lower frequency bound is shown by Wei *et al.* [6.14], frequencies below which no longer contribute higher crack growth rates, except due to sustained-load SCC. This is known as a saturation

or plateau level associated with low frequencies. Wave form will also effect corrosion fatigue crack growth rates. Reference [6.15] studied corrosion fatigue crack propagation varying cyclic stress rise, hold and decay intervals at a number of cyclic frequencies. This concluded that the crack growth rate is proportional to the time the crack tip is exposed. The elaborate chemical processes and multivariable relative nature of corrosion fatigue makes it practically impossible to theoretically predict the frequency range at which corrosion fatigue is most severe. Fig 6.11 [6.16] shows a similar frequency dependence of corrosion fatigue propagation in 3.5% NaCl solution of X65 pipeline steel. This study found that the tensile ductility of X65 steel is reduced if loading is carried out in 3.5% NaCl solutions at potentials less than -0.8V. The ductility decreases as the potential and strain rate are decreased. Reference [6.17] also shows X65 corrosion fatigue behaviour, but in hydrogen sulphide. A study on a relevant connector steel, 708M40 [6.18] shows (Fig 6.12) the crack growth dependence on frequency, when the steel is cyclically tensioned in a hydrogen gas environment. In this high pressure situation a progressive enhancement of crack growth rates was observed as the frequency was reduced over the range 10 - 0.01 Hz. The difference in acceleration reached a factor of twenty between both extremes. It was observed that the enhancement of crack growth by hydrogen was associated with the appearance of quasi-cleavage facets on the otherwise ductile transgranular fracture surface. Besides frequency, one of the most important parameters that influences corrosion fatigue crack growth rates is the level of mean stress or R ratio (Fig 6.13 [6.8]). Increasing R ratio pushes the threshold stress intensity factor lower, decreasing frequency increases the crack growth rate to a lessening degree at higher stress ranges.

Hydrogen embrittlement has been identified as the main cause of material degradation in corrosive environments. The striking characteristic of hydrogen which sets it apart from other causes of embrittlement is its large diffusity. There is no significant variation in diffusity between various metals and alloys that will greatly effect embrittlement, but it is severely dependent upon temperature. Fig 6.14 [6.19] shows this dependence in terms of fatigue crack growth rate. Hydrogen embrittlement is more pronounced in cold worked or unstressed relieved materials. Fig 6.15 [6.20] shows the results of fatigue pressure tests on a 34CrMo4 steel

(equivalent to 4135). Upper and lower bounds are shown, between which the results fall for each test series. Once more the adverse effect of hydrogen is apparent relative to the tests in hydraulic oil.

Fig 6.16 [6.21] shows the effect of various environments on fatigue crack growth rates in HY130 steel. The curve for the 0.6M NaCl solution is the same as for cracking in distilled water (not shown), indicating that the chloride ion is relatively innocuous and that water is the apparent cause of the increased crack growth rate when compared to the air curve. The effect of pH can be observed considering the two curves 0.1N HCl (pH ~ 1) and 0.1NaOH (pH ~ 13). There is no measurable difference between the behaviour of the steel in 0.1N HCl solution compared with that in 0.6M NaCl (pH ~ 6). However a threefold decrease in crack growth rate was observed in 0.1N NaOH solution at stress intensity factor values up to $30MPa\sqrt{m}$. Here the behaviour in the alkaline solution is similar to that obtained in air. At higher values of stress intensity factor, the alkaline environment induces crack growth rates approximately midway between those in air and in the more acidic environments. The final curve in a 0.6 M NaCl solution with an applied electrochemical potential of -0.1V, and shows a negligible effect of potential on crack growth below $30MPa\sqrt{m}$, but the effect increases with increasing stress intensity factor to approximately twice the crack growth rate in freely corroding conditions.

Like loading frequency, electrode potential strongly influences rates of corrosion fatigue crack propagation for alloys in aqueous environments. Controlled changes in the potential can result in either the complete elimination or the dramatic increase of fatigue cracking at certain stresses. Fig 6.17 [6.13] shows the effect of applied potential on 4140 steel in 3% NaCl. The effect is quite startling, the fatigue life in the range -0.55V to -0.85V is some one hundred times greater than that at the corrosion potential (-0.38V).

As well as the existence of a critical potential, a critical corrosion rate exists below which the aqueous environment no longer affects fatigue life at stresses below the fatigue limit. Fig 6.18 [6.9] shows the critical corrosion rates are about the same for both values of applied stress within experimental variations of the test.

Table 6.6 [6.22] compares the effects of cadmium and chromium electroplates and plasma sprayed tungsten carbide on 4340 steel in air and sea water. Coricone is an organic film for enhanced corrosion resistance. As expected the NaCl solution significantly degrades the fatigue strength of the bare steel. The degradation is more severe under conditions of rotating bending fatigue. Although the fatigue strength of WC + solid film lubricant coated steel is unaffected by the NaCl solution in rotating bending fatigue, it is significantly reduced in corrosion axial tension. NaCl solution degrades the rotating bending fatigue strength of both the Cd and Cr plated steel, but these are greatly more resistant than the bare specimens, but in axial tension, further degradation is limited to the Cr plated alloy.

Finally two material states are mentioned which are not solely functions of corrosion fatigue, but do effect fatigue performance of threaded fasteners and other components. The first is the forming of a component - whether it is cast or wrought steel. Fig 6.19 [6.19] shows two similar steels one cast (4135) the other wrought (4140). In general, if the longitudinal and transverse ductility, impact or fatigue property values of rolled steel are averaged, they will be about the same as properties of the cast steel. However, depending upon the size and complexity of geometry, the casting may be more prone to contain serious defects.

In fatigue sensitive areas surface condition is very important. Cold rolling of threads is a common procedure often used to obtain a good surface finish at thread roots. However the rolling has the added advantage of imposing compressive internal stresses at the material surface, reducing the damaging service tensile stress, thus leading to an improvement of fatigue strength. Fig 6.20 [6.23] shows fatigue results of rolled 50B40 (Rc 23-33) steel threads. In the case of rolling before heat treating, the induced compressive stresses have been relieved by the heat treatment, showing a reduction in fatigue strength relative to the cold rolled state.

6.5 Summary

This chapter brings to the fore problems associated with the siting of threaded connections during service. The steels and their designations that are most commonly encountered in the manufacture of nuts and bolts are introduced and defined. Coatings and lubricants frequently employed are discussed regarding their influence on the fatigue resistance (if any) of the steel on which they have been applied. Mechanisms of corrosion and stress corrosion cracking are discussed in terms of under what conditions these thrive and ways in which they can be controlled or contained.

A literature review of corrosion fatigue data of relevant steels is presented. This highlights the significance of material choice and helps to quantify the extent of the divergence of corrosion fatigue behaviour from that in an air environment.

6.6 References

[6.1] "Specification for ISO Metric Precision Hexagon Bolts, Screws and Nuts", BS 3692: 1967.

[6.2] Metals Handbook 10th Ed., vol 1, "Properties and Selection: Iron, Steels, and High Performance Alloys", ASM International, 1990.

[6.3] Rabia, H., "Fundamentals of Casing Design", ISBN 0-86010-863-5, 1987.

[6.4] "Recommended Practice for Drill Stem Design and Operating Limits", API RP 7G, 14th Ed., 1990.

[6.5] Craig, B. D., "Practical Oil-Field Metallurgy", 1984.

[6.6] Chung, Y., "Threshold Preload Levels for Avoiding Stress Corrosion Cracking in High Strength Bolts", Corrosion Cracking, Proceedings for the Corrosion Cracking Program and Related Papers Presented at the International Conference and Exposition of Fatigue, Corrosion Cracking, Fracture Mechanics and Failure Analysis, Ed. V. S. Goel ASM, 1986.

[6.7] Brown, B. Floyd, "Effects of Cathodic Protection on Corrosion Fatigue", Corrosion Fatigue: Mechanics, Metallurgy, Electrochemistry, and Engineering, ASTM STP 801, T. W. Crooker and B. N. Leis, Eds., American Society for Testing and Materials, pp. 508-515, 1983.

[6.8] Bamford, W. H., "Implementing Corrosion-Fatigue Crack Growth Rate Data for Engineering Applications", Corrosion Fatigue: Mechanics, Metallurgy, Electrochemistry, and Engineering, ASTM STP 801, T. W. Crooker and B. N. Leis, Eds., American Society for Testing and Materials, pp. 405-422, 1983.

[6.9] Lee, H. H. and Uhlig, H. H., "Corrosion Fatigue of Type 4140 High Strength Steel", Metallurgical Transactions, vol 3, pp 351-359, November 1972.

[6.10] Rajpathak, S. S. and Hartt, W. H., "Keyhole Compact Tension Specimen Fatigue of Selected High-Strength Steels in Sea water", Environmentally Assisted Cracking: Science and Engineering, ASTM STP 1049, W. B. Lisagor, T. W. Crooker, and B. N. Leis, Eds., American Society for Testing and Materials, Philadelphia, pp 425-446, 1990.

[6.11] Hartt, W. H., "Corrosion Fatigue Testing of Steels Applicable to Offshore Structures", Corrosion in Natural Waters, ASTM STP 1086, C. H. Baloun, Ed., ASTM, pp 54-69, 1990.

[6.12] Shih, T. T. and Clark, W. G., Jr., "An Evaluation of Environment - Enhanced Fatigue Crack Growth Rate Testing as an Accelerated Static Load Corrosion Test", Environment - Sensitive Fracture: Evaluation and Comparison of Test Methods, ASTM STP 821, S.W. Dean, E. N. Pugh and G. M. Ugiansky, Eds., ASTM, 1984.

[6.13] Metals Handbook 9th Ed., vol 13., "Evaluation of Corrosion Fatigue", ASM International, 1987.

[6.14] Wei, R. P. and Shim, G., "Fracture Mechanics and Corrosion Fatigue", Corrosion Fatigue: Mechanics, Metallurgy, Electrochemistry, and Engineering ASTM STP 801, T. W. Crooker and B. N. Leis, Eds., ASTM, pp 5-25, 1983.

[6.15] Toshimitsu Yokobori, A., Takeo Yokoboai, Tomokazu Kosumi and Nobuo Takasu, "Effects of Frequency, Stress Rising Time and Stress Hold Time on Corrosion Fatigue Crack Growth Behaviour of Low Alloy Cr-Mo Steel", Corrosion Cracking, ASM, 1986.

[6.16] Hinton, B. R. W., Procter R. P. M., "The Effects of Cathodic Protection and Over Protection on the Tensile Ductility and Corrosion Fatigue Behaviour of X-65 Pipeline Steel", Hydrogen Effects in Metals, AIME, 1981.

[6.17] Scott, P. M., "Chemistry Effects in Corrosion Fatigue", Corrosion Fatigue: Mechanics, Metallurgy, Electrochemistry, and Engineering, ASTM STP 801, T. W. Crooker and B. N. Leis, Eds., ASTM, pp 319-350, 1983.

[6.18] McIntyre, P., "Hydrogen-Steel Interactions During Cyclic Loading", Corrosion Fatigue, The Metals Society, 1980.

[6.19] "Atlas of Fatigue Curves", Ed., H. E. Boyer, American Society for Metals, 1986.

[6.20] Kesten, M. and Windgassen, K. F., "Hydrogen - Assisted Fatigue of Periodically Pressurized Steel Cylinders", Hydrogen Effects in Metals, AIME, 1981.

[6.21] Fujii, C. T. and Smith, J. A., "Environmental Influences on the Aqueous Fatigue Crack Growth Rates of HY-130 Steel", Corrosion Fatigue: Mechanics, Metallurgy, Electrochemistry, and Engineering, ASTM STP 801, T. W. Crooker and B. N. Leis, Eds., ASTM, pp 390-402, 1983.

[6.22] Levy, M. and Swindlehurst, C. E. Jr., "Corrosion Fatigue Behaviour of Coated 4340 Steel for Blade Retention Bolts of the AH-1 Helicopter", "Risk and Fatigue Analysis for Improved Performance and Reliability", Sagamore Army Materials Research Conference Proceedings, 24, Ed. J. J. Burke and Volker Weiss, pp 263-279, 1980.

[6.23] Kern, R. F. and Suess, M. E., "Steel Selection", Wiley, New York, 1979.

Nominal Diameter	Strength Grade Designation									
(mm)	4.6	4.8	5.6	5.8	6.6	6.8	8.8	10.9	12.9	14.9
1.6-8	fcs	fcs	fcs	fcs	C .24 /.53 P .06 S .07	fcs	C .32 /.5 P .04 S .05	C .32 /.5 P .04 S .05	TAC 0.9 C .19 /.52	TAC 1.5 C .19 /.52
8-12									P.035 S.035	P.035 S.035 Mo.15
12-18			C .24 /.53 P .06 S .07					TAC 0.9		
18-24								C .19 /.5 P .04 S .04	TAC 0.9 C .19 /.52 P.035 S.035 Mo.15	TAC 2.5 C .19 /.52
24-39							TAC 0.5 C .32 /.5 P .04 S .05		TAC 1.5 C .19 /.52 P.035 S.035 Mo.15	P.035 S.035 Mo.2
39-52							TAC 1.1 C .19 /.5	TAC 2.2 C .19 /.5	TAC 2.2 C .19 /.5 P.035 S.035 Mo .2	TAC 2.8 C .27 /.5
52-68							P.035 S.035 Mo .2	P.035 S.035 Mo .2	TAC 2.8 C .27 /.5 P.035 S.035 Mo .4	P.035 S.035 Mo .4

fcs: Free Cutting Steels, max: S - 0.34%, P - 0.1%, Pb - 0.5%-0.35%

TAC Minimum Total Alloy Content, i.e., Cr + Ni + Mo + V + (Mn higher than 0.8%)

Values of P and S are maximum values, values of Mo are minimum values

Table 6.1

Chemical Composition of Steel Bolts and Screws

	Strength Grade Designation									
	4.6	**4.8**	**5.6**	**5.8**	**6.6**	**6.8**	**8.8**	**10.9**	**12.9**	**14.9**
Tensile Strength (MPa)	392	392	490	490	588	588	785	981	1177	1373
Yield Strength (MPa)	235	314	294	392	353	471	-	-	-	-
% Elongation	25	14	20	10	16	8	12	9	8	7
Brinell Hardness (min)	110	110	140	140	170	170	225	280	330	390
Vickers Hardness (min)	110	110	140	140	170	170	225	280	330	400
Charpy Impact Strength (min) (J)	-	-	-	-	-	-	29.8	19.0	14.9	14.9

Table 6.2

Mechanical Properties of Steel Bolts and Screws

SAE No	AISI No	C	Mn	P	S	Si	Ni	Cr	Mo
4130	4130	0.28-0.33	0.4-0.6	0.035	0.04	0.15-0.35	-	0.8-1.0	0.15-0.25
4135	-	0.33-0.38	0.7-0.9	0.035	0.04	0.15-0.35	-	0.8-1.0	0.15-0.25
4137	4137	0.35-0.4	0.7-0.9	0.035	0.04	0.15-0.35	-	0.8-1.0	0.15-0.25
4140	4140	0.38-0.43	0.75-1.0	0.035	0.04	0.15-0.35	-	0.8-1.0	0.15-0.25
4142	4142	0.4-0.45	0.75-1.0	0.035	0.04	0.15-0.35	-	0.8-1.0	0.15-0.25
4340	4340	0.38-0.43	0.6-0.8	0.035	0.04	0.15-0.35	1.65-2.0	0.7-0.9	0.2-0.3
50B40	-	0.38-0.43	0.75-1.0	0.035	0.04	0.15-0.35	-	0.4-0.6	-
5132	5132	0.3-0.35	0.6-0.8	0.035	0.04	0.15-0.35	-	0.75-1.0	-
5135	5135	0.33-0.38	0.6-0.8	0.035	0.04	0.15-0.35	-	0.8-1.05	-
5140	5140	0.38-0.43	0.7-0.9	0.035	0.04	0.15-0.35	-	0.7-0.9	-
8630	8630	0.28-0.33	0.7-0.9	0.035	0.04	0.15-0.35	0.4-0.7	0.4-0.6	0.15-0.25
8637	8637	0.35-0.4	0.75-1.0	0.035	0.04	0.15-0.35	0.4-0.7	0.4-0.6	0.15-0.25
8640	8640	0.38-0.43	0.75-1.0	0.035	0.04	0.15-0.35	0.4-0.7	0.4-0.6	0.15-0.25
8740	8740	0.38-0.43	0.75-1.0	0.035	0.04	0.15-0.35	0.4-0.7	0.4-0.6	0.2-0.3

Table 6.3

Ladle Chemical Composition of Hot-rolled and Cold-finished Bars used for Threaded Connections

US (SAE)	Germany (DIN)	Japan (JIS)	UK (BS)	France (AFNOR NF)	Italy (UNI)
4130	-	G4105SCM1 G4105SCM432 G4105SCM2 G4105SCM430 G4106SCM2	1717CDS110 970708A30	A35-55230CD4 A35-55630DC4 A35-55730DC4	30CrMo4 692935CrMo4F 735634CrMo4KB 784530CrMo4 787430CrMo4
4135	1.2330,35CrMo4 1.7220,34CrMo4 1.7220,GS-34CrMo4 1.7226,34CrMoS4 1.7231,33CrMo4	G4054SCM3H G4054SCM435H G4105SCM1 G4105SCM432 G4105SCM3 G4105SCM435	970708A37 970708H37	35CD4 A35-55235CD4 A35-55335CD4 A35-55635CD4 A35-55734CD4	533235CrMo4 692935CrMo4F 735634CrMo4KB 784535CrMo4 787435CrMo4
4137	1.7225,GS-42CrMo4	G4052SCM4H G4052SCM440H G4105SCM4	3100 ty 5 970708A37 970708H37 970709A37	40CD4 42CD4 A35-55238CD4 A35-55738CD4	533240CrMo4 533338CrMo4 735638CrMo4KB
4140	1.3563,43CrMo4 1.72223,41CrMo4 1.7225,42CrMo4 1.7225,GS-42CrMo4 1.7227,42CrMoS4	G4052SCM4H G4052SCM440H G4103SNCM4 G4105SCM4 G4105SCM440	3100 ty 5 4670711M4G 970708A40 970708A42(En19C) 970708H42 970708M40 970709A40 970709M40	40CD4 A35-55342CD4,42CDTS A35-55342CD4,42CDTS A35-55642CD4,42CDTS A35-55742CD4,42CDTS	3160G40CrMo4 533240CrMo4 784542CrMo4 784741CrMo4 787442CrMo4
4142	1.3563,43CrMo4 1.7223,41CrMo4	-	970708A42(En19C) 970708H42 970708A42	40CD4 A35-55342CD4,42CDTS A35-55342CD4,42CDTS A35-55642CD4,42CDTS A35-55742CD4,42CDTS	784542CrMo4 787442CrMo4
4340	1.6565,40NiCrMo6	G4103SNCM8 G4103SNM439 G4103SNB23-1-S G4103SNB24-1-S	4670818M40 9702S.119	-	533240NiCrMo7 692640NiCrMo7 784540NiCrMo7 787440NiCrMo7 735640NiCrMo7KB
50B40	1.7003,38Cr2 1.7023,28CrS2	G4052SMnC3H G4052DMnC443H G4106SMnC3 G4106SMnC443 G5111SCMnCr4	-	A35-55238C4 A35-55638C4 A35-55738C2 A35-55242C2 A35-55642C2 A35-55742C2	735641Cr2KB
5132	1.7033,34Cr4 1.7037,34CrS4	G4104SCr3 G4104SCr435	970530A32(En18B) 970530A36(En18C) 970530H32	A35-55232C4 A35-55332C4 A35-55632C4 A35-55732C4	735634Cr4KB 787434Cr4
5135	1.7034,37Cr4 1.7038,37CrS4 1.7043,38Cr4	G4052SCr3H G4052SCr435H	3111 ty 3 970530A36(En18C) 970530H36	38C4 A35-55238Cr4 A35-55338Cr4 A35-55638Cr4 A35-55738Cr4	533235CrMn5 640335CrMn5 533336CrMn4 784736CrMn4 735638Cr4KB 784536CrMn5 787436CrMn5 784738Cr4
5140	1.7035,41Cr4 1.7039,41CrS4 1.7045,42Cr4	G4052SCr4H G4052SCr440H G4104SCr4 G4104SCr440	3111 ty 3 9702S.117 970530A40(En18D) 970530H40 970530M40	A35-55242C4 A35-55742C4 A35-55642C4	533240Cr4 735641Cr4KB 784541Cr4 787441Cr4
8630	1.6545,30NiCrMo22	-	-	30NCD2	735630NiCrMo2KB
8637	-	-	970945M38(En100)	40NCD3	533238NiCrMo4 735638NiCrMo4KB 784539NiCrMo3 787439NiCrMo3
8640	1.6546,40NiCrMo22	-	3111 ty 7,2S.147 970945A40(En100C)	40NCD2 40NCD2TS 40NCD3TS 40NCD3	533340NiCrMo4 735640NiCrMo2KB 784540NiCrMo2 787440NiCrMo2 784740NiCrMo3
8740	1.6546,40NiCrMo22	-	3111 ty 7,2S.147	40NCD2 40NCD2TS 40NCD3TS	735640NiCrMo2KB 784540NiCrMo2 787440NiCrMo2

Table 6.4

International Equivalent Steel Standards

	HY80	A710	QT80	QT108	EH36	A537dq	A537ac	X70	HY130
C	0.13	0.04	0.08	0.11	0.13	0.12	0.07	0.09	0.10
Si	0.16	0.30	0.23	0.23	0.37	0.41	0.26	0.41	0.14
Mn	0.28	0.45	1.40	0.86	1.42	1.3	1.35	1.43	0.80
P	0.005	0.004	0.01	0.004	0.018	0.014	0.011	0.018	0.006
S	0.005	0.002	0.002	0.003	0.002	0.003	0.003	0.002	0.005
Cu	0.02	1.14	0.01	0.24	0.01	0.01	0.14	0.01	0.12
Ni	3.08	0.82	0.43	0.98	0.01	0.03	0.14	0.01	5.09
Cr	1.70	0.67	0.09	0.43	0.02	0.04	0.01	0.02	0.46
Mo	0.44	0.18	0.06	0.44	0.01	0.05	0.02	0.10	0.51
Nb	-	0.037	0.002	-	0.025	-	0.017	0.032	-
V	0.006	0.004	0.04	0.027	0.003	0.044	-	0.063	0.062
B	0.0001	0.0001	0.0001	0.0009	-	-	-	-	-
Ti	0.004	0.002	0.005	-	0.022	-	-	0.018	0.008
N	0.0089	0.0047	0.0026	-	0.0038	-	-	0.0026	0.01
Sol.Al	0.019	0.034	0.051	-	0.046	-	-	0.026	0.021
O	0.0031	-	-	-	-	-	-	-	0.0012
C_{equiv}	0.7108[1]	0.4165[2]	0.3807[2]	0.4853[1]	0.3890[1]	0.3781[1]	0.3163[1]	0.3700[2]	-
σ_y (MPa)	655	563	537	745	416	500	452	509	985
σ_{UTS} (MPa)	743	622	613	824	536	598	551	613	1006

[1] C_{equiv} C + Mn/6 + Si/24 + Ni/40 + Cr/5 + Mo/4 + V/14

[2] C_{equiv} C + Mn/6 + Cu/15 + Ni/15 + Cr/5 + Mo/5 + V/5

Table 6.5

Chemical Composition and Mechanical Properties
of Selected Thread Steels

Plating	Axial		Rotating Bend	
	Air	3.5% NaCl	Air	3.5% NaCl
-	1103	758	724	138
Cd + Chromate	1138	1138	724	552
Cr + Dry Film	1207	621	655	621
WC + Dry Film	965	414	621	621
WC + Coricone + Dry Film	965	414	621	621

Table 6.6

Fatigue Endurance (MPa) of Plated 4340 Steel

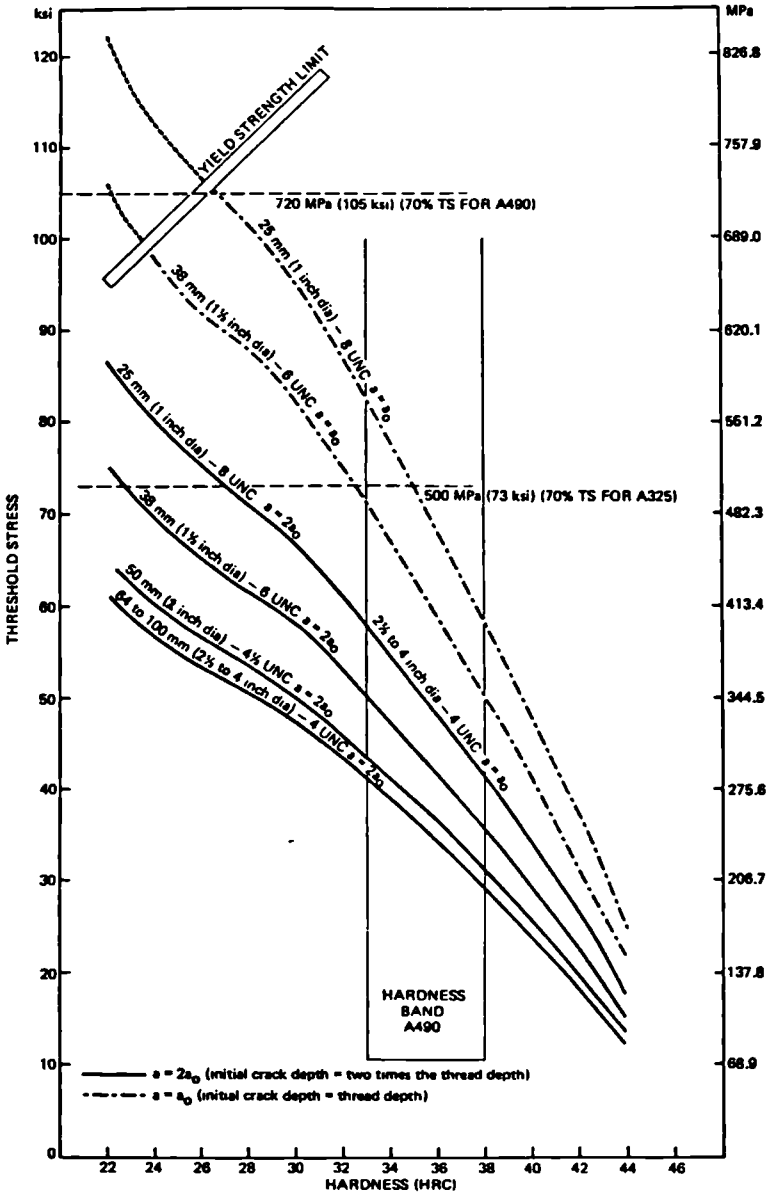

Fig 6.1

Threshold Stresses for SCC in HSLA Bolting Steels with Different Hardness Levels

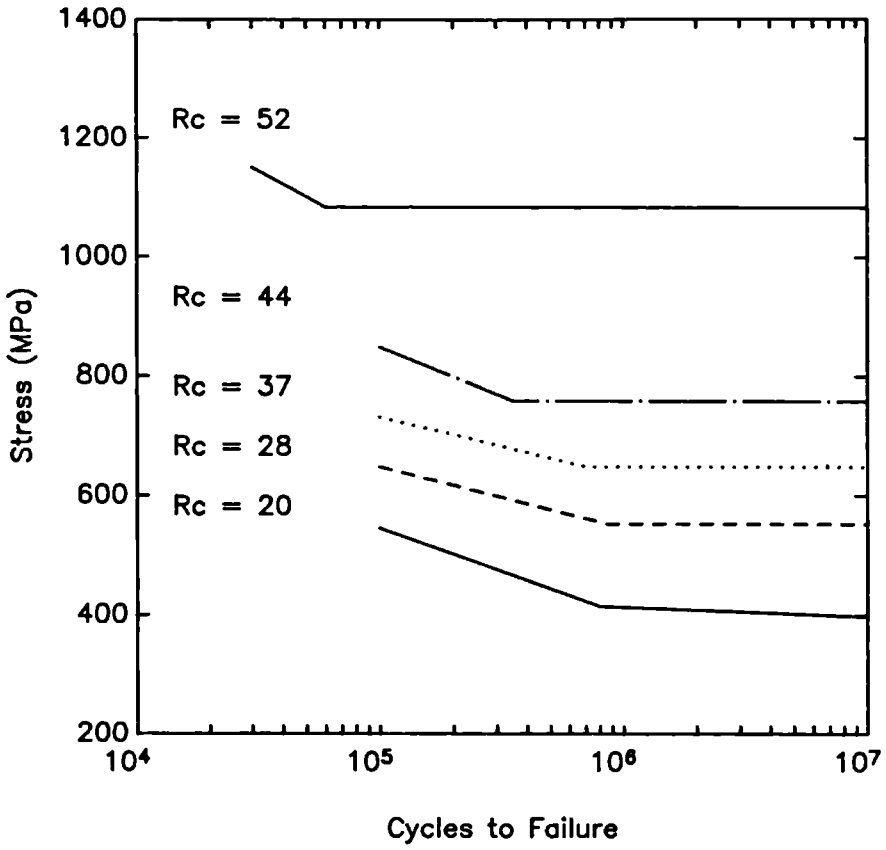

Fig 6.2

Fatigue Life of 4140 Steel with Different Hardness Levels in Air

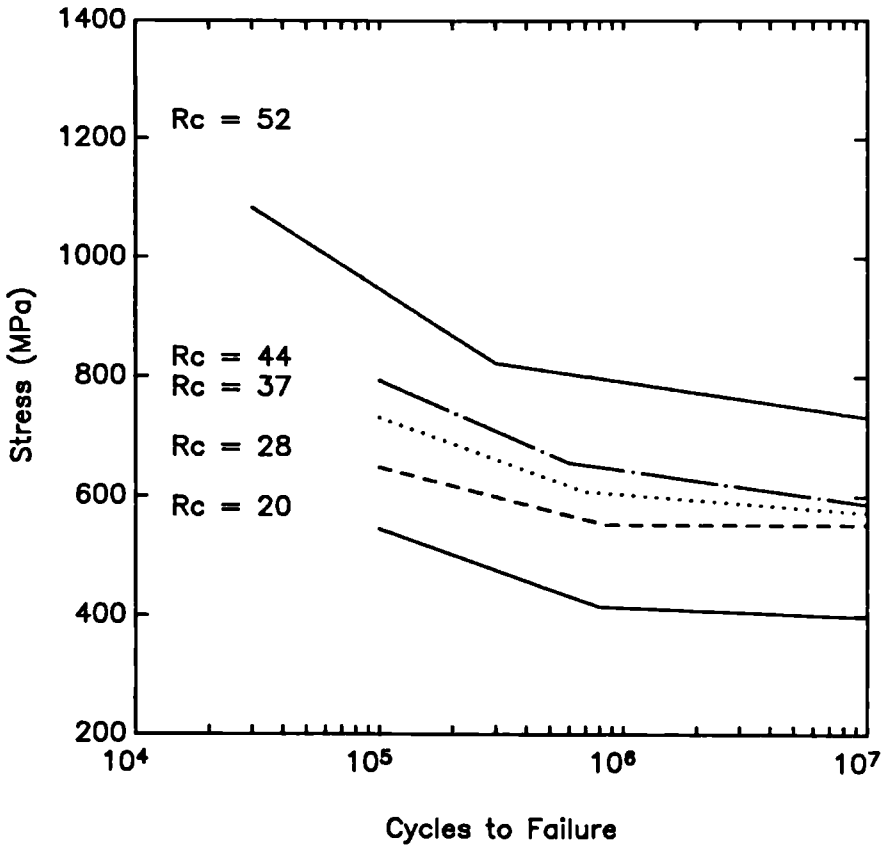

Fig 6.3

Fatigue Life of 4140 Steel with Different Hardness Levels in Deaerated 3% NaCl

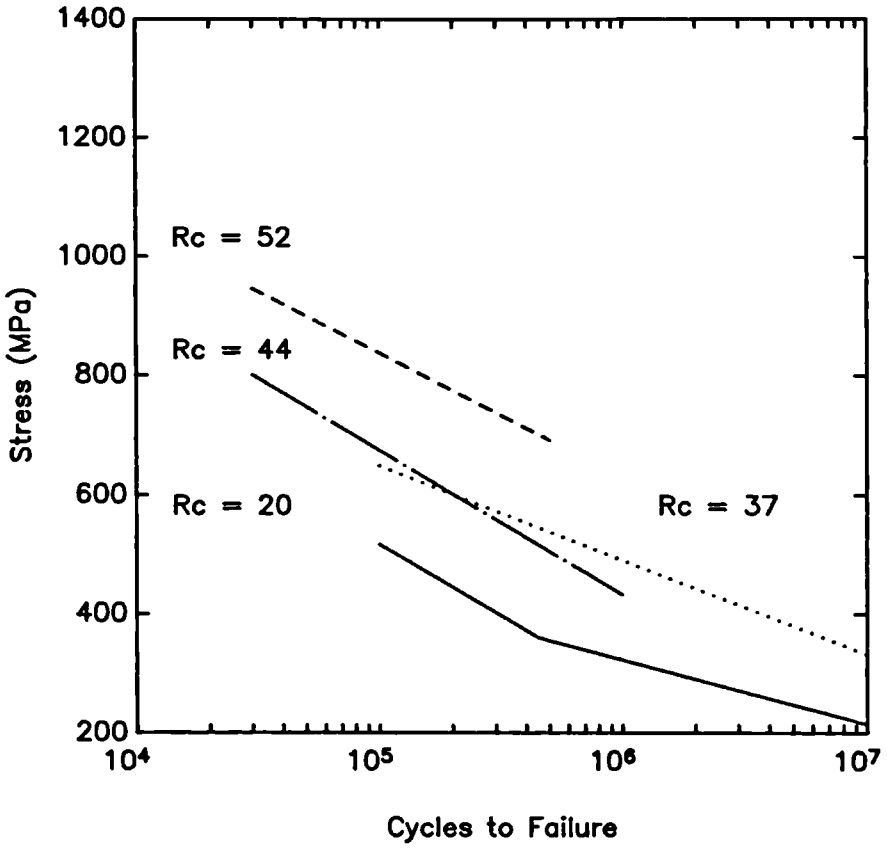

Fig 6.4

Fatigue Life of 4140 Steel with Different Hardness Levels in Aerated 3% NaCl

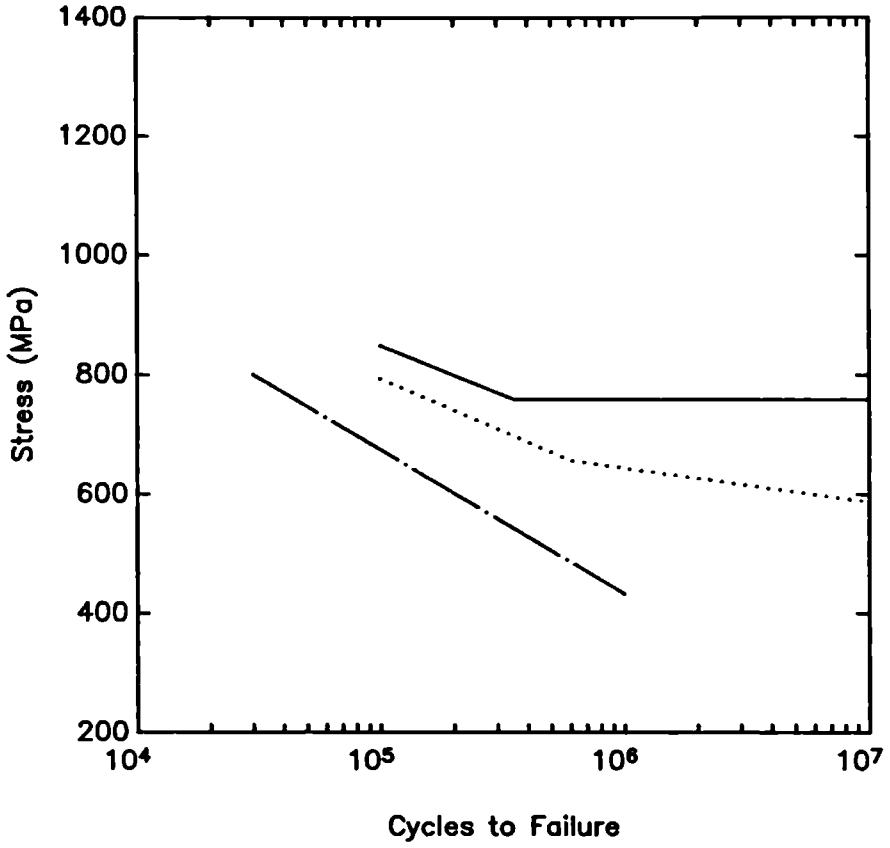

——————— Air

..... Deaerated 3% NaCl

——·—— Aerated 3% NaCl

Fig 6.5

Fatigue Life of 4140 Steel (Rc = 44),
in Different Environments

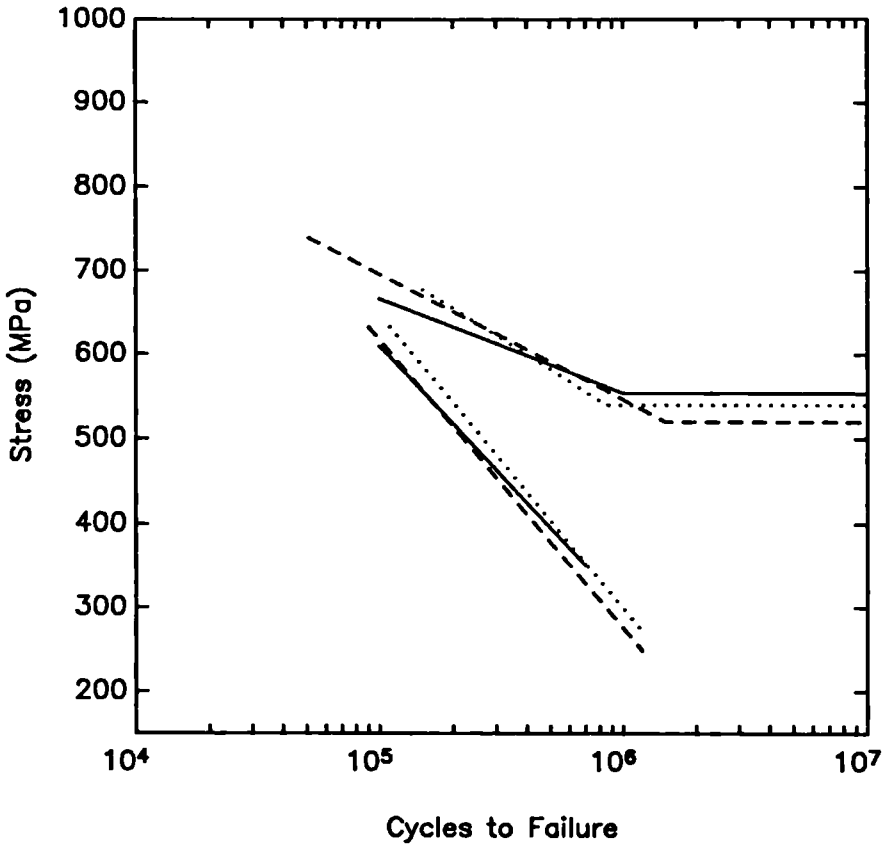

——————— HY80

..... A710

- - - - - - - - - - QT80

Fig 6.6

Fatigue Life of HY80, A710 and QT80 Steels Cathodically Protected and Freely Corroding in Sea Water

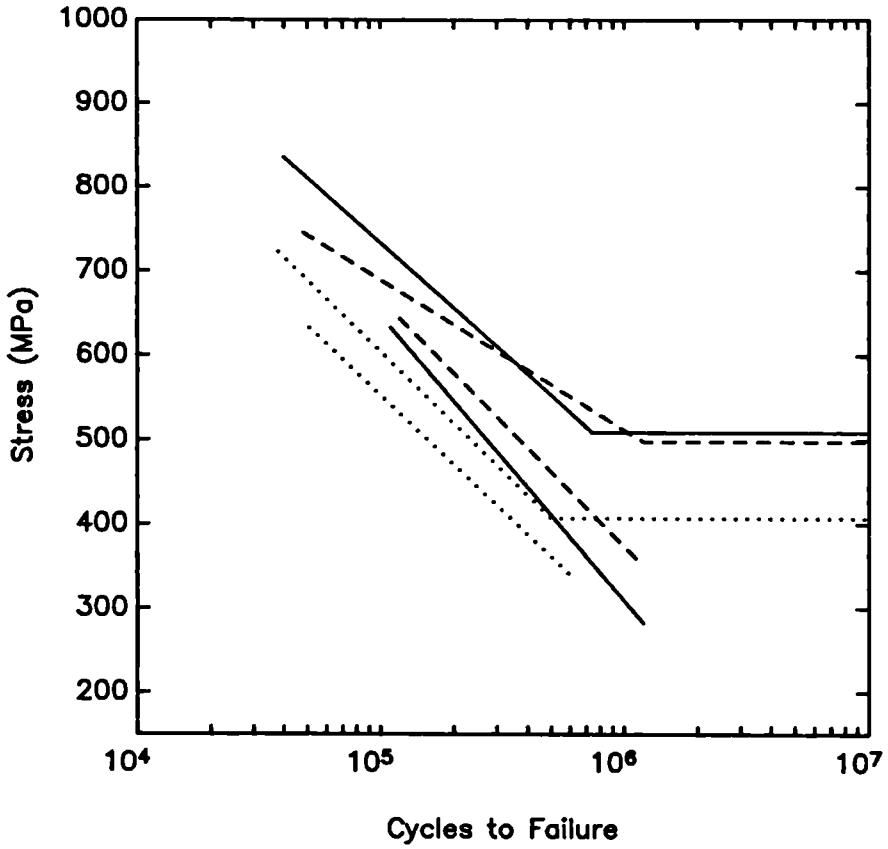

——————— QT108

..... EH36

- - - - - - - - - - A537dq

Fig 6.7

Fatigue Life of QT108, EH36 and A537dq Steels Cathodically Protected and Freely Corroding in Sea Water

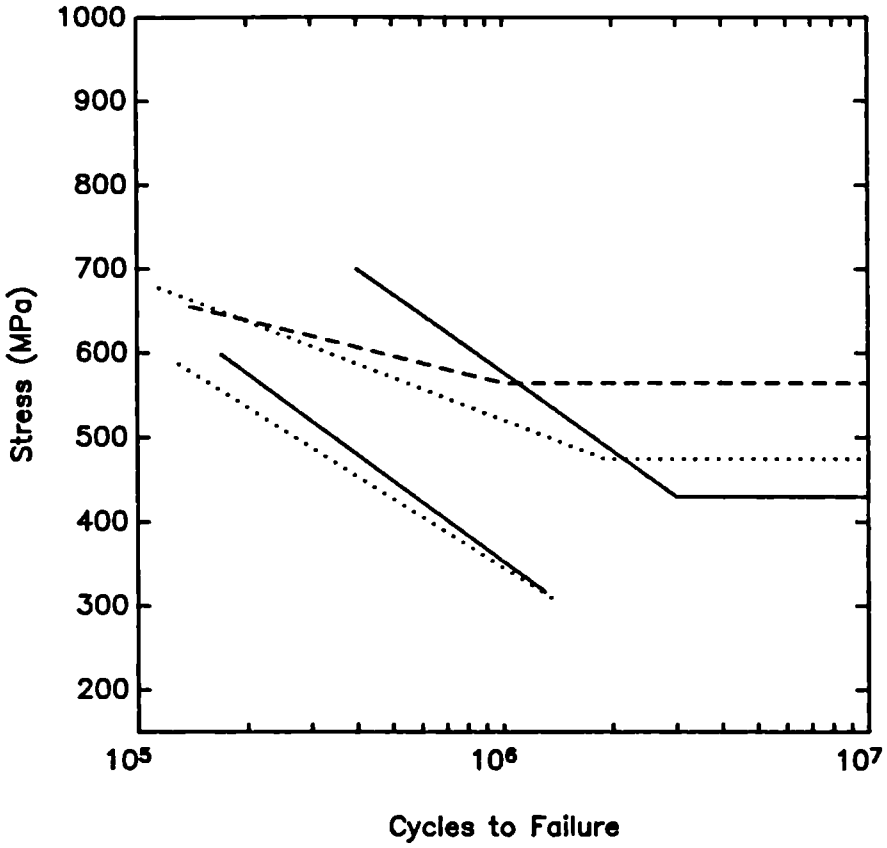

——————— A537ac

..... X70

- - - - - - - - - - HY130

Fig 6.8

Fatigue Life of A537ac, X70 and HY130 Steels Cathodically Protected and Freely Corroding in Sea Water

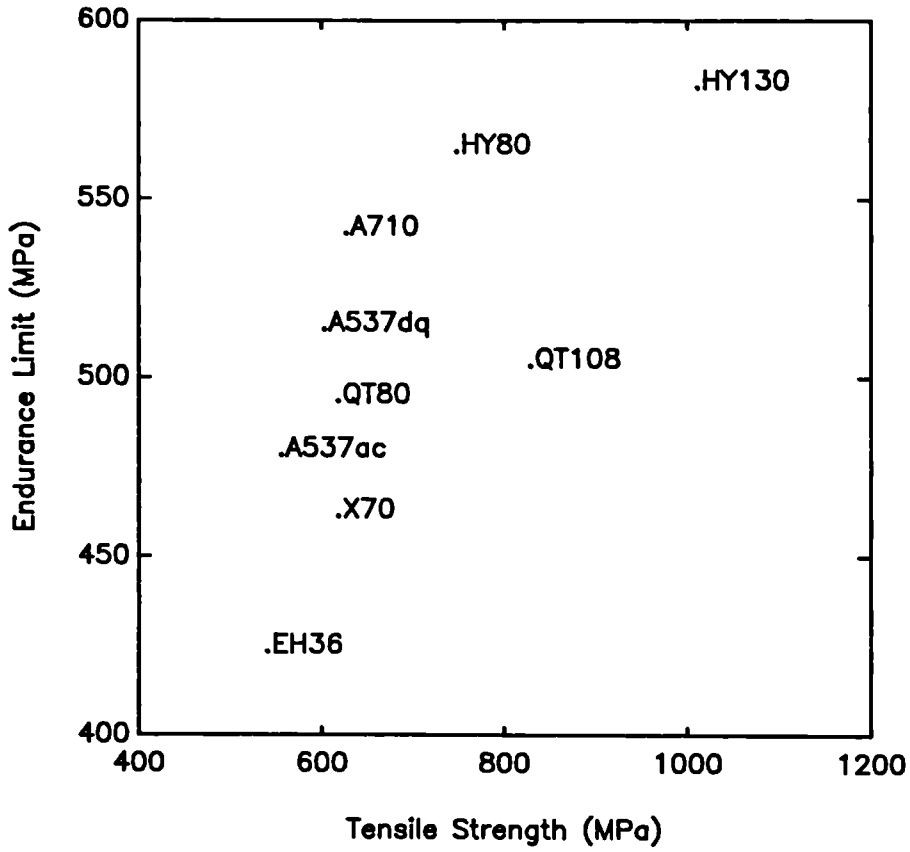

Fig 6.9

Yield Strength Versus Fatigue Endurance Limit
for Selected Bolt Steels

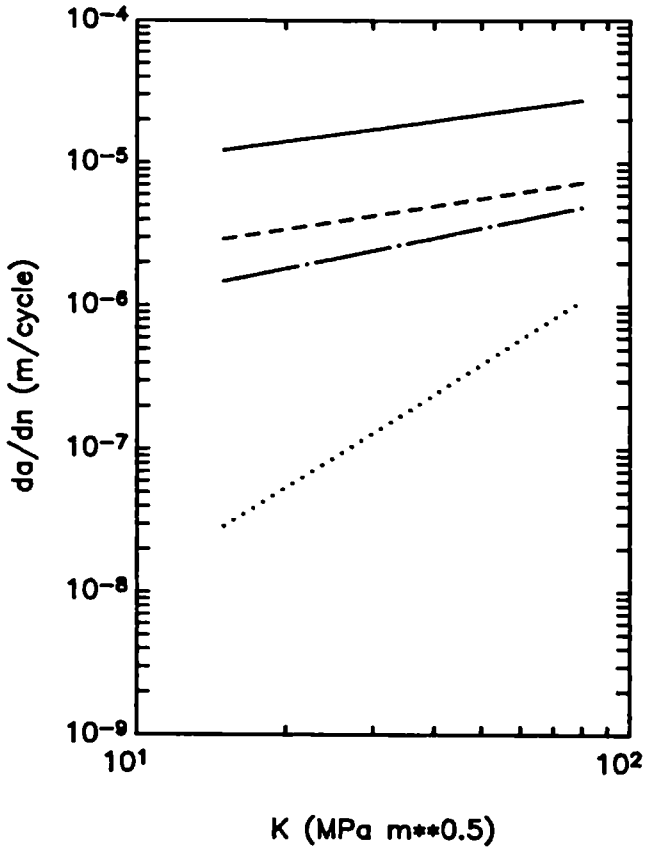

——————— Distilled Water - 0.04 Hz

- - - - - - - - - - Distilled Water - 0.2 Hz

——·—— Distilled Water - 0.4 Hz

..... Argon - 0.4 Hz

Fig 6.10

Effect of Stress Intensity Factor Range and Loading Frequency
on Corrosion Fatigue Crack Growth in Ultra-High Strength 4340 Steel

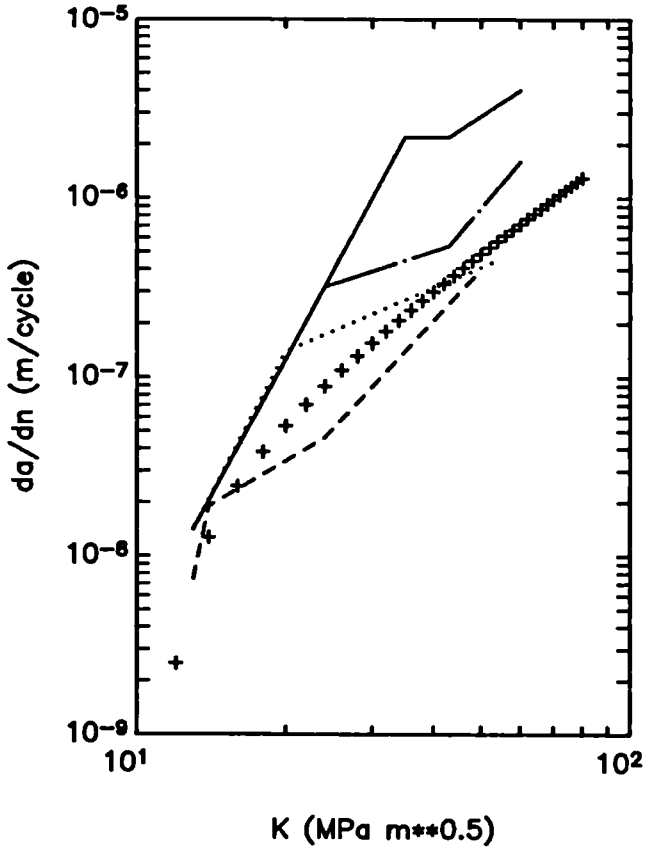

++++++++++++++++	Air
- - - - - - - - - -	Sine - 10 Hz
.....	Sine - 1 Hz
——·——	Sine - 0.1 Hz
————————	Triangular - 0.01 Hz

Fig 6.11

Crack Growth Rates for X65 Steel in 3.5% NaCl Solution at -0.8V CP, for Different Cycling Frequencies

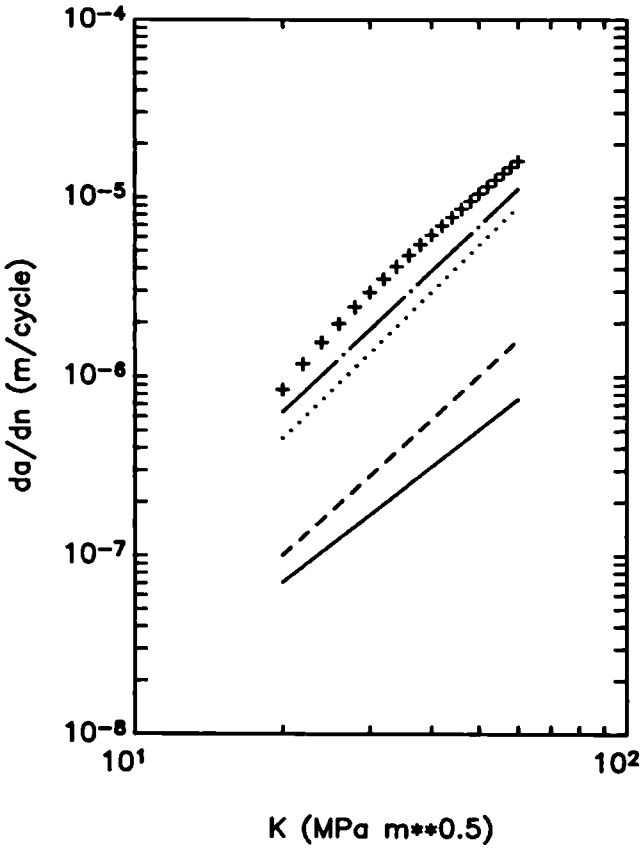

++++++++++++++++	H_2 Sine - 0.01 Hz
- - - - - - - - - -	H_2 Sine - 10 Hz
.....	H_2 Sine - 1 Hz
——·——	H_2 Sine - 0.1Hz
————————	N_2

Fig 6.12

Crack Growth Rates for 708M40 Steel in Hydrogen Gas at 42 Bar Pressure for Different Cycling Frequencies (R = 0.3)

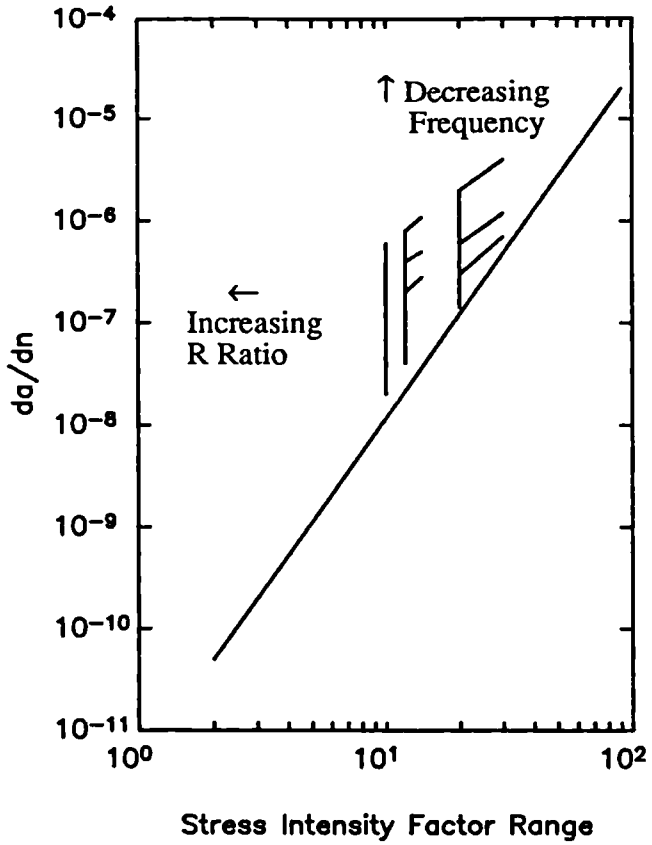

Fig 6.13

Schematic of Frequency and R-ratio Effects for HSLA Steels in Corrosive Environments

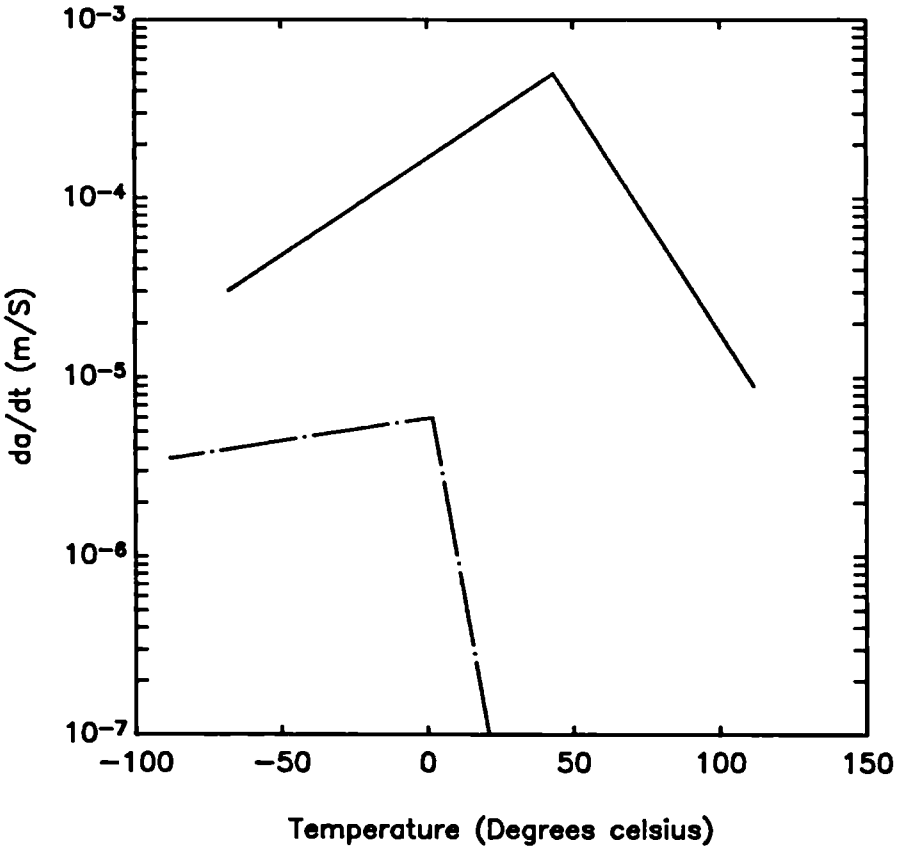

—————— σ_y = 1300 MPa
σ_{UTS} = 1660 MPa

——·—— σ_y = 1190 MPa
σ_{UTS} = 1310 MPa

Fig 6.14

Crack Growth Rate Versus Temperature in Hydrogen Gas,
for 4130 Steel ($K = 40MPa\sqrt{m}$)

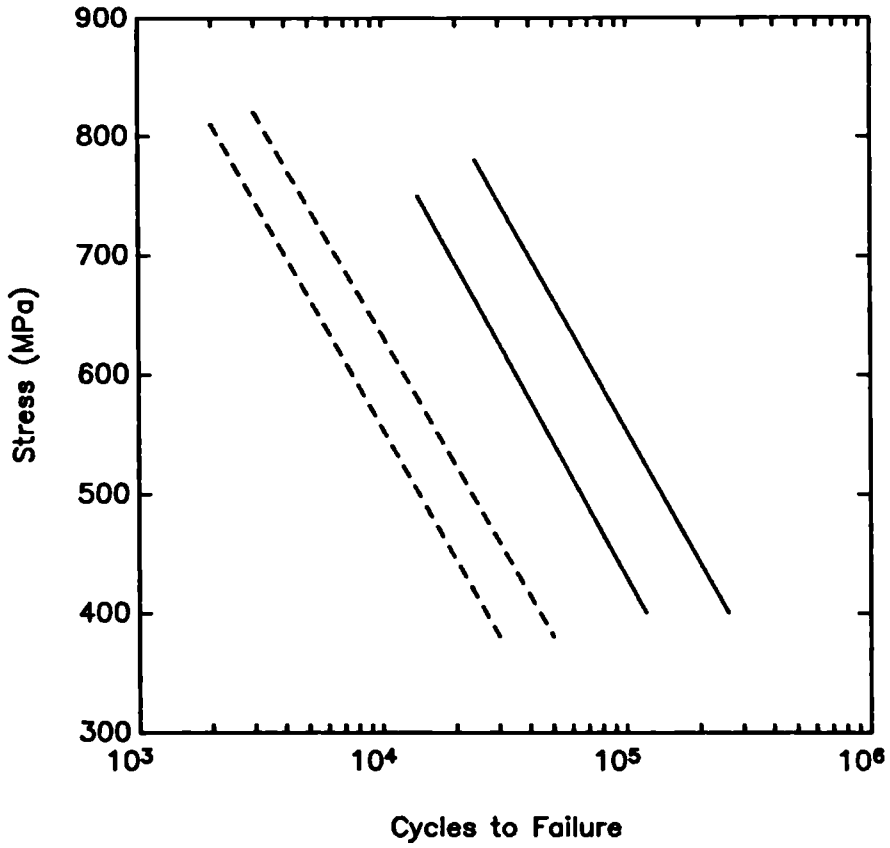

——————— Upper and Lower Bounds for Oil Tests

- - - - - - - - - - Upper and Lower Bounds for Hydrogen Tests

Fig 6.15

34CrMo4 Quenched and Tempered Steel in Hydrogen and Oil ($\sigma_y = 847MPa$)

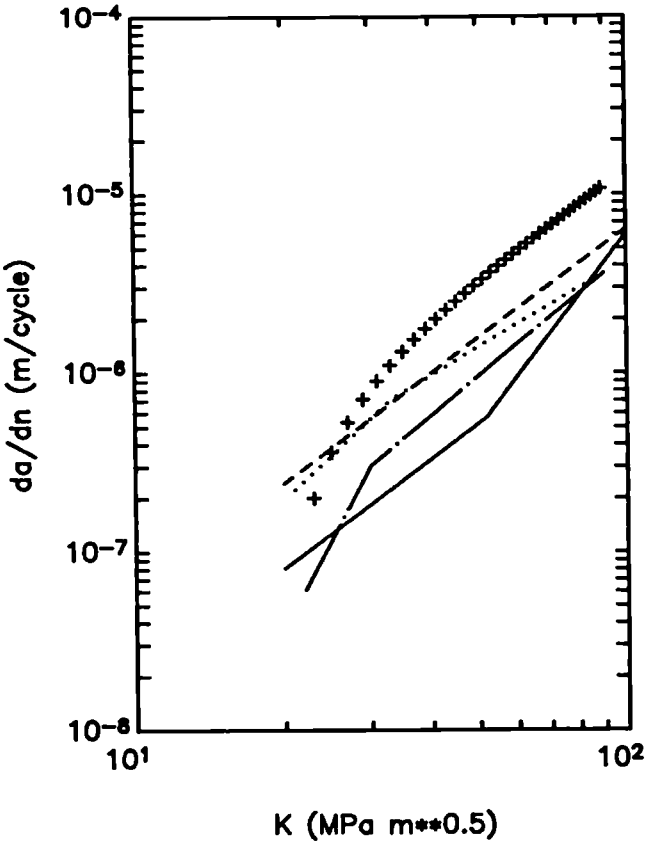

++++++++++++++++	0.6 M NaCl, CP: -1.0V
- - - - - - - - - -	0.6 M NaCl
.....	0.1 N HCl
——·——	0.1 N NaOH
————————	Air

Fig 6.16

Effect of Various Environments on the Fatigue Crack Growth Rates in HY130 Steel

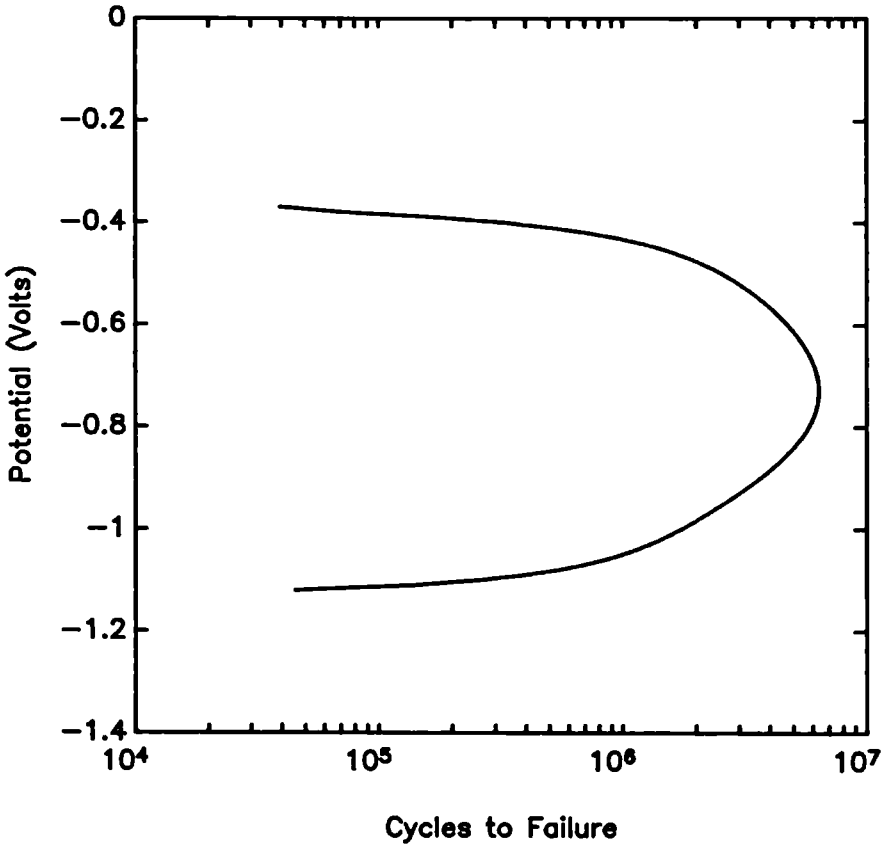

Fig 6.17

Effect of Applied Potential on 4140 Steel (Rc = 52),
Stressed Below the Fatigue Limit in Aerated 3% NaCl

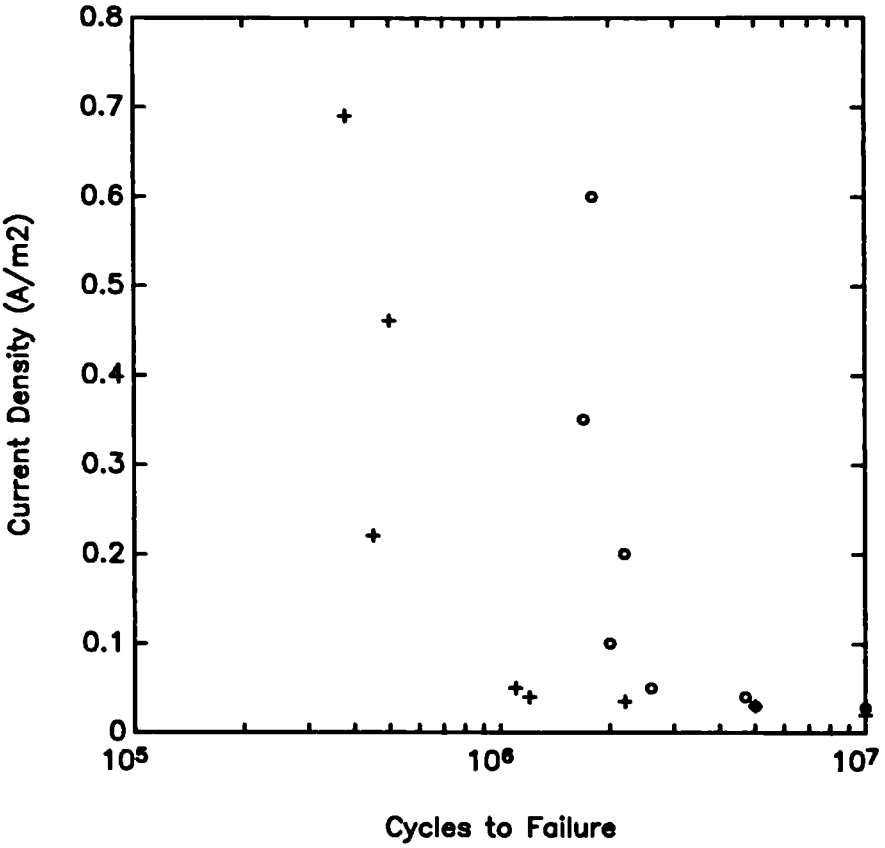

o Applied Stress Range: 276 MPa

\+ Applied Stress Range: 379 MPa

Fig 6.18

Effect of Applied Anodic Current Density
on the Fatigue Life of 4140 Steel (Rc = 20),
Stressed at Two Values Below the Fatigue Limit

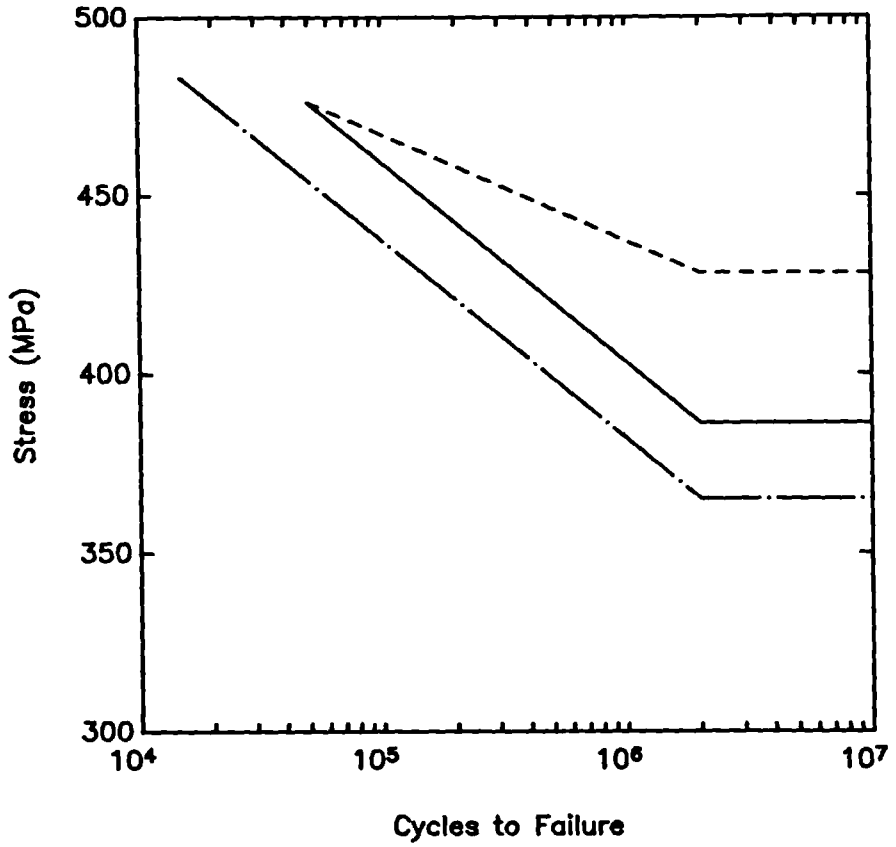

——————— 4135 Cast Steel

- - - - - - - - - - 4140 Longitudional Direction

——— · ——— 4140 Transverse Direction

Fig 6.19

Fatigue Lives of Cast, Wrought Longitudinal Direction and Wrought Transverse Direction Normalised and Tempered 4135 and 4140 Steels

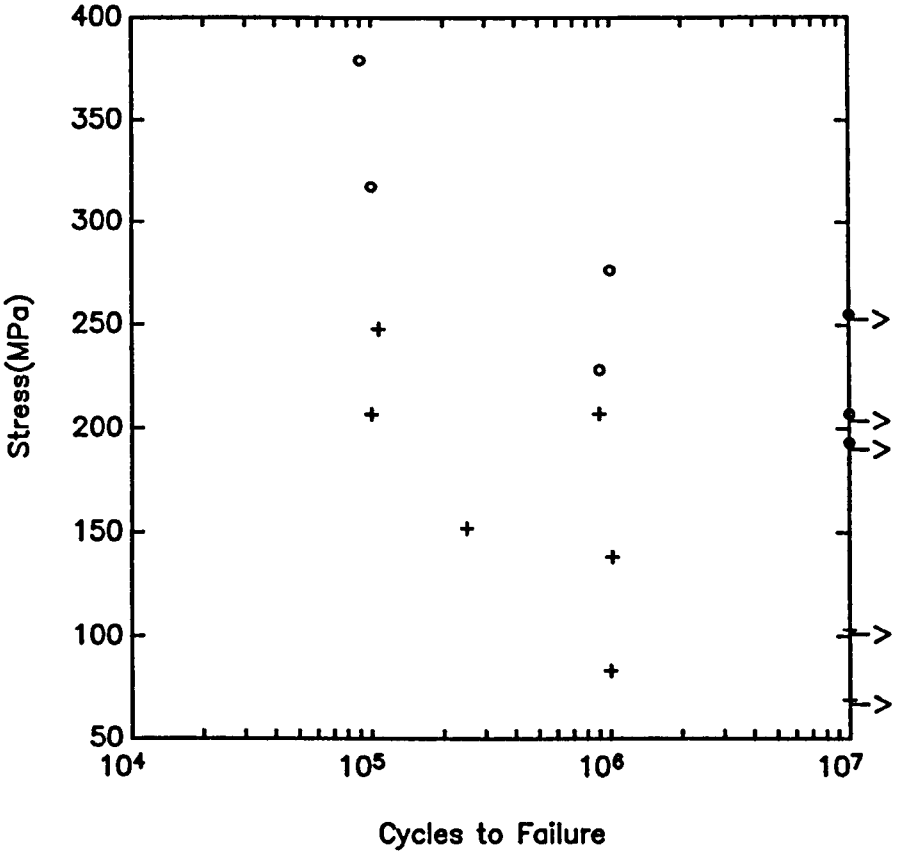

o	Threads Rolled after Heat Treating
+	Threads Rolled Before Heat treating

Fig 6.20

Effect of Rolling Threads Before and After Head Treatment

CHAPTER SEVEN - Review / Future Recommendations

7.1 Introduction

This study was prompted by the growing need to improve the understanding of fatigue behaviour in threaded connections. Recent developments in materials and inspection technology is leading to an industrial environment in which flaws and cracks in structural components can be tolerated, without compromising safety margins. However, for this, a high level of understanding and definition of the structural mechanisms operating within the system is essential. There always exists a compromise between conducting an elaborate analytical or computer analysis and providing a "handbook" engineering solution to complex novel technology. Most often individuals who appreciate the practical problems associated with engineering components, do not have the means required to carry out a highly detailed, advanced structural analysis. Likewise those who are conversant with advanced stress analysis techniques often do not fully understand the practical engineering operation of the component. A compromise must also be made between the effort of the analysis and the significance of structural failure. These considerations motivated this study to set out the framework for a comprehensive generic engineering approach to the evaluation of fatigue lives in threaded connections.

This thesis is made up of four main sections, these are the description and application of threaded connections, stress analysis of threaded connections, and fatigue crack propagation in threaded connections. The main topics addressed for each of the above are set out in the following sections, highlighting any conclusions made. The final section will summarise and recommend areas for further development.

7.2 Threaded Connections

Threaded connections are efficient reversible mechanical fasteners. Chapter one identified two basic functions, either or both of which are demanded of threaded joints. These are that the connection should make a strong structural joint, and that it should make a pressure sealed joint. The appearance of threaded members are

discussed in terms of their function. The attributes or otherwise of these features were discussed, and the standardisation authorities concerned with recommending safe designs of screw connections for specific applications were identified. Chapter four described in detail two case studies where threaded connections were required to perform structurally under different loading and environmental conditions. These provided a concise insight into the functions and operation of several features of threaded joints. Thin walled casing joints were studied for use in Tension Leg Platform tethers. The application of torque and subsequent preload was studied in these connections. The significance of galling was also emphasised. The use of thick walled pressurised threaded tubes was also introduced, and their operation in drill strings was described. Chapter six discussed features of threaded connections in terms of environmental degradation. Steels, coatings and lubricants frequently employed in the fabrication and operation of threaded connections were investigated with regard to their influence (if any) on the fatigue resistance of the connections under inert and corrosive environments.

7.3 Stress Analysis of Threaded Connections

No new stress analysis of threaded connections was undertaken in this thesis. However, an extensive review of studies by other investigators was presented in chapter one. This reported that the stress analysis is generally divided into two phases: (i) evaluation of the load distribution within the entire connection, and (ii) evaluation of the stress state in the region of a loaded projection (i.e. critically loaded tooth). Specific values of stress concentration factors are not reported for thread forms, as the critical tooth root stress is a function of many geometric variables as well as the level of applied torque and loading mode. The most efficient overall stress analysis method was reported to be a hybrid finite element-electrical analogue model, where the electrical analogue analogy predicted the fraction of the overall load taken by the critical thread, and the finite element analysis determined the stress distribution through the thickness due to the loaded tooth. Stress analysis for the geometries used in the experimental work was undertaken by other investigators as part of separate studies. It was concluded in chapter five that the greatest discrepancies between experimental results and the fracture mechanics predictions

were due to the lack of a load shedding model to describe the change in stress distribution within connections as a result of the presence of a sizeable crack in the connection.

Studies of analysing variable amplitude stress histories in chapters one, two and four showed how an equivalent stress range could be evaluated for use with an *S-N* or fracture mechanics analysis.

7.4 Fatigue Crack Initiation in Threaded Connections

Chapter two studied the approaches available to predict fatigue crack initiation at critically loaded tooth roots. The material mechanisms of strain cycling were investigated with reference to cyclic hardening (and softening) and crack nucleation. Several methods of describing local strain to number of cycles to crack initiation were studied. These were the four point correlation method, two universal slopes approximations and using cyclic strength and ductility material properties. In a sensitivity analysis it was reported that overestimation of the strength and ductility coefficients and underestimation of their respective exponents lead to unconservative life predictions and vice versa. In the high cycle regime, errors in the ductility properties give small changes in life predictions but over overestimation of the strength properties can lead to large underpredictions in life. Stress-strain relationships were investigated for inelastic behaviour. Notch sensitivity and fatigue concentration factors were identified as important aspects of fatigue crack initiation. Mean, residual and variable amplitude stresses were discussed in terms of their effect on fatigue crack generation in thread roots. Methods of quantifying these were also considered. In the plane strain loading at thread roots, a linear relationship between the strain concentration factor and stress concentration factor (or fatigue concentration factor) is the most appropriate. Secondary crack initiation mechanisms (e.g. fretting) and phenomena that are difficult to quantify (e.g. coaxing, rest periods) were also highlighted in a general discussion of aspects that may influence the generation of cracks, specifically in threaded connections. Chapter six also builds on this, extending the discussion to environmental effects on fatigue crack initiation. Finally chapter five examined the results of seventeen full scale

fatigue tests (fourteen of which were fully reported in this thesis). Although a detailed crack initiation comparison was not practical due to the lack of appropriate materials data, good agreement was found between the experimental results and a generalised prediction using cyclic material properties from a representative material. The two universal slopes approximations for the same material almost enclose the experimental results as upper and lower bounds.

7.5 Fatigue Crack Propagation in Threaded Connections

Chapter one introduced the linear elastic fracture mechanics approach to predicting fatigue crack growth. The weight function approach to the calculation of stress intensity factors was also discussed. However, in chapter three a new approach to weight function theory was scrutinised and compared in detail with traditional methods. This new multiple reference states (MRS) technique requires at least two reference stress intensity factor distributions and corresponding stress distributions from distinct symmetrical loading modes. The second set of reference data effectively eliminates the necessity of a formal derivation of crack opening displacement. A further adaptation is to directly define the derivative of crack opening displacement, as it is this, not the actual crack profile that is needed for the weight function. The resulting weight function is considerably less involved mathematically and far more computationally stable than traditional or contemporary approaches. This stability is due to the elimination of the numerical differentiation normally associated with the other approaches. Published reference stress intensity factors were compiled for geometries related to threaded connections. By virtue of the definition of the weight function being a unique property of geometry, the influences it represents can be isolated and combined. This mathematical manipulation of related solutions resulted in a dedicated generic weight function for two and three dimensional cracks in threaded connections. The solutions were compared in chapter five with the crack growth data from the full scale experimental data. This encompassed three basic thread forms, three different materials, variations in remote section geometry and resulted in both pin and box failures under axial tension and rotating bending. On the whole the predictions were very good, representing most cases perfectly during the first half of the wall

thickness. Most predictions were conservative; the predicted growth rates being much faster than the experimental results towards the latter stages of the connection's life. This discrepancy (as mentioned earlier) was suggested to be due to the load redistribution within the connection, due to the presence of a relatively large crack.

Crack aspect ratio definition is an important feature of any stress intensity factor solution. Evolution of crack aspect ratio was discussed in detail for solid threaded bars in chapter three. However, chapter five found that the published solutions did not adequately describe the experimental results. Three new crack aspect ratio relations were derived from simple geometric considerations. These all excellently describe the crack evolution behaviour of all tests with the exception of one initially damaged specimen.

7.6 Future Improved Analyses

The fatigue models developed in this thesis are by no means complete. A framework has been set out within which variables can be better defined or applicability limits extended. Recommendations for areas of clarification and development are listed below.

- A study on mean and residual stresses at thread roots is required to develop the fatigue crack initiation model. Relaxation models of these for specific materials during service are essential, particularly for high cycle fatigue.

- The effect of preload on the local stress state at a thread root is still unknown. A study of this, with a series of make-up-break fatigue tests (without any other applied loading) would greatly benefit the understanding of this mechanism.

- A load redistribution model with respect to a crack emanating from the critical tooth should be developed.

- For future fatigue testing, it would be of immense benefit to use an inspection system capable of continuously monitoring crack development during fatigue testing.

- A weight function should be developed in a similar manner to that described in chapter three to accommodate mode II loading.

- For the development of the weight function for commercial use, a series of finite element analyses should be conducted to give appropriate reference SIFs and corresponding stress distributions, in tension and bending. The present solutions are sufficient within the applicability limits of the constitutive equations.

- With the availability of more extensive experimental results, the crack aspect ratio models can be upgraded and expressed as empirical functions of the local stress state.

- The entire analysis should be studied in terms of the sensitivity of prediction to variables. This should pre-empt a probabilistic evaluation of the solution as a whole.

Finally a flow chart summarising the main design equations in this thesis for the fatigue analysis of threaded connections is given below.

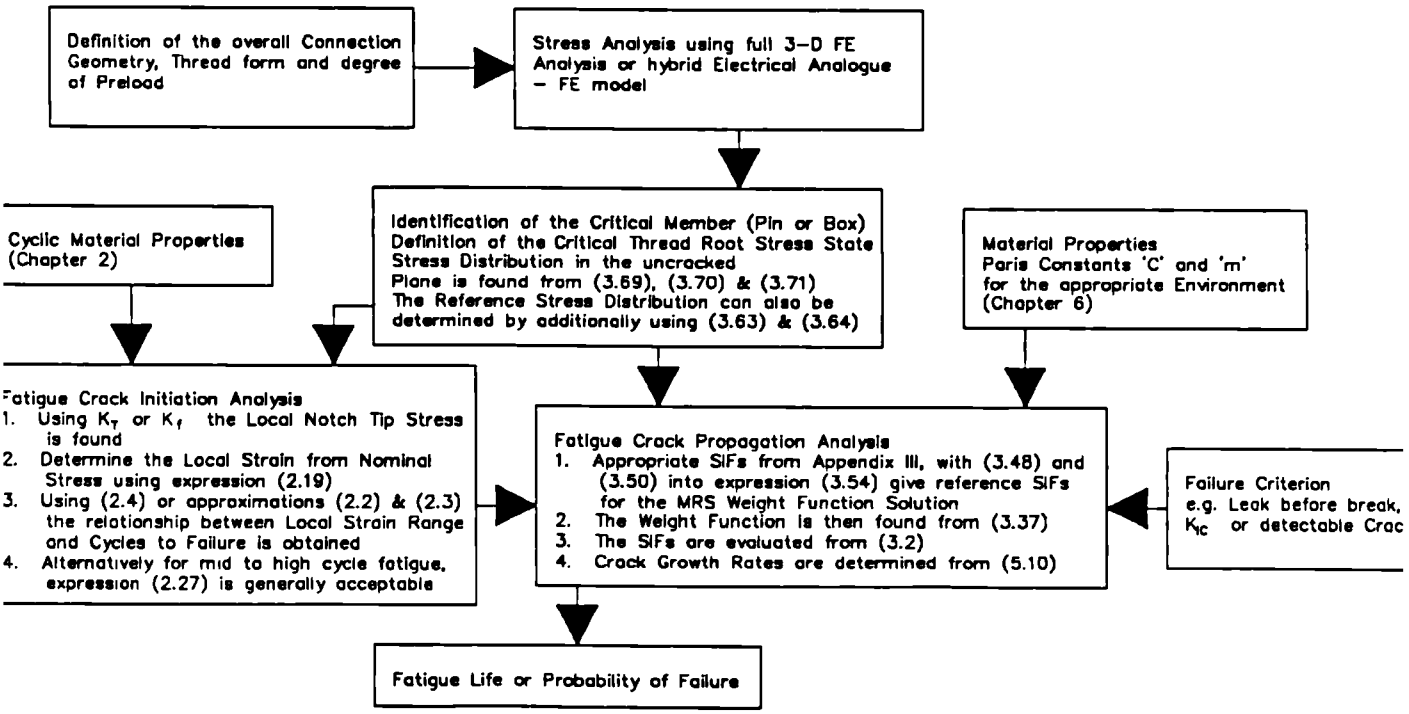

Appendix I

Determination of Fatigue Crack Growth Rates for API C75 Steel

Introduction

Fatigue crack growth in structural components is most generally modelled using a Linear-Elastic Fracture Mechanics (LEFM) approach. This assumes that the global relationship between the applied loads and resulting displacements to a component is linear.

Based on LEFM, the Paris law is given by:

$$da/dn = C\Delta K^m$$

Originally suggested by Paris and Erdogan [A1], it is the most widely accepted relationship between crack growth rate *da/dn* and stress intensity factor range ΔK. This stress intensity factor describes the crack tip stress field as a single parameter, and is a function of the nominal stress and geometry of the component. The stress intensity factor also depends upon the mode in which the crack has grown, i.e. opening, edge sliding or shear mode. In this case we are assuming that any significant crack growth we are interested in occurs entirely in mode I (opening mode). The parameters '*C*' and '*m*' are material properties for inert environments. It is these material constants which are required so that the crack propagation data from the threaded connections, fabricated from similar material can be interpreted in terms of K_{exp}.

Specimen

The LEFM method of crack growth analysis assumes that yielding and plastic zone size at the crack tip is confined to a relatively small region of the overall component, so that the elastic stress field is hardly affected. This becomes important when deciding upon the dimensions of the specimen to be tested in order to acquire the constants 'C' and 'm'.

The specimen type naturally should be one for which a well established stress intensity factor calibration exists. The Compact Tension (CT) specimen and the Centre Crack Tension (CCT) specimen have been the preferred testing configurations in the ASTM and BS determination of fatigue crack growth measurement guide-lines. The CCT specimen is recommended for tests at negative R ratios whereas the CT specimen is preferable for tension to tension loading, and for measurement of low crack growth rates. For these reasons the CT specimen was chosen as the most apt configuration for our purposes. For fracture toughness 'K_{Ic}' measurement, a plane strain specimen is necessary, as in cases of high crack growth rates triaxial effects become important as do R ratios. However, for low growth rates relatively thin specimens can minimise the effects of crack front straightness and curvature [A2]. The lower thickness limit of this plane stress specimen is to offset the possibility of buckling. The limiting criterion of the planar size is that it should be sufficient in order that the specimen remains predominantly elastic during testing.

The specimen and procedure of testing were in accordance with the ASTM standard E647-88. The specimen geometry and the standard limitations are shown in Fig A1. The material used was API grade 5A C75 steel, the composition and properties of which are set out in Chapter four. For the CT specimen, the following expression [A3], assuming linear-elastic, isotropic and homogeneous material without effects of residual stress, gives ΔK in terms of load range 'ΔP', crack length 'a' and geometrical dimensions 'B' and 'W':

$$\Delta K = \frac{\Delta P}{B\sqrt{W}} \frac{(2+\alpha)}{(1-\alpha)^{1.5}} (0.886 + 4.64\alpha - 13.32\alpha^2 + 14.72\alpha^3 - 5.6\alpha^4)$$

where $\alpha = a/W$

expression valid for $a/W \geq 0.2$

Test Apparatus and Procedure

The tests were carried out on an Instron Servo Electro-Mechanical 50 kN Dynamic Actuator, Fig A2 shows a block diagram of the test system. The controller incorporated a built in sinusoidal signal generator and cycle counter. Two clevis and pin joints were used in series to fix each end of the specimen to the test rig. The clevis pin assemblies to the specimen allowed in-plane rotation during loading. The second joints (perpendicular and adjacent to the former) ensured the specimen was free to align itself between the actuator and load cell. The pins were lubricated in order to minimise friction. These conditions are important so that the loading of the specimen conforms with the boundary conditions assumed in deriving the stress intensity factors.

A travelling microscope (magnification 50 x) fixed to a vernier scale was levelled and focused on to the specimen so that optical measurements could be made of the cracks progression. To make the optical readings clearer, the specimen was polished and reference marks applied to the crack path at 5mm intervals.

Two specimens similar in geometry were tested. Both were precracked at an applied constant amplitude cyclic load of 0.9 kN at 3 Hz until the crack was 4 mm long. The purpose of precracking is to provide a sharp, straight crack of adequate size as to eliminate the effect of the machine starter notch from the K-calibration and of crack growth characteristics caused by changing crack curvature or precrack load history. After precracking both tests were sinusoidally loaded at a constant amplitude. The loading details being:

Test No	ΔP	R Ratio	Frequency
1	1.45 kN	0.033	1.5 Hz
2	1.15 kN	0.042	1.5 Hz

Results

Fig A3 shows the fatigue crack growth curves for both tests. In order to determine the rate of fatigue crack growth from crack size versus cycles data, an incremental polynomial method was used. To do this a second order polynomial was fitted to sets of seven successive data points, the derivative of the resulting curve giving *da/dn*. The results of both tests were processed in this way and Fig A4 shows the resulting fatigue crack growth rate. A line was fitted to the combined data of tests 1 and 2 using the least squares method, the equation of which, hence the Paris material constants could be evaluated.

i.e.

$$C = 5.4 \times 10^{-13}$$
$$m = 3.77$$

References

[A1] Paris, P. C. and Erdogan, F., Journal of Basic Engineering, Trans of the ASME, pp 528-534, December 1963.

[A2] Bucci, R. J., "Development of Basic Material(s) Data for Evaluating Crack Growth Life", Part-Through Crack Fatigue Life Prediction, ASTM STP 687, J. B. Chang, ED., ASTM, pp 47-73, 1979.

[A3] Newman, Jr., J. C., "Stress Analysis of the Compact Specimen Including the Effects of Pin Loading" Fracture Analysis (8th conference), ASTM STP 560, pp 105-121, 1974.

[A4] Instron Limited, Coronation Road, High Wycombe, Buckinghamshire, England HP12 3SY.

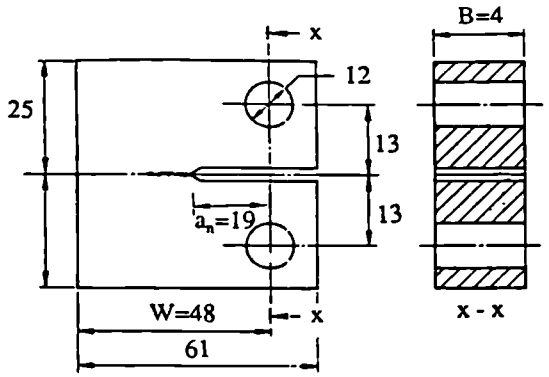

Recommended Thickness: $W/20 \leq B \leq W/4$

Minimum Dimensions: $W = 25$ mm

$a_n = 0.20W$

Fig A1 Compact Tension (CT) Specimen

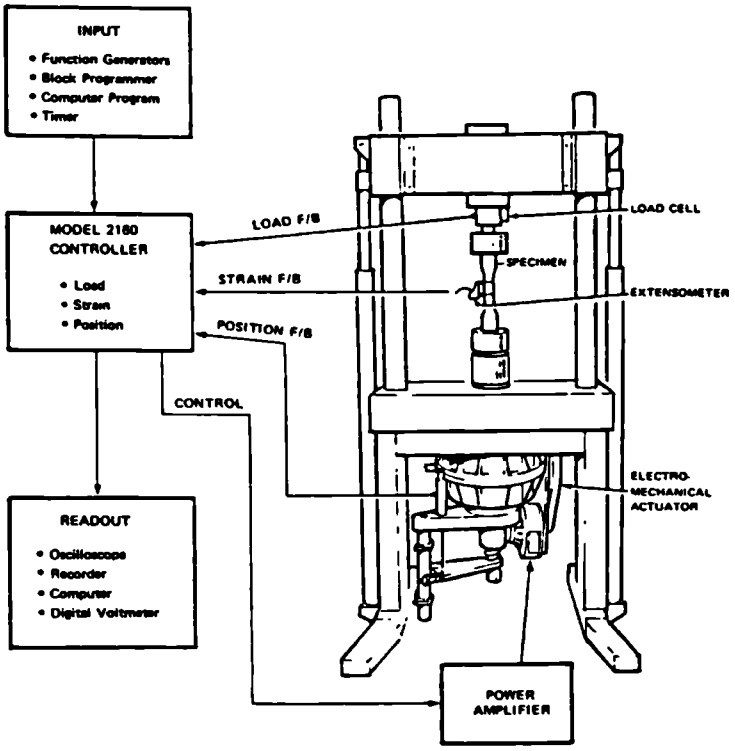

Fig A2 Block Diagram of Fatigue Testing System (from Instron [A4])

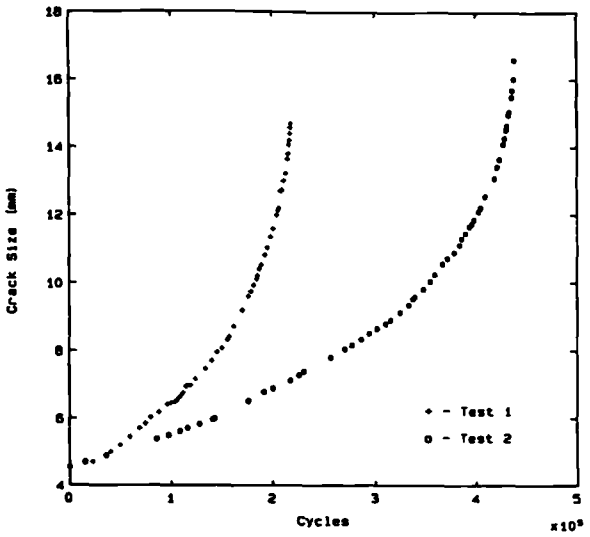

Fig A3 Crack Growth Curves for CT Specimens

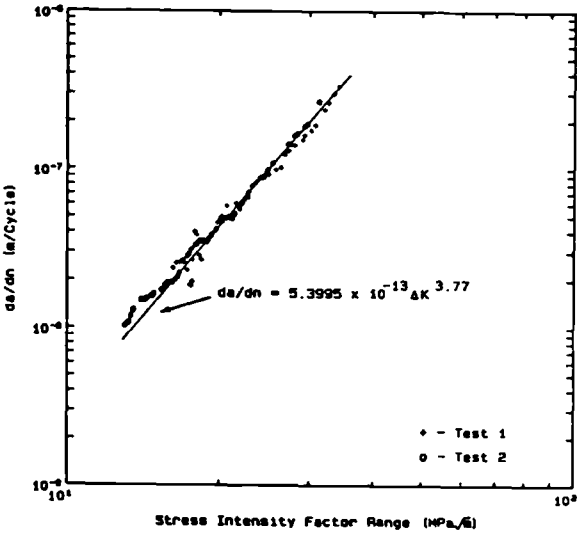

Fig A4 Crack Growth Rate for API C75 Steel

Appendix II

Derivation of the Preload Formulae

The mechanical model relating the applied torsional force to translational movement of a screw thread is analogous to the motion of a body of weight P_t up an inclined plane, under the action of a horizontal force P_h.

l = Pitch of Screw
d_m = Mean diameter of thread
α = Slope of the thread at d_m

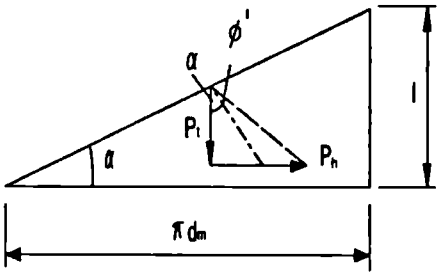

$$\Rightarrow \tan\alpha = \frac{l}{\pi d_m}$$

Induced Moment (Make-up Torque) $M_t = \frac{P_h d_m}{2}$

$$= \frac{P_t d_m}{2}\tan(\alpha + \phi')$$

$$= \frac{P_t d_m}{2}\left(\frac{\tan\alpha + \tan\phi'}{1 - \tan\alpha\tan\phi'}\right)$$

Taking $\mu = \tan\phi$, where ϕ is the true angle of friction

Then,

$$\frac{\mu}{\cos\theta} = \tan\phi'$$

ϕ' being the virtual angle of friction
θ is the tooth flank angle

$$\Rightarrow M_t = \frac{P_t d_m}{2}\left(\frac{l + \pi d_m \mu \sec\theta}{\pi d_m - l\mu \sec\theta}\right)$$

However, this does not take account of the friction at the Pin - Box shoulder interface. The effect of this is given by:

$$M_t = \frac{P_t d_c \mu_c}{2}$$

d_c = Mean diameter of pin face
μ_c = Coefficient of friction at pin and box shoulder

So the total Make-up Torque can be expressed,

$$M_t = \frac{P_t d_m}{2}\left(\frac{l + \pi d_m \mu \sec\theta}{\pi d_m - l\mu \sec\theta} + \frac{\mu_c d_c}{d_m}\right)$$

Appendix III

Constitutive Equations for 3-D Solution

$$\frac{K_{rod}^{surface}}{\sigma_{ten}\sqrt{\pi a}} = \left(1.6189A - 0.7389\left(\frac{a}{D}\right)B + 3.9238\left(\frac{a}{D}\right)^2 C\right) \quad /Q$$

$$A = 0.4827 + 0.8084\left(\frac{a}{c}\right) - 0.2911\left(\frac{a}{c}\right)^2$$

$$B = -6.5112 + 16.824\left(\frac{a}{c}\right) - 9.3128\left(\frac{a}{c}\right)^2$$

$$C = 5.547 - 7.5001\left(\frac{a}{c}\right) + 2.9531\left(\frac{a}{c}\right)^2$$

(A 1)

$$\frac{K_{rod}^{surface}}{\sigma_{bend}\sqrt{\pi a}} = \left(0.6477A - 1.042\left(\frac{a}{D}\right)B + 0.9651\left(\frac{a}{D}\right)^2 C\right)$$

$$A = 1.5633 - 0.3107\left(\frac{a}{c}\right) - 0.2526\left(\frac{a}{c}\right)^2$$

$$B = -3.8985 + 11.4667\left(\frac{a}{c}\right) - 6.5684\left(\frac{a}{c}\right)^2$$

$$C = 0.5395 + 5.0658\left(\frac{a}{c}\right) - 4.6053\left(\frac{a}{c}\right)^2$$

(A 2)

$$Q = 1.0 + 1.464\left(\frac{a}{c}\right)^{1.65}$$

Both valid for:

$$0.6 \le \left(\frac{a}{c}\right) \le 1.0$$

$$0.05 \le \left(\frac{a}{D}\right) \le 0.35$$

$$\frac{K_{tube\,ext}^{surface}}{\sigma_{ten}\sqrt{\pi a}} = \left(1.5877M_0 - 0.0067\left(\frac{a}{t}\right)M_1 + 0.1667\left(\frac{a}{t}\right)^2 M_2\right)FA_{RC}$$

$$A_{RC} = 0.6361 + 0.087\left(\frac{a}{c}\right) + 0.4543\left(\frac{a}{c}\right)^2 - 0.1783\left(\frac{a}{c}\right)^3$$

$$M_0 = e^{\left(-0.013\log_e\left(\frac{r}{t}\right) + 0.0045\log_e\left(\frac{r}{t}\right)^2 - 0.0003\log_e\left(\frac{r}{t}\right)^4\right)}$$

$$M_1 = e^{\left(3.434 - 0.6816\log_e\left(\frac{r}{t}\right) - 0.2386\log_e\left(\frac{r}{t}\right)^2 + 0.0421\log_e\left(\frac{r}{t}\right)^3\right)} - 30.0$$

$$M_2 = e^{\left(0.2624 - 0.7251\log_e\left(\frac{r}{t}\right) - 0.387\log_e\left(\frac{r}{t}\right)^2 + 0.0615\log_e\left(\frac{r}{t}\right)^3\right)} - 0.3$$

$$F = K_0 + K_1\left(\frac{a}{t}\right) + K_2\left(\frac{a}{t}\right)^2$$

$$K_0 = 1.266A_0 - 0.361\left(\frac{a}{c}\right)B_0 + 0.095\left(\frac{a}{c}\right)^2 C_0$$

$$K_1 = -1.1755A_1 + 3.0118\left(\frac{a}{c}\right)B_1 - 1.8363\left(\frac{a}{c}\right)^2 C_1$$

$$K_2 = 3.6505A_2 - 7.8267\left(\frac{a}{c}\right)B_2 + 4.1762\left(\frac{a}{c}\right)^2 C_2$$

$$A_0 = e^{\left(-0.0342\log_e\left(\frac{r}{t}\right) - 0.0494\log_e\left(\frac{r}{t}\right)^2 + 0.019\log_e\left(\frac{r}{t}\right)^3\right)}$$

$$A_1 = e^{\left(0.2624 - 1.3662\log_e\left(\frac{r}{t}\right) - 0.4102\log_e\left(\frac{r}{t}\right)^2 + 0.0655\log_e\left(\frac{r}{t}\right)^4\right)} - 0.3$$

$$A_2 = e^{\left(-1.2585\log_e\left(\frac{r}{t}\right) - 0.0056\log_e\left(\frac{r}{t}\right)^2 + 0.0563\log_e\left(\frac{r}{t}\right)^3\right)}$$

$$B_0 = e^{\left(0.0011\log_e\left(\frac{r}{t}\right) - 0.6149\log_e\left(\frac{r}{t}\right)^2 + 0.0772\log_e\left(\frac{r}{t}\right)^4\right)}$$

$$B_1 = e^{\left(0.1823 - 1.2621\log_e\left(\frac{r}{t}\right) - 0.7508\log_e\left(\frac{r}{t}\right)^2 + 0.1206\log_e\left(\frac{r}{t}\right)^4\right)} - 0.2$$

$$B_2 = e^{\left(-1.3068\log_e\left(\frac{r}{t}\right) - 0.1289\log_e\left(\frac{r}{t}\right)^2 + 0.1121\log_e\left(\frac{r}{t}\right)^3\right)}$$

$$C_0 = e^{\left(0.1398 - 0.4506\log_e\left(\frac{r}{t}\right) - 0.6224\log_e\left(\frac{r}{t}\right)^5 + 0.1044\log_e\left(\frac{r}{t}\right)^7\right)} - 0.15$$

$$C_1 = e^{\left(0.098 - 0.3746\log_e\left(\frac{r}{t}\right) - 2.7365\log_e\left(\frac{r}{t}\right)^2 + 0.6759\log_e\left(\frac{r}{t}\right)^3\right)} - 0.103$$

$$C_2 = e^{\left(-1.3299\log_e\left(\frac{r}{t}\right) - 0.287\log_e\left(\frac{r}{t}\right)^2 + 0.1786\log_e\left(\frac{r}{t}\right)^3\right)}$$

(A3)

$$\frac{K_{tube\,ext}^{surface}}{\sigma_{bend}\sqrt{\pi a}} = 0.6417G_0A - 0.21\left(\frac{a}{t}\right)G_1B + 0.0333\left(\frac{a}{t}\right)^2G_2C$$

$$A = 2.1887H_{01} - 1.8208\left(\frac{a}{c}\right)H_{02} + 0.6320\left(\frac{a}{c}\right)^2H_{03}$$

$$B = 4.5053H_{11} - 9.0278\left(\frac{a}{c}\right)H_{12} + 5.5225\left(\frac{a}{c}\right)^2H_{13}$$

$$C = 71.8333H_{21} - 156.25\left(\frac{a}{c}\right)H_{22} + 85.4167\left(\frac{a}{c}\right)^2H_{23}$$

$$G_0 = e^{\left(-0.0062\log_e\left(\frac{r}{t}\right) - 0.0197\log_e\left(\frac{r}{t}\right)^2 + 0.0073\log_e\left(\frac{r}{t}\right)^3\right)}$$

$$G_1 = e^{\left(0.4055 - 0.2349\log_e\left(\frac{r}{t}\right) - 0.7301\log_e\left(\frac{r}{t}\right)^2 + 0.1945\log_e\left(\frac{r}{t}\right)^3\right)} - 0.5$$

$$G_2 = e^{\left(0.8755 + 3.0812\log_e\left(\frac{r}{t}\right) - 7.5796\log_e\left(\frac{r}{t}\right)^2 + 2.5192\log_e\left(\frac{r}{t}\right)^3\right)} - 1.4$$

$$H_{01} = e^{\left(-0.0106\log_e\left(\frac{r}{t}\right) - 0.0839\log_e\left(\frac{r}{t}\right)^2 + 0.0273\log_e\left(\frac{r}{t}\right)^3\right)}$$

$$H_{02} = e^{\left(0.0411\log_e\left(\frac{r}{t}\right) - 0.3857\log_e\left(\frac{r}{t}\right)^2 + 0.1248\log_e\left(\frac{r}{t}\right)^3\right)}$$

$$H_{03} = e^{\left(0.2456\log_e\left(\frac{r}{t}\right) - 0.9949\log_e\left(\frac{r}{t}\right)^2 + 0.3187\log_e\left(\frac{r}{t}\right)^3\right)}$$

$$H_{11} = e^{\left(-2.3566\log_e\left(\frac{r}{t}\right) + 4.1208\log_e\left(\frac{r}{t}\right)^2 - 1.3076\log_e\left(\frac{r}{t}\right)^3\right)}$$

$$H_{12} = e^{\left(-1.6407\log_e\left(\frac{r}{t}\right) + 3.0752\log_e\left(\frac{r}{t}\right)^2 - 1.0156\log_e\left(\frac{r}{t}\right)^3\right)}$$

$$H_{13} = e^{\left(-0.7512\log_e\left(\frac{r}{t}\right) + 1.643\log_e\left(\frac{r}{t}\right)^2 - 0.5956\log_e\left(\frac{r}{t}\right)^3\right)}$$

$$H_{21} = e^{\left(1.6094 - 19.0466\log_e\left(\frac{r}{t}\right) + 41.5177\log_e\left(\frac{r}{t}\right)^2 - 33.985\log_e\left(\frac{r}{t}\right)^3 + 12.2611\log_e\left(\frac{r}{t}\right)^4 - 1.6421\log_e\left(\frac{r}{t}\right)^5\right)} - 4$$

$$H_{22} = e^{\left(1.6094 - 17.808\log_e\left(\frac{r}{t}\right) + 38.0919\log_e\left(\frac{r}{t}\right)^2 - 30.6045\log_e\left(\frac{r}{t}\right)^3 + 10.8423\log_e\left(\frac{r}{t}\right)^4 - 1.427\log_e\left(\frac{r}{t}\right)^5\right)} - 4$$

$$H_{23} = e^{\left(1.6094 - 16.8793\log_e\left(\frac{r}{t}\right) + 36.1353\log_e\left(\frac{r}{t}\right)^2 - 29.0707\log_e\left(\frac{r}{t}\right)^3 + 10.313\log_e\left(\frac{r}{t}\right)^4 - 1.3592\log_e\left(\frac{r}{t}\right)^5\right)} - 4$$

(A 4)

Both valid for:

$$0.6 \le \left(\frac{a}{c}\right) \le 1.0$$

$$1.0 \le \left(\frac{r_i}{t}\right) \le 10.0$$

$$0.2 \le \left(\frac{a}{t}\right) \le 0.8$$

$$\frac{K_{tubei}^{surface}}{\sigma_{ten}\sqrt{\pi a}} = 0.817A_T M_{0T} - 0.0073B_T M_{1T}\lambda - 0.0133C_T M_{2T}\lambda^2$$

$$M_{0T} = 1.3868 - 1.8666\left(\frac{a}{t}\right) - 0.5508\left(\frac{a}{t}\right)^2 + 1.071\left(\frac{a}{t}\right)^3$$

$$M_{1T} = 1.3636 - 2.9545\left(\frac{a}{t}\right) + 6.8182\left(\frac{a}{t}\right)^2 - 5.6818\left(\frac{a}{t}\right)^3$$

$$M_{2T} = -5.4 + 50.5\left(\frac{a}{t}\right) - 105.0\left(\frac{a}{t}\right)^2 + 62.5\left(\frac{a}{t}\right)^3$$

$$A_T = 0.869E_{A0} + 0.16E_{A1}\left(\frac{c}{t}\right) - 0.031E_{A2}\left(\frac{c}{t}\right)^2 + 0.002E_{A3}\left(\frac{c}{t}\right)^3$$

$$B_T = 1.9078E_{B0} - 1.2443E_{B1}\left(\frac{c}{t}\right) + 0.3641E_{B2}\left(\frac{c}{t}\right)^2 - 0.0277E_{B3}\left(\frac{c}{t}\right)^3$$

$$C_T = 1.5489E_{C0} - 0.6312E_{C1}\left(\frac{c}{t}\right) + 0.0861E_{C2}\left(\frac{c}{t}\right)^2 - 0.0039E_{C3}\left(\frac{c}{t}\right)^3$$

$$E_{A0} = 1.3347 - 1.8487\left(\frac{a}{t}\right) + 0.8128\left(\frac{a}{t}\right)^2 + 0.3209\left(\frac{a}{t}\right)^3$$

$$E_{A1} = -1.4575 + 14.567\left(\frac{a}{t}\right) - 11.8057\left(\frac{a}{t}\right)^2 + 2.0415\left(\frac{a}{t}\right)^3$$

$$E_{A2} = -2.5535 + 25.2223\left(\frac{a}{t}\right) - 47.5707\left(\frac{a}{t}\right)^2 + 21.4835\left(\frac{a}{t}\right)^3$$

$$E_{A3} = -2.9337 + 29.1045\left(\frac{a}{t}\right) - 53.235\left(\frac{a}{t}\right)^2 + 30.2755\left(\frac{a}{t}\right)^3$$

$$E_{B0} = 6.5652 - 42.4399\left(\frac{a}{t}\right) + 82.7447\left(\frac{a}{t}\right)^2 - 48.3707\left(\frac{a}{t}\right)^3$$

$$E_{B1} = 12.4616 - 88.4639\left(\frac{a}{t}\right) + 176.9573\left(\frac{a}{t}\right)^2 - 105.8838\left(\frac{a}{t}\right)^3$$

$$E_{B2} = 11.8087 - 86.4218\left(\frac{a}{t}\right) + 185.4145\left(\frac{a}{t}\right)^2 - 117.615\left(\frac{a}{t}\right)^3$$

$$E_{B3} = 11.5392 - 85.366\left(\frac{a}{t}\right) + 187.6396\left(\frac{a}{t}\right)^2 - 121.4498\left(\frac{a}{t}\right)^3$$

$$E_{C0} = -2.6867 + 31.3505\left(\frac{a}{t}\right) - 75.2248\left(\frac{a}{t}\right)^2 + 53.2041\left(\frac{a}{t}\right)^3$$

$$E_{C1} = -11.5468 + 106.8068\left(\frac{a}{t}\right) - 256.7343\left(\frac{a}{t}\right)^2 + 181.8505\left(\frac{a}{t}\right)^3$$

$$E_{C2} = -26.7973 + 237.3067\left(\frac{a}{t}\right) - 573.1079\left(\frac{a}{t}\right)^2 + 407.5403\left(\frac{a}{t}\right)^3$$

$$E_{C3} = -46.6842 + 407.5522\left(\frac{a}{t}\right) - 986.1083\left(\frac{a}{t}\right)^2 + 702.2599\left(\frac{a}{t}\right)^3$$

(A5)

$$\frac{K_{tubei}^{surface}}{\sigma_{bend}\sqrt{\pi a}} = 0.804A_B M_{0B} - 0.002B_B M_{1B}\lambda - 0.024C_B M_{2B}\lambda^2$$

$$M_{0B} = 1.3806 - 1.4956\left(\frac{a}{t}\right) - 2.6119\left(\frac{a}{t}\right)^2 + 2.8762\left(\frac{a}{t}\right)^3$$

$$M_{1B} = -15.0 + 118.6111\left(\frac{a}{t}\right) - 216.6667\left(\frac{a}{t}\right)^2 + 118.0556\left(\frac{a}{t}\right)^3$$

$$M_{2B} = -0.3333 + 10.6481\left(\frac{a}{t}\right) - 22.2222\left(\frac{a}{t}\right)^2 + 11.5741\left(\frac{a}{t}\right)^3$$

$$A_B = 0.8572D_{A0} + 0.1744D_{A1}\left(\frac{c}{t}\right) - 0.0337D_{A2}\left(\frac{c}{t}\right)^2 + 0.0021D_{A3}\left(\frac{c}{t}\right)^3$$

$$B_B = -2.505D_{B0} + 4.3063D_{B1}\left(\frac{c}{t}\right) - 0.8543D_{B2}\left(\frac{c}{t}\right)^2 + 0.053D_{B3}\left(\frac{c}{t}\right)^3$$

$$C_B = 2.1731D_{C0} - 1.4784D_{C1}\left(\frac{c}{t}\right) + 0.3272D_{C2}\left(\frac{c}{t}\right)^2 - 0.022D_{C3}\left(\frac{c}{t}\right)^3$$

$$D_{A0} = -4.3542 + 50.1316\left(\frac{a}{t}\right) - 139.3859\left(\frac{a}{t}\right)^2 + 112.9196\left(\frac{a}{t}\right)^3$$

$$D_{A1} = 29.0825 - 263.9355\left(\frac{a}{t}\right) + 737.3531\left(\frac{a}{t}\right)^2 - 598.6862\left(\frac{a}{t}\right)^3$$

$$D_{A2} = 10.4899 - 94.4364\left(\frac{a}{t}\right) + 282.1632\left(\frac{a}{t}\right)^2 - 236.1437\left(\frac{a}{t}\right)^3$$

$$D_{A3} = 6.8219 - 60.821\left(\frac{a}{t}\right) + 191.5071\left(\frac{a}{t}\right)^2 - 164.7433\left(\frac{a}{t}\right)^3$$

$$D_{B0} = 5.2107 - 31.22\left(\frac{a}{t}\right) + 57.6829\left(\frac{a}{t}\right)^2 - 34.2506\left(\frac{a}{t}\right)^3$$

$$D_{B1} = 3.9118 - 21.2918\left(\frac{a}{t}\right) + 38.0775\left(\frac{a}{t}\right)^2 - 22.0663\left(\frac{a}{t}\right)^3$$

$$D_{B2} = 3.4665 - 16.6297\left(\frac{a}{t}\right) + 23.6933\left(\frac{a}{t}\right)^2 - 11.0313\left(\frac{a}{t}\right)^3$$

$$D_{B3} = 3.1868 - 13.6682\left(\frac{a}{t}\right) + 14.4172\left(\frac{a}{t}\right)^2 - 3.7347\left(\frac{a}{t}\right)^3$$

$$D_{C0} = 0.9183 + 2.0163\left(\frac{a}{t}\right) - 9.9581\left(\frac{a}{t}\right)^2 + 9.5987\left(\frac{a}{t}\right)^3$$

$$D_{C1} = 0.752 + 4.7942\left(\frac{a}{t}\right) - 21.9163\left(\frac{a}{t}\right)^2 + 20.7321\left(\frac{a}{t}\right)^3$$

$$D_{C2} = 0.3634 + 9.0476\left(\frac{a}{t}\right) - 35.8356\left(\frac{a}{t}\right)^2 + 32.5657\left(\frac{a}{t}\right)^3$$

$$D_{C3} = 0.1277 + 11.569\left(\frac{a}{t}\right) - 43.9066\left(\frac{a}{t}\right)^2 + 39.3513\left(\frac{a}{t}\right)^3$$

(A6)

$$\lambda = (12(1-\nu^2))^{\frac{1}{4}} \frac{a}{\sqrt{rt}}, \qquad \nu = 0.3$$

Both valid for:

$$1.0 \le \left(\frac{c}{t}\right) \le 8.0$$

$$0.2 \le \left(\frac{a}{t}\right) \le 0.8$$

$$0 \le (\lambda) \le 8.0$$

Appendix IV

Full-Scale Fatigue Test Details

Test no / ID	VAM CA1	n (cycles)	a (mm)	c (mm)	$\frac{2c}{a}$	a_{mid} (mm)	da/dn	a/t	Y_{mp} $\frac{a=5.4x10^{-13}}{m=3.77}$
Description	$5^1/_2$" VAM	1.36×10^6	0.6	4.6	15.3	0.7	3.3×10^{-9}	0.09	1.15
Mat^L Ref	API C75	1.39×10^6	0.7	5.3	15.2	1.1	8.8×10^{-9}	0.14	1.19
Torque (ft lbs)	8,600	1.47×10^6	1.4	7.0	10.0	1.6	6.7×10^{-9}	0.21	0.92
Finish	As Machined	1.53×10^6	1.8	7.8	8.7	2.9	36.7×10^{-9}	0.38	1.07
Anti-Gall	none	1.59×10^6	4.0	11.5	5.6	5.5	50.0×10^{-9}	0.71	0.85
Lubricant	Alvania EP2	1.65×10^6	7.0	-					
Δ P (KN)	600								
R	0.1								
Freq (Hz)	1.0								
$\Delta \sigma_{nom}$ (MPa)	185.0								
$\Delta \sigma_{local}$ (MPa)	762.0								
Failure	Pin								
Thread no	17								
Initiation (cycles)	1.20×10^6								
Life (cycles)	1.65×10^6								

notes:
"No confidence is placed in the initiation life obtained for this specimen", Ref [5.1].

r (mm) = 65.6
t (mm) = 7.0
ρ (mm) = 0.203
h (mm) = 1.6
θ (degrees) = 10
SCF = 4.12

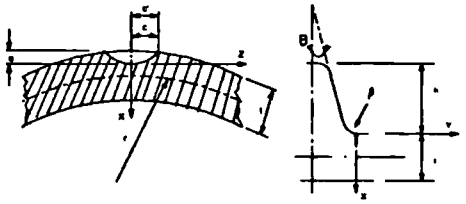

Test no / ID	VAM CA2	n (cycles)	a (mm)	c (mm)	$\frac{2c}{a}$	a_{mid} (mm)	da/dn	a/t	Y_{exp} $\frac{c=5.4x10^{-15}}{m=3.77}$
Description	$5^1/_2$" VAM	1.88×10^5	1.82	62.8	69.0	2.1	45.8×10^{-9}	0.27	1.34
Mat'l Ref	API C75	2.00×10^5	2.37	62.8	53.0	2.8	55.0×10^{-9}	0.36	1.21
Torque (ft lbs)	7,600	2.14×10^5	3.14	62.8	40.0	5.1	42.9×10^{-8}	0.66	1.55
Finish	As Machined	2.23×10^5	7.0	62.8	17.9				
Anti-Gall	none								
Lubricant	Alvania EP2								
Δ P (KN)	600								
R	0.1								
Freq (Hz)	1.0								
$\Delta \sigma_{nom}$ (MPa)	185.0								
$\Delta \sigma_{local}$ (MPa)	762.0								
Failure	Pin								
Thread no	17								
Initiation (cycles)	1.15×10^5								
Life (cycles)	2.23×10^5								

notes:

r (mm) = 65.6
t (mm) = 7.0
ρ (mm) = 0.203
h (mm) = 1.6
θ (degrees) = 10
SCF = 4.12

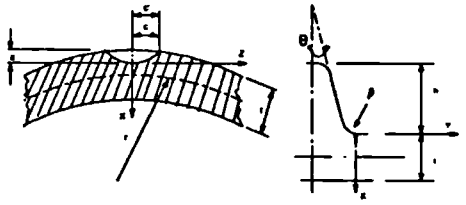

Test no / ID	VAM CA3	n (cycles)	a (mm)	c (mm)	$\frac{2c}{a}$	a_{mid} (mm)	da/dn	a/t	Y_{exp} $\frac{c=5.4\times10^{-13}}{m=3.77}$
Description	$5^1/_2$" VAM	1.87×10^5	1.55	64.6	83.4	2.0	79.2×10^{-9}	0.26	1.58
Mat^L Ref	API C75	1.99×10^5	2.50	64.6	51.7	2.7	38.9×10^{-9}	0.35	1.13
Torque (ft lbs)	7,080	2.08×10^5	2.85	64.6	45.3	3.5	24.0×10^{-8}	0.45	1.61
Finish	As Machined	2.13×10^5	4.05	64.6	31.9	5.5	59.0×10^{-8}	0.71	1.63
Anti-Gall	none	2.18×10^5	7.00	64.6	18.5				
Lubricant	Alvania EP2								
Δ P (KN)	600								
R	0.1								
Freq (Hz)	1.0								
$\Delta \sigma_{nom}$ (MPa)	185.0								
$\Delta \sigma_{local}$ (MPa)	762.0								
Failure	Pin								
Thread no	17								
Initiation (cycles)	1.25×10^5								
Life (cycles)	2.18×10^5								

notes:

r (mm) = 65.6
t (mm) = 7.0
ρ (mm) = 0.203
h (mm) = 1.6
θ (degrees) = 10
SCF = 4.12

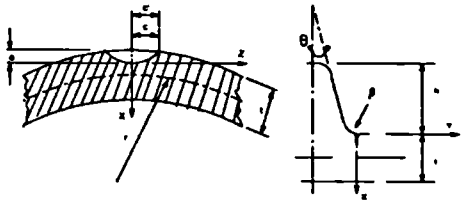

Test no / ID	VAM VA1	n (cycles)	a (mm)	c (mm)	$\frac{2c}{a}$	a_{mid} (mm)	da/dn	a/t	Y_{exp} $\frac{a=5.4x10^{-13}}{m=3.77}$
Description	$5^1/_2$" VAM	0.95×10^6	0.7	6.8	19.4	1.2	1.43×10^{-9}	0.16	1.67
Mat^L Ref	API C75	1.65×10^6	1.7	15.0	17.6	2.1	2.42×10^{-9}	0.27	1.45
Torque (ft lbs)	1. 7,330 2. 5,860	1.98×10^6	2.5	16.8	13.4	3.3	4.57×10^{-9}	0.43	1.37
Finish	As Machined	2.33×10^6	4.1	18.1	8.8	5.3	9.60×10^{-9}	0.69	1.32
Anti-Gall	none	2.58×10^6	6.5	22.0	6.8	6.8	4.17×10^{-9}	0.88	0.93
Lubricant	Alvania EP2	2.70×10^6	7.0	-					
Δ P (KN)	253.0								
Clipping Ratio	3.44								
f_z (Hz)	1.5								
$\Delta \sigma_{nom}$ (MPa)	78.2								
$\Delta \sigma_{local}$ (MPa)	322.0								
Failure	Pin								
Thread no	17								
Initiation (cycles)	0.4×10^6								
Life (cycles)	2.7×10^6								

notes:

1. Initial Makeup Torque
2. Subsequent Makeup Torque after 0.4×10^6 cycles

f_z - mean zero crossing freq.

r (mm) = 65.6
t (mm) = 7.0
ρ (mm) = 0.203
h (mm) = 1.6
θ (degrees) = 10
SCF = 4.12

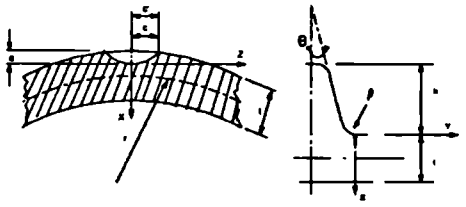

Test no / ID	VAM VA2	n (cycles)	a (mm)	c (mm)	$\frac{2c}{a}$	a_{mid} (mm)	da/dn	a/t	Y_{mp} $\frac{c=5.4\times10^{-13}}{m=3.77}$
Description	$5^1/_2$" VAM	1.65×10^6	0.5	4.1	16.4	0.7	1.05×10^{-9}	0.01	2.01
Mat^L Ref	API C75	2.03×10^6	0.9	6.6	14.7	1.3	2.50×10^{-9}	0.17	1.86
Torque (ft lbs)	5,650	2.31×10^6	1.6	9.2	11.5	1.8	2.14×10^{-9}	0.23	1.52
Finish	As Machined	2.45×10^6	1.9	10.5	11.1	2.2	4.17×10^{9}	0.29	1.64
Anti-Gall	none	2.57×10^6	2.4	12.7	10.6	3.5	6.0×10^{-9}	0.45	1.43
Lubricant	Alvania EP2	2.92×10^6	4.5	15.4	6.8				
Δ P (KN)	253.0								
Clipping Ratio	3.44								
f_z (Hz)	1.5								
$\Delta \sigma_{nom}$ (MPa)	78.2								
$\Delta \sigma_{local}$ (MPa)	322.0								
Failure	Pin								
Thread no	17								
Initiation (cycles)	1.2×10^6								
Life (cycles)	3.2×10^6								

notes:

f_z - mean zero crossing freq.

r (mm) = 65.6
t (mm) = 7.72
ρ (mm) = 0.203
h (mm) = 1.6
θ (degrees) = 10
SCF = 4.12

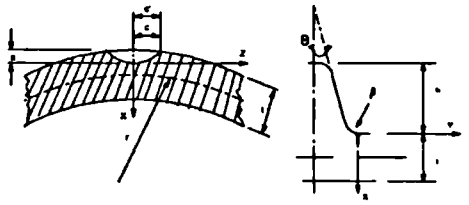

Test no / ID	Axial 1	n (cycles)	a (mm)	c (mm)	$\frac{2c}{a}$	a_{mid} (mm)	da/dn	a/t	Y_{exp} $\frac{c = 2.09 \times 10^{-11}}{m = 2.61}$
Description	NC50 $6^1/_2$" x $2^1/_2$" Standard	1.56×10^6	0.8	6.5	16.3	4.3	3.2×10^{-9}	0.16	1.56
Mat^L Ref	AISI 4145H	3.75×10^6	7.8	16.8	4.3	9.1	6.4×10^{-9}	0.34	1.40
Torque (ft lbs)	none	4.14×10^6	10.3	20.6	4.0	11.3	8.3×10^{-9}	0.43	1.39
Finish	As Machined	4.38×10^6	12.3	-	-	13.6	8.6×10^{-9}	0.52	1.28
Anti-Gall	Kemplate	4.67×10^6	14.8	22.9	3.1	18.3	41.2×10^{-9}	0.70	1.35
Lubricant	Koper-kote	4.84×10^6	21.8	29.4	2.7	24.1	37.5×10^{-9}	0.92	1.13
Δ P (KN)	1. 698.0 2. 1043.0	4.96×10^6	26.3	30.3	2.42				
R	1. 0.02 2. 0.03								
Freq (Hz)	1. 4.0 2. 2.5								
$\Delta \sigma_{nom}$ (MPa)	1. 38.3 2. 57.2								
$\Delta \sigma_{local}$ (MPa)	1. 421.3 2. 629.2								
Failure	Box								
Thread no	11								
Initiation (cycles)	0.8×10^6								
Life (cycles)	5.21×10^6								

notes:
At load range '1', test was cycled for 4.67×10^6 cycles and for 5.4×10^5 cycles at load range '2'.

r (mm) = 70.0
t (mm) = 25.0
ρ (mm) = 0.97
h (mm) = 3.09
θ (degrees) = 30
SCF = 11.0

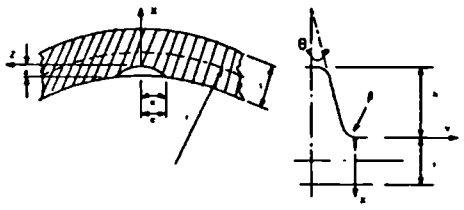

Test no / ID	Axial 2	n (cycles)	a (mm)	c (mm)	$\frac{2c}{a}$	a_{mod} (mm)	da/dn	a/t	Y_{exp} $\frac{c = 2.08 \times 10^{-11}}{m = 2.61}$
Description	NC50 $6^{1}/_{2}$" x $3^{1}/_{4}$" Standard	2.01 x 10^{6}	6.5	9.4	2.9	8.3	6.04 x 10^{-9}	0.33	1.14
Mat^{L} Ref	AISI 4145H	2.59 x 10^{6}	10.0	17.0	3.4	12.8	12.5 x 10^{-9}	0.51	1.21
Torque (ft lbs)	28,000	3.03 x 10^{6}	15.5	32.6	4.2	18.3	9.65 x 10^{-9}	0.73	0.92
Finish	As Machined	3.60 x 10^{6}	21.0	84.0	8.0	22.8	7.29 x 10^{-9}	0.91	0.74
Anti-Gall	Kemplate	4.08 x 10^{6}	24.5	117.6	9.6				
Lubricant	Koper-kote								
Δ P (KN)	776.0								
R	0.05								
Freq (Hz)	4.0								
$\Delta \sigma_{nom}$ (MPa)	48.3								
$\Delta \sigma_{local}$ (MPa)	342.7								
Failure	Box								
Thread no	11								
Initiation (cycles)	0.5 x 10^{6}								
Life (cycles)	4.13 x 10^{6}								

notes:

r (mm) = 70.0
t (mm) = 25.0
ρ (mm) = 0.97
h (mm) = 3.09
θ (degrees) = 30
SCF = 7.09

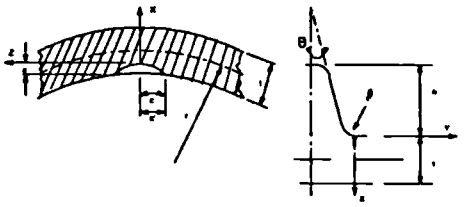

Test no / ID	Axial 3(b)	n (cycles)	a (mm)	c (mm)	$\frac{2c}{a}$	a_{mid} (mm)	da/dn	a/t	Y_{exp} $\frac{\sigma = 2.05 \times 10^{-11}}{m = 2.61}$
Description	$6^{5}/_{8}$" Reg $7^{1}/_{2}$" x $2^{13}/_{16}$" BB & SR	0.30 x 10^{6}	7.4	90.5	24.5	9.1	11.0 x 10^{-9}	0.34	1.35
Mat^{L} Ref	AISI 4145H	0.60 x 10^{6}	10.7	92.5	17.3	15.2	29.7 x 10^{-9}	0.56	1.52
Torque (ft lbs)	none	0.90 x 10^{6}	19.6	98.5	10.1	23.3	14.8 x 10^{-8}	0.86	2.28
Finish	As Machined	0.95 x 10^{6}	27.0	104.5	7.7				
Anti-Gall	Kemplate								
Lubricant	Koper-kote								
Δ P (KN)	1200								
R	0.04								
Freq (Hz)	1.5								
$\Delta \sigma_{nom}$ (MPa)	49.0								
$\Delta \sigma_{local}$ (MPa)	640.9								
Failure	Box								
Thread no	7								
Initiation (cycles)	-								
Life (cycles)	0.95 x 10^{6}								

notes:

Specimen was torqued to 60,000 ft lbs and cycled for 7.0 x 10^{6} cycles @ σ_{nom} = 34 MPa before this test.

Test 3(a), SCF = 9.24

=> $\Delta\sigma_{local}$ = 314.2 MPa

Initiation - 6.0 x 10^{6} cycles

r (mm) = 82.8

t (mm) = 25.0

ρ (mm) = 0.635

h (mm) = 3.75

θ (degrees) = 30

SCF = 13.08

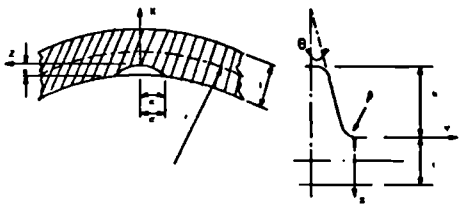

Test no / ID	Axial 4	n (cycles)	a (mm)	c (mm)	$\frac{2c}{a}$	a_{mid} (mm)	da/dn	a/t	Y_{exp} $\frac{c=2.05\times10^{-11}}{m=2.61}$
Description	$6^{3}/_{8}$" Reg $7^{1}/_{2}$" x $3^{1}/_{4}$" BB & SR	0.42×10^{6}	-	-	-	-	-	-	-
Mat^{L} Ref	AISI 4145H								
Torque (ft lbs)	48,000								
Finish	As Machined								
Anti-Gall	Kemplate								
Lubricant	Koper-kote								
Δ P (KN)	1340								
R	0.023								
Freq (Hz)	1.5								
$\Delta \sigma_{nom}$ (MPa)	57.9								
$\Delta \sigma_{local}$ (MPa)	492.2								
Failure	none								
Thread no	-								
Initiation (cycles)	-								
Life (cycles)	-								

notes:
Specimen had been cycled at σ_{nom} = 44.8 MPa for 6.3×10^{6} cycles. - RUNOUT

r (mm) = 82.8
t (mm) = 25.0
ρ (mm) = 0.635
h (mm) = 3.75
θ (degrees) = 30
SCF = 8.5

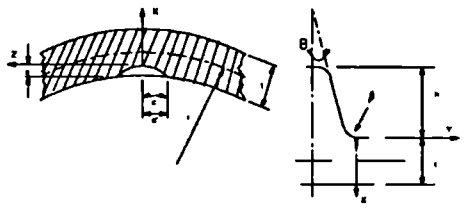

Test no / ID	Axial 5	n (cycles)	a (mm)	c (mm)	$\frac{2c}{a}$	a_{end} (mm)	da/dn	a/t	Y_{mp} $\frac{c=1.23\times10^{-12}}{m=3.42}$
Description	NC50 $6^{1}/_{2}$" x $2^{13}/_{16}$" BB & SR	0.88×10^{6}	2.3	27.7	24.1	4.0	11.5×10^{-9}	0.17	2.27
Mat^{L} Ref	AG17	1.17×10^{6}	5.7	52.0	18.3	11.4	39.7×10^{-9}	0.50	1.93
Torque (ft lbs)	30,000	1.46×10^{6}	17.1	114.0	13.3	20.1	64.1×10^{-9}	0.87	1.67
Finish	As Machined	1.55×10^{6}	23.0	124.0	10.8				
Anti-Gall	Kemplate								
Lubricant	Koper-kote								
Δ P (KN)	1000.0								
R	0.021								
Freq (Hz)	1.84								
$\Delta \sigma_{nom}$ (MPa)	56.9								
$\Delta \sigma_{local}$ (MPa)	418.8								
Failure	Box								
Thread no	11								
Initiation (cycles)	0.5×10^{6}								
Life (cycles)	1.55×10^{6}								

notes:
The first fully formed box thread is no 7.

r (mm) = 71.6
t (mm) = 22.0
ρ (mm) = 0.97
h (mm) = 3.09
θ (degrees) = 30
SCF = 7.36

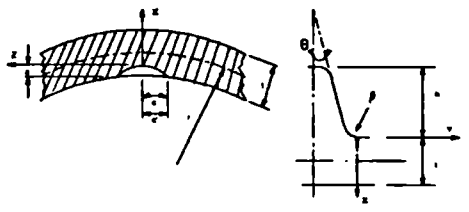

Test no / ID	Axial 6	n (cycles)	a (mm)	c (mm)	$\frac{2c}{a}$	a_{mid} (mm)	da/dn	a/t	Y_{esp} $\frac{c=1.23\times10^{-12}}{m=3.42}$
Description	NC50 $6^1/_2$" x $3^1/_4$" Standard	1.96×10^6	-	-	-	-	-	-	-
Mat^L Ref	AG17								
Torque (ft lbs)	28,000								
Finish	As Machined								
Anti-Gall	Bondarite								
Lubricant	Koper-kote								
Δ P (KN)	1061.0								
R	0.017								
Freq (Hz)	1.35								
$\Delta \sigma_{nom}$ (MPa)	66.1								
$\Delta \sigma_{local}$ (MPa)	522.2								
Failure	none								
Thread no	-								
Initiation (cycles)	-								
Life (cycles)	-								

notes:
Specimen had been cycled at σ_{nom} = 40.5 MPa for 5.0×10^6 cycles. - RUNOUT

r (mm) = 71.6
t (mm) = 22.0
ρ (mm) = 0.97
h (mm) = 3.09
θ (degrees) = 30
SCF = 7.09

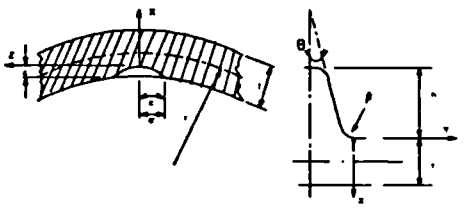

Test no / ID	Rotating Bend 1	n (cycles)	a (mm)	c (mm)	$\frac{2c}{a}$	a_{mid} (mm)	da/dn	a/t	Y_{app} $\frac{a=2.05\times10^{-11}}{m=2.61}$
Description	NC50 $6^1/_2$" x $2^1/_2$" Standard	1.27×10^6	2.5	-	-	3.0	1.33×10^{-9}	0.12	1.12
Mat^L Ref	4145H	2.02×10^6	3.5	8.1	4.6	4.0	2.04×10^{-9}	0.16	1.14
Torque (ft lbs)	30,000	2.51×10^6	4.5	9.0	4.0	5.2	2.77×10^{-9}	0.21	1.13
Finish	As Machined	2.98×10^6	5.8	9.0	3.1	7.2	2.81×10^{-9}	0.29	0.96
Anti-Gall	Kemplate	3.94×10^6	8.5	13.2	3.1	11.7	6.85×10^{-9}	0.47	1.06
Lubricant	Koper-kote	4.86×10^6	14.8	25.9	3.5	19.9	11.1×10^{-9}	0.80	0.98
M (KNm)	1. 19.7 2. 22.4	5.78×10^6	25.0	30.0	2.4				
R	-1								
Freq (Hz)	4.0								
$M R_{max} / I$ (MPa)	1. 45.6 2. 51.8								
$\Delta\sigma_{local}$ (MPa)	1. 562.0 2. 638.2								
Failure	Box								
Thread no	11								
Initiation (cycles)	0.8×10^6								
Life (cycles)	5.78×10^6								

notes:

Moment Arm = 0.726m

Loading '2' - Beach Marking only

$P(kN) = [0.0267 F(psi)]^{0.947}$

$I = 35.67 \times 10^{-6} m^4$

$R_{max} = 82.55 \times 10^{-3} m$

r (mm) = 70.0

t (mm) = 25.0

ρ (mm) = 0.97

h (mm) = 3.09

θ (degrees) = 30

SCF = 8.8

$C_B = 0.7$

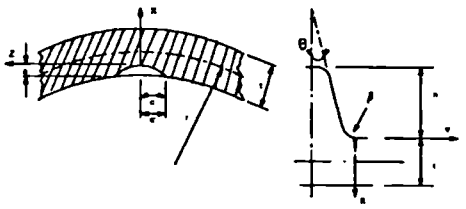

Test no / ID	Rotating Bend 2	n (cycles)	a (mm)	c (mm)	$\frac{2c}{a}$	a_{end} (mm)	da/dn	a/t	Y_{esp} $\frac{c=2.09\times10^{-11}}{m=2.61}$
Description	NC50 $6^1/_2$" x $3^1/_4$" Standard	0.66 x 10^6	13.0	81.3	12.5	16.5	15.9 x 10^{-9}	0.66	0.92
Mat^L Ref	4145H	1.10 x 10^6	20.0	105.0	10.5	22.0	28.6 x 10^{-9}	0.88	1.00
Torque (ft lbs)	28,000	1.24 x 10^6	24.0	138.0	11.5				
Finish	As Machined								
Anti-Gall	Kemplate								
Lubricant	Koper-kote								
M (KNm)	1. 25.5 2. 22.4								
R	-1								
Freq (Hz)	4.0								
$M R_{max} / I$ (MPa)	1. 61.3 2. 54.1								
$\Delta\sigma_{local}$ (MPa)	1. 608.4 2. 537.0								
Failure	Box								
Thread no	11								
Initiation (cycles)	0								
Life (cycles)	1.24 x 10^6								

notes:

Moment Arm = 0.726m

Loading '2' - Beach Marking only

$P(kN) = [0.0267\ F(psi)]^{0.947}$

$I = 34.19 \times 10^{-6} m^4$

$R_{min} = 82.55 \times 10^{-3} m$

r (mm) = 70.0

t (mm) = 25.0

ρ (mm) = 0.97

h (mm) = 3.09

θ (degrees) = 30

SCF = 7.09

$C_B = 0.7$

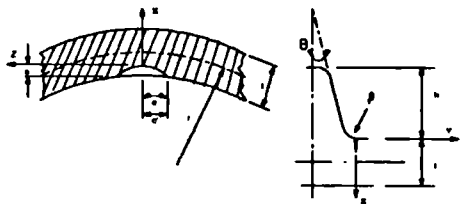

Test no / ID	Rotating Bend 3	n (cycles)	a (mm)	c (mm)	$\frac{2c}{a}$	a_{mid} (mm)	da/dn	a/t	Y_{exp} $\frac{c=1.23\times10^{-12}}{m=3.42}$
Description	NC50 $6^{1}/_{2}$" x $2^{13}/_{16}$" BB & SR	0.58×10^{6}	5.5	25.0	9.1	7.9	8.3×10^{-9}	0.316	1.28
Mat^{L} Ref	AG17	1.15×10^{6}	10.3	54.0	10.5	17.7	81.7×10^{-9}	0.706	1.67
Torque (ft lbs)	32,000	1.33×10^{6}	25.0	80.0	6.4				
Finish	As Machined								
Anti-Gall	Bondarite								
Lubricant	Koper-kote								
M (KNm)	1. 27.8 2. 21.2								
R	-1								
Freq (Hz)	2.75								
$M R_{max}/I$ (MPa)	1. 65.2 2. 49.7								
$\Delta\sigma_{local}$ (MPa)	1. 700.6 2. 534.0								
Failure	Box								
Thread no	11								
Initiation	0								
Life (cycles)	1.33×10^{6}								

notes:

Moment Arm = 0.726m

Loading '2' - Beach Marking only

$P(kN) = [0.0267\ F(psi)]^{0.947}$

$I = 35.19 \times 10^{-6} m^{4}$

$R_{max} = 82.55 \times 10^{-3}$ m

The first fully formed box thread is no 7.

r (mm) = 71.6

t (mm) = 22.0

ρ (mm) = 0.97

h (mm) = 3.09

θ (degrees) = 30

SCF = 7.36

$C_{\theta} = 0.73$

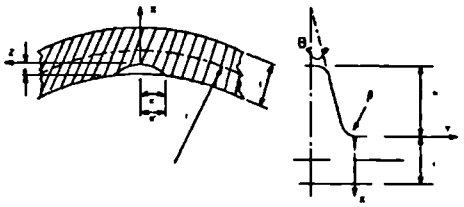

Test no / ID	Rotating Bend 4	n (cycles)	a (mm)	c (mm)	$\frac{2c}{a}$	a_{mid} (mm)	da/dn	a/t	Y_{exp} $\frac{c=1.23\times10^{-12}}{m=3.42}$
Description	NC50 $6^1/_2$" x $3^1/_4$" Standard	0.26×10^6	6.0	17.5	5.8	7.0	4.8×10^{-9}	0.33	1.48
Mat^L Ref	AG17	0.67×10^6	8.0	40.0	10.0	9.0	7.5×10^{-9}	0.43	1.49
Torque (ft lbs)	30,000	1.00×10^6	10.5	80.0	15.2	11.8	5.3×10^{-9}	0.56	1.17
Finish	As Machined	1.48×10^6	13.0	130.0	20.0	14.5	9.3×10^{-9}	0.69	1.24
Anti-Gall	Bondarite	1.80×10^6	16.0	170.0	21.3	17.0	5.2×10^{-9}	0.81	0.97
Lubricant	Koper-kote	2.19×10^6	18.0	172.5	19.2	19.5	13.8×10^{-9}	0.93	1.20
M (KNm)	1. 21.2 2. 18.4	2.41×10^6	21.0	175.0	16.7				
R	-1								
Freq (Hz)	2.75								
$M\,R_{max}\,/\,I$ (MPa)	1. 51.2 2. 44.4								
$\Delta\sigma_{local}$ (MPa)	1. 291.8 2. 253.1								
Failure	Pin								
Thread no	15								
Initiation (cycles)	0								
Life (cycles)	2.41×10^6								

notes:

Moment Arm = 0.7785m

Loading '2' - Beach Marking only

$P(kN) = [0.0267\ F(psi)]^{0.947}$

$I = 34.19 \times 10^{-6} m^4$

$R_{max} = 82.55 \times 10^3$ m

$SCF_{Bend} = 7.09$

r (mm) = 51.8

t (mm) = 21.0

ρ (mm) = 0.97

h (mm) = 3.09

θ (degrees) = 30

SCF = 3.75

$C_B = 0.76$

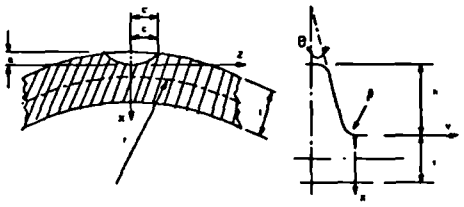

Test no / ID	Rotating Bend 5	n (cycles)	a (mm)	c (mm)	$\frac{2c}{a}$	a_{mod} (mm)	da/dn	a/t	Y_{exp} $\frac{a=2.08\times10^{-11}}{m=2.61}$
Description	$6^5/_8$" Reg $7^1/_2$" x $3^1/_4$" BB & SR	4.92×10^6	4.0	17.5	8.8	7.0	26.1×10^{-9}	0.24	1.28
Mat^L Ref	4145H	5.15×10^6	10.0	25.0	5.0	12.5	10.4×10^{-9}	0.43	0.67
Torque (ft lbs)	48,000	5.63×10^6	15.0	40.0	5.3	17.5	8.5×10^{-9}	0.60	0.53
Finish	As Machined	6.22×10^6	20.0	61.0	6.1	21.5	8.6×10^{-9}	0.85	0.48
Anti-Gall	Kemplate	6.57×10^6	23.0	75.0	6.5	26.0	42.9×10^{-9}	0.90	0.81
Lubricant	Koper-kote	6.71×10^6	29.0	91.5	6.3				
M (KNm)	1. 38.8 2. 21.2 3. 53.5								
R	-1								
Freq (Hz)	3.94								
$M R_{max}/I$ (MPa)	1. 59.3 2. 32.4 3. 81.7								
$\Delta\sigma_{local}$ (MPa)	1. 379.1 2. 207.2 3. 522.4								
Failure	Pin								
Thread no	15								
Initiation	3.8×10^6								
Life (cycles)	6.71×10^6								

notes:

Moment Arm = 0.726m

Specimen was cycled under moment '1' for 4.92×10^6 cycles, then raised to '3'

Loading '2' - Beach Marking

$P(kN) = [0.0267\ F(psi)]^{0.947}$

$I = 62.37 \times 10^{-6} m^4$

$R_{min} = 95.25 \times 10^{-3}$ m

$SCF_{Box} = 8.5$

r (mm) = 55.8

t (mm) = 29.0

ρ (mm) = 0.635

h (mm) = 3.75

θ (degrees) = 30

SCF = 4.32

$C_B = 0.74$

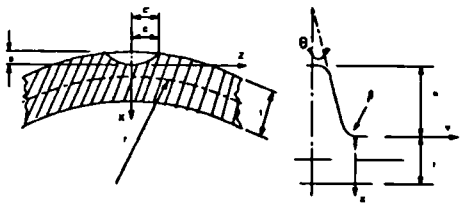

Test no / ID	Rotating Bend 6	n (cycles)	a (mm)	c (mm)	$\frac{2c}{a}$	a_{mid} (mm)	da/dn	a/t	Y_{exp} $\frac{c = 2.08 \times 10^{-11}}{m = 2.61}$
Description	$6^{5}/_{8}$" Reg $7^{1}/_{2}$" x $3^{1}/_{4}$" BB & SR	0.63 x 10^{6}	12.5	55.0	8.8	14.5	29.9 x 10^{-9}	0.69	1.08
Mat^{L} Ref	4145H	0.76 x 10^{6}	16.5	62.5	7.6	18.0	83.3 x 10^{-9}	0.86	1.43
Torque (ft lbs)	48,000	0.80 x 10^{6}	19.5	74.0	7.6	20.3	7.7 x 10^{-9}	0.96	0.54
Finish	As Machined	0.99 x 10^{6}	21.0	97.5	9.3				
Anti-Gall	Kemplate								
Lubricant	Koper-kote								
M (KNm)	1. 46.7 2. 21.2								
R	-1								
Freq (Hz)	3.94								
$M R_{max}/I$ (MPa)	1. 71.3 2. 32.4								
$\Delta\sigma_{local}$ (MPa)	1. 933.4 2. 424.2								
Failure	Box								
Thread no	11								
Initiation	0								
Life (cycles)	0.99 x 10^{6}								

notes:

Moment Arm = 0.726m

Loading '2' - Beach Marking only

$P(kN) = [0.0267\ F(psi)]^{0.947}$

$I = 62.37 \times 10^{-6} m^{4}$

$R_{max} = 95.25 \times 10^{-3}$ m

THe first fully formed box thread is no 7.

r (mm) = 84.3

t (mm) = 22.0

ρ (mm) = 0.635

h (mm) = 3.75

θ (degrees) = 30

SCF = 8.5

$C_B = 0.77$